# Study of Meson Photoproduction resulting in Multitrack-Final States using CLAS-g12 Data

Z. Akbar, V. Crede, A. Goncalves, T. Hu, A. Hurley, K. Romines, C. Zeoli
Florida State University

August 22, 2018

**Abstract**

The study of baryon resonances provides a deeper understanding of the strong interaction because the dynamics and relevant degrees of freedom hidden within them are reflected by the properties of the excited states of baryons. Higher-lying excited states at and above 1.7 GeV/$c^2$ are generally predicted to have strong couplings to final states involving a heavier meson, e. g. one of the vector mesons, $\rho$, $\omega$, $\phi$, as compared to a lighter pseudoscalar meson, e. g. $\pi$ and $\eta$. Decays to the $\pi\pi N$ final states via $\pi\Delta$ also become more important through the population of intermediate resonances. We observe that nature invests in mass rather than momentum. The excited states of the nucleon are usually found as broadly-overlapping resonances which may decay into a multitude of final states involving mesons and baryons. Polarization observables make it possible to isolate single-resonance contributions from other interference terms. The CLAS-g12 experiment, as part of the $N^*$ spectroscopy program at Jefferson Laboratory, accumulated photoproduction data using circularly-polarized tagged photons incident on an unpolarized liquid-hydrogen target in the photon energy range from about 1.1 to 5.4 GeV. This document summarizes the FSU analyses of reactions and observables which involve two charged pions (or two charged Kaons), either in the fully exclusive reaction $\gamma p \to p\,\pi^+\pi^-$ ($\gamma p \to p\,\phi \to p\,K^+K^-$) or in the semi-exclusive reaction with a missing neutral pion, $\gamma p \to p\,\omega$ ($p\eta$) $\to p\,\pi^+\pi^-$ ($\pi^0$) and $\gamma p \to K^0\,\Sigma^+ \to p\,\pi^+\pi^-$ ($\pi^0$).

The group at FSU has extracted the beam-helicity asymmetry, $I^{\odot}$, for the two-$\pi$ reaction $\gamma p \to p\pi^+\pi^-$ and has studied the cross sections for the reactions $\gamma p \to p\,\omega$ ($p\,\eta$, $K^0\,\Sigma^+$) $\to$ $p\,\pi^+\pi^-$ ($\pi^0$) as well as $\gamma p \to p\,\phi \to p\,K^+K^-$ and determined the spin-density matrix elements for the $\omega$, $\phi$ [1]. These g12-analyses complement our comprehensive FSU program on vector-meson photoproduction which also includes results from CLAS-g8b and CLAS-g9 (FROST). The $\omega$ and the $\phi$ meson are observed and studied directly from the data and the information on the (broad) $\rho$ can be extracted from the double-pion reaction in a partial-wave analysis. We also observed a small $\phi \to \pi^+\pi^-$ ($\pi^0$) contribution in our g12 data but did not further investigate this decay.

With the high-statistics CLAS-g12 data sample and a measured differential cross section procured, a Dalitz Plot (DP) analysis of the $\omega \to 3\pi$ decay dynamics in close cooperation with the Joint Physics Analysis Center (JPAC) at JLab has been conducted. In addition to fitting the Dalitz-Plot expansion parameters (e.g. $\alpha$, $\beta$, $\gamma$, and $\delta$), a first-time, real-data fit to an Isobar and Unitarity based decay model, JPAC decay amplitude, has been made. As a consequence of unitarity, this amplitude also accounts for both elastic (i.e. $\pi$-$\pi$) and inelastic (e.g. $K$-$\bar{K}$) rescattering effects. The novel separation and parameterization of these latter contributions are unique features of this model which set it apart from alike models.

[1] The work on the $\gamma p \to p\,\phi$ reaction and the $\omega$ Dalitz plot is still ongoing and will be added to this note later.

# Contents

# 1 Introduction

sEffective theories and models have been developed to better understand the properties of baryon resonances. Various constituent quark models (CQMs) are currently still the best approach to make predictions for the properties of the baryon ground states and excited states. However, the predictions for the hadron spectrum made by these models do not match accurately the states measured by experiment, especially at high energies. These models for example predict many more resonances than have been observed, leading to the so-called "missing resonance" problem. The latest results in baryon spectroscopy suggest that three-body final states are very important in order to establish higher-mass resonances. Moreover, the photoproduction of vector mesons, such as $\omega$, $\rho$, and $\phi$ has remained underexplored in recent years but will also give us very useful insight into high-mass resonances. It has been generally accepted that a nucleon resonance needs to be observed in many different decay modes to be considered convincingly established. The two-pion final states are the dominant contributors to the total photo-absorption cross section above $W \approx 1.9$ GeV ($E_\gamma \approx 1.46$ GeV). In this analysis, we extracted the beam-helicity asymmetry, $I^\odot$, for the reaction $\gamma p \to p\,\pi^+\pi^-$, the cross sections for the reactions $\gamma p \to p\,\omega$ $(p\,\eta,\, K^0\,\Sigma^+) \to p\,\pi^+\pi^-\,(\pi^0)$, $\gamma p \to p\,\phi \to p\,K^+K^-$, and the spin-density matrix elements for the $\omega$ and $\phi$ [2] mesons.

From an experimental and an analysis point-of-view, the reaction $\gamma p \to p\,\pi^+\pi^-$ as well as $\gamma p \to p\,\pi^+\pi^-\,(\pi^0)$ have the same charged particles in the final state and therefore, it was straight forward to unify the analysis of these two hadronic final states in terms of extracting the observables. The subsequent interpretation of the results will certainly proceed in different ways.

| Thesis Topic | Student Name |
|---|---|
| Cross Sections in $\omega$, $\eta$, and $K^0\,\Sigma$ Production<br>Spin-Density Matrix Elements in $\omega$ Production<br>Beam-Helicity Asymmetry $I^\odot$ in $\pi^+\pi^-$ Production | Zulkaida Akbar (PhD Thesis) |
| Cross Sections in $K^0\,\Sigma$ Production | K. Romines (Honors Thesis, Spring 2017) |
| Dalitz-Plot Analysis of $\omega \to \pi^+\pi^-\pi^0$ | C. Zeoli (PhD Thesis, Fall 2016) |
| Cross Sections in $\phi \to K^+K^-$ Production | A. Hurley (Honors Thesis, Spring 2016) |
| Cross Sections in $\phi \to K^+K^-$ Production<br>Spin-Density Matrix Elements in $\phi$ Production | T. Hu (PhD Thesis) |
| Dalitz-Plot Analysis of $\omega$, $\phi \to \pi^+\pi^-\pi^0$ | A. Goncalves (PhD Thesis) |

Table 1: *Completed and ongoing thesis topics. The Dalitz-plot analyses are not part of this review.*

# 2 The g12 Experiment at Jefferson Lab

The experimental Hall B at Jefferson Lab provided a unique set of experimental devices for the g12 experiment. The CEBAF Large Acceptance Spectrometer (CLAS) [1], which was housed in Hall B, was a nearly-$4\pi$ spectrometer optimized for hadron spectroscopy. The bremsstrahlung

[2] At this point, the work on $\gamma p \to p\,\phi$ is still ongoing and will be added to this note later.

tagging technique, which was used by the broad-range photon tagging facility [2] at Hall B, could tag photon energies over a range from about 20 % to 95 % of the incident electron energy and was capable of operating with CEBAF beam energies up to 5.5 GeV. The g12 experiment used a circularly-polarized photon beam in combination with an unpolarized liquid-hydrogen target. The incident-photon energy range covered in the experiment was about 1.1 to 5.4 GeV.

The CLAS-g12 group is the first run grup which went through a formal run-group review. The document *The g12 Analysis Procedures, Statistics, and Systematics* was produced. The goal of the review and the document was to identify, review and approve common analysis procedures relevant to most of the g12 analyses. This will allow the collaboration to streamline subsequent reviews of individual g12 physics analyses. The following procedures are common for most analyses and have been approved by the g12 procedure review committee in the g12 analysis procedures manuscript:

- Calibration and *cooking* of the data sets.
- Momentum and beam-energy corrections as described in the general g12 analysis note.
- Fiducial cuts (as described in Section 5.3 of the analysis note): Three different scenarios were studied and cuts derived in terms of *nominal, tight, loose*. We chose *nominal* for our analyses.

Other common g12 procedures include:

- Inclusive *good run list* as described in Table 7 of the g12 note.
- Target density and its uncertainty.
- Photon flux calculation and its uncertainty.
- Degree of circular beam polarization and its uncertainty.
- Monte Carlo GPP and GSIM parameters.
- Drift chamber efficiency map.
- Knockout list of EC and TOF paddles.
- Lepton identification (ID) approved as "di-lepton ID."

However, the following analysis procedures are subject to individual reviews and are thus discussed in this document:

- Particle ID and event selection.
- Kinematic fitting.
- Trigger simulation (and efficiency studies).
- Accounting for multiple (accidental) photons.

This analysis note is organized as follows. In Section 3, we discuss the experimental conditions of the g12 data set, the identification of the photon and final-state particles, kinematic fitting, and additional cuts, which were used to tune the data set. Moreover, some details on the beam polarization relevant for the $I^{\odot}$ analysis are introduced. Section 4 describes the extraction of the observables for the reactions $\gamma p \to p\pi^+\pi^-$, $\gamma p \to p\,\omega$, $\gamma p \to p\,\eta$, $\gamma p \to K^0\,\Sigma^+$, and $\gamma p \to p\,\phi$. The systematic uncertainties are discussed in Section 5 and the final results and conclusions of the analyses are presented in Section 6.

| Period | Runs | Trigger Configuration |
|---|---|---|
| 1 | 56519 and earlier | not prescaled, trigger change at 4.4 GeV |
| 2 | 56520 - 56594, 56608 - 56646 | not prescaled, trigger change at 3.6 GeV |
| 3 | 56601 - 56604, 56648 - 56660 | prescaled |
| 4 | 56665 - 56667 | prescaled |
| 5 | 56605, 56607, 56647 | prescaled |
| 6 | 56668 - 56670 | prescaled |
| 7 | 56897 and later | prescaled |
| 8 | 57094 and later | prescaled |
| 9 | 56585, 56619, 56637 | single-sector, not prescaled |
| 10 | 56663 and later | single-sector, not prescaled |

Table 2: *The different trigger configurations used in g12 (from the g12 wiki and Ref. [3]).*

# 3 Event Selection

## 3.1 The CLAS-g12 Data Set

This section summarizes the experimental conditions of the g12 data set. The data for this experiment were taken between April 1st and June 9th, 2008. The data set was further divided into ten different groups of runs according to different trigger configurations.

Table 2 shows the different g12 trigger configurations. We used only Period 2 (starting from run 56520) for our analyses at FSU. For these data, the trigger required either (at least) three charged tracks with no restrictions on the photon energy or only two tracks with the additional requirement of having at least one photon detected with an energy above 3.6 GeV. Since our primary motivation initially was to extract the $\omega$ (and $\pi^+\pi^-$) cross sections with high quality, we decided not to mix trigger configurations and thus, avoided the prescaled data and those using an Electromagnetic Calorimeter (EC)-based photon or lepton trigger (Period 3 - 8). Period 1 suffered from lower statistics and using it would not have significantly improved the statistical uncertainties of our results. Moreover, this period switched from a three-track requirement to a two-track requirement at a different energy and also used a different beam current.

The information included in the raw data consisted of QDC (Charge to Digital Convertor) and TDC (Time to Digital Converter) channel IDs and values. In a first step, the data had to undergo reconstruction, or be *cooked.* This process converted the data into physical quantities like particle IDs, positions, angles, energies, and momenta. The data calibration was carried out independently for each detector component of CLAS. After the detectors had been calibrated and the particle tracks had been reconstructed, the data were made available for physics analysis. Each event had its information organized in CLAS data banks[3]. These data banks contained not only the properties of the particles involved in a reaction but also information about detector hits.

[3] http://clasweb.jlab.org/bos/browsebos.php?bank=gpid&build=64bit/STABL

Here we list the most relevant data banks that we used in our g12 analyses:

1. **PART** – This bank contained most of the details about the detected particles, such as the particle IDs, 4-vectors, vertex of each particle, and other information from various detectors.
2. **TAGR** – In this bank, information about all incident photons was stored, e.g. the energy of the photon(s), the time of the photon(s) after the reconstruction in the Tagger, the time of the photon(s) after the RF correction, the status of the photon(s) (used to identify those which were not reconstructed properly), and the E - and T - counter ID information of the corresponding scattered electron.
3. **TBER** – Time-based tracking error bank containing fit parameters and the covariance matrix.
4. **TBID** – Bank containing information on time-based particle ID (including $\beta$ ($= \frac{v}{c}$) values).
5. **TGBI** – Trigger bank; it also stored polarization information, e.g. the helicity bit.
6. Any other bank of importance?

### 3.2 Reaction Channels and General Event Selection

The final states of interest in this analysis are $\gamma p \to p\,\pi^+\pi^-$ and $\gamma p \to p\,\pi^+\pi^-\,(\pi^0)$. These three-track channels were broken up into different topologies as shown in Table 3. A topology is defined according to the detected particles in the final state: the two-particle final states (Topologies 1 - 3) and the three-particle final states (Topologies 4 - 6). A particle which was not detected in a given topology could be identified through the missing-mass technique. For this method, the Lorentz vectors of the incoming beam and the target were used. The four-momentum of a missing particle in the reaction was then determined from the measured three-momenta and the particle energies. The missing four-momentum was given by:

$$x^\mu \;=\; k^\mu \;+\; P^\mu \;-\; \sum_{i=1}^{2,3} p_i^\mu \,, \tag{1}$$

where $k^\mu$ and $P^\mu$ are the initial photon and target-proton four-momenta and $p_i^\mu$ are the four-momenta of the two or three detected final-state particles. The missing mass $m_X$ was defined as:

$$m_X^2 \;=\; x^\mu x_\mu \,. \tag{2}$$

The missing-mass distribution was used for a data quality check after all corrections and cuts had been applied. The four-momentum vector $x^\mu$ in Equation 1 was used to complete the set of four-vectors for Topology 5 Table 3). The other two-track final states with a missing particle (Topology 1-3) were more complicated to analyze owing to the special trigger configuration in Period 2.

Events were pre-selected based on the particles' identification number (PID), which was determined during the cooking process. Events that did not meet this requirement (Table 3) were ignored and subsequently omitted from the analysis. The calculation of the detected particles' masses, which was necessary to determine the PIDs, used two independently-measured quantities, the momentum, $p$, and the velocity as a fraction of the speed of light, $\beta$. The magnitude of a particle's momentum was determined with an uncertainty of $< 1\,\%$ using information from the CLAS

Drift Chambers (DC) [4]. The quantity $\beta$ of a detected final-state particle was determined with an uncertainty of up to 5 % [5] using a combination of the Start Counter (SC), the Time-of-Flight (TOF) spectrometer, and the particle's trajectory through CLAS. The detected particle's mass could then be calculated by:

$$m^2_{\text{particle } X} = \frac{p^2\,(1\,-\,\beta^2)}{\beta^2}\,. \tag{3}$$

After the particle's mass had been calculated, it was compared to the masses of known particles (hadrons and leptons). If this calculated mass matched that of a known particle (within resolution), the PID associated with that mass was assigned to the final-state particle. This value could then be used to select certain final-states for analysis. In this analysis, the physical properties of the final-state particles (e.g. their 4-vectors, vertex information, etc.) were extracted from the PART data banks. Photon and final-state particle selection was further improved by applying cuts and corrections (see Section 3.3). We also used kinematic fitting (see Section 3.5) to fine-tune the initial- and final-state momenta by imposing energy- and momentum conservation. Finally, to separate signal events from the remaining background, we used an event-based $Q$-factor method which is discussed in more details in Section 3.12.

In a short summary, listed below are the cuts and (in the right order) corrections that were applied to the g12 data in these FSU analyses.

**General g12 Corrections**

- Tagger-sag corrections (done in the cooking process).
- ELoss corrections using the standard CLAS package [6].
- Beam-energy corrections based on the CLAS-approved run-group approach [3].
- Momentum corrections based on the CLAS-approved run-group approach [3].

| Reaction | Topology | Reconstructed Particles | | | | Missing Particle of Interest |
|---|---|---|---|---|---|---|
| | | Total | p | $\pi^+\,(K^+)$ | $\pi^-\,(K^-)$ | |
| $\gamma p \to p\,\pi^+\,(\pi^-)$ | 1 | 2 | 1 | 1 | 0 | $m_{\pi^-}$ |
| $\gamma p \to p\,\pi^-\,(\pi^+)$ | 2 | 2 | 1 | 0 | 1 | $m_{\pi^+}$ |
| $\gamma p \to (p)\,\pi^+\pi^-$ | 3 | 2 | 0 | 1 | 1 | $m_p$ |
| $\gamma p \to p\,\pi^+\pi^-$ | 4 | 3 | 1 | 1 | 1 | 0 |
| $\gamma p \to p\,\pi^+\pi^-\,(\pi^0)$ | 5 | 3 | 1 | 1 | 1 | $m_{\pi^0}$ |
| $\gamma p \to p\,K^+K^-$ | 6 | 3 | 1 | 0 (1) | 0 (1) | 0 |

Table 3: *Classification of the reactions, $\gamma p \to p\,\pi^+\pi^-$, $\gamma p \to p\,K^+K^-$, and $\gamma p \to p\,\pi^+\pi^-\,(\pi^0)$, using different topologies. Reconstructed particles were identified by their PID information from the TBID bank. Note that we did not analyze Topologies 1 - 3 because of the dominant three-track trigger condition in our data set.*

**Florida State U. Cuts**

- Vertex cut: $-110.0 < z$-vertex $< -70.0$ cm.
- Photon selection & accidentals
  (nGammaRF() = 1 & TAGR_ID equal for all tracks; information from TAGR bank)
- Particle ID cut [4], $\Delta\beta = |\beta_c - \beta_m| \leq 3\sigma$, and timing cut, $|\Delta t_{\,\mathrm{TBID}}| < 1$ ns [5].
- Confidence-level cut of CL $> 0.001$ for $\gamma p \to p\,\pi^+\pi^-\,(\pi^0)$ and $\gamma p \to p\,K^+K^-$.
- Fiducial cuts: *nominal* scenario [3].

The order of these applied cuts and corrections was quite flexible with the exception of a few cases. Momentum corrections were applied after the energy-loss corrections. The following sections describe the applied cuts and corrections in more detail.

## 3.3 Photon and Particle Identification

### 3.3.1 Initial-Photon Selection (Cuts on Timing and Accidental Photons)

The electrons, which were used to produce the beam of polarized photons via bremsstrahlung radiation, were delivered from the accelerator into Hall B in the form of 2-ns bunches. Since each bunch contained many electrons, there were several potential photon candidates per recorded event that could have triggered the reaction inside the target. Random electron hits could also occur from various background sources (e.g. cosmic rays). These did not create bremsstrahlung photons but the hits were registered in the tagger scintillators. It was important to determine the correct photon in each event (out of about five candidates on average) because the corresponding photon energy was key to understanding the initial state of the event. The analysis steps taken in the photon selection were as follows:

1. The Start Counter time per track at the interaction point, $t_{\mathrm{track}}$, was given by:

$$t_{\mathrm{track}} = t_{\,\mathrm{ST}} - \frac{d}{c\,\beta_{\mathrm{calc}}}\,, \tag{4}$$

   where $t_{\,\mathrm{ST}}$ was the time when the particle was detected by the Start Counter, $d$ was the length of the track from the interaction point to the Start Counter, and $c\,\beta_{\mathrm{calc}}$ was the calculated velocity of the particle. These (track) times could be averaged to give an event time, $t_{\mathrm{event}}$.

   The time at which a candidate photon arrived at the interaction point, $t_\gamma$, was given by:

$$t_\gamma = t_{\mathrm{center}} + \frac{d'}{c}\,, \tag{5}$$

   where $t_{\mathrm{center}}$ was the time at which the photon arrived at the center of the target and $d'$ was the distance between the center of the target and the event vertex along the beam-axis. We did not consider the $x$- and $y$-coordinates of the event vertex because they were comparable to the vertex resolution. In this analysis, the $t_\gamma$ values were obtained from TAGR[].TPHO.

[4] In the final analysis, we applied the $\Delta\beta \leq 3\sigma$ cut on either the proton or the $\pi^+$ (no cut on the $\pi^-$).
[5] $\Delta t_{\,\mathrm{TBID}} = stVtime() - vtime()$ is the coincidence time between the vertex and the photon time.

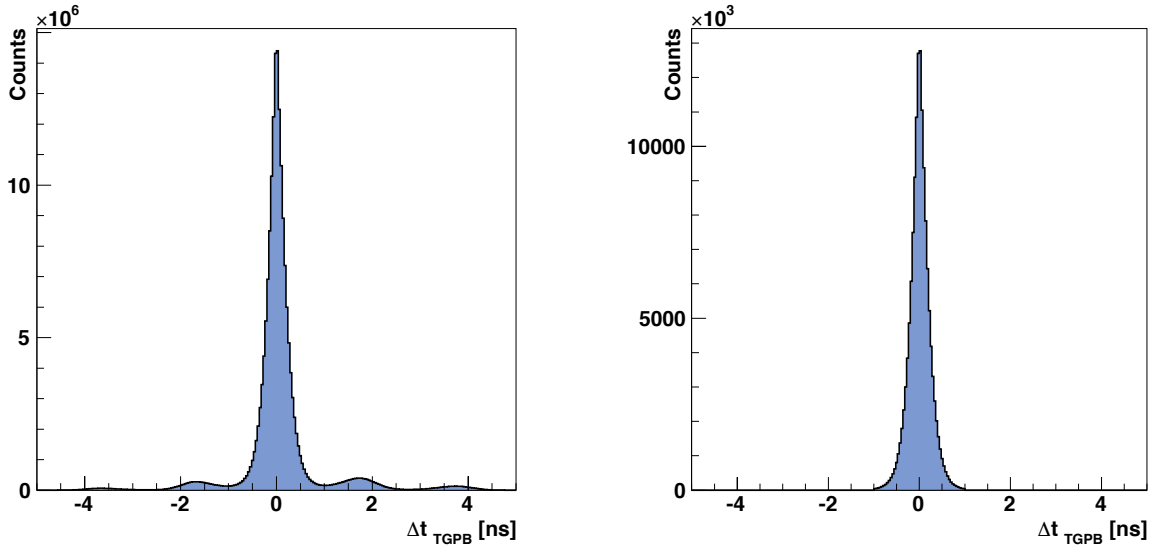


Figure 1: *Left: Example of a coincidence-time distribution,* $\Delta t_{\mathrm{TGPB}}$*, for the inclusive* $p\pi^+\pi^-$ *final-state topology. The 2-ns bunching of the photon beam is clearly visible in the histogram. Right: Distribution of* $\Delta t_{\mathrm{TBID}} = t_{\mathrm{event}} - t_\gamma$ *for the selected photon (one entry per event) after PID cuts. The event vertex time,* $t_{\mathrm{event}}$*, was based on Equation 4. We only considered events which had exactly one candidate photon in the same RF bucket per track; each identified track had to be associated with the same photon.*

Both, $t_\gamma$ as well as $t_{\mathrm{event}}$, describe the time of the $\gamma p$ interaction – based on initial- and final-state particles, respectively. To find the correct initial photon, we looked at the corresponding time differences. The *coincidence time*, $\Delta t_{\mathrm{TBID}}$, was thus defined per photon as the difference between the Tagger time and the Start Counter time at the interaction point, $t_{\mathrm{event}} - t_\gamma$. Since each event had several candidate photons, several $\Delta t_{\mathrm{TBID}}$ values were available, which could be obtained from information in the TBID bank. Figure 1 (left) shows an example distribution of the coincidence time, $\Delta t_{\mathrm{TBID}}$. The figure clearly shows the 2-ns bunching of the photons that arrived at the target. In each event, the information on energy and timing, $t_\gamma$, was written to the event's TAGR bank for all photons. The total number of photon candidates per event was also available. *The* photon selection itself was performed by the CLAS offline software in the cooking process. However, we applied a timing cut of $\Delta t_{\mathrm{TBID}} < 1$ ns in this analysis.

2. Occasionally, events could have more than one candidate photon with $|\Delta t_{\mathrm{TBID}}| < 1$ ns. In such cases, the photon selection could not be made based on their time information. The fraction of these events was about 13 % in the g12 experiment. To prevent any ambiguity, only events with exactly one photon candidate in the same RF bucket for all selected tracks (nGammaRF() = 1) were considered in this analysis. In addition, we also ensured that the selected photon was the same for all reconstructed tracks (TAGR_ID equal for all tracks). Figure 1 (right) shows an example of the coincidence-time distribution for the selected initial photon (one entry per event) after PID cuts.

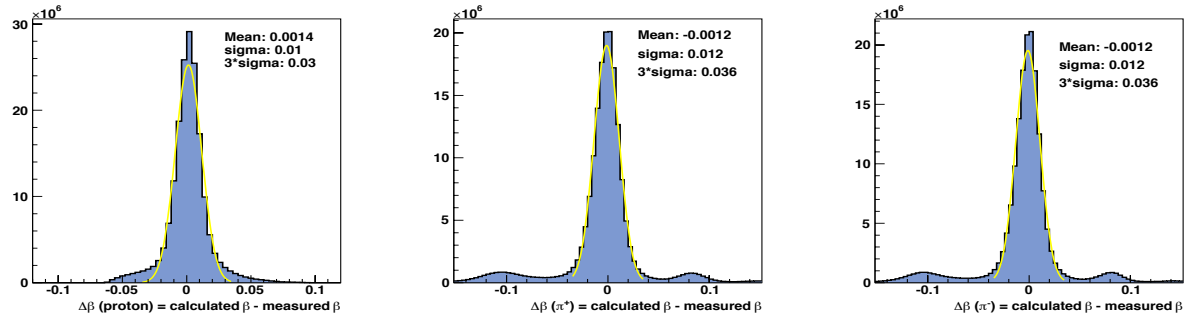


Figure 2: *Distributions of* $\Delta\beta = \beta_{\rm c} - \beta_{\rm m}$ *for protons (left) as well as for the* $\pi^+$ *(middle) and for the* $\pi^-$ *(right) from the g12 experiment (full statistics used in our FSU analyses, Period 2 (see Table 2)). The quantity* $\beta_{\rm c}$ *was calculated based on the particle's PDG mass [7]. Events in the center peak were selected after applying a* $|\beta_{\rm c} - \beta_{\rm m}| \leq 3\sigma$ *cut. See text for more details.*

### 3.3.2 Proton and Pion Selection

The photon energy for each event was selected according to the procedure outlined in Section 3.3.1. In the next step, the identification of the final-state particles, proton, $\pi^+$, and $\pi^-$, was needed. As mentioned in Section 3.2, we initially used particle ID information from the PART bank and selected those events which belonged to the topologies of our interest (Table 3). For a more refined selection of the particles, we used the information on the measured and calculated $\beta$ values of each particle. The TBID bank contained the CLAS-measured momentum of a particle; a theoretical value, $\beta_{\rm c}$, for that particle could then be calculated from this measured momentum and an assumed mass. The $\beta_c$ values for all possible particle types were compared to the CLAS-measured empirical $\beta_{\rm m} = \frac{v}{c}$ value. Particle identification then proceeded by choosing the calculated $\beta_{\rm c}$ closest to the measured $\beta_{\rm m}$. Figure 2 shows the differences, $\Delta\beta = \beta_{\rm c} - \beta_{\rm m}$ for the different final-state particles based on the full g12 statistics that we used in our FSU analyses, (Period 2, see Table 2). Assuming a PDG mass $m$ for the particle [7], $\Delta\beta$ was given by:

$$\Delta\beta = \beta_{\rm c} - \beta_{\rm m} = \sqrt{\frac{p^2}{m^2 + p^2}} - \beta_{\rm m}\,. \tag{6}$$

The prominent peaks around $\Delta\beta = 0$ shown in Figure 2 correspond to the particles of interest. It can be seen in the figures that the $\Delta\beta$ distributions for the pions are slightly broader than for the proton and long tails including a prominent enhancement on either side of the central peak are visible. When the PART bank was created during the track reconstruction, electrons were not separated from pions. The additional features in the $\Delta\beta$ distributions for the pions represent these electrons which need to be filtered out. To identify the protons and pions, loose cuts on $|\beta_{\rm c} - \beta_{\rm m}|$ were applied. The cut values were determined by fitting the main peak around $\Delta\beta = 0$ with a Gaussian. Figure 3 shows the measured momentum, $p$, versus the measured $\beta_{\rm m}$ for protons and pions before (left) and after (right) applying the $|\beta_{\rm c} - \beta_{\rm m}| < 3\sigma$ cut. The bands for the pions and protons (lower band) are clearly visible.

Although the $\Delta\beta$-PID cuts significantly help avoid misidentified tracks in the selected event sample, we applied only a loose $|\Delta\beta| < 3\sigma$ cut in our final event selection on either the proton or the $\pi^+$ (no cut on the $\pi^-$). This allowed us to retain as many signal events as possible. Particle ID was

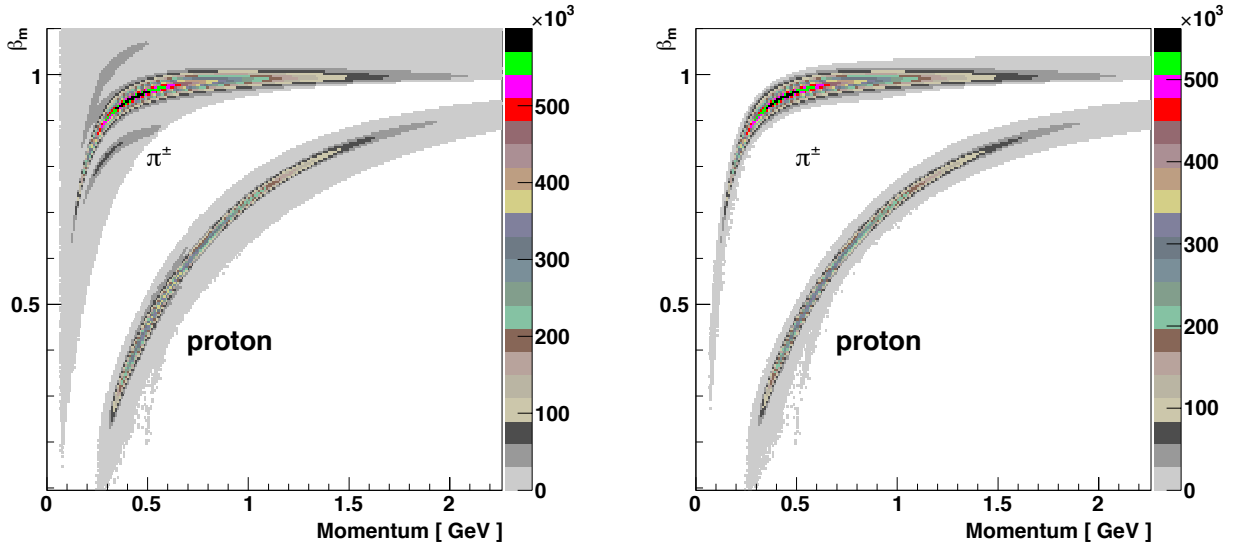


Figure 3: *Left: The measured $\beta_{\rm m}$ versus momentum on a logarithmic color scale. Note a thin horizontal line close to one for electrons, and the broad stripes for pions (top) followed by protons (bottom). Right: The measured $\beta_{\rm m}$ versus momentum after applying the $3\sigma$ cut based on the difference $\Delta\beta = \beta_{\rm c} - \beta_{\rm m}$. Clean pion and proton bands are visible. These figures were made using the full statistics used in our FSU analyses, (Period 2, see Table 2).*

further verified in kinematic fitting (Section 3.5) where any substantial misidentification of either the proton or one of the $\pi$ tracks would lead to systematic effects in the pull distributions; we did not observe this. The remaining background caused by misidentified tracks did not cause structures under the signal in the relevant mass distributions and was taken care of by our background-subtraction technique (see Section 3.12). The loose cuts were also in line with an earlier CLAS analysis of the $\omega$ and $\eta$ photoproduction cross sections [8, 9, 10].

### 3.4 Vertex Cut

In the g12 experiment, the liquid hydrogen target was not located at the center of CLAS but moved 90 cm upstream to increase the angular resolution for heavier-meson photoproduction in the forward direction. The target itself was 40 cm long and 2 cm in diameter. Therefore, a $z$-vertex cut of $-110 < z$ vertex $< -70$ cm was applied; the full $z$-vertex distribution is shown in Fig. 4.

### 3.5 Introduction to Kinematic Fitting

The 4-vectors of the final-state particles were determined in the *cooking* or reconstruction phase. Kinematic fitting [11] slightly modified these *raw* 4-vectors by imposing energy-momentum conservation on the event as a physical constraint. In a brief summary, all measured components of the Lorentz 4-vectors (the magnitude of the momentum as well as the two angles used in the drift-chamber reconstruction – $p$, $\lambda$, $\phi$, respectively) in addition to the initial photon energy were modified within their given uncertainties until the event satisfied energy-momentum conservation exactly. The determination of the correct uncertainties (or covariance matrix) was important in

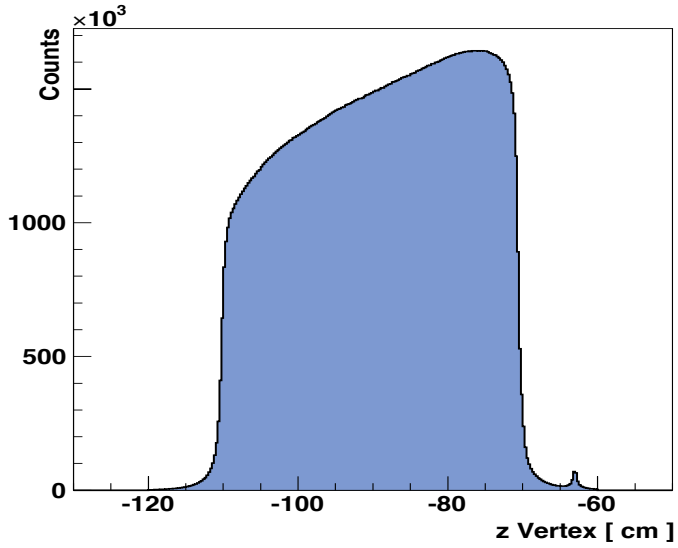


Figure 4: *The z-vertex distribution (axis along the beam line) of all reconstructed particles we used in our FSU analyses. The shape of the liquid hydrogen target is clearly visible. The small enhancement at about $z = -63$ cm originates from the exit window of the vaccuum chamber.*

this fitting procedure. The kinematically-fitted event had then several quantities which could be used to inspect the quality of the kinematic fitting: a pull value for each measured quantity and an overall $\chi^2$ value. The latter could be converted to a confidence-level (CL) value to judge the goodness-of-fit. The pull distributions were used to evaluate the initial uncertainty estimation and to study systematics. It turned out that kinematic fitting provided an effective tool to verify kinematic corrections, e. g. momentum corrections.

### 3.5.1 Confidence Level

To check the *goodness-of-fit* or the agreement between the fit hypothesis and the data, the fit $\chi^2$ value was used. The corresponding CL value was defined as:

$$CL = \int_{\chi^2}^{\infty} f(z;n)\,dz\,, \tag{7}$$

where $f(z;n)$ was the $\chi^2$ probability density function with $n$ degrees of freedom. It denoted the probability distribution for certain external constraints, e. g. energy-momentum conservation or also a missing-particle constraint. In the ideal case where all events satisfied the fit hypothesis and the measured quantities were all independent and had only statistical uncertainties, the confidence-level distribution would be flat from $(0, 1]$. However, the real data had a confidence-level distribution which showed a peak near zero (Fig. 5, left side). This peak contained events which did not satisfy the imposed constraints. These events could be hadronic background events, poorly-reconstructed events with significant systematic uncertainties, or events with misidentified particles. A cut on small CL values eliminated the majority of these background events while only a relatively small amount of good data was lost.

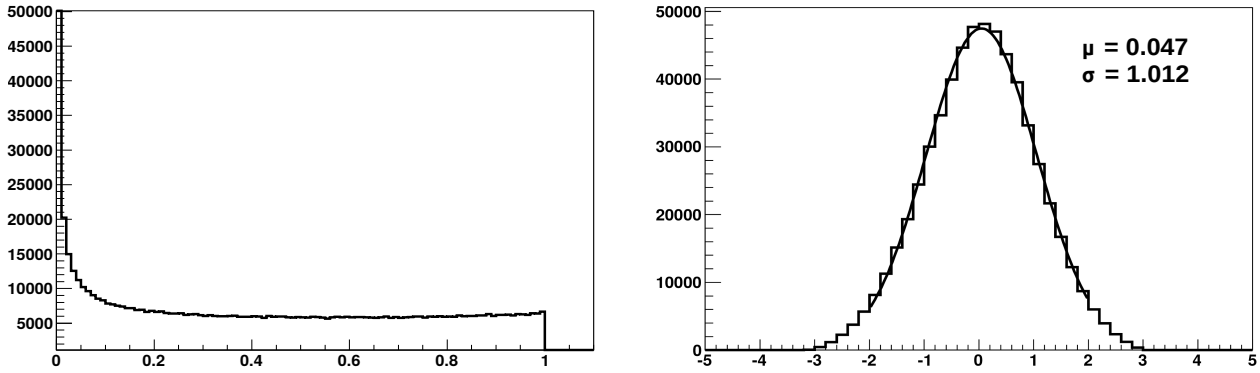


Figure 5: *Example of results from kinematic fitting. Energy and momentum conservation was imposed on Topology 4 in* $\gamma p \to p\,\pi^+\pi^-$. *Left: A confidence-level distribution. It peaks toward zero but flattens out toward one. Right: Pull distribution of the incoming photon energy. Ideally, such a distribution is Gaussian in shape, centered at the origin* ($\mu = 0$) *with a width of one* ($\sigma = 1$).

### 3.5.2 Pulls

A *pull value* is a measure of how much and in what direction the kinematic fitter has to alter a measured parameter – or to *pull* at it – in order to make the event fulfill the imposed constraint. All three fit parameters for every detected final-state particle had pull distributions. The pull value for the $i^{\text{th}}$ fit parameter was given by:

$$z_i \;=\; \frac{\epsilon_i}{\sigma(\epsilon_i)}\,, \tag{8}$$

where $\epsilon_i = \eta_i - y_i$ was the difference between the fitted value, $\eta_i$, and the measured value, $y_i$. The quantity $\sigma$ represents the standard deviation of the parameter $\epsilon_i$. Therefore, the $i^{\text{th}}$ pull can be written as:

$$z_i \;=\; \frac{\eta_i - y_i}{\sqrt{\sigma^2(\eta_i) - \sigma^2(y_i)}}\,. \tag{9}$$

The reaction $\gamma p \to p\,\pi^+\pi^-$ (using Topology 4, see Table 3) had three detected final-state particles: proton, $\pi^+$, and $\pi^-$. Since the reconstruction of each particle was based on three parameters, this topology had ten pull distributions including a pull for the initial photon energy. In the ideal case that the error matrix of these parameters was correctly determined and all remaining systematic uncertainties were negligible, the pull distributions would be Gaussian in shape with a width of one ($\sigma = 1$) and centered at zero ($\mu = 0$); such an example is shown in Figure 5 (right side). A systematic problem with the data in the quantity $\eta_i$ would be observed as an overall shift away from zero. Similarly, if the uncertainties of $\eta_i$ were consistently (overestimated) underestimated, then the corresponding pull distribution would be too (narrow) broad, and the slope of the CL distribution toward $CL = 1$ would be (positive) negative. The uncertainties of the measured parameters could be corrected from the pull distributions in an iterative procedure.

In our analysis, kinematic fitting served as an effective tool to double-check the final-state corrections approved in Ref. [3]. We used Topology 4 (all final-state particles detected) for this. The final mean and $\sigma$ values of Gaussian fits to our g12 pull distributions (after all corrections) are shown in Table 4. The distributions themselves are presented in Fig. 6, 7, and 8.

| | proton | | | $\pi^+$ ($K^+$) | | | $\pi^-$ ($K^-$) | | | $\gamma$ |
|---|---|---|---|---|---|---|---|---|---|---|
| | mom. | $\lambda$ | $\phi$ | mom. | $\lambda$ | $\phi$ | mom. | $\lambda$ | $\phi$ | E |
| CLAS-g12: $\gamma p \to p\,\pi^+\pi^-$ | | | | | | | | | | |
| $\bar{x}$ | 0.112 | −0.043 | −0.001 | 0.075 | −0.005 | −0.018 | −0.003 | −0.019 | −0.059 | −0.080 |
| $\sigma$ | 1.226 | 0.964 | 1.148 | 1.160 | 1.011 | 1.118 | 1.166 | 1.011 | 1.137 | 1.248 |
| CLAS-g12: $\gamma p \to p\,\pi^+\pi^-\,(\pi^0)$ | | | | | | | | | | |
| $\bar{x}$ | 0.140 | 0.001 | −0.211 | −0.150 | −0.023 | −0.192 | −0.194 | −0.029 | −0.164 | 0.190 |
| $\sigma$ | 1.167 | 1.182 | 1.173 | 1.193 | 1.178 | 1.161 | 1.194 | 1.179 | 1.143 | 1.209 |
| CLAS-g12: $\gamma p \to p\,K^+K^-$ | | | | | | | | | | |
| $\sigma$ | 1.071 | 0.947 | 1.019 | 0.938 | 0.941 | 0.955 | 1.026 | 0.960 | 0.967 | 1.060 |

Table 4: *Final mean, $\bar{x}$, and $\sigma$ values of Gaussian fits to our g12 pull distributions after applying all corrections. We have used the tuning parameters for the covariance matrix that were developed by Daniel Lersch (FZ Jülich) and that were recommended by the g12 run group. Note that the values for $p\,\pi^+\pi^-\,(\pi^0)$ are based on distributions which could not be perfect Gaussians owing to the missing-particle hypothesis.*

### 3.6 Kinematic Corrections

The following subsections briefly summarize some of the standard CLAS corrections. We only give a brief description here (in the order of application) without showing the actual effect on the data. The latter was discussed in Ref. [3] and has been approved by the collaboration.

#### 3.6.1 Tagger-Sag Correction

The energy of the incoming photons was determined by the Hall-B tagging system. It was observed in previous experiments that a physical sagging of the holding structure supporting the E-counter scintillator bars could be attributed to gravitational forces [12]. The consequence of this time-dependent sagging was a misalignment of the scintillator bars which led to a small shift of the scattered electron's energy [13]. In the CLAS-g12 experiment, the tagger sag was taken into account and corrected in the offline reconstruction code. No further photon energy correction was applied.

#### 3.6.2 Enery-Loss (ELoss) Correction

As charged particles traveled from the production vertex to the active components of the CLAS spectrometer, they lost energy through inelastic scattering, atomic excitation or ionization when interacting with the target, target walls, support structures, beam pipe, Start Counter, and the air gap between the Start Counter and the Region 1 Drift Chambers. Therefore, the momentum reconstructed from the drift chambers was smaller than the momentum of the particle at the

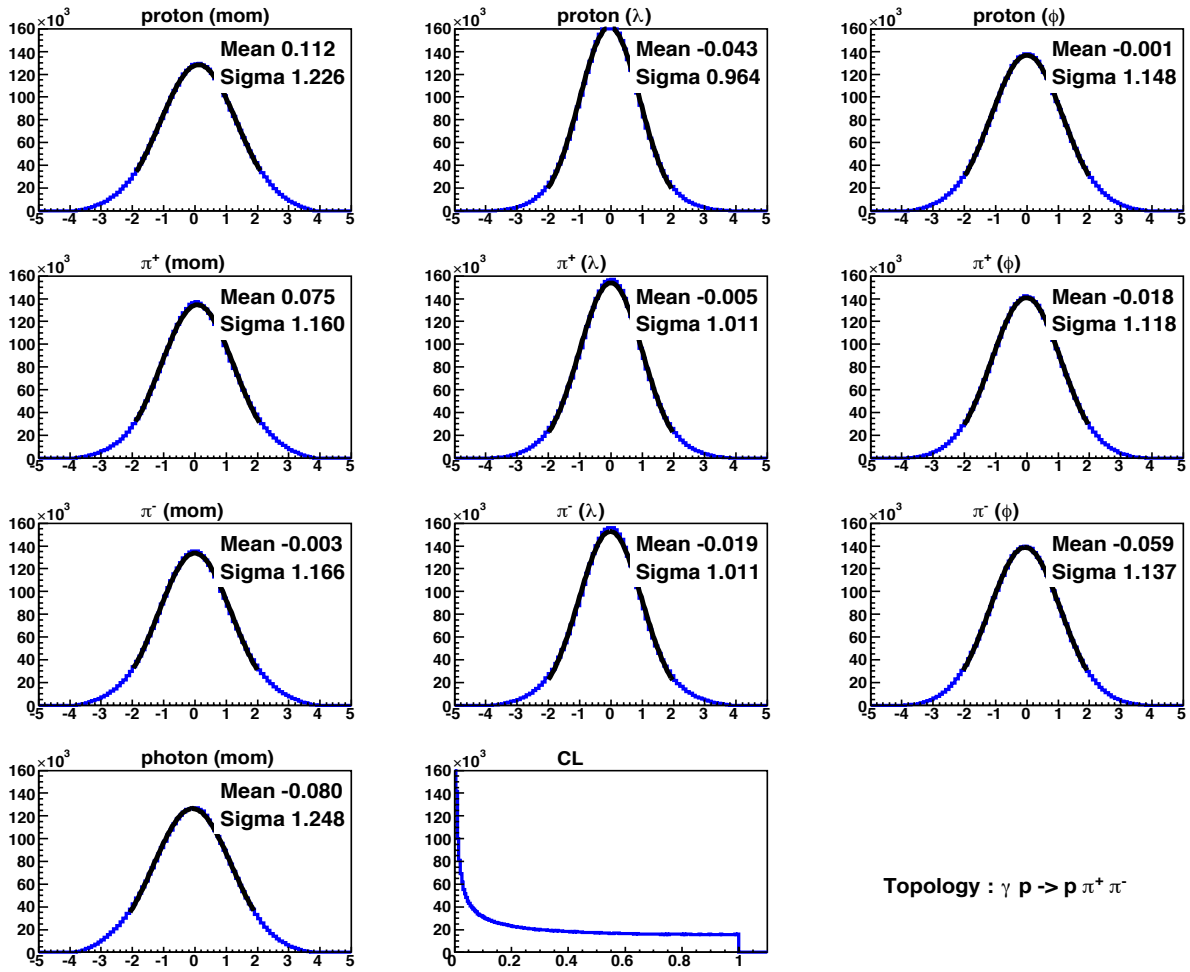


Figure 6: *The g12 pull and CL distributions for the exclusive reaction $\gamma p \to p\,\pi^+\pi^-$ (full statistics of Period 2). A summary of the mean and $\sigma$ values of the fits can also be found in Table 4.*

production vertex. To account and correct for this, the 4-vectors of the final-state particles were modified event-by-event using the "ELoss" package, which was developed for charged particles moving through CLAS [6]. This ELoss package determined the lost momentum of each particle in the materials it had interacted with. In this procedure, the particle's 4-momentum – as measured by the Region 1 Drift Chambers – was used to track the particle back to the reaction vertex in the target cell. The energy loss was then calculated based on the distance and the materials it traversed. The corresponding 4-vector was corrected by multiplying an ELoss correction factor to the magnitude of the momentum:

$$P_{\text{particle (ELoss)}} \;=\; \eta_{\text{particle}} \cdot P_{\text{particle (CLAS)}} \tag{10}$$

where $P_{x\,(\text{ELoss})}$ is the momentum of the particle $x$ after applying the energy-loss correction, $P_{x\,(\text{CLAS})}$ is the raw momentum measured in CLAS and $x$ is either the proton, $\pi^+$, or $\pi^-$. The parameters $\eta_p$, $\eta_{\pi^+}$, and $\eta_{\pi^-}$ are the ELoss correction factors which modified the momentum by a few MeV, on average.

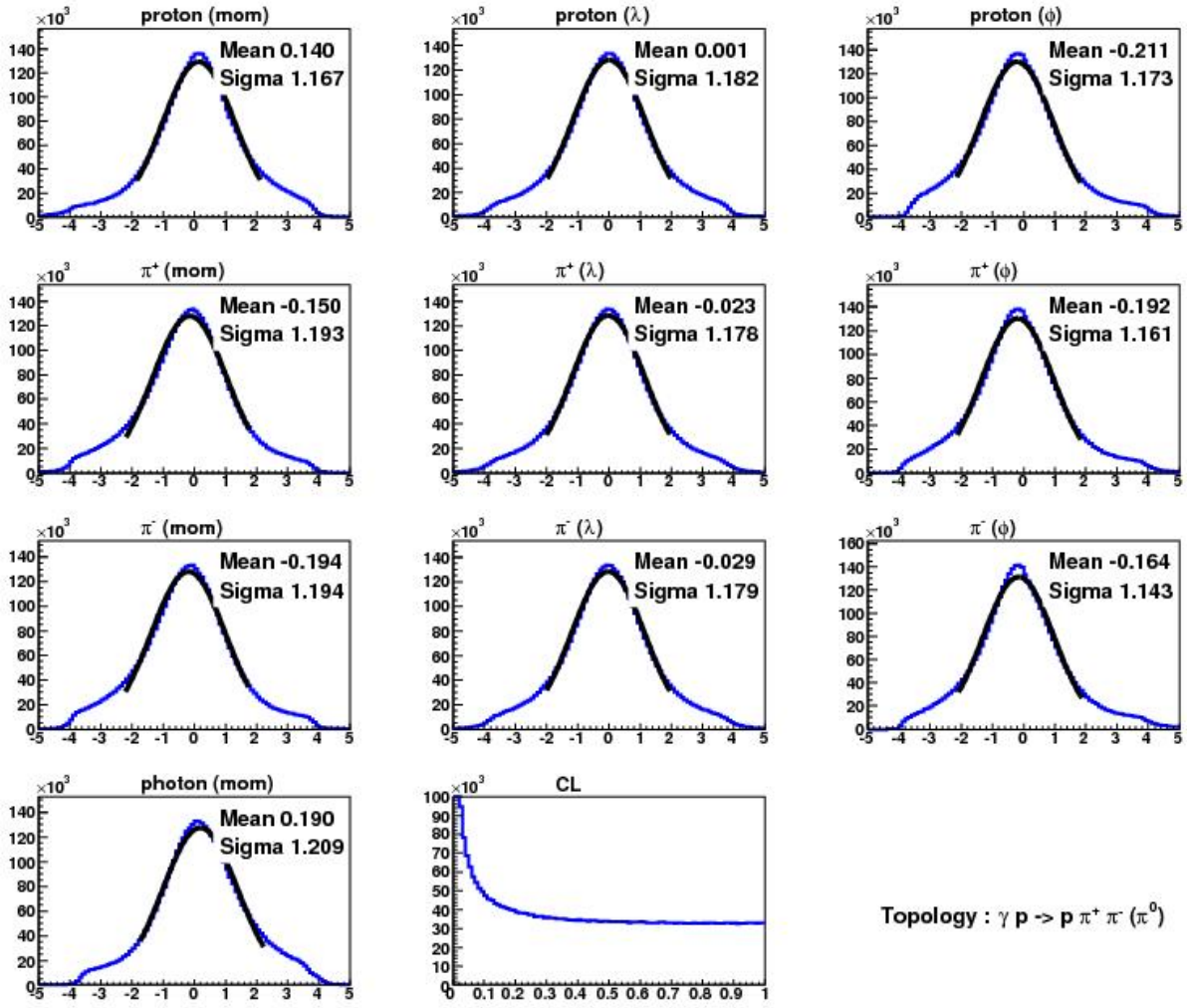


Figure 7: *The g12 pull and CL distributions for the reaction* $\gamma p \to p\pi^+\pi^-(\pi^0)$ *(full statistics of Period 2). Note that the pull distributions are not Gaussian over the full range owing to the missing-particle hypothesis. The confidence-level distribution looks nicely flat, though. A summary of the mean and* $\sigma$ *values of these fits can also be found in Table 4. Resolution.*

### 3.6.3 Momentum Corrections

The CLAS-g12 experimental setup was not absolutely perfect. For this reason, corrections of a few MeV had to be determined and applied to the final-state particles' momenta to account for unknown variations in the CLAS magnetic field (Torus Magnet) as well as inefficiencies and misalignments of the drift chambers. As a matter of fact, the momenta of the tracks as measured by the drift chambers exhibited a systematic shift within each sector as a function of the azimuthal angle $\phi$ of one of the tracks [3]. In our FSU analyses, we have followed the CLAS-approved procedure outlined in Ref. [3].

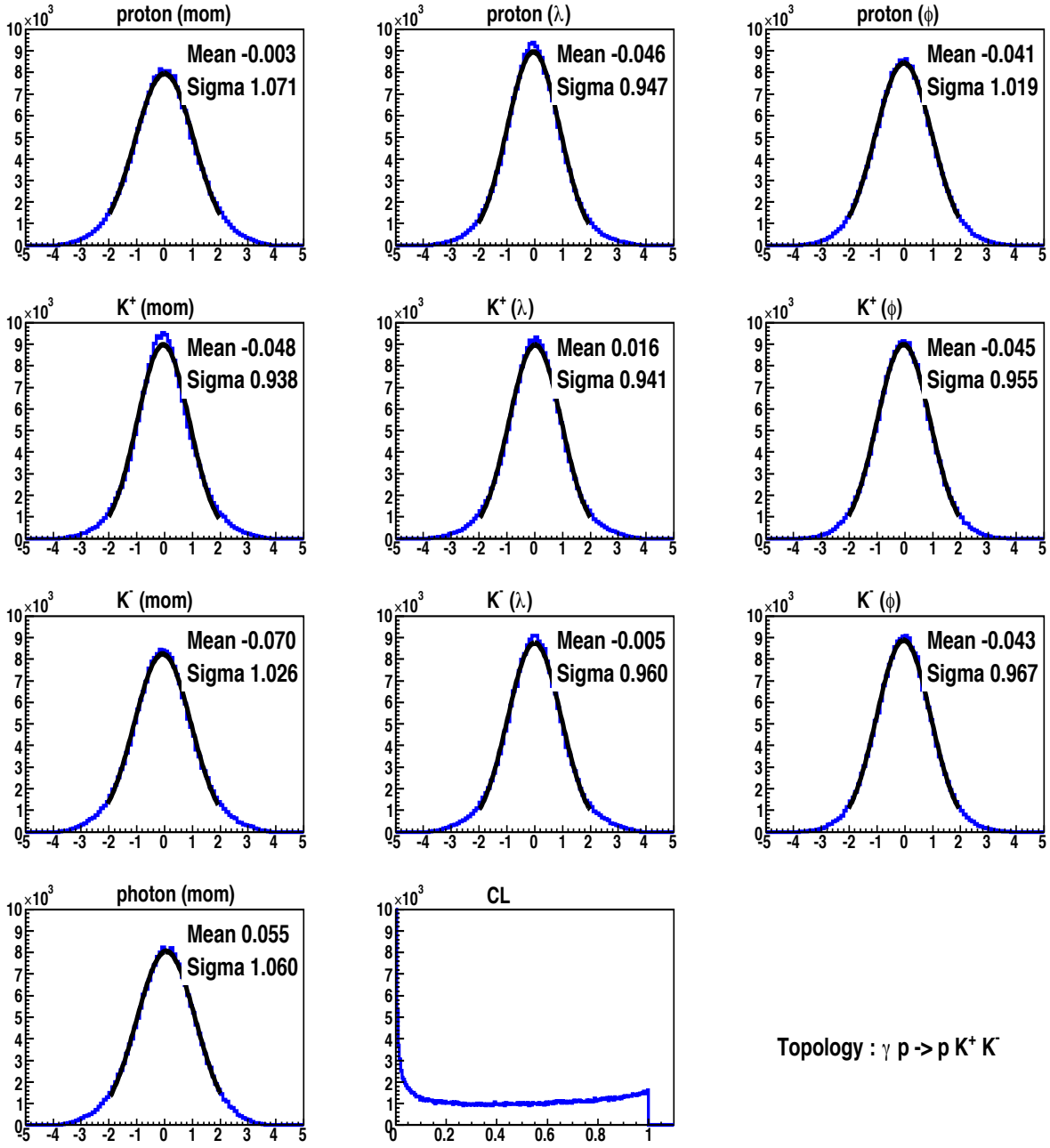


Figure 8: *The g12 pull and CL distributions for the exclusive reaction $\gamma p \to p K^+ K^-$ (full statistics of Period 2). A summary of the mean and $\sigma$ values of the fits can also be found in Table 4. The CL distribution is still rising toward one (positive slope) which is correlated with several $\sigma$ values that are smaller than one. We will go through an additional iteration of pull adjustments for the second round of this review.*

### 3.6.4 Bad or Malfunctioning Time-of-Flight Paddles

Some TOF paddles of the CLAS spectrometer were dead or malfunctioning during the g12 experiment. The timing resolution of each paddle was investigated on a run-by-run basis to determine the stability throughout the experiment. Reference [3] contains the results of an extensive study on bad TOF paddles in CLAS-g12. The list of identified bad paddles recommended to knock out was taken directly from Table 19 of Ref. [3] and is also given in Table 5 for convenience.

| Sector Number | Bad TOF Paddles in CLAS-g12 |
|---|---|
| 1 | 6, 25, 26, 35, 40, 41, 50, 56 |
| 2 | 2, 8, 18, 25, 27, 34, 35, 41, 44, 50, 54, 56 |
| 3 | 1, 11, 18, 32, 35, 40, 41, 56 |
| 4 | 8, 19, 41, 48 |
| 5 | 48 |
| 6 | 1, 5, 24, 33, 56 |

Table 5: *The list of bad time-of-flight paddles recommended to knock out [3].*

## 3.7 Monte Carlo Simulations

To extract the differential cross sections for the reactions (1) $\gamma p \to p\omega$, (2) $\gamma p \to p\eta$, (3) $\gamma p \to K^0\Sigma^+$, and (4) $\gamma p \to p\phi$, we needed to apply detector-acceptance corrections, where the latter accounted for the probability that an event of certain kinematics would be detected and recorded (also called efficiency corrections). The performance of the detector was simulated in GEANT3 - based Monte-Carlo studies. We followed the steps outlined in Ref. [3] for generating events, digitization and smearing, as well as reconstruction.

The generated raw events were processed by GSIM to simulate the detector acceptance for each propagated track from the event vertex through the GEANT3-modeled CLAS detector. The CLAS smearing package known as GPP then processed the output to reflect the resolution of the detector. Finally, the A1C package was used to perform the *cooking*. We generated a total of 175 million $\gamma p \to p\omega \to p\pi^+\pi^-\pi^0$ phase-space events for the whole range of incident-photon energies, i.e. $1.1 < E_\gamma < 5.4$ GeV. We have also generated 11 million $\gamma p \to p\eta \to p\pi^+\pi^-\pi^0$ and 40 million $\gamma p \to K^0\Sigma^+ \to p\pi^+\pi^-\pi^0$ Monte Carlo events. To guarantee phase-space (generated) events which are flat in $\cos\theta^{\rm meson}_{\rm c.m.}$, we chose a $t$-slope of *zero*.

In this section, we show the quality of the simulated events by comparing various data distributions with Monte Carlo events:

1. In the CLAS-g12 experiment, the 40-cm-long liquid-hydrogen target was pulled upstream by 90 cm from the center of the CLAS detector. Figure 9 compares the $z$-vertex distribution for data and Monte Carlo events after applying our cut of $-110 < z$ vertex $< -70$ cm: $\gamma p \to p\omega$ (left) and $\gamma p \to K_S\Sigma^+$ (right). This figure shows that the vertex distribution is very well modeled.

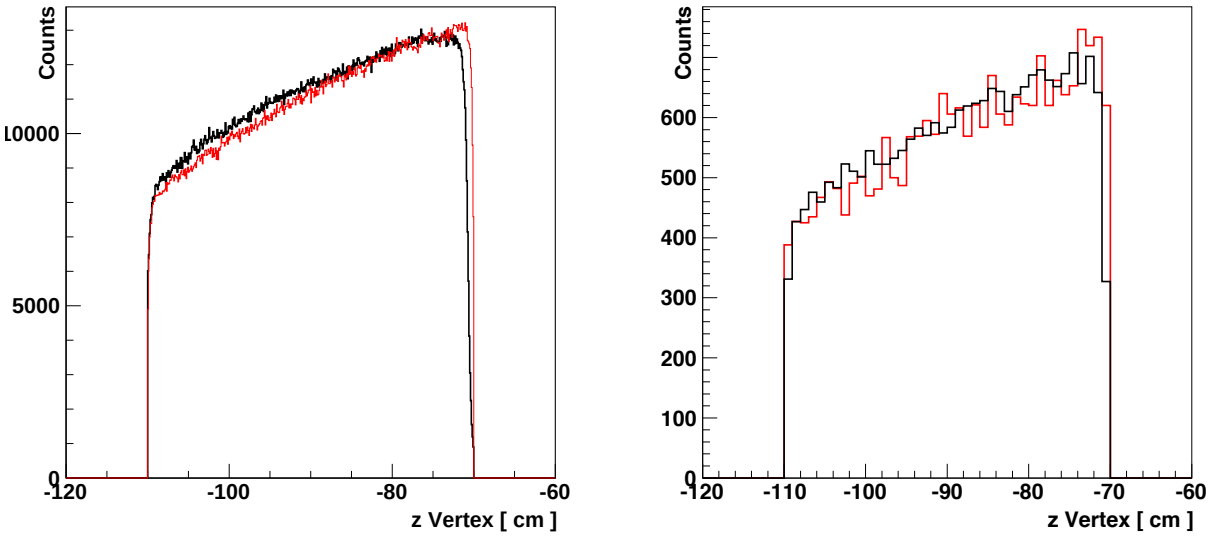


Figure 9: *Left: The z-vertex distribution of $\gamma p \to p\omega$ events. The black line denotes the data, the red line denotes the Monte Carlo distribution; good agreement is observed. These figures were made using the full data statistics of 4.4 million events and an equal amount of Monte Carlo events after applying our z-vertex cut of $-110 < z < -70$ cm. Right: The z-vertex distribution of $\gamma p \to K_S\,\Sigma^+$ events.*

2. We also checked all the signal distributions (peaks for $\omega$, $\eta$, and $K_S$) to see if our Monte Carlo mass resolution matches the real detector resolution. Figure 10 shows invariant-mass distributions for both data (black line) and Monte Carlo (red line) events. Since the mass resolution is slightly energy dependent, we compare data and Monte Carlo for $E_\gamma < 3$ GeV (left) and $E_\gamma > 3$ GeV (right). It is observed in this figure that the MC resolution is in reasonable agreement with the actual detector resolution.

| Reaction | Resolution (Gaussian $\sigma$ in [MeV]) | | | |
|---|---|---|---|---|
| | Low Energy | | High Energy | |
| | Data | MC | Data | MC |
| $\gamma p \to p\omega$ | 7.68 | 7.98 | 12.0 | 12.0 |
| $\gamma p \to p\eta$ | 6.5 | 6.9 | 7.2 | 7.1 |
| $\gamma p \to p\phi$ | | | | |
| $\gamma p \to K_S\,\Sigma^+$ | $K_S$ Peak | | $\Sigma$ Peak | |
| | 5.4 | 4.4 | 6.5 | 6.2 |

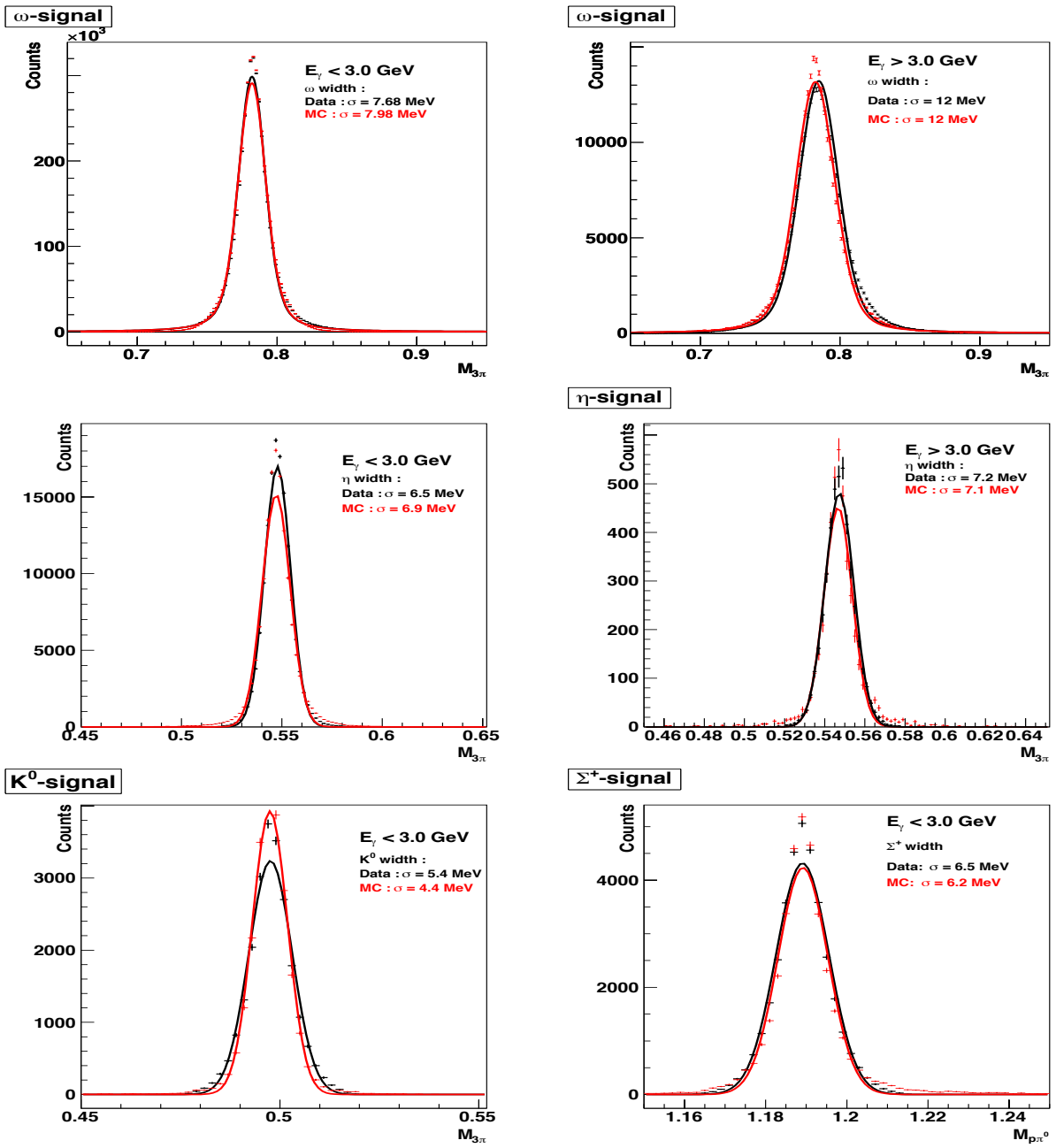


Figure 10: *Invariant mass (signal) distributions for data (black line) and Monte Carlo (red line). The left distributions are for $E_\gamma < 3.0$ GeV, the right distibutions are for $E_\gamma > 3.0$ GeV. Top row: The $M_{\pi^+\pi^-\pi^0}$ distribution showing the $\omega$ meson. Middle row: The $M_{\pi^+\pi^-\pi^0}$ distribution showing the $\eta$ meson. Bottom row: The $M_{\pi^+\pi^-}$ distribution showing the $K_S$ signal (left) and the $M_{p\pi^0}$ distribution showing the $\Sigma$ signal (right). The overall agreement between the data and Monte Carlo distributions indicates that the GEANT simulations model the resolution of the actual detector reasonably well.*

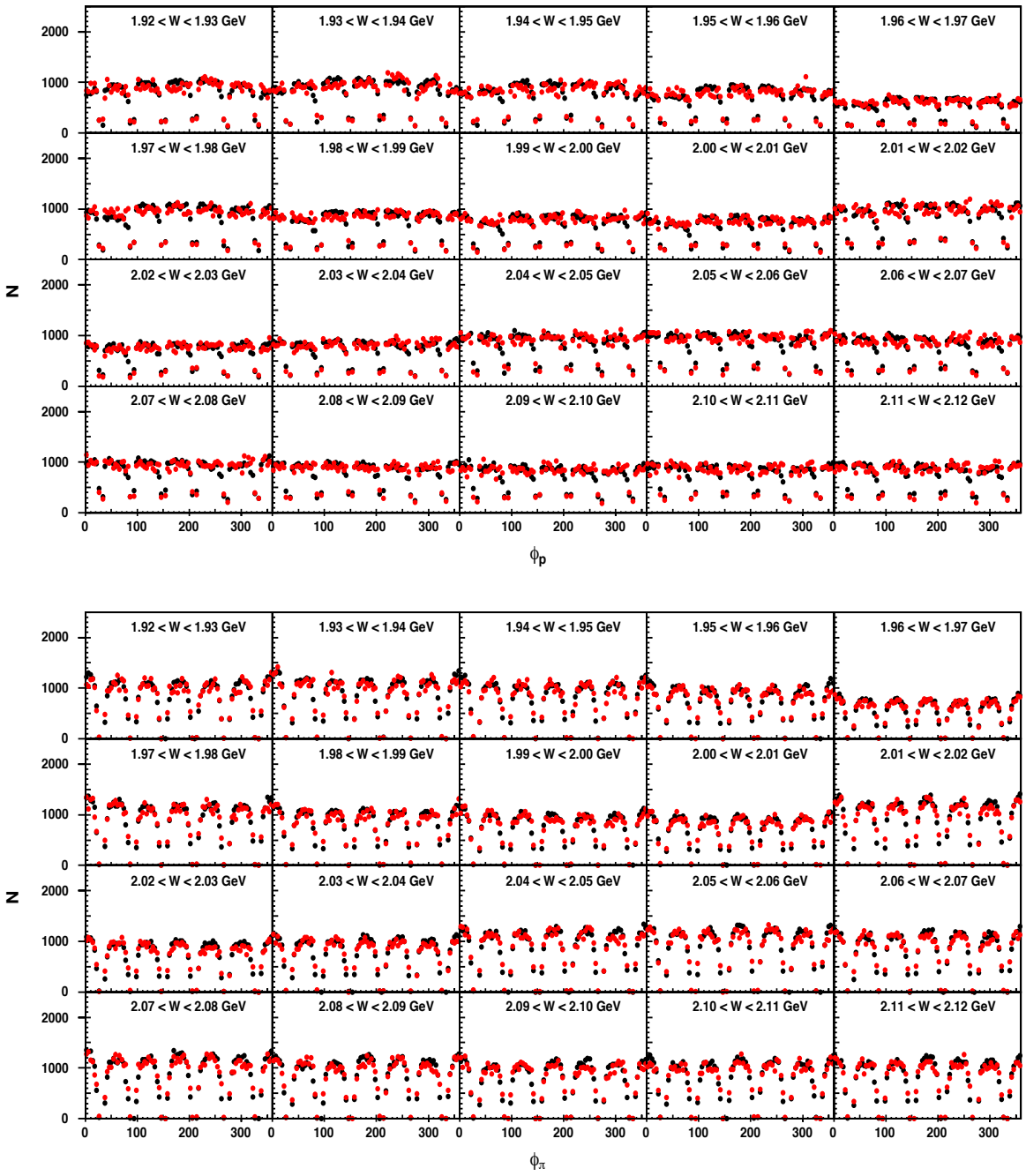


Figure 11: *The data and Monte Carlo comparison in the azimuthal ($\phi$) angle for the proton (top) and the $\pi^+$ (bottom).*

3. Figure 11 shows the distribution of the lab $\phi$ (azimuthal) angle for the proton (top) and for the $\pi^+$ (bottom). We believe the agreement looks sufficiently good for our analysis.

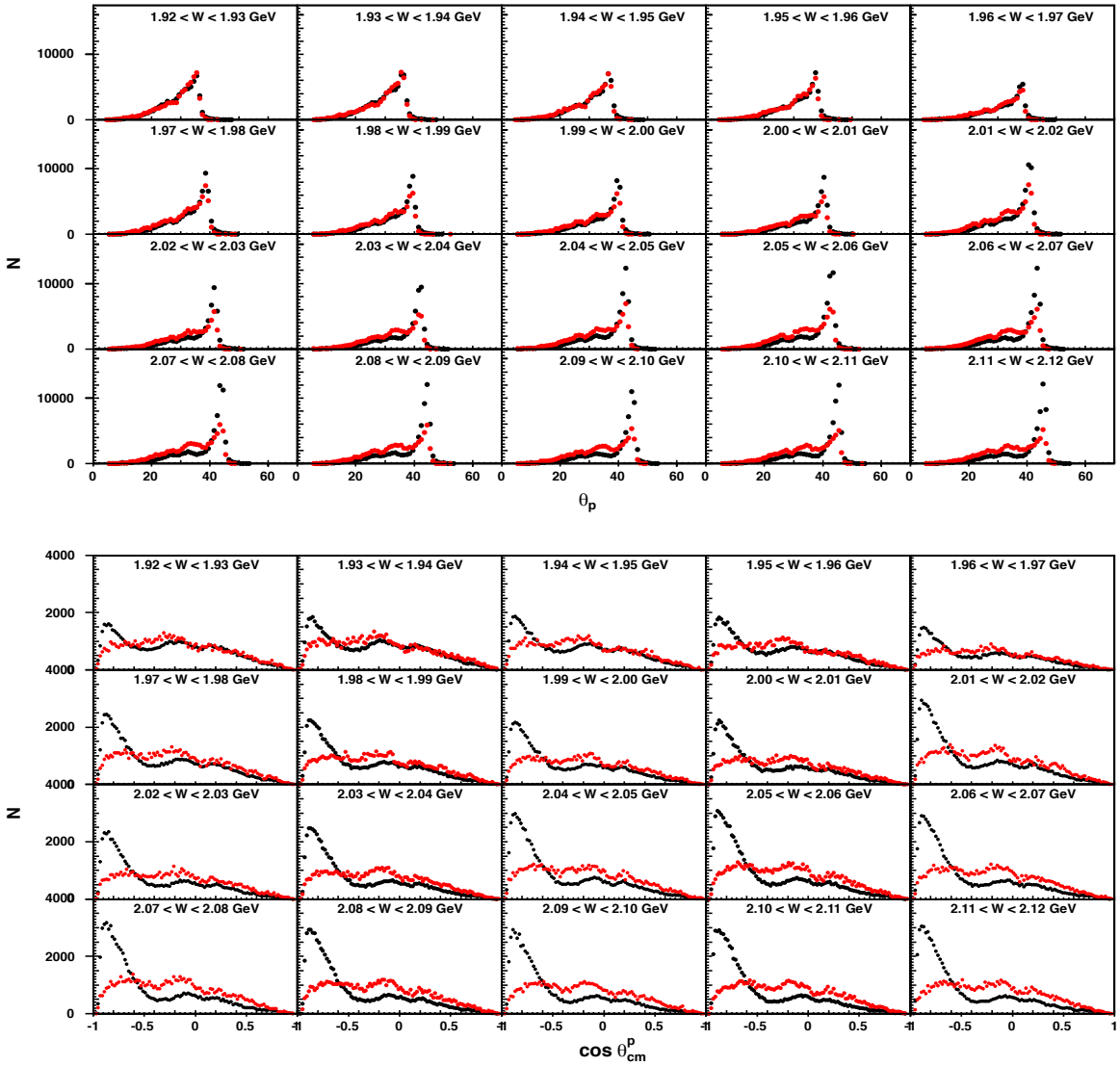


Figure 12: *The data and Monte Carlo comparison in the polar ($\theta$) angle for the proton in the laboratory frame (top) and the proton in the center-of-mass frame (bottom).*

4. Figure 12 shows the distribution of the polar ($\theta$) angle for the proton in the laboratory frame and for the proton in the center-of-mass frame. Figure 13 shows the distribution of the polar ($\theta$) angle for the $\pi^+$ in the laboratory frame and for the $\pi^-$ in the $\omega$ rest frame. Please note that the $\omega$ meson decays fairly symmetrically into $\pi^+\pi^-\pi^0$ (symmetric Dalitz plot) so that the $\pi$ distributions are almost isotropic. For this reason, the agreement between Monte Carlo and data is almost perfect for the pion. Any deviations from the symmetric decay form part of the motivation for our $\omega$ Dalitz-plot analysis. For the proton, the full physics dynamics of the $\omega$ production leads to larger deviations from the isotropic phase space distributions.

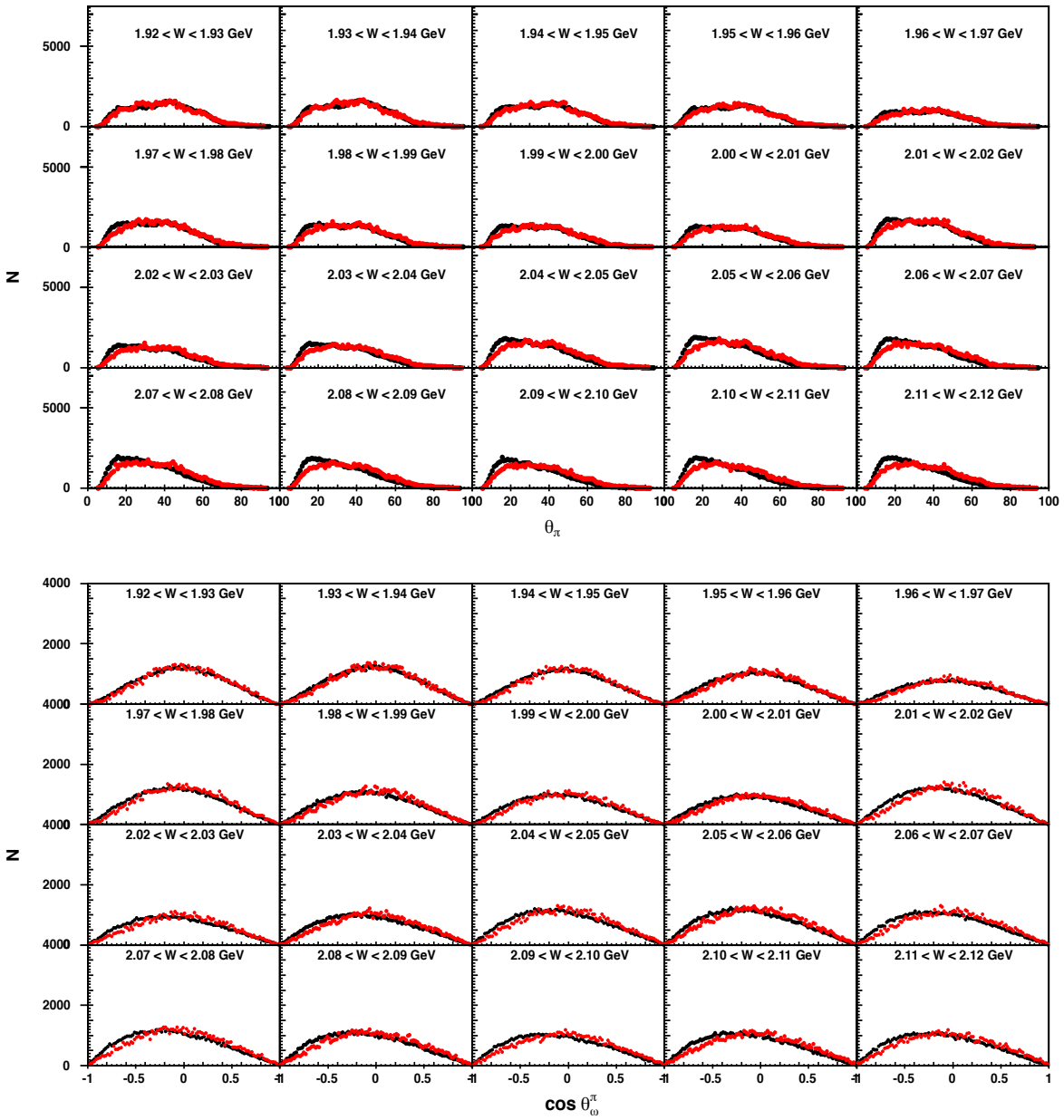


Figure 13: *The data and Monte Carlo comparison in the polar ($\theta$) angle for the $\pi^+$ in the laboratory frame (top) and the $\pi^-$ in the $\omega$ rest frame frame (bottom).*

5. Figure 14 shows the distributions for the $\cos\theta^{\pi^-}_{\rm c.m.}$ versus $z$ vertex for $\gamma p \to p\,\omega$ data and Monte Carlo events; the distributions are almost identical. In the very backward region of the target, an angle range of only about $-0.6 < cos\,\theta^{\pi^-}_{c.m.} < 0.8$ is covered, whereas $-0.8 < cos\,\theta^{\pi^-}_{c.m.} < 0.8$ is covered in the very forward region.

| | proton | | | $\pi^+$ | | | $\pi^-$ | | | $\gamma$ |
|---|---|---|---|---|---|---|---|---|---|---|
| | mom. | $\lambda$ | $\phi$ | mom. | $\lambda$ | $\phi$ | mom. | $\lambda$ | $\phi$ | E |
| Monte Carlo: $\gamma p \to p\,\pi^+\pi^-$ | | | | | | | | | | |
| $\bar{x}$ | 0.023 | 0.003 | 0.042 | 0.053 | −0.002 | 0.041 | 0.053 | 0.004 | 0.040 | −0.056 |
| $\sigma$ | 1.117 | 1.045 | 1.010 | 1.017 | 1.028 | 0.997 | 1.018 | 1.048 | 0.994 | 1.102 |
| Monte Carlo: $\gamma p \to p\,\pi^+\pi^-\,(\pi^0)$ | | | | | | | | | | |
| $\bar{x}$ | 0.040 | 0.018 | 0.024 | 0.027 | 0.000 | 0.024 | 0.022 | 0.004 | 0.030 | −0.052 |
| $\sigma$ | 1.078 | 1.054 | 1.081 | 1.045 | 1.056 | 1.015 | 1.055 | 1.056 | 1.004 | 1.086 |
| Monte Carlo: $\gamma p \to p\,K^+K^-$ | | | | | | | | | | |
| $\bar{x}$ | | | | | | | | | | |
| $\sigma$ | | | | | | | | | | |

Table 6: *Final mean ($\bar{x}$) and $\sigma$ values of Gaussian fits to our g12 pull distributions after applying all corrections. Note that the values for $p\,\pi^+\pi^-\,(\pi^0)$ are based on distributions which cannot be perfect Gaussians owing to the missing-particle hypothesis.*

6. The quality of the kinematic fitting for the Monte Carlo events is shown in the pull and confidence-level (CL) distributions for the reaction $\gamma p \to p\pi^+\pi^-$ (Fig. 16) and for the reaction $\gamma p \to p\,\omega \to p\pi^+\pi^-\pi^0$ (Fig. 17). A summary of the mean and $\sigma$ values is given in Table 6. Recall that each of these distributions should have a mean of *zero* and width of *one.* The agreement of the extracted values with these ideal values is very good. The CL distributions are flat toward *one*.

   To further check the quality of the confidence level in all kinematic regions, we considered the normalized slope of the distribution:

$$\bar{a} = \frac{a}{a/2 + b}\,, \tag{11}$$

   where $a$ is the slope and $b$ is the intercept obtained by fitting the confidence-level distribution to a linear function. Figure 15 shows examples of confidence-level distributions and their respective normalized slopes. If the errors are overestimated (underestimated), then the confidence-level distribution will have a positive (negative) slope. In line with the procedure outlined in Ref. [10], we would consider the covariance matrix to be aceptable if all kinematic regions yielded normalized slopes in the range $[-0.5, 0.5]$. Figure 18 shows the normalized slopes extracted in ($p$, $\cos\theta$) bins for the proton and the $\pi^-$. Notice that all kinematic regions (excluding edge bins with low statistics) have $|\bar{a}| < 0.5$. Thus, we conclude that the covariance matrix is acceptable.

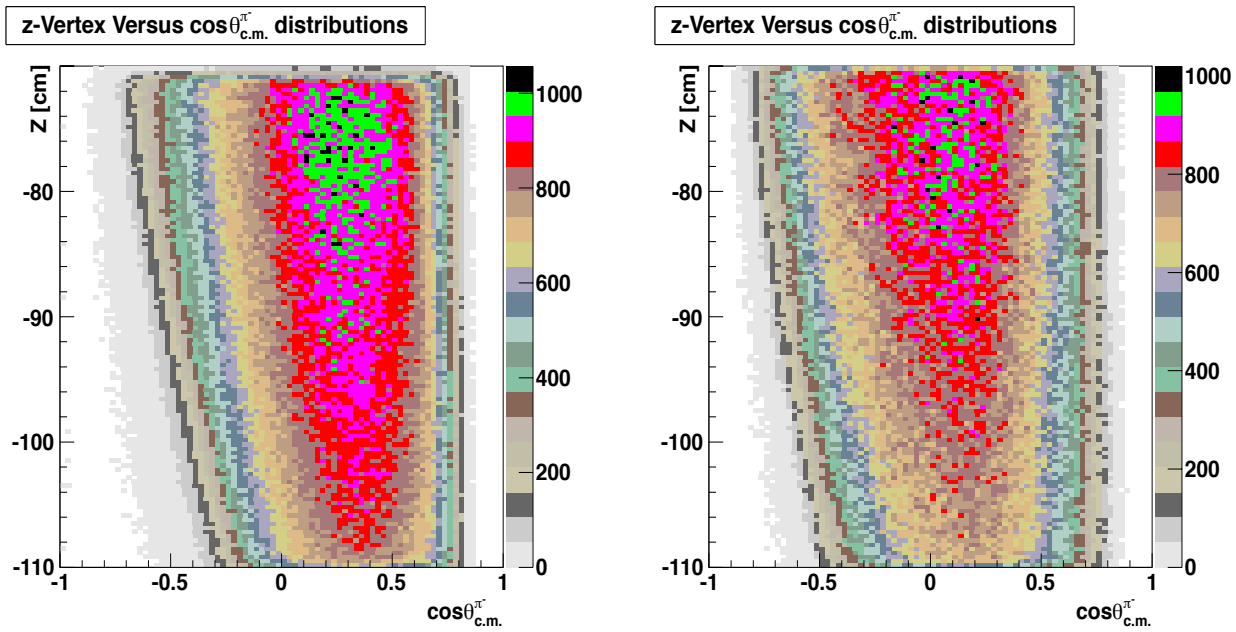


Figure 14: *The z-vertex vs. $cos\,\theta^{\pi^-}_{c.m.}$ distributions using a logarithmic color scale for data (left) and Monte Carlo events (right); the distributions are very similar. In the very backward region of the target, an angle range of only about $-0.6 < cos\,\theta^{\pi^-}_{c.m.} < 0.8$ is covered, whereas $-0.8 < cos\,\theta^{\pi^-}_{c.m.} < 0.8$ is covered in the very forward region.*

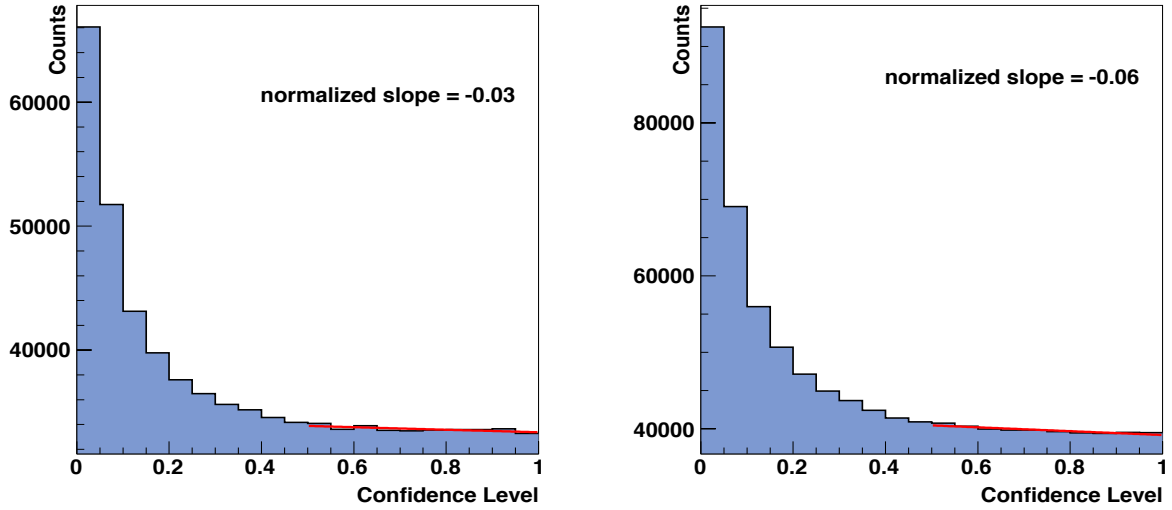


Figure 15: Examples of normalized slopes from confidence-level distributions for the proton (left) and for the $\pi^-$ (right): Normalized slopes have been extracted by fitting the distributions in the range (0.5, 1) to a linear function.

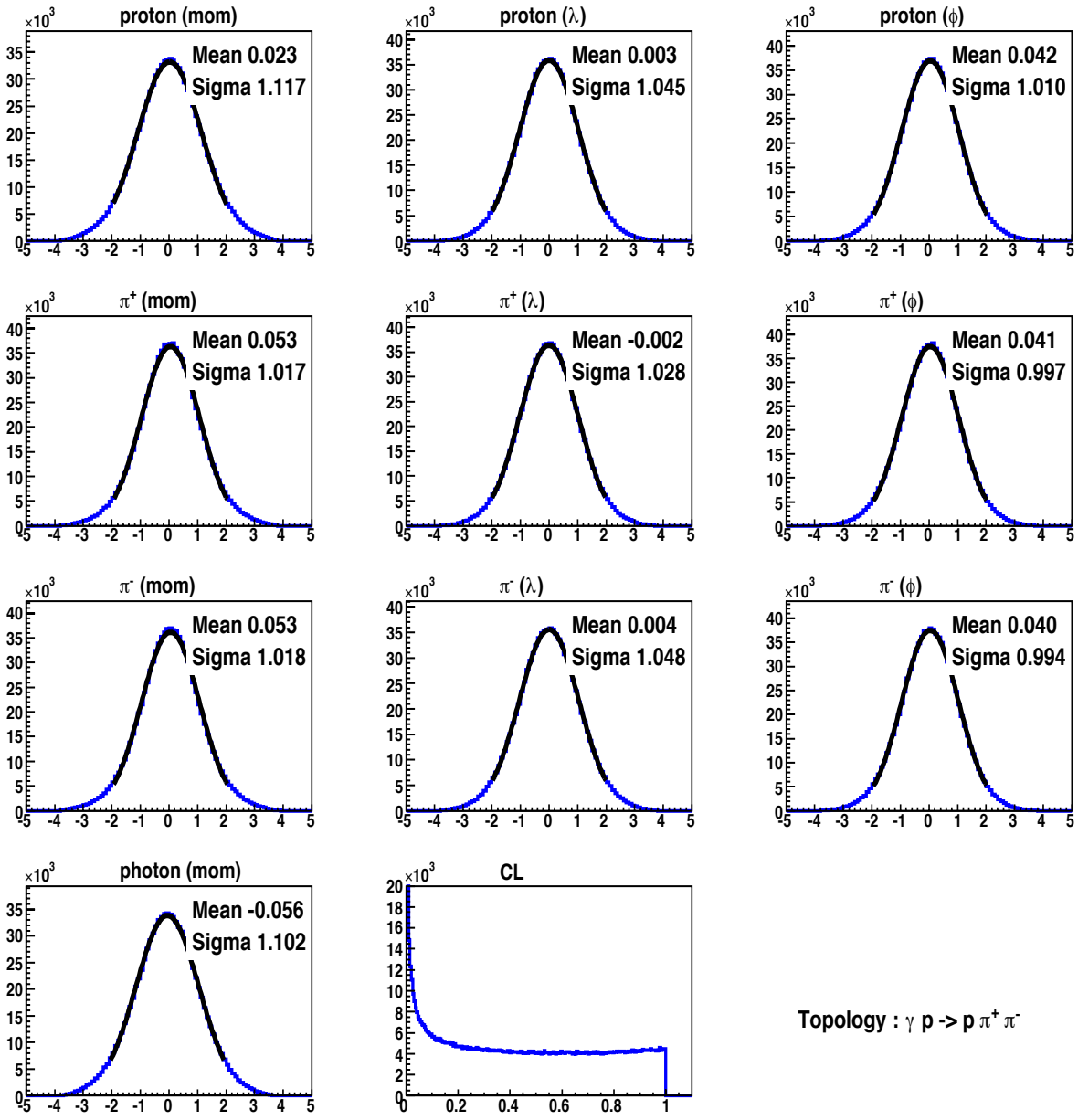


Figure 16: *Monte Carlo (reaction: $\gamma p \to p\,\omega \to p\,\pi^+\pi^-$) pull and confidence-level distributions for the four-constraint fit to $p\,\pi^+\pi^-$ (check for energy and momentum conservation, no mass constraint) along with the mean and $\sigma$ values of the fits. A summary of the mean and $\sigma$ values of these fits (for data and Monte Carlo) can also be found in Table 6.*

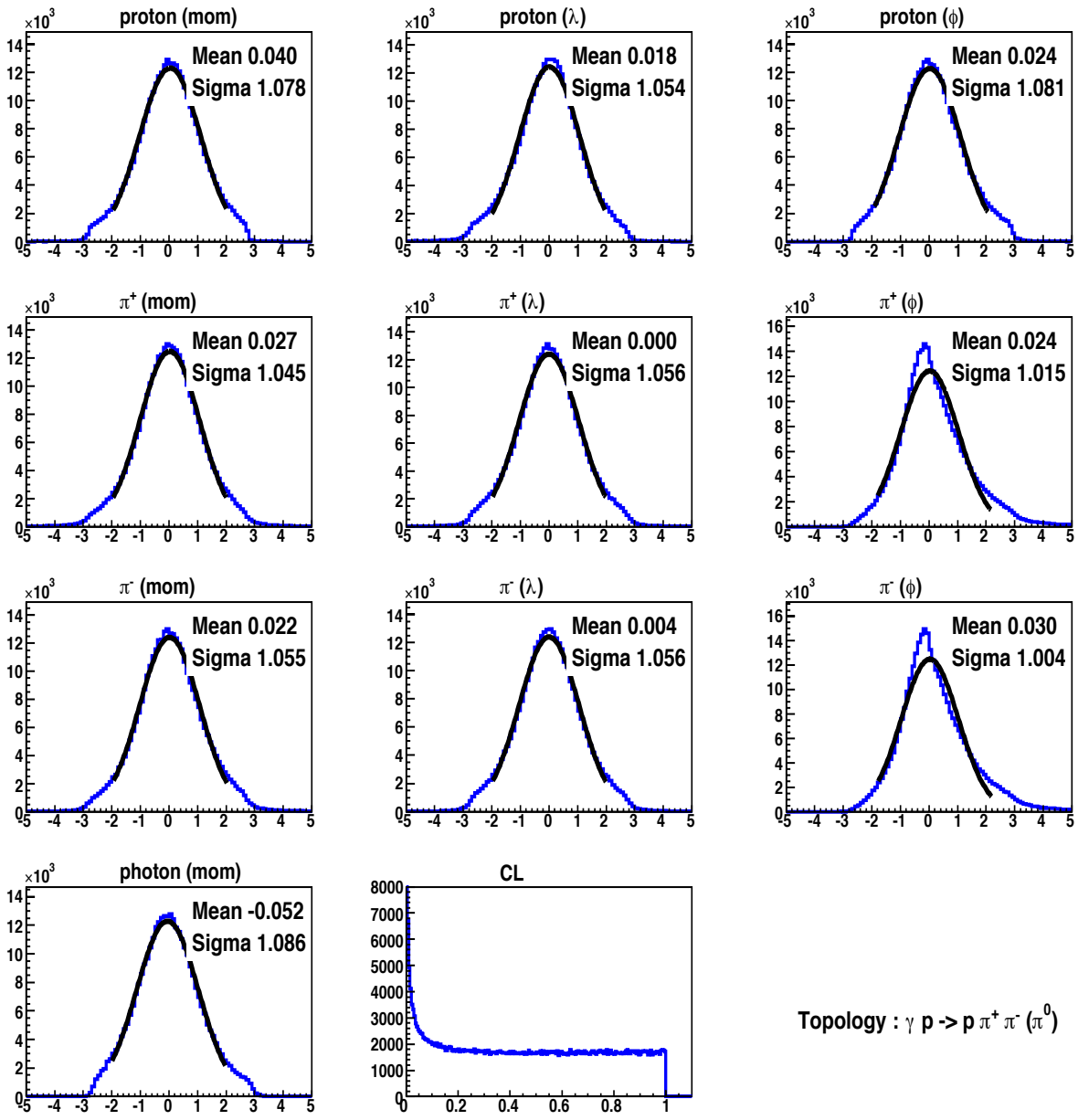


Figure 17: *Monte Carlo (reaction: $\gamma p \to p\omega \to p\pi^+\pi^-\pi^0$) pull and confidence-level distributions for the one-constraint fit to $p\pi^+\pi^-(\pi^0)$ (no $\omega$-mass constraint) along with the mean and $\sigma$ values of the fits. Note that the pull distributions are not Gaussian over the full range owing to the missing-particle hypothesis. A summary of the mean and values of these fits (for data and Monte Carlo) can also be found in Table 6.*

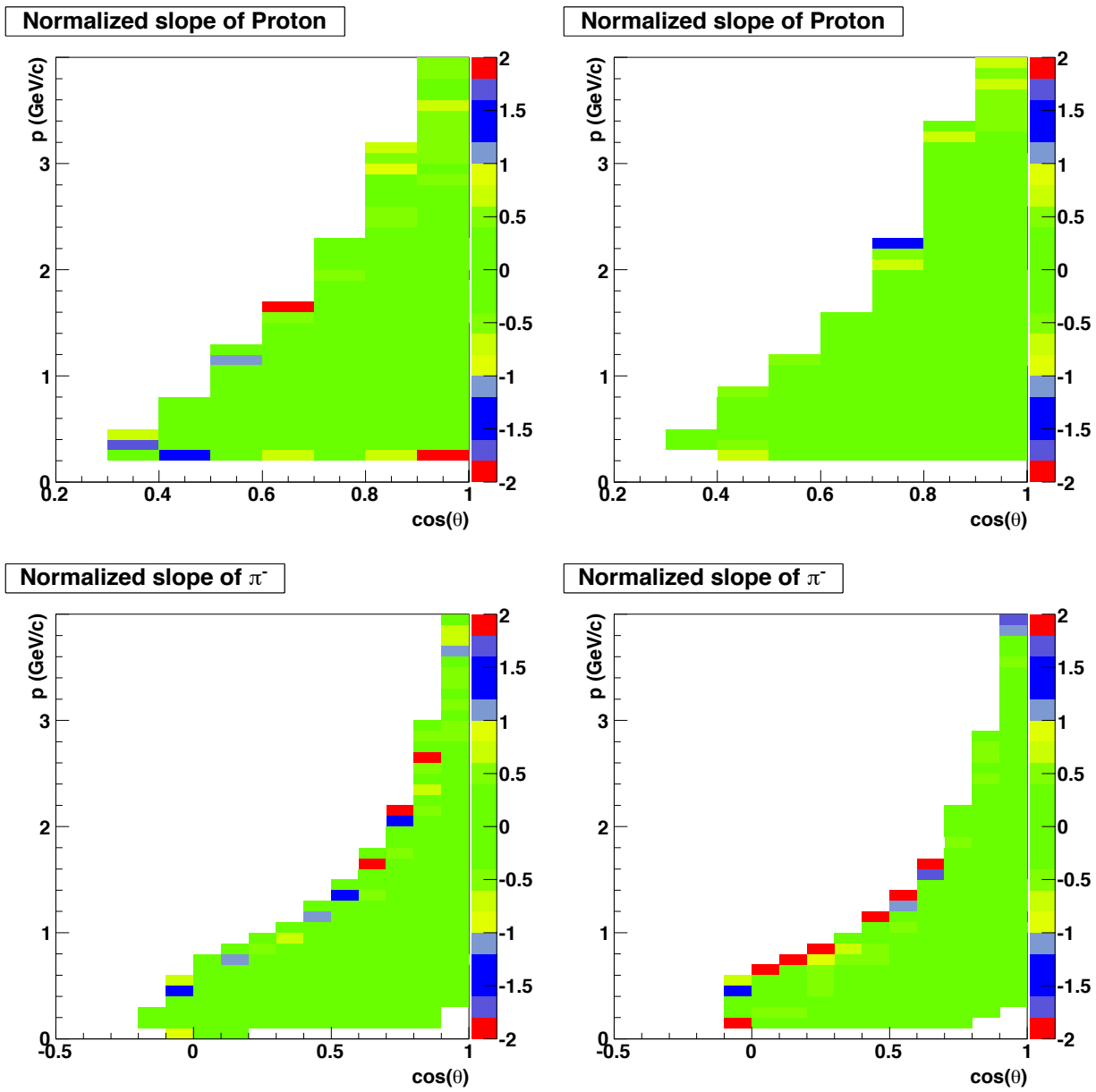


Figure 18: *Confidence-Level Checks. Normalized confidence-level slopes presented in* $\cos\theta$ *versus* $p$ *[GeV/c] distributions for the proton (top row) and for the* $\pi^-$ *(bottom row). The results for the g12-data are shown on the left and for Monte Carlo on the right. Notice that - excluding edge bins with low statistics - all kinematic regions have* $|\bar{a}| < 0.5$.

### 3.7.1 Trigger Simulation

To simulate the trigger conditions for our g12 data, we used the same technique that was developed for the measurement of the $\omega$ and $\eta$ cross sections in the g11a experiment [8, 9]. The procedure is outlined in Ref. [14]. This technique used the *trigger word* or *trigger bit*, which was written into the BOS data during the cooking. Reminder: The trigger conditions for the data that we used are described on Page 5 of Ref. [3]. In summary, the recorded events had:

1. Either three charged time-of-flight hits in three different sectors (three-sector events),
2. Or two hits in different sectors (two-sector events), in combination with at least one photon in the beam bucket whose energy was above 3.6 GeV. The term "beam bucket" refers to all photons that were detected during the life time of the trigger (detector).

Therefore, to simulate the trigger conditions in the Monte Carlo events, two pieces of information were needed:

1. The efficiency of the trigger as a function of particle type, momentum, and detector position (trigger efficiency map).
2. The probability for having at least one photon with $E_\gamma > 3.6$ GeV (two-sector events).

(1) The trigger efficiency map was derived using $\gamma p \to p\,\pi^+\pi^-$ events and required all three tracks to be detected in three different sectors. If the trigger were 100 % efficient, then all three detected particles would also be recorded in the trigger word, i.e. contributed to the trigger decision. However, if the trigger were not 100 %, an event with three charged tracks would still be

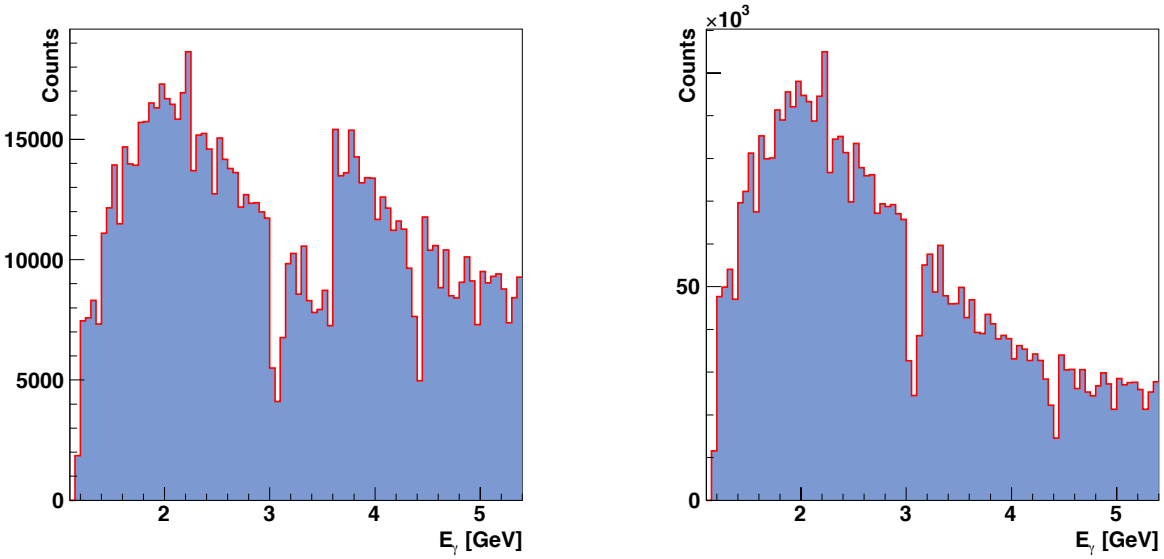


Figure 19: *The distribution of events as a function of beam energy. The left figure shows the distribution for two-sector events. It clearly shows a discontinuity at 3.6 GeV. The right figure shows the distribution for three-sector events. The distribution is smooth since there is no additional photon-energy requirement.*

reconstructed, although one of the tracks would not fire the trigger (and be recorded in the trigger word). Therefore, it was possible to build a map of the trigger efficiency for each particle type as a function of sector, time-of-flight paddle, and azimuthal angle. The trigger efficiency map for the $\pi^-$, $\pi^+$, and the proton are shown in Fig. 21, 22, and 23.

(2) The probability for two-sector events of having at least one photon with $E_\gamma > 3.6$ GeV in the beam bucket could be determined by comparing energy-dependent intensity distributions of two-sector and three-sector events. These distributions are shown in Fig. 19. A discontinuity at about 3.6 GeV is clearly observed in the top distribution (two-sector events) due to the additional photon-energy requirement. Further structures can be seen around 3 GeV and 4.4 GeV owing to broken tagger scintillators. On the other hand, the bottom figure shows a smooth distribution for three-sector events because events were recorded independent of their photon energy.

Figure 20 shows the ratio of two-sector events and three-sector events. Since the physics for using an unpolarized beam is independent of the azimuthal angle, we expect the ratio to be flat. And we clearly see two flat distributions that disconnect at about 3.6 GeV. By fitting the two plateaus using a zeroth-order polynomial below and above 3.6 GeV, we concluded that the probability for two-sector events of having at least one photon with an energy above 3.6 GeV is about 0.51.

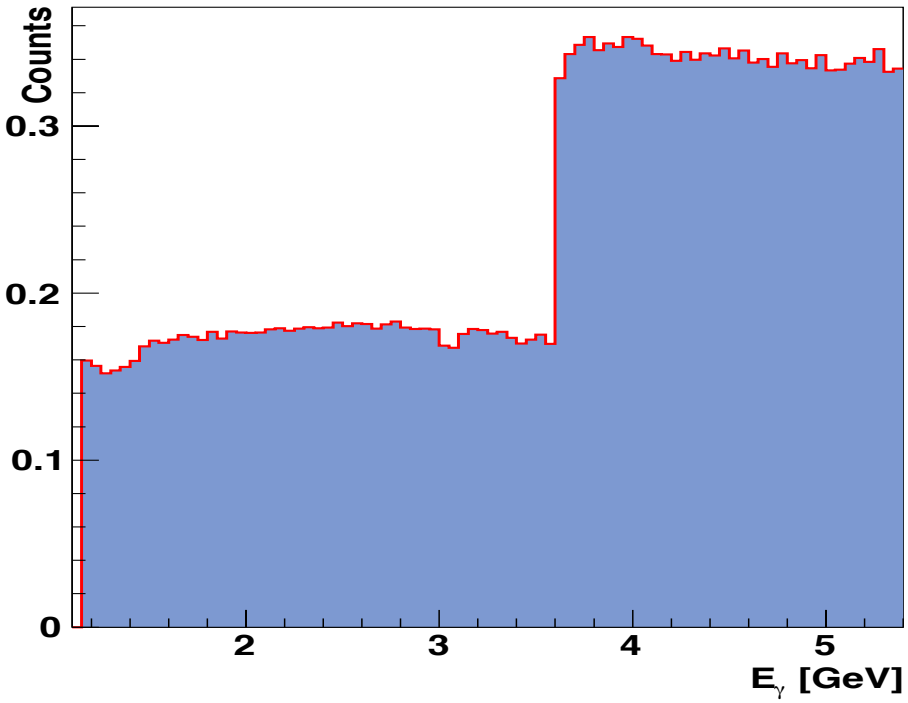


Figure 20: *The ratio of two-sector and three-sector events. The discontinuity at 3.6 GeV is an effect of the trigger condition. The ratios are flat as expected because the physics of using an unpolarized beam must be independent of the azimuthal angle. By fitting these ratio distributions below and above 3.6 GeV, we studied the probability for tow-sector events of having at least one photon in the beam bucket with* $E_\gamma > 3.6$ *GeV. This probability was determined to be 0.51.*

After building the efficiency map and determining the probability for having at least one photon with an energy above 3.6 GeV for two-sector events, we simulated the Monte Carlo events using the following steps:

1. The efficiency map was based on events that had all three particles in different sectors. Therefore, we cut out events if two particles ended up in the same sector (for both data and MC events).

2. For each event, we generated three random numbers between 0 and 1 for the three final-state particles, denoted by $R_p$, $R_{\pi^+}$, and $R_{\pi^-}$.

   (a) Denoting the trigger efficiency for each particle $P_p$, $P_{\pi^+}$, and $P_{\pi^-}$, then the particles were considered to fire the trigger if the generated random number were smaller than the efficiencies. For example, we considered the proton to fire the trigger if $R_p < P_p$.

   (b) If all particles fired the trigger, we kept the Monte Carlo event no matter what the photon energy was.

   (c) If only two particles fired the trigger and the photon energy was above 3.6 GeV, we kept the event.

   (d) If only two particles fired the trigger and the photon energy was below 3.6 GeV, then we generated another random number, $R_{\text{tagger}}$ . If $R_{\text{tagger}} < 0.51$, then we kept the event. Otherwise, if If $R_{\text{tagger}} > 0.51$, the Monte Carlo event was discarded.

3. If no particle or only one particle fired the trigger, then the Monte Carlo event was discarded.

In a brief summary: For the trigger simulation, we followed the g11a recipe and determined an overall effect of about 16 %. This is comparable with the g11 studies, which resulted in an effect of the trigger simulation of roughly 15 %.

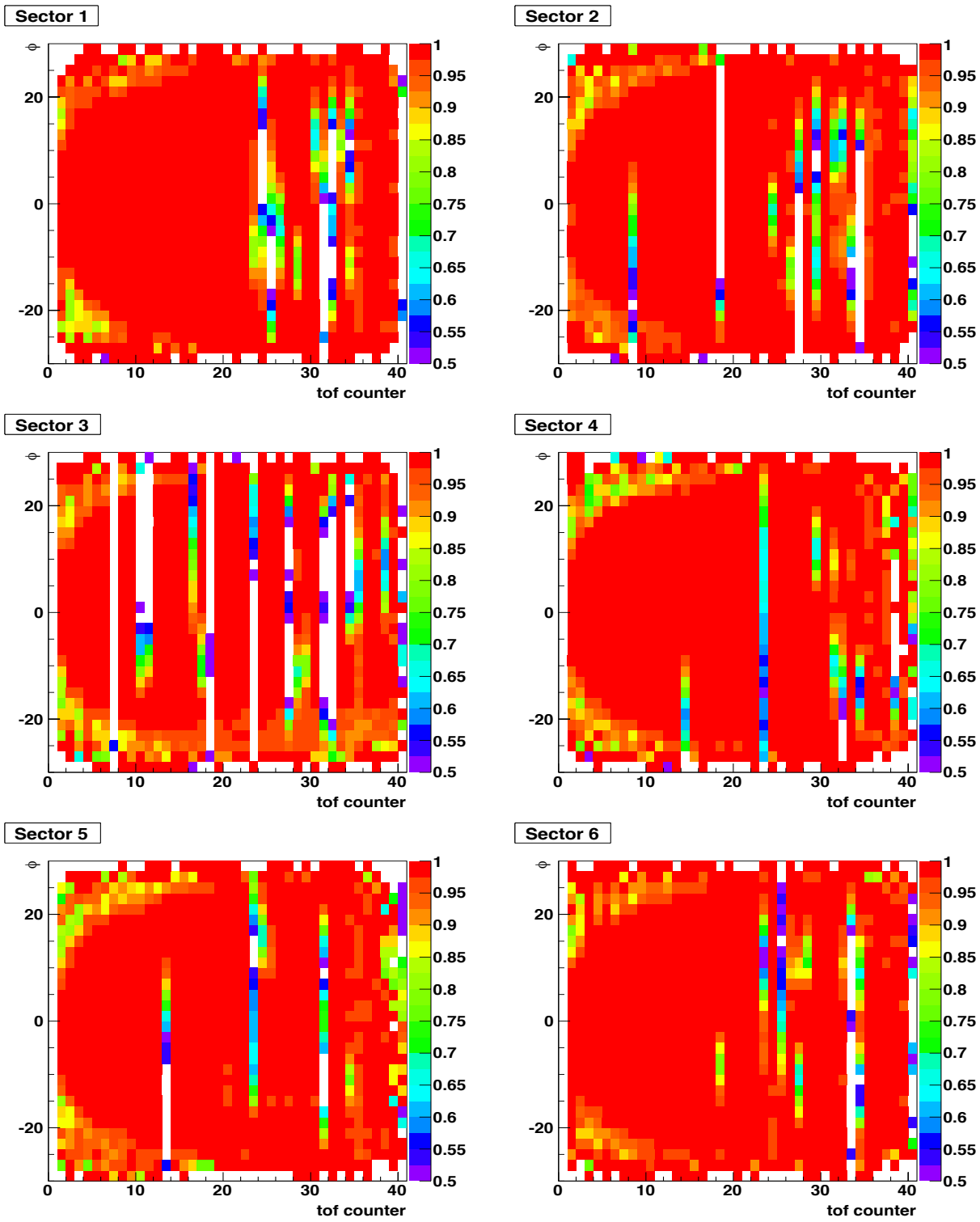


Figure 21: *Trigger efficiency map for the $\pi^-$ as a function of sector, tof-paddle number, and azimuthal angle.*

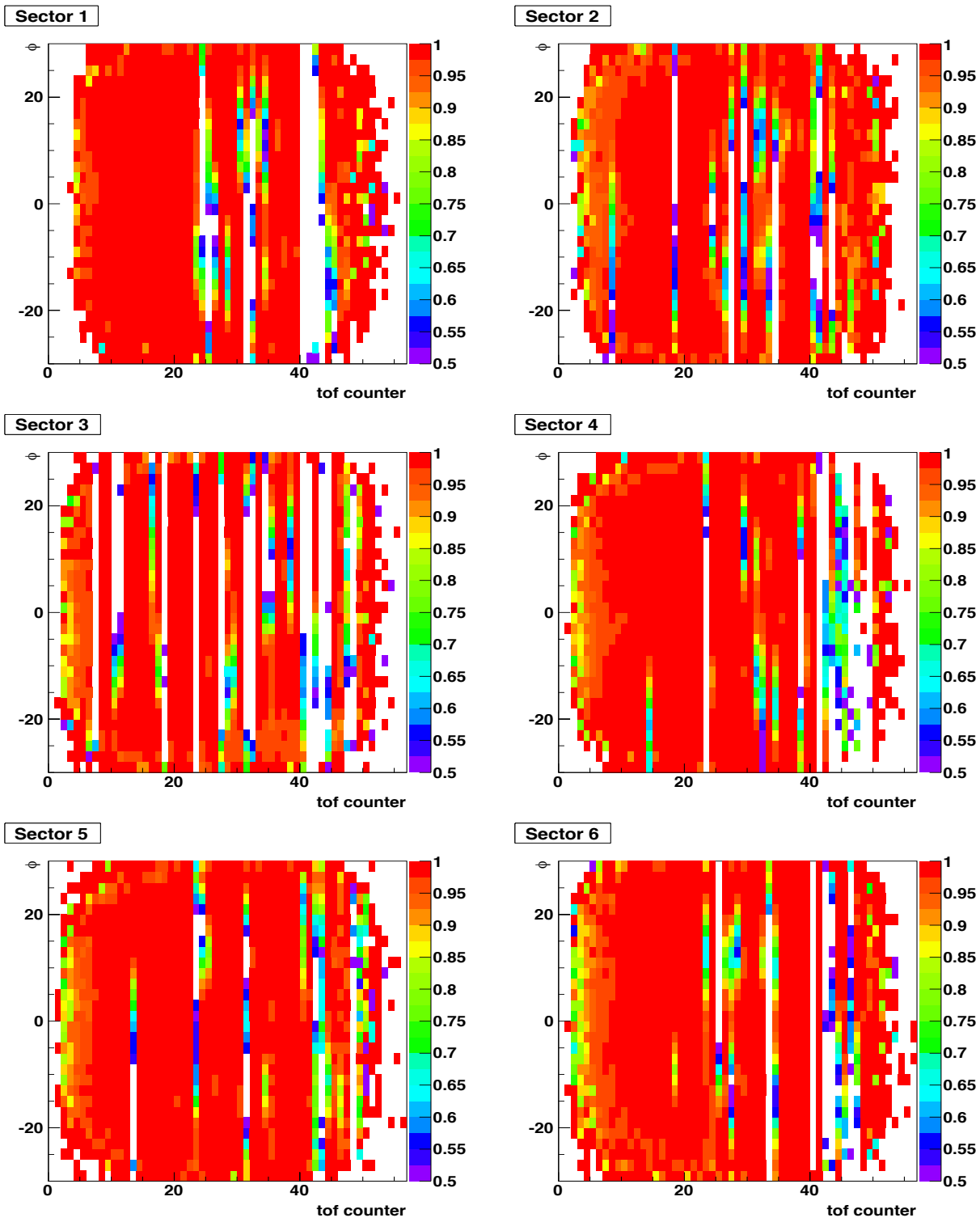


Figure 22: *Trigger efficiency map for the $\pi^+$ as a function of sector, tof-paddle number, and azimuthal angle.*

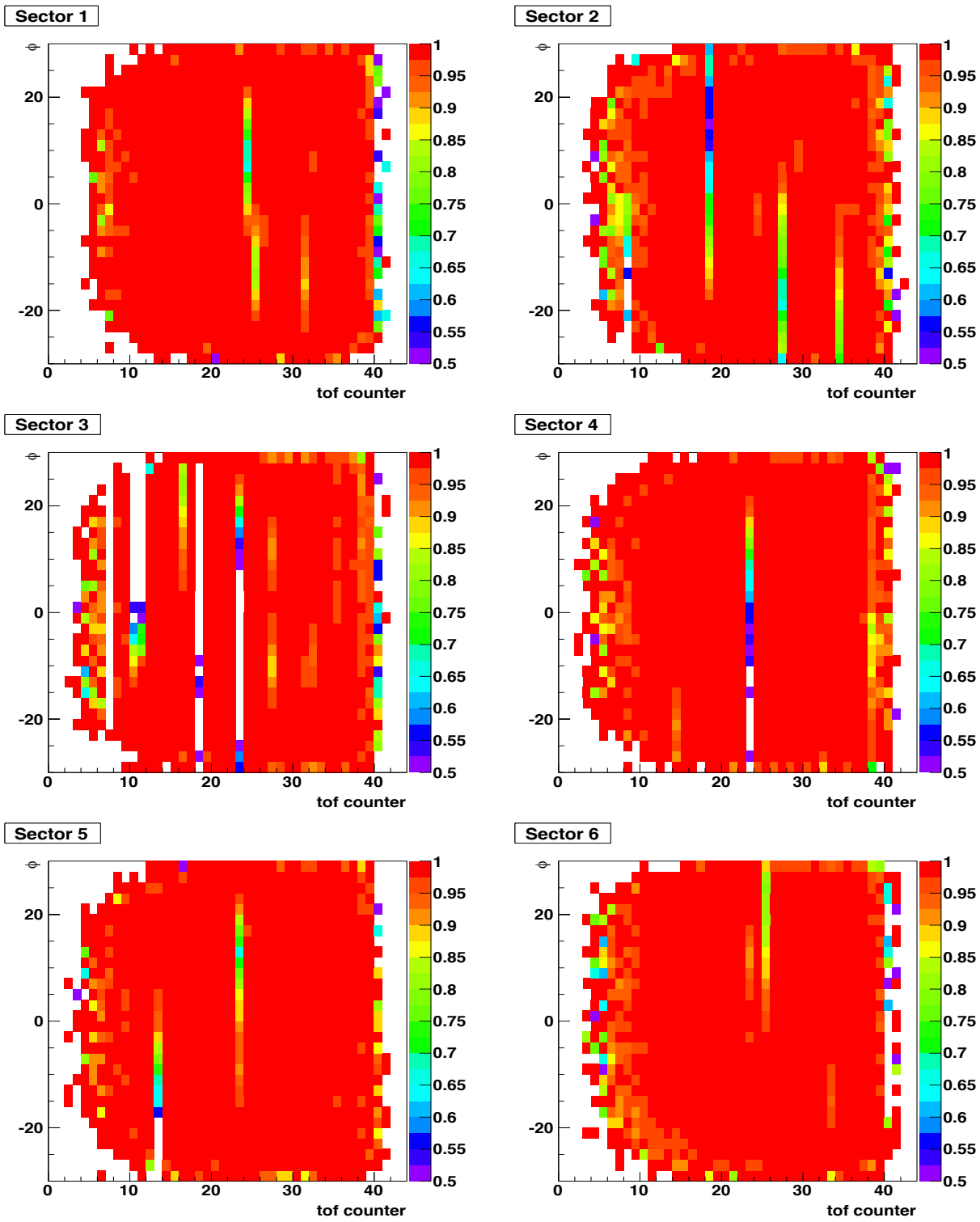


Figure 23: *Trigger efficiency map for the proton as a function of sector, tof-paddle number, and azimuthal angle.*

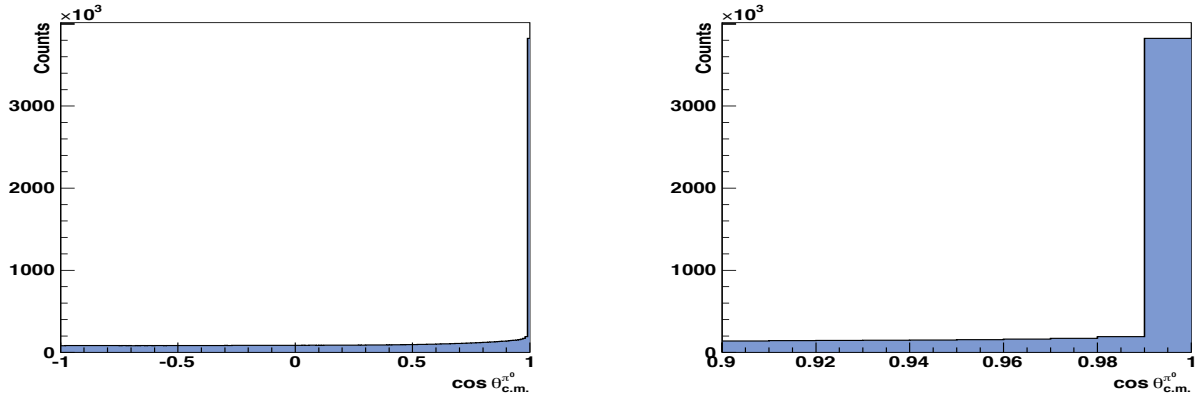


Figure 24: *Left: The* $\cos\theta^{\pi^0}_{\rm c.m.}$ *distribution of all 18 million* $\gamma p \to p\,\pi^+\pi^-\,(\pi^0)$ *events which passed a* $p > 0.001$ *CL cut. This figure shows an excess of events in the very forward region. Right: The same figure zoomed in on the forward region.*

## 3.8 Angular Distribution of the Undetected $\pi^0$

### The $\cos\theta^{\pi^0}_{\rm c.m.}$ Distribution

The channel $\gamma p \to p\,\pi^+\pi^-$ has a significantly larger cross section than $\gamma p \to p\,\pi^+\pi^-\,(\pi^0)$. This fact, coupled with the relatively small difference in the missing masses of the two channels, makes $p\,\pi^+\pi^-$ leakage into the $p\,\pi^+\pi^-\,(\pi^0)$ sample a cause for concern. In this section, we consider the possibility of $p\,\pi^+\pi^-$ leakage resulting from selecting the wrong photon.

If the incorrect photon has a higher energy than the correct one, the extra energy will create a fake $\pi^0$ that will move along the beam direction. Consider a $\gamma p \to p\,\pi^+\pi^-$ event that was produced in the detector. Our analysis procedure will attempt to reconstruct a $\pi^0$ from the missing momentum, $\vec{p}_{\rm miss}$. Since the event produced was actually a $p\,\pi^+\pi^-$ event, the missing transverse momentum measured should be approximately zero, regardless of whether the correct photon has been found. Thus, the momentum vector of the reconstructed $\pi^0$ must point (approximately) along the beam direction: $\vec{p}_{\rm miss} \approx \pm|\vec{p}_{\rm miss}|\,\hat{z}$.

Therefore, we expect any leakage from the $\gamma p \to p\,\pi^+\pi^-$ channel, due to an incorrect photon selection, to result in an excess of events in the very forward direction with $\cos\theta^{\pi^0}_{\rm c.m.} \approx +1$. Figure 24 clearly shows a pronounced excess of events in the very forward direction. Therefore, we cut out all events with $\cos\theta^{\pi^0}_{\rm c.m.} > 0.99$.

## 3.9 Fiducial Volume Cuts

Geometric fiducial volume cuts have been applied according to the *nominal* scenario outlined in Section 5.3 of the analysis note [3]. These volumes were regions of the detector that were not well modeled and needed to be removed from the analysis. For example, the magnetic field varied rapidly close to the torus coils making these regions difficult to simulate. Thus, any particle whose trajectory was near a torus coil was identified and suvsequently, the event was excluded from our analysis. The effect of this particular cut was most dramatic in the forward region, where the coils occupied a larger amount of the solid angle.

In a brief summary (taken directly from Ref. [3]), such regions for all the g12 data, where the detector acceptance was well behaved and reliably reproduced in simulations, were expressed as an upper and lower limit of the difference in azimuthal angle between the center of a given sector and a particle track. Because of the hyperbolic geometry of CLAS and the presence of the toroidal magnetic field, the fiducial boundaries on $\phi$ were functions of momentum $p$, charge, and polar angle $\theta$ of each track. The boundaries were evaluated separately in each sector, nominally defined as the $\phi$ values in which occupancy drops below 50 % of that in the respective sector's flat region. The flat regions were defined as $10^\circ < \phi < 10^\circ$. The nominal upper and lower $\phi$ limits depended strongly on particle charge, $p$ and $\theta$, hence the need for functional characterization and extrapolation.

In order to determine the fiducial limits for charged hadrons, a sample of exclusive $p\,\pi^+\pi^-$ events were sliced into $5 \times 15 \times 6$ bins in $p$, $\theta$, and sector, respectively. The $\phi$ distributions for $\pi^+$ and $\pi^-$ were then plotted separately in each bin. The upper and lower $\phi$ limits of these first-generation plots were found according to the *nominal* fiducial definition of 50 % occupancy. The results from the first-generation fits were represented in second-generation plots of $\phi_{\min}$ and $\phi_{\max}$ vs. $\theta$ and fit with hyperbolas, chosen since they replicate the projection of the detector. In a last step, the second-generation fitting parameters were plotted vs. $p$ in third-generation plots. These third-generation plots were fit to power functions and the fit results defined the sought-after functional form $\phi_{\min}(\theta, p)$ and $\phi_{\max}(\theta, p)$ for each sector. The sector-integrated results for positive and negative hadron tracks compose the nominal fiducial region.

### 3.10 Event Statistics after Applying all Cuts and Corrections

The process of developing and applying energy, momentum and other necessary corrections during the course of this analysis served the purpose of correcting for the effects of the experimental setup, therefore resulting in a data set that was as nature intended it. Additionally, determining and enforcing cuts used in the analysis served not only to remove the remaining instrumental effects of the experimental setup but also to remove the contributions from physics events not of interest to the analysis (the hadronic or electromagnetic background). Through the application of the proper vertex position, photon and particle identification variables, this background could be reduced considerably. Table 7 shows how many events survived after applying various cuts.

| Cuts | # of Events | | | |
|---|---|---|---|---|
| Inclusive three tracks $(p, \pi^+, \pi^-)$ | not available | | | |
| Vertex & $\Delta\beta$ cuts + Topology (CL) Cut | Topology 4 | Topology 5 | | |
| | 6.8 M | 23.8 M | | |
| Final # of events | $\gamma p \to p\,\pi^+\pi^-$ | $\gamma p \to p\,\omega$ | $\gamma p \to p\,\eta$ | $\gamma p \to K^0\,\Sigma$ |
| | 6.8 M | 4.2 M | 138271 | 22890 |

Table 7: *The table shows the remaining statistics after various cuts. Note that Topology 4 implies kinematic fitting imposing no missing particle as well as energy and momentum conservation. The exclusive two-pion final state is then considered background-free. Loose confidence-level (CL) cuts of* $p > 0.001$ *were applied in both topologies and remaining background subtracted using Q values.*

## 3.11 Beam and Target Polarization

### 3.11.1 Circularly-Polarized Photon Beam - Degree of Polarization

Circularly-polarized photons were produced via bremsstrahlung of longitudinally-polarized electrons from an amorphous radiator. The degree of circular polarization of these bremsstrahlung photons, $\delta_{\odot}$, could be calculated from the longitudinal polarization of the electron beam, $\delta_{e^-}$, multiplied by a numerical factor. Using $x = E_{\gamma}/E_{e^-}$, the degree of polarization was given by the Maximon-Olson formula [15]:

$$\delta_{\odot}(x) \;=\; \delta_{e^-} \;\cdot\; \frac{4x - x^2}{4 - 4x + 3x^2}\,. \tag{12}$$

Figure 25 shows that the degree of circular polarization is roughly proportional to the photon-beam energy. In this figure, the incident-photon energy, $E_{\gamma}$, is given as a fraction of the electron-beam energy, $E_{e^-}$ (left) and for the actual g12 incident-photon energy range (right). In the g12 experiment, the electron beam (CEBAF) energy was 5.715 GeV for all the runs that we used in this analysis.

The polarization of the electron beam was measured regularly using the Møller polarimeter, which makes use of the helicity-dependent nature of Møller scattering. Table 8 summarizes the Møller measurements of the electron-beam polarization, $\delta_{e^-}$. Note that only the measurement for the second run range (56476 - 56643) was used here. During the g12 experiment, Hall B did not have priority and as a result, the polarization of the beam was delivered as a byproduct (based on the requirements of the other halls). Although the polarization fluctuated, the majority of the g12 runs had a beam polarization close to 70 % with a total uncertainty estimated to be 5 %.

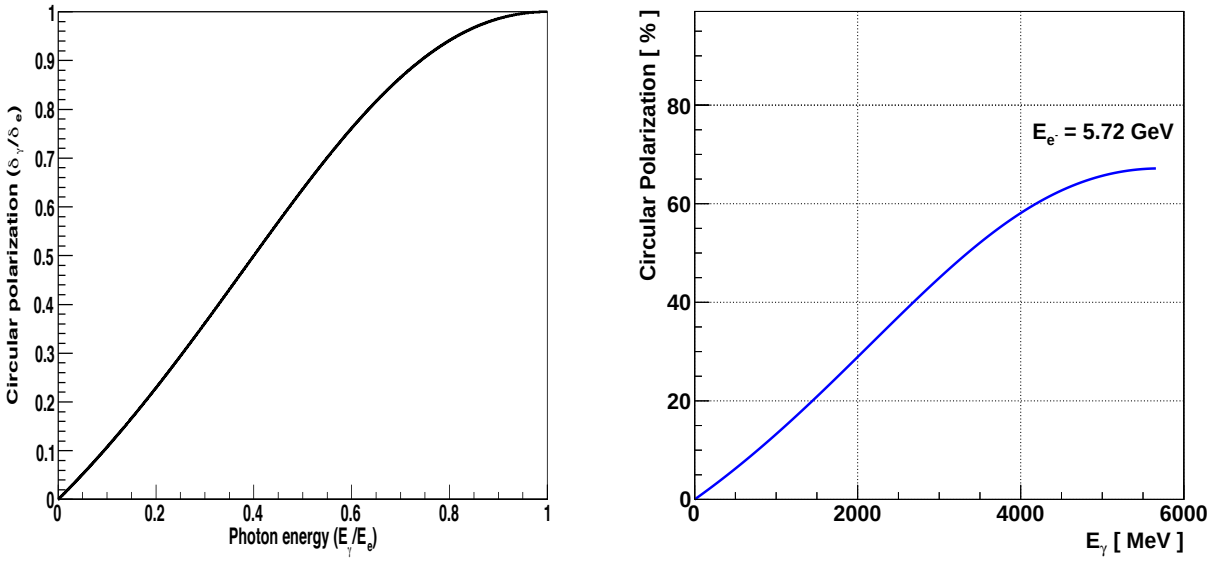


Figure 25: *Left: Degree of circular polarization in units of* $[\delta_{\gamma}/\delta_{e^-}]$ *as a function of the fraction of the photon/electron energy. Right: Degree of circular-photon polarization as a function of incident-photon energy for the g12 CEBAF-energy of 5.715 GeV; the electron-beam polarization was 67.17 %.*

| Run Range | Electron-Beam Polarization $\delta_{e^-}$ (Møller Readout) |
|---|---|
| 56355 - 56475 | $(81.221 \pm 1.48)\,\%$ |
| 56476 - 56643 | $(67.166 \pm 1.21)\,\%$ |
| 56644 - 56732 | $(59.294 \pm 1.47)\,\%$ |
| 56733 - 56743 | $(62.071 \pm 1.46)\,\%$ |
| 56744 - 56849 | $(62.780 \pm 1.25)\,\%$ |
| 56850 - 56929 | $(46.490 \pm 1.47)\,\%$ |
| 56930 - 57028 | $(45.450 \pm 1.45)\,\%$ |
| 57029 - 57177 | $(68.741 \pm 1.38)\,\%$ |
| 57178 - 57249 | $(70.504 \pm 1.46)\,\%$ |
| 57250 - 57282 | $(75.691 \pm 1.46)\,\%$ |
| 57283 - 57316 | $(68.535 \pm 1.44)\,\%$ |

Table 8: *Møller measurements of the electron-beam polarization. Only the measurement for the run range 56476 - 56643 (highlighted in blue) was used in our analysis (see also Table 2).*

The degree of circular polarization was not a continuous function of the center-of-mass energy. Therefore, we used the following equation to determine the polarization for center-of-mass bins:

$$\bar{\delta}_{\odot} = \frac{1}{N^{+} + N^{-}} \sum_{i \in \Delta\tau} \delta_{\odot}(W)\,, \tag{13}$$

where $N^{\pm}$ was the total number of $\gamma p \to p\,\pi^{+}\pi^{-}$ events (used for the observable $I^{\odot}$) for the two helicity states and $W$ was the center-of-mass energy; $\delta_{\odot}(W)$ was calculated from Equation 12. Average values were derived for each center-of-mass bin and are shown in Table 9.

### 3.11.2 Circularly-Polarized Photon Beam - Orientation of the Helicity States

The direction of the beam polarization depended on the condition of the half-wave plate (HWP) which was either IN or OUT. In CLAS-g12, the longitudinal polarization of the electron beam was flipped pseudo-randomly at a high rate with many sequences of helicity $(+\,,-)$ or $(-\,,+)$ signal per second. Occasionally, the HWP was inserted in the circularly-polarized laser beam of the electron gun to reverse helicities and thus, the beam polarization phase was changed by 180°. The HWP was inserted and removed at semi-regular intervals throughout the experimental run to ensure that no polarity-dependent bias was manifested in the measured asymmetries.

For most of the g12 runs, we had direct reporting of the electron-beam helicity and the information could be retrieved from the "level1-trigger latch word" of the TGBI bank. Bit 16 in this word described the photon helicity-state corresponding to the sign of the electron-beam polarization as shown in Table 10.

| Center-of-Mass Energy [GeV] | Average Degree of Circular Polarization, $\bar{\delta}_{\odot}$ $E_{e^-} = 5.715$ GeV |
|---|---|
| 1.70 - 1.75 | 0.150 |
| 1.75 - 1.80 | 0.164 |
| 1.80 - 1.85 | 0.179 |
| 1.85 - 1.90 | 0.194 |
| 1.90 - 1.95 | 0.210 |
| 1.95 - 2.00 | 0.226 |
| 2.00 - 2.05 | 0.243 |
| 2.05 - 2.10 | 0.261 |
| 2.10 - 2.15 | 0.279 |
| 2.15 - 2.20 | 0.298 |
| 2.20 - 2.25 | 0.317 |
| 2.25 - 2.30 | 0.336 |
| 2.30 - 2.35 | 0.356 |
| 2.35 - 2.40 | 0.377 |
| 2.40 - 2.45 | 0.397 |
| 2.45 - 2.50 | 0.418 |
| 2.50 - 2.55 | 0.438 |
| 2.55 - 2.60 | 0.459 |
| 2.60 - 2.65 | 0.479 |
| 2.65 - 2.70 | 0.500 |
| 2.70 - 2.75 | 0.519 |
| 2.75 - 2.80 | 0.538 |
| 2.80 - 2.85 | 0.556 |
| 2.85 - 2.90 | 0.574 |
| 2.90 - 2.95 | 0.590 |
| 2.95 - 3.00 | 0.605 |
| 3.00 - 3.05 | 0.619 |
| 3.05 - 3.10 | 0.631 |
| 3.10 - 3.15 | 0.642 |
| 3.15 - 3.20 | 0.651 |
| 3.20 - 3.25 | 0.658 |

Table 9: *The average degree of circular (incident-photon) polarization for g12 W-bins.*

| TGBI latch1 | Beam Helicity | |
|---|---|---|
| Bit 16 | $\lambda/2$ (OUT) | $\lambda/2$ (IN) |
| 1 | + | − |
| 0 | − | + |

Table 10: *Helicity signal from the TGBI bank for the two half-wave-plate positions. In the table, the sign + (−) denotes the beam polarization was parallel (anti-parallel) to the beam direction. We believe that this is the correct assignment. However, this information is not crucial for our analysis since we also double-checked the polarization in different ways.*

Alternatively, the g12 run-group provided the following method:

```
int GetHelicity(clasHEVT_t *HEVT)
{
   int helicity = 0;
   int readout = HEVT->hevt[0].trgprs;
   if(readout > 0) helicity = 1;
   if(readout < 0) helicity = -1;
   return helicity;
}
```

When the HWP was OUT, a bit-16 value of "one" meant that the beam polarization was parallel to the beam direction and a value of "zero" that the beam polarization was antiparallel to the beam. When the HWP was IN, the directions of the beam polarization were switched. Table 11 shows the HWP settings in the g12 data sets. The information shown in this table was experimentally confirmed by studying the beam asymmetries $I^{\odot}$ in the two-pion channel.

| Period | Run Range | HWP Condition |
|---|---|---|
| 1 | 56519 and earlier | |
| 2 | 56520 - 56594, 56608 - 56646 | |
| 3 | 56601 - 56604, 56648 - 56660 | |
| 4 | 56665 - 56667 | |
| 5 | 56605, 56607, 56647 | |
| 6 | 56668 - 56670 | |
| 7 | 56897 and later | |
| 8 | 57094 and later | |

Table 11: *The half-wave plate (HWP) condition in the g12 data sets. In our analysis, only Period 2 (highlighted in blue) was used (see also Table 2).*

### 3.11.3 Beam-Charge Asymmetry in Data Sets with Circularly-Polarized Photons

The electron-beam polarization was toggled between the helicity-plus ($h^+$) and the helicity-minus ($h^-$) state at a rate of about 30 Hz. At this large rate, the photon-beam flux for both helicity states should be the same, on average. However, small beam-charge asymmetries of the electron beam could cause instrumental asymmetries in the observed *hadronic* asymmetries and had to be considered. The beam-charge asymmetry could be calculated from the luminosities of $h^+$ and $h^-$ events:

$$\Gamma^{\pm} = \alpha^{\pm}\,\Gamma = \frac{1}{2}\,(1 \pm \bar{a}_c)\,\Gamma\,, \tag{14}$$

where $\Gamma$ was the total luminosity and the parameters $\alpha^{\pm}$ denoted the fraction of $h^+$ and $h^-$ events. The parameters $\alpha^{\pm}$ depended on the mean value of the electron-beam charge asymmetry, $\bar{a}_c$, which was studied in other CLAS experiments and typically less than 0.2 %, e.g. Ref. [16, 17]. Since the beam-charge asymmetry was very small, it could be considered negligible.

## 3.12 Signal-Background Separation: $Q$-Factor Method

The remaining step in preparing a clean event sample of the reaction in question is the removal of background underneath the signal peak. Figure 26 shows an example of the missing-mass distribution for the exclusive $p\,\pi^+\pi^-$ final state where the proton was artificially removed from the data sample and then the missing mass was calculated. The figure shows an almost background-free distribution and thus, no further background-subtraction method was applied.

The (event-based) $Q$-factor method used for the background separation in the $p\,\phi \to p\,K^+K^-$ and $p\,\pi^+\pi^-\,\pi^0$ final states (including $\gamma p \to p\,\omega \to p\,\pi^+\pi^-\pi^0$, $\gamma p \to p\,\eta \to p\,\pi^+\pi^-\pi^0$, as well as $\gamma p \to K^0\,\Sigma^+ \to p\,\pi^+\pi^-\pi^0$) is described in the following sections.

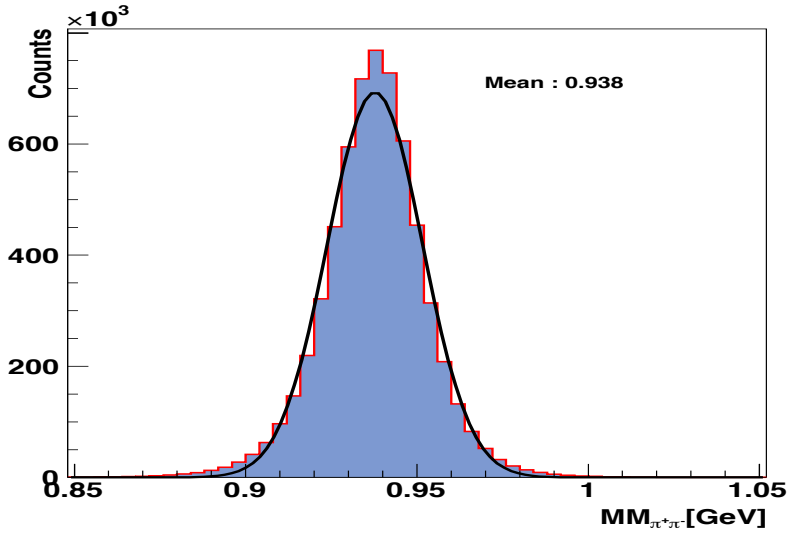


Figure 26: *Example of a (background-free) missing-mass distribution for the exclusive $\gamma p \to p\,\pi^+\pi^-$ reaction. Though detected, the proton was removed from the event sample and the missing-mass was calculated.*

### 3.12.1 General Description of the Method

In this event-based method, the set of coordinates that described the multi-dimensional phase space of the reaction was categorized into two types: *reference* and *non-reference* coordinates. The signal and background shapes had to be known *a priori* in the reference coordinate but this knowledge was not required in the non-reference coordinates. Mass was typically chosen as the reference coordinate. For each event, we then set out to find the $N_c$ nearest neighbors in the phase space of the non-reference coordinates. This was similar to binning the data using a dynamical bin width in the non-reference coordinates and making sure that we had $N_c$ events per fit.

The mass distribution of the $N_c$ events (including the candidate event) in the reference coordinate was then fitted with a total function defined as:

$$f(x) \,=\, N \,\cdot\, [f_s \,\cdot\, S(x) \,+\, (1 \,-\, f_s) \,\cdot\, B(x)]\,, \tag{15}$$

where $S(x)$ denoted the signal and $B(x)$ the background probability density function. $N$ was a normalization constant and $f_s$ was the signal fraction with a value between 0 and 1. The RooFit package of the CERN ROOT software [18] was used for the fit procedure. Since $N_c$ was usually a small number (of the order of a few hundred events), an unbinned maximum likelihood method was used for the fitting. The $Q$ factor itself was given by:

$$Q \,=\, \frac{s(x)}{s(x) \,+\, b(x)}\,, \tag{16}$$

where $x$ was the value of the reference coordinate for the candidate event, $s(x) = f_s \cdot S(x)$ and $b(x) = (1 - f_s) \cdot B(x)$. The $Q$ factor could then be used as an event weight to determine the signal contribution to any physical distribution.

### 3.12.2 The $Q$-Factor Method for the Reaction $\gamma p \to p\,\omega \to p\,\pi^+\pi^-\pi^0$

The kinematic variables that described the reaction $\gamma p \to p\,\omega$ were chosen to be the incident-photon energy, $E_\gamma$, and the center-of-mass angle of the outgoing $\omega$, $\cos\theta^{\omega}_{\mathrm{c.m.}}$. Since we reconstructed the $\omega$ from its decay into $\pi^+\pi^-$ ($\pi^0$), we also considered the relevant kinematic variables which described the five-dimensional phase space of the $3\pi$ system. The $\omega$ decay was thus entirely defined by five independent kinematic variables (including the invariant $\pi^+\pi^-\pi^0$ mass we used as *reference* variable). In total, we chose six *non-reference* variables:

- The incident photon energy $E_\gamma$ (or alternatively, the total center-of-mass energy $W$),
- The two angles of the $\omega$ meson in the helicity frame, $\cos\theta_{\mathrm{HEL}}$ and $\phi_{\mathrm{HEL}}$,
- The center-of-mass azimuthal and polar angles of the $\omega$, and
- The decay parameter $\lambda \propto |\,\vec{p}_{\pi^+} \,\times\, \vec{p}_{\pi^-}\,|^2$ [10].

The six non-reference coordinates and their maximum ranges used in the $Q$-factor method are summarized in Table 12.

For the signal-background separation in the $\omega \to \pi^+\pi^-\pi^0$ analysis, we initially applied a small $CL > 0.001$ cut (from kinematic fitting) on the $\gamma p \to p\,\pi^+\pi^-$ ($\pi^0$) final state. This loose $CL$ cut significantly reduced the background, in particular from $\gamma p \to p\,\pi^+\pi^-$ events. We then used the event-based technique to select $\omega$ events.

| $\Gamma_i$ | Non-Reference Coordinate | Maximum Range $\Delta_i$ |
|---|---|---|
| $\Gamma_0$ | $\cos\Theta^{\omega}_{\text{c. m.}}$ | 2 |
| $\Gamma_1$ & $\Gamma_2$ | $\cos\theta_{\text{HEL}}$ and $\phi_{\text{HEL}}$ | 2 & $2\pi$ [radians] |
| $\Gamma_3$ | $\phi^{\omega}_{\text{lab}}$ | $2\pi$ [radians] |
| $\Gamma_4$ | $\lambda$ | 1 |
| $\Gamma_5$ | incident photon energy $E_\gamma$ (or $W$) | 20 MeV (10 MeV below $W = 2.1$ GeV) |

Table 12: *The non-reference coordinates $\Gamma_i$ and their ranges $\Delta_i$.*

The data were divided into data subsets based on the photon energy (20-MeV wide bins). We chose the number of 1000 nearest-neighbor events for each candidate event in the phase space spanned by the non-reference coordinates. The $\pi^+\pi^-\pi^0$ invariant mass distribution of these 1000 events was then fitted over the mass range 650 - 900 MeV using the unbinned maximum-likelihood technique. Since the natural width of the $\omega$ meson is 8.49 MeV and thus, at the level of the detector resolution, we chose a Voigtian function for the signal pdf. The Voigtian function is a convolution of a Gaussian, which was used to describe the resolution, and a Breit-Wigner, which described the natural line shape of the resonance. The background shape was modeled with a second-order Chebychev polynomial for incident photon energies above 1400 MeV. Close to the reaction threshold of $E_\gamma \approx 1109$ MeV, the $\omega$ signal peak is located very close to the upper $3\pi$ phase space boundary. For this reason, we chose an Argus function instead of a Chebychev polynomial to describe the background shape.

Table 13 shows the parameters of the signal and background pdfs and the constraints imposed on them. The two pdfs were used to construct a total pdf (see Equation 15) and the $Q$ factor of the candidate event was extracted using Equation 16.

| Probability Density Function | Parameters | Initial Value | Fit Range |
|---|---|---|---|
| Voigtian | mean, $\mu$ | 782.65 MeV [7] | fixed |
| | width, $\sigma$ | 8.0 MeV | 0 - 30 MeV |
| | natural width, $\Gamma$ | 8.49 MeV [7] | fixed |
| Chebychev ($E_\gamma > 1.4$ GeV) | $c_0$ | 0.5 | 0.0 - 1.8 |
| | $c_1$ | 0.1 | $-1.2$ - 1.2 |
| Argus ($E_\gamma < 1.4$ GeV) | endpoint, $m_0$ | 820 MeV | 790.0 - 950.0 MeV |
| | slope, $c$ | $-1.0$ | $-10.0$ - 0.2 |

Table 13: *Parameters of the signal and background probability-density functions. A Voigtian was used to describe the $\omega$ signal and a second-order Chebychev polynomial (an Argus function for $E_\gamma < 1.4$ GeV) was used to describe the background over the $\pi^+\pi^-\pi^0$ mass range 650 - 900 MeV.*

**Quality Checks**

1. Once the fit parameters were determined in an individual likelihood fit, we performed a least-square "fit" of the same mass distribution from the 1000 events. Among other things, this allowed us to plot the distribution of reduced-$\chi^2$ values as a goodness-of-fit measure. The left column of Figure 27 shows several such reduced-$\chi^2$ distributions for a few randomly-selected example $E_\gamma$ bins: (top to bottom row) $E_\gamma \in [1.64, 1.66]$ GeV, $E_\gamma \in [2.10, 2.12]$ GeV, $E_\gamma \in [4.00, 4.02]$ GeV, $E_\gamma \in [5.00, 5.02]$ GeV. These reduced-$\chi^2$ distributions peak fairly close to the ideal value of *one*. Given the fairly small number of events in these distributions, we also concluded that the fitter picks up statistical fluctuations. This resulted in overconstrained fits and slightly smaller reduced-$\chi^2$ values, about 0.7 - 0.8 on average.

2. Defined in terms of the pion momenta in the rest frame of the $\omega$ meson, the quantity $\lambda = |\vec{p}_{\pi^+} \times \vec{p}_{\pi^-}|^2 / \lambda_{\max}$ is proportional to the $\omega \to \pi^+\pi^-\pi^0$ decay amplitude as a consequence of isospin conservation [8] with $\lambda_{\max}$ defined as [19]:

$$\lambda_{\max} = T^2 \left( \frac{T^2}{108} + \frac{mT}{9} + \frac{m^2}{3} \right) \tag{17}$$

   for a totally symmetric decay, where $T = T_1 + T_2 + T_3$ is the sum of the $\pi^{\pm,0}$ kinetic energies and $m$ is the $\pi^\pm$ mass. The parameter $\lambda$ varies between 0 and 1 and shows a linearly-increasing distribution as expected for a vector meson.

   Figure 27 (center column) shows the $\lambda$ distributions for the same energy bins as for the corresponding reduced-$\chi^2$ distributions in the left column. The (red) signal was generated by weighting event-by-event the (black) full distribution with the $Q$ values; the (blue) background distribution was generated by weighting the full distribution with $1 - Q$. The linear behavior of the $\omega$ signal events is clearly visible.

Finally, $\omega \to \pi^+\pi^-\pi^0$-mass distributions showing the full statistics in a given energy bin are presented in Figure 27 (right column) for the selected $E_\gamma$ bins discussed above and in 10-MeV-wide center-of-mass $W$ bins for the entire CLAS-g12 energy range in Figures 28 - 42.

**The Photon-Energy Range below 2 GeV**

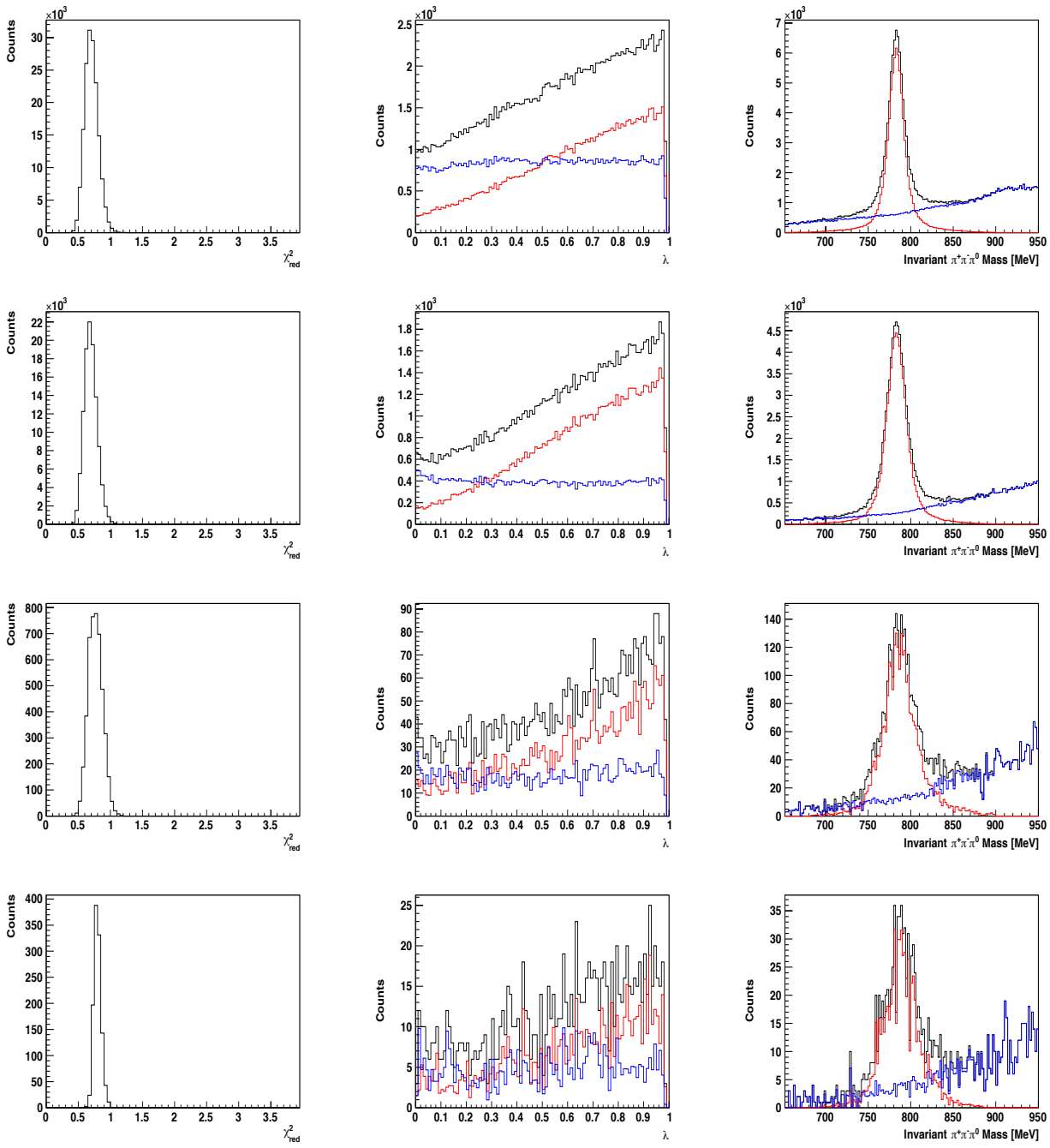


Figure 27: *Quality checks - shown are randomly selected $E_\gamma$ bins across a wide range in the incident photon energy: (top to bottom row) $E_\gamma \in [1.64, 1.66]$ GeV, $E_\gamma \in [2.10, 2.12]$ GeV, $E_\gamma \in [4.00, 4.02]$ GeV, $E_\gamma \in [5.00, 5.02]$ GeV. (Left column) Examples of reduced-$\chi^2$ distributions. (Center) Examples of $\lambda$ distributions. (Right) The full mass distribution for the energy bin. The black line denotes the full distribution, the red line the signal, and the blue solid line the background distribution.*

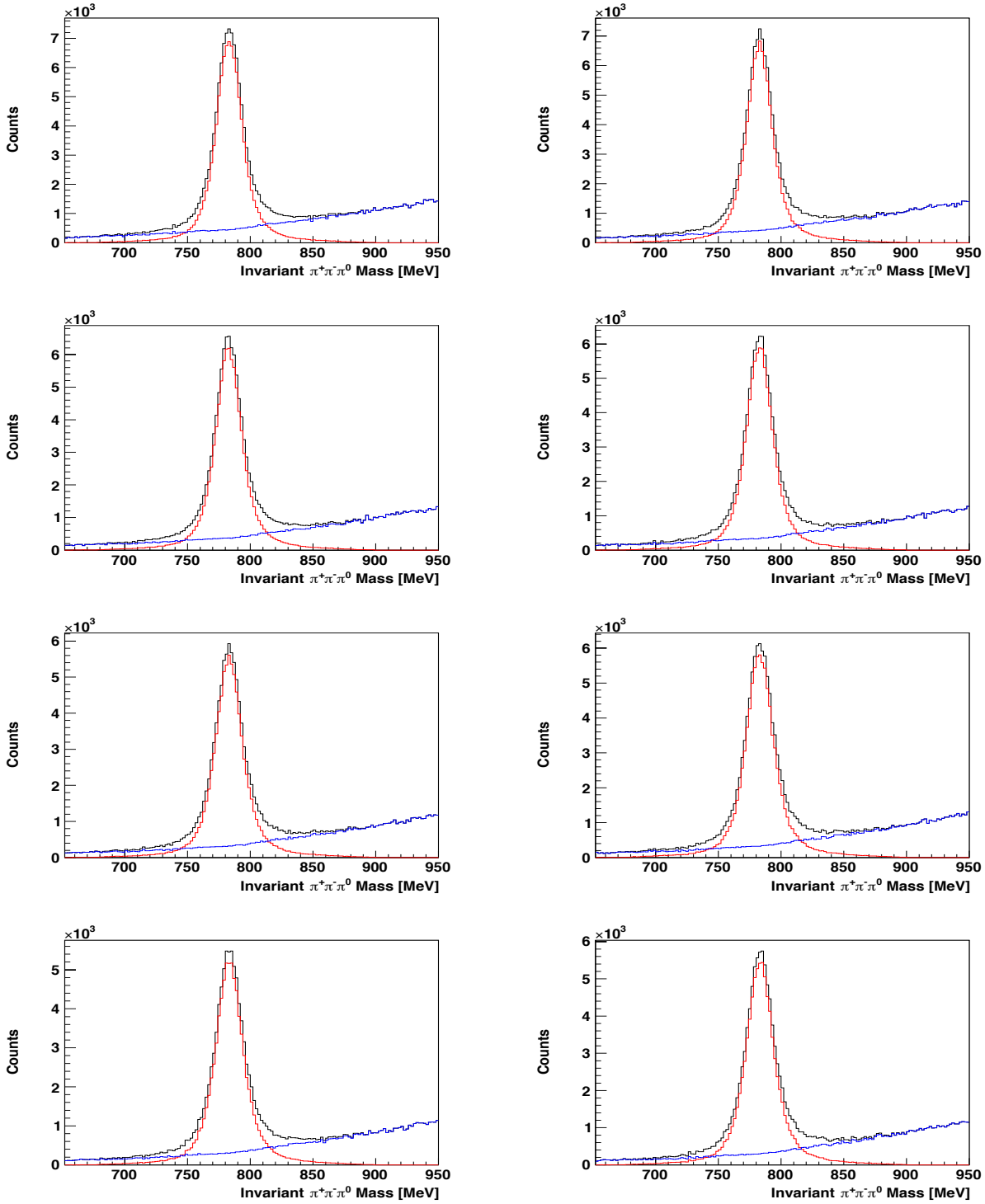


Figure 28: *Invariant $\pi^+\pi^-\pi^0$ mass distributions for $\gamma p \to p\omega$. Shown are 10-MeV-wide $W$ bins starting at $W \in [2120, 2130]$ MeV (top left), $W \in [2130, 2140]$ MeV (top right), etc.*

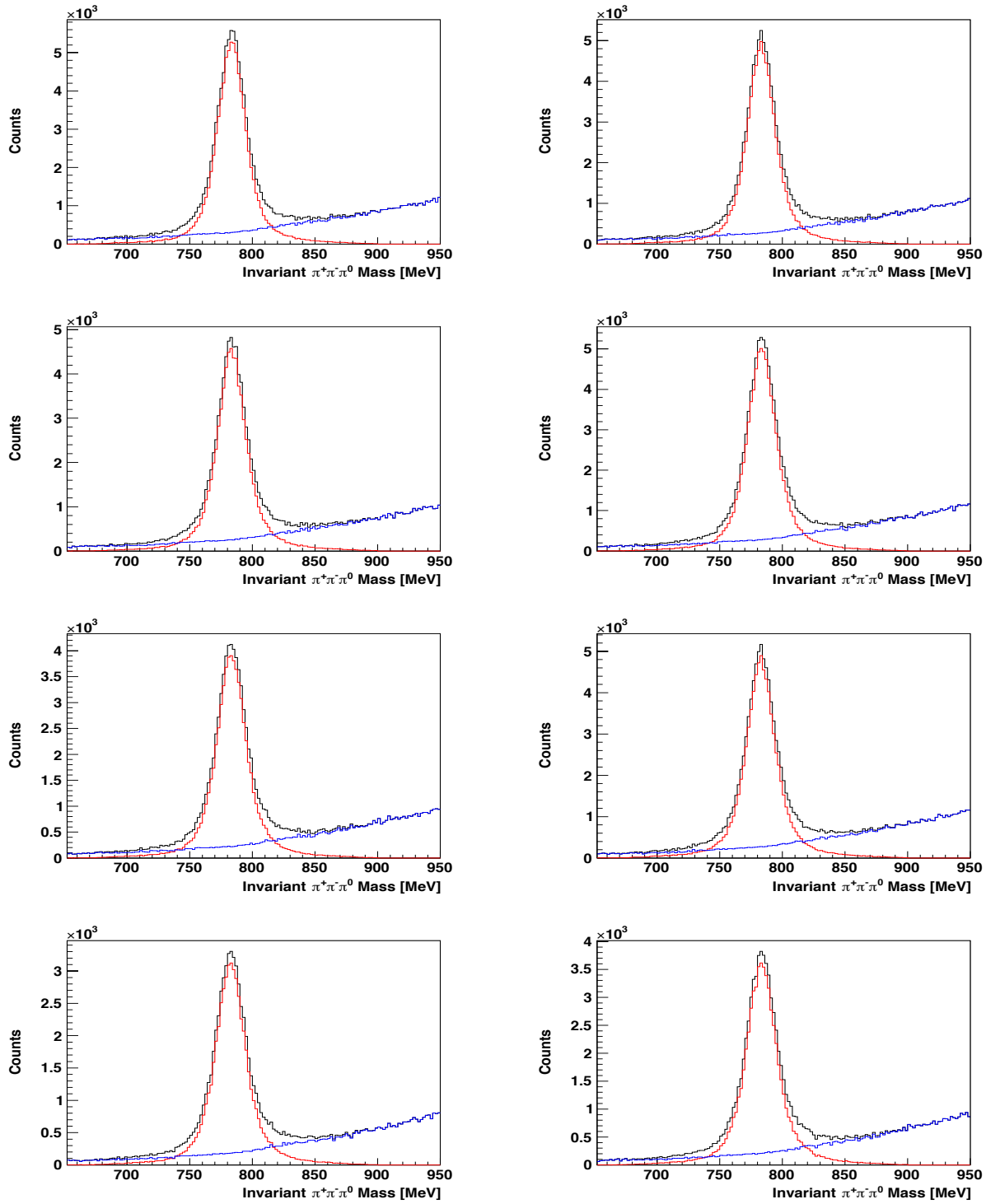


Figure 29: *Invariant $\pi^+\pi^-\pi^0$ mass distributions for $\gamma p \to p\omega$. Shown are 10-MeV-wide $W$ bins starting at $W \in [2200, 2210]$ MeV (top left), $W \in [2210, 2220]$ MeV (top right), etc.*

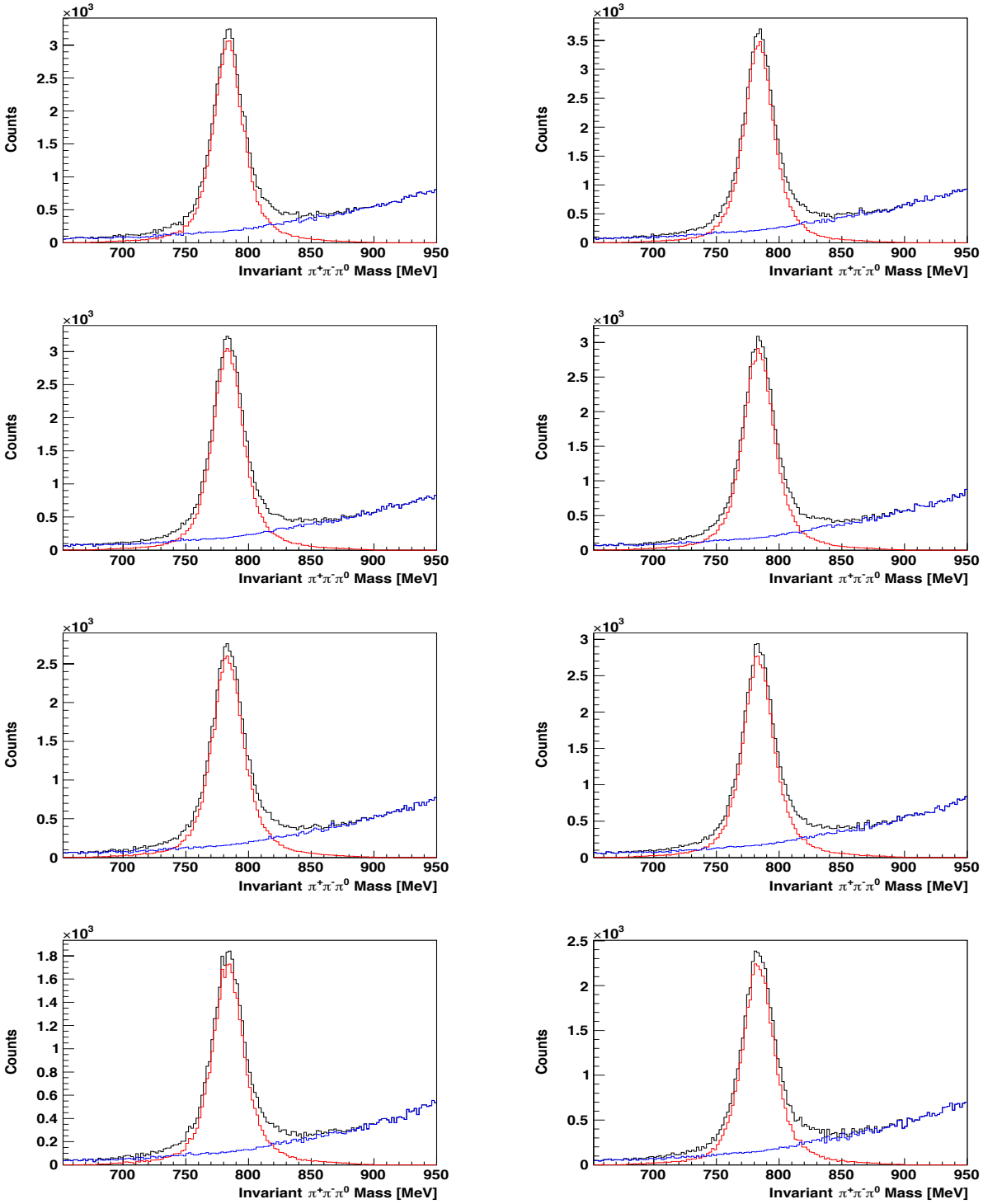


Figure 30: *Invariant $\pi^+\pi^-\pi^0$ mass distributions for $\gamma p \to p\omega$. Shown are 10-MeV-wide $W$ bins starting at $W \in [2280, 2290]$ MeV (top left), $W \in [2290, 2300]$ MeV (top right), etc.*

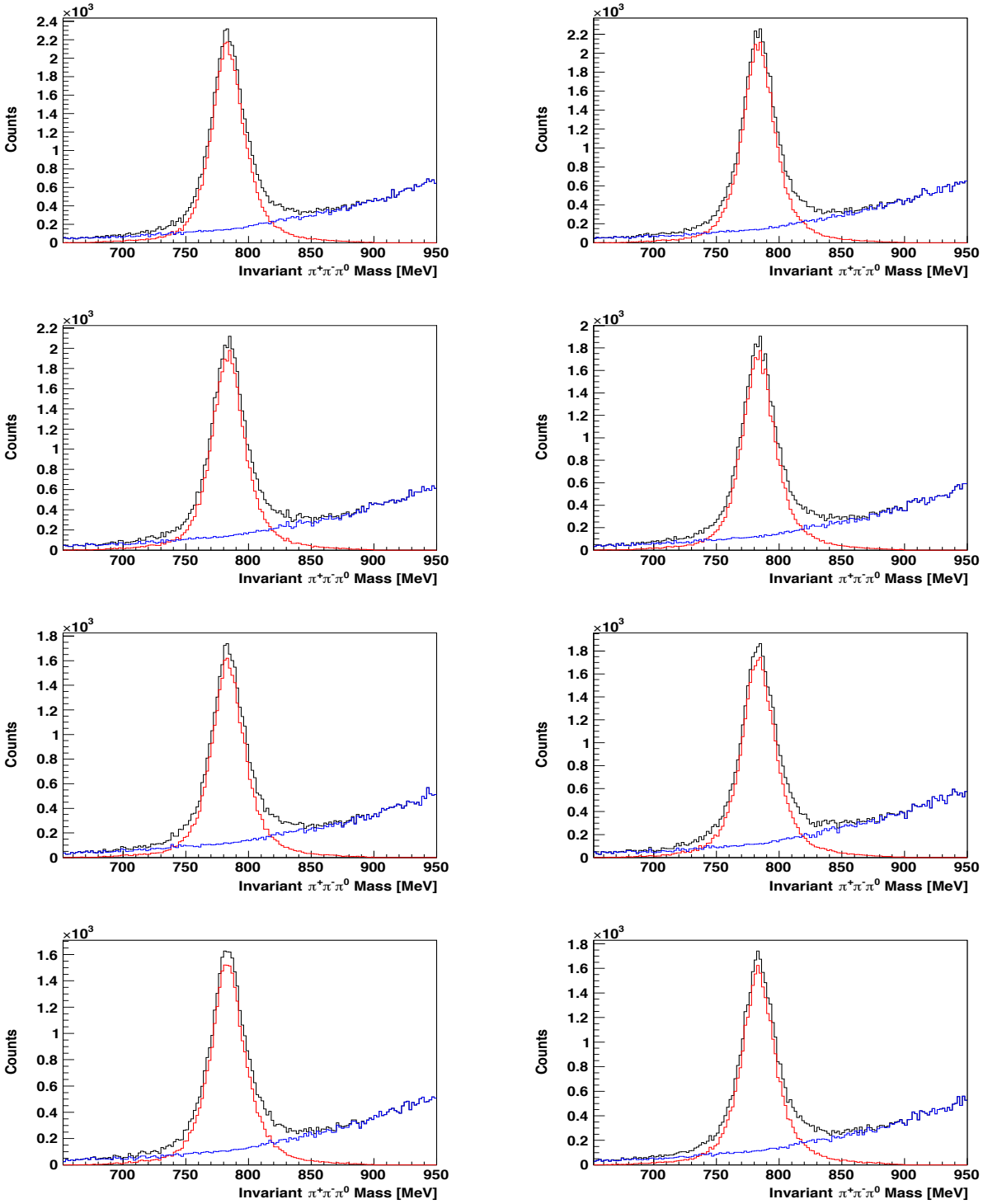


Figure 31: *Invariant $\pi^+\pi^-\pi^0$ mass distributions for $\gamma p \to p\omega$. Shown are 10-MeV-wide $W$ bins starting at $W \in [2360, 2370]$ MeV (top left), $W \in [2370, 2380]$ MeV (top right), etc.*

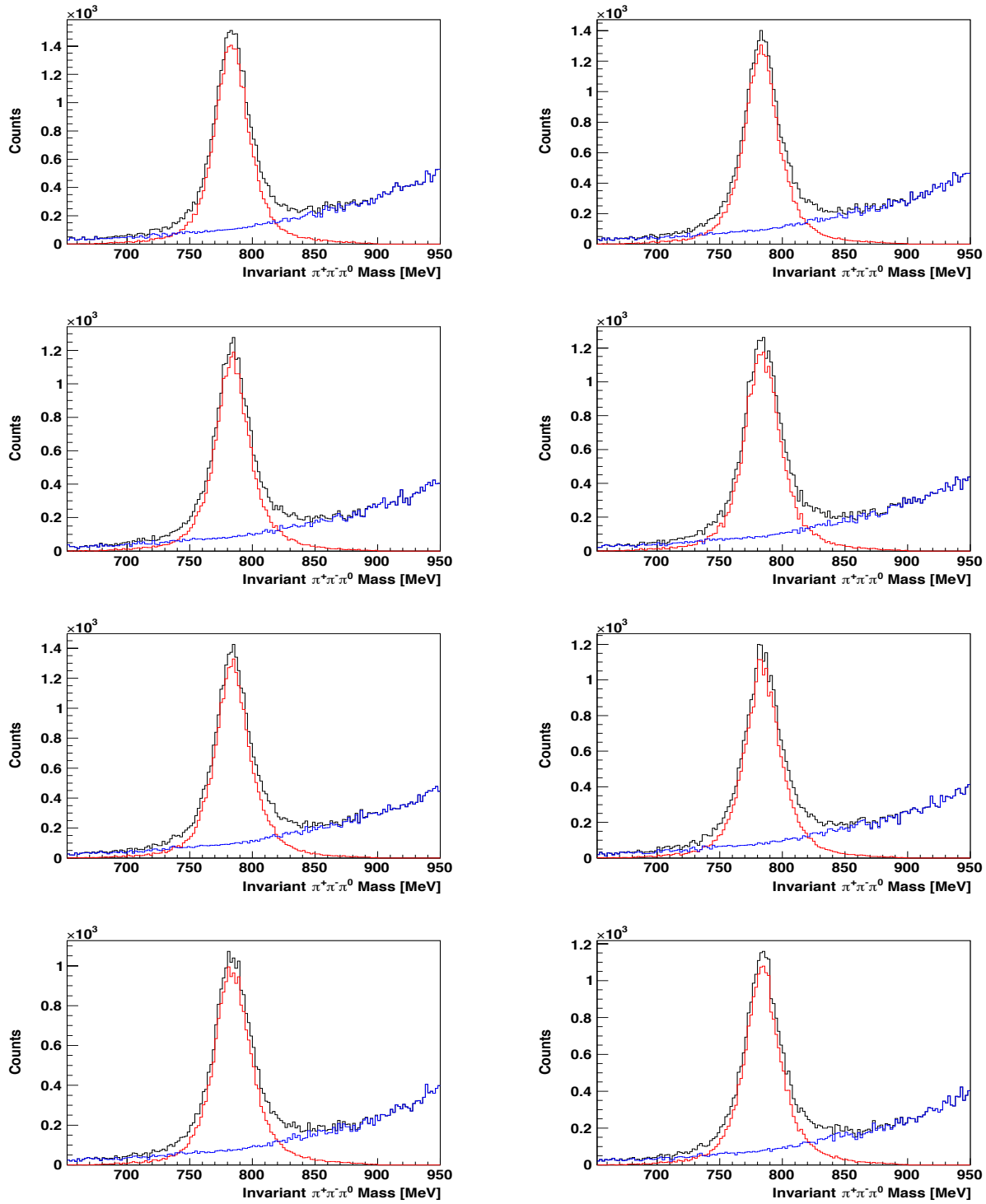


Figure 32: *Invariant $\pi^+\pi^-\pi^0$ mass distributions for $\gamma p \to p\omega$. Shown are 10-MeV-wide $W$ bins starting at $W \in [2440, 2450]$ MeV (top left), $W \in [2450, 2460]$ MeV (top right), etc.*

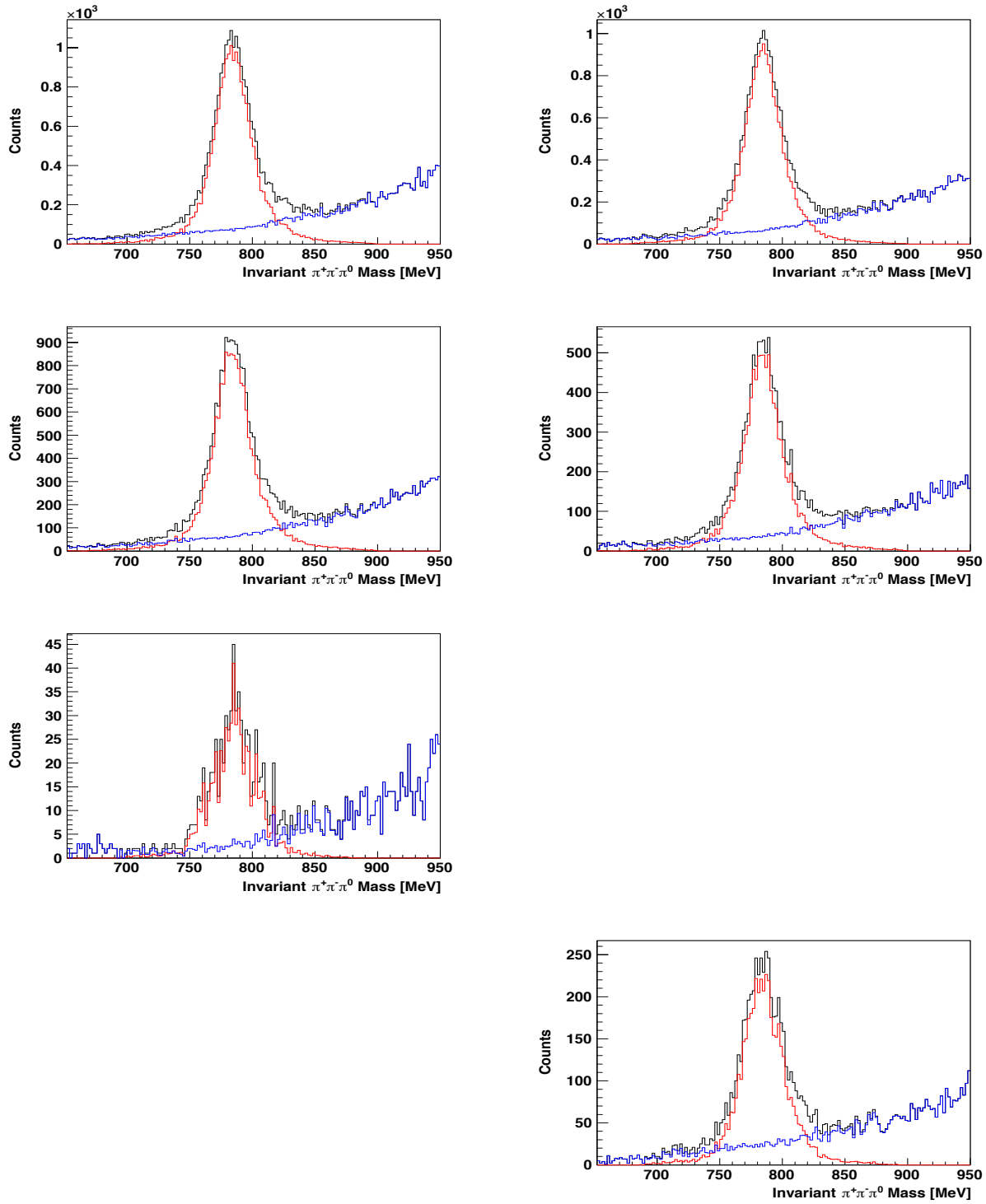


Figure 33: *Invariant $\pi^+\pi^-\pi^0$ mass distributions for $\gamma p \to p\omega$. Shown are 10-MeV-wide $W$ bins starting at $W \in [2520, 2530]$ MeV (top left), $W \in [2530, 2540]$ MeV (top right), etc.*

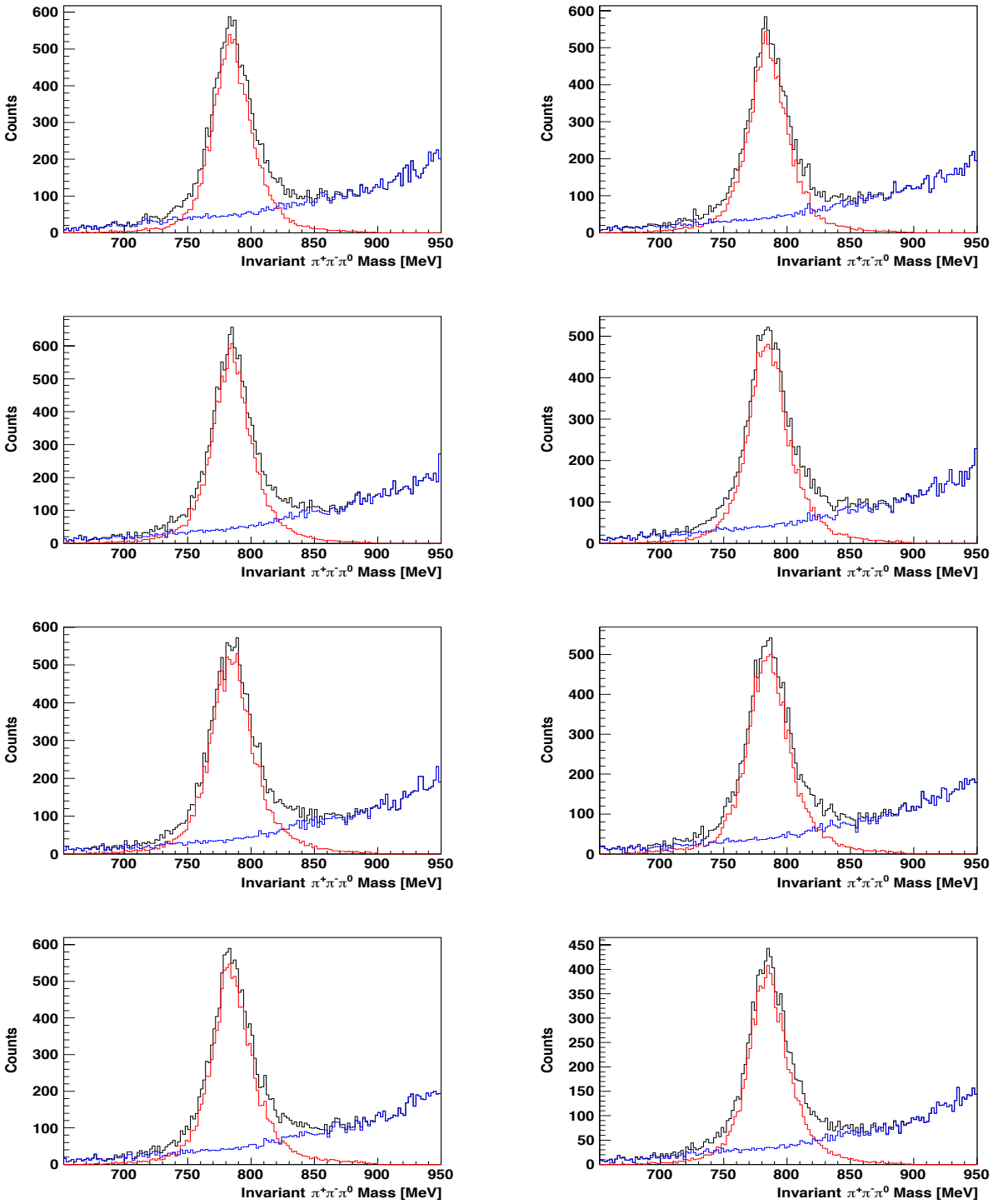


Figure 34: *Invariant $\pi^+\pi^-\pi^0$ mass distributions for $\gamma p \to p\omega$. Shown are 10-MeV-wide $W$ bins starting at $W \in [2600, 2610]$ MeV (top left), $W \in [2610, 2620]$ MeV (top right), etc.*

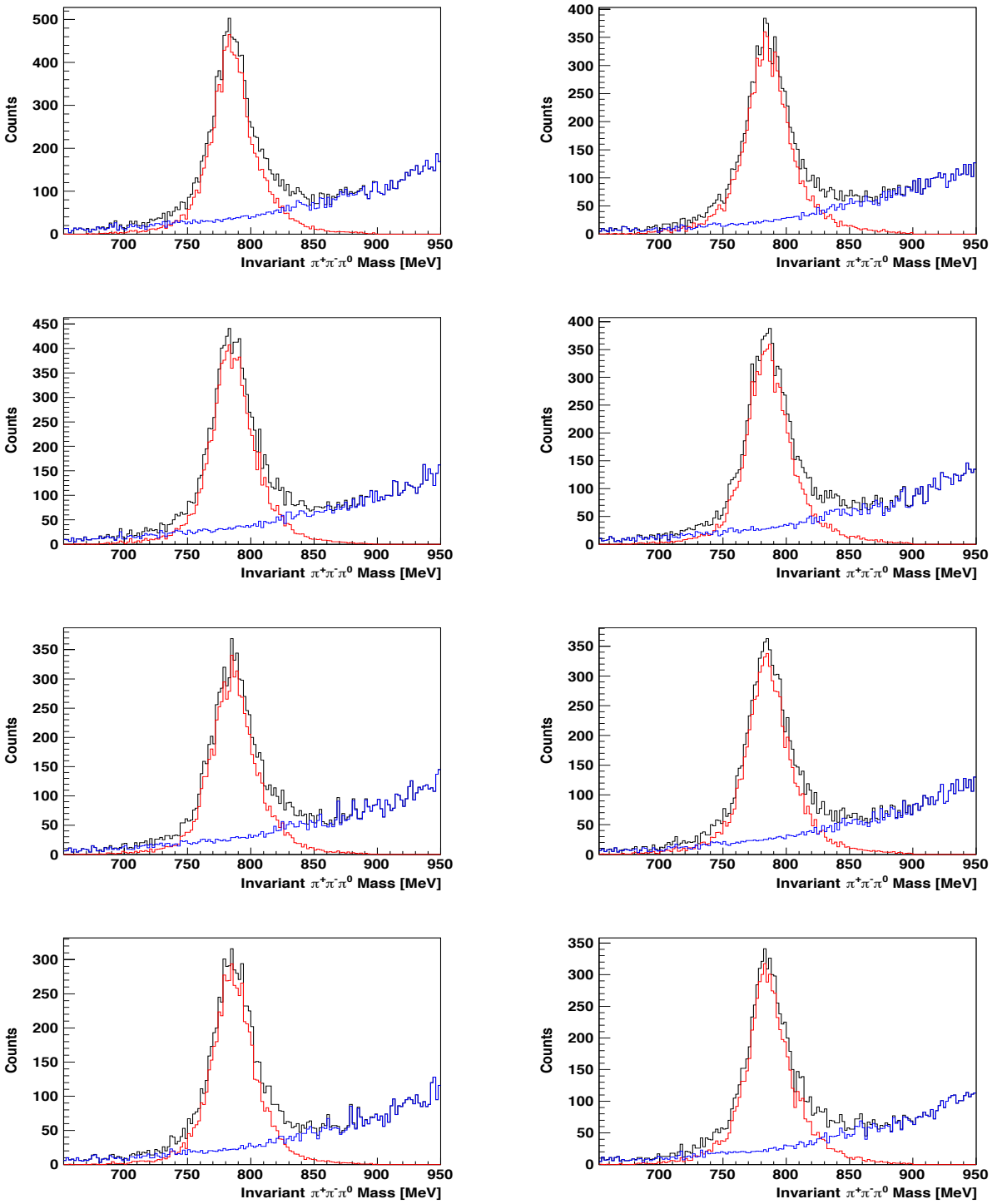


Figure 35: *Invariant $\pi^+\pi^-\pi^0$ mass distributions for $\gamma p \to p\omega$. Shown are 10-MeV-wide $W$ bins starting at $W \in [2680, 2690]$ MeV (top left), $W \in [2690, 2700]$ MeV (top right), etc.*

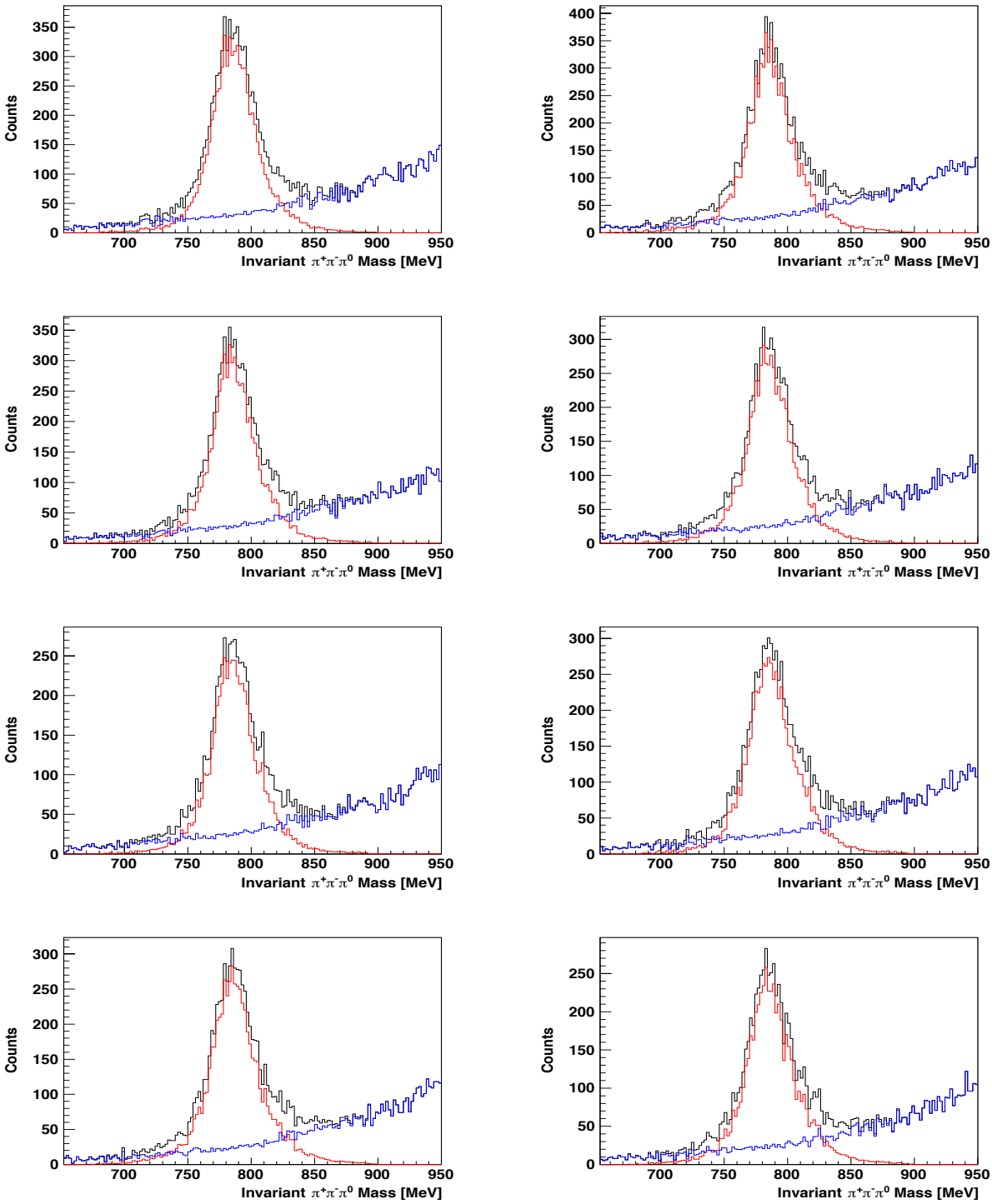


Figure 36: *Invariant $\pi^+\pi^-\pi^0$ mass distributions for $\gamma p \to p\omega$. Shown are 10-MeV-wide $W$ bins starting at $W \in [2760, 2770]$ MeV (top left), $W \in [2770, 2780]$ MeV (top right), etc.*

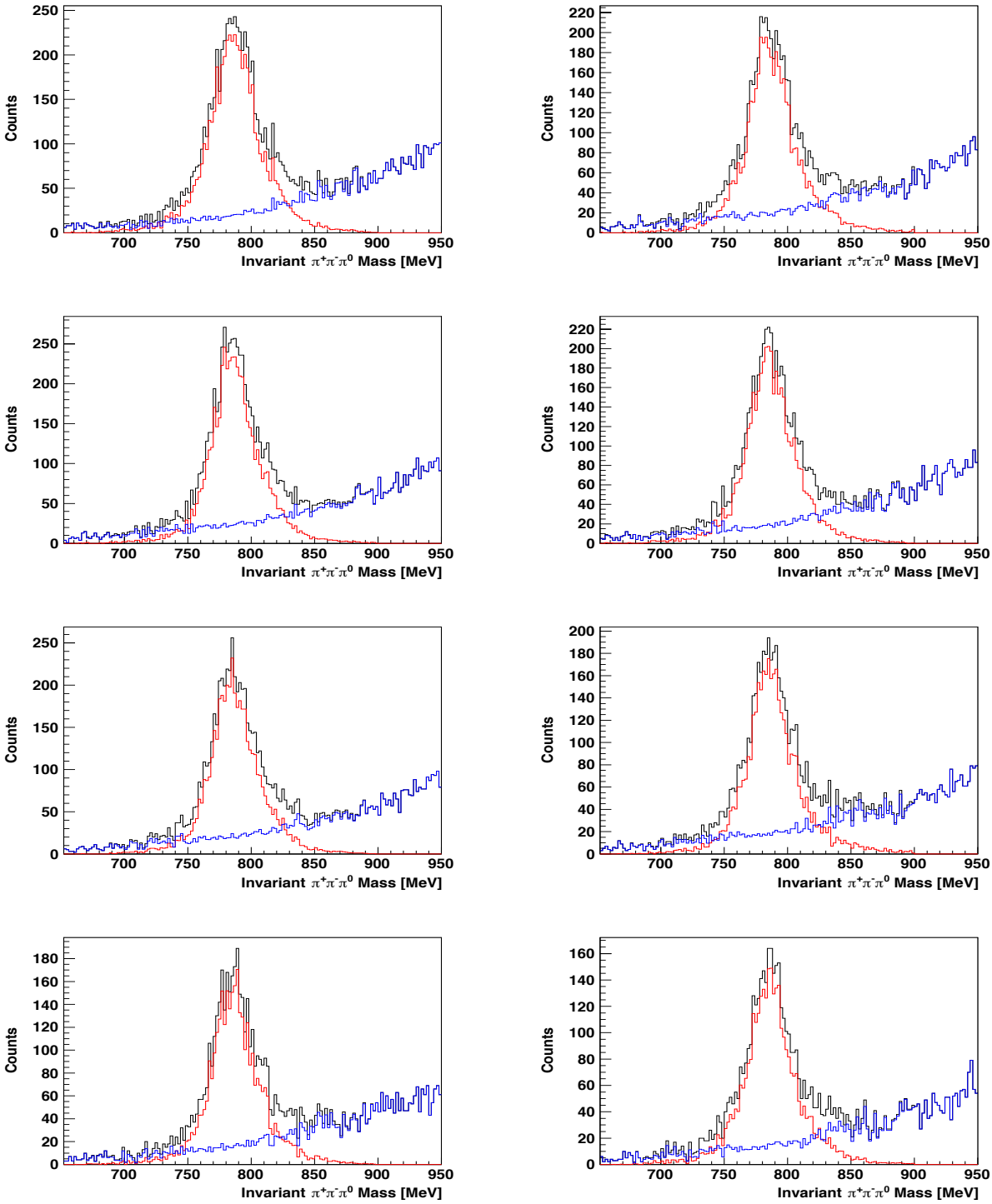


Figure 37: *Invariant $\pi^+\pi^-\pi^0$ mass distributions for $\gamma p \to p\omega$. Shown are 10-MeV-wide $W$ bins starting at $W \in [2840, 2850]$ MeV (top left), $W \in [2850, 2860]$ MeV (top right), etc.*

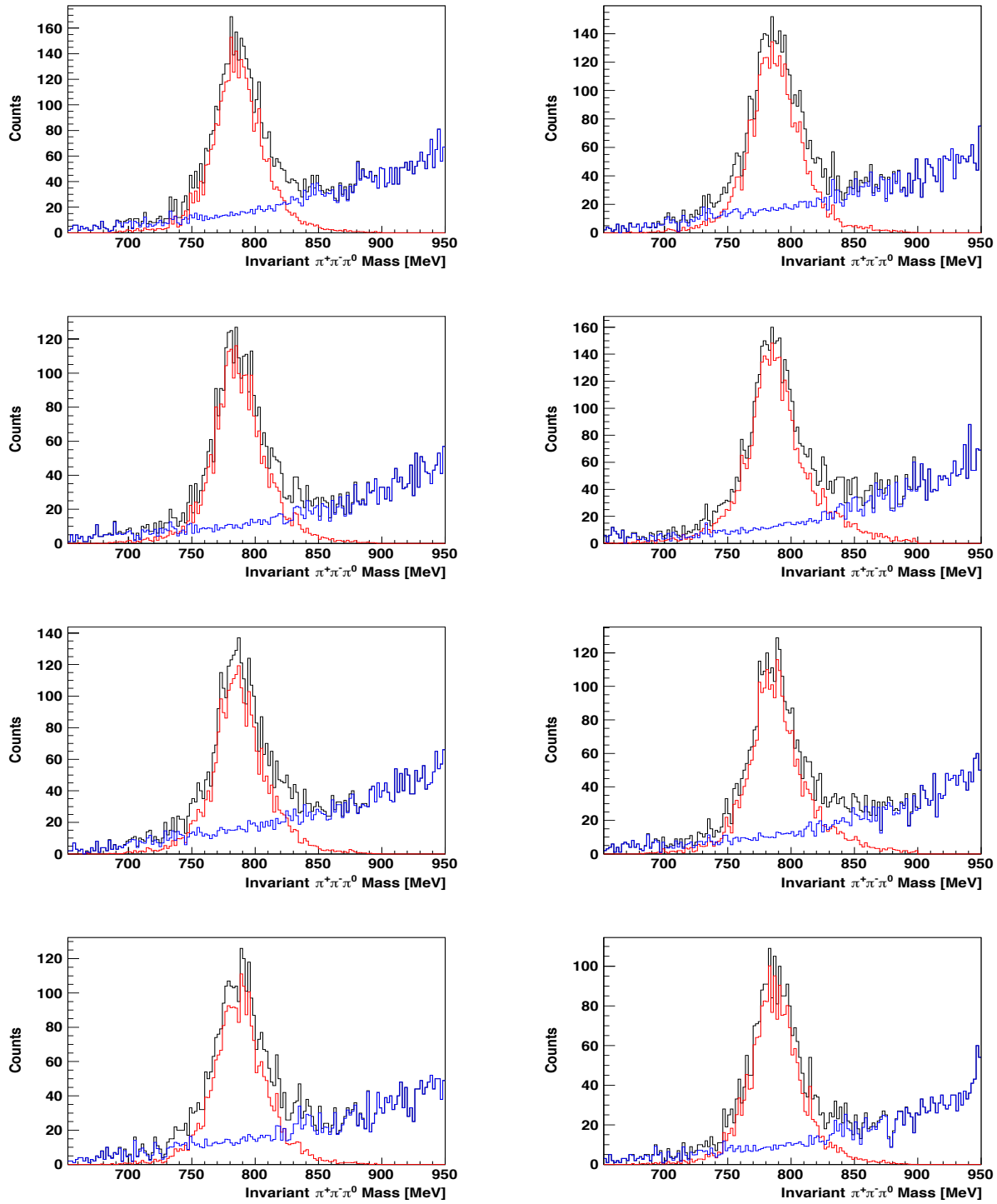


Figure 38: *Invariant $\pi^+\pi^-\pi^0$ mass distributions for $\gamma p \to p\omega$. Shown are 10-MeV-wide $W$ bins starting at $W \in [2920, 2930]$ MeV (top left), $W \in [2930, 2940]$ MeV (top right), etc.*

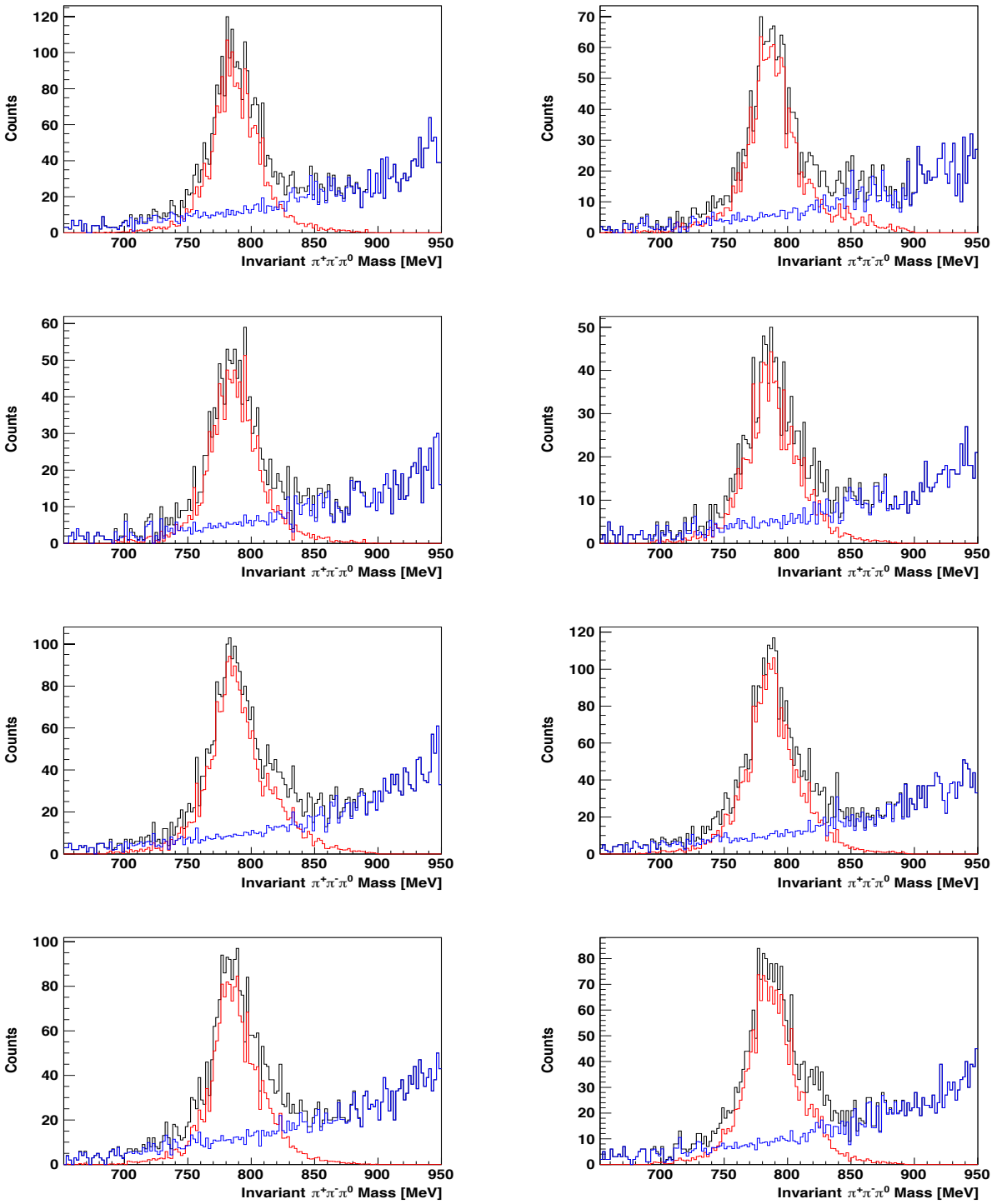


Figure 39: *Invariant $\pi^+\pi^-\pi^0$ mass distributions for $\gamma p \to p\omega$. Shown are 10-MeV-wide $W$ bins starting at $W \in [3000, 3010]$ MeV (top left), $W \in [3010, 3020]$ MeV (top right), etc.*

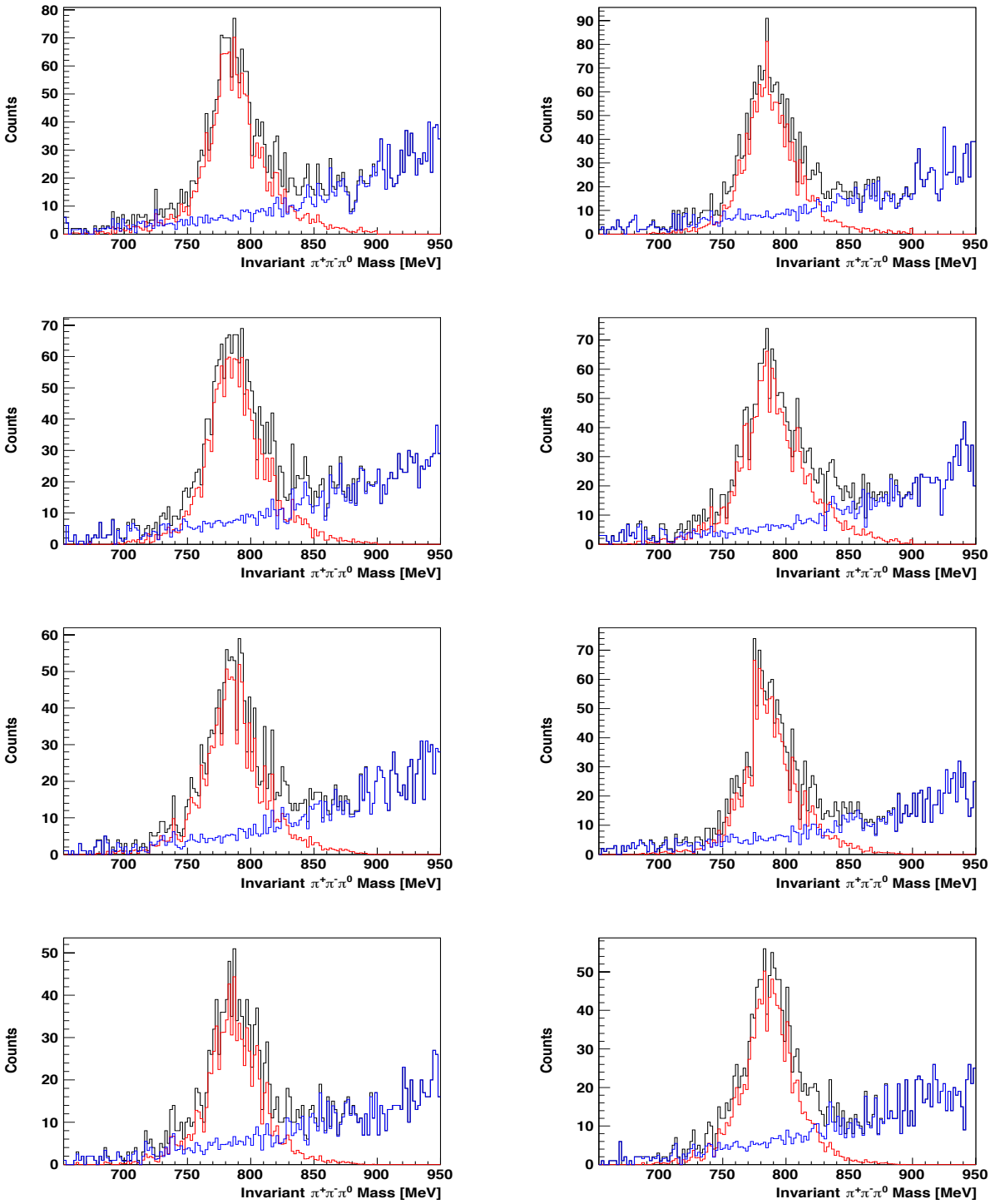


Figure 40: *Invariant $\pi^+\pi^-\pi^0$ mass distributions for $\gamma p \to p\omega$. Shown are 10-MeV-wide $W$ bins starting at $W \in [3080, 3090]$ MeV (top left), $W \in [3090, 3100]$ MeV (top right), etc.*

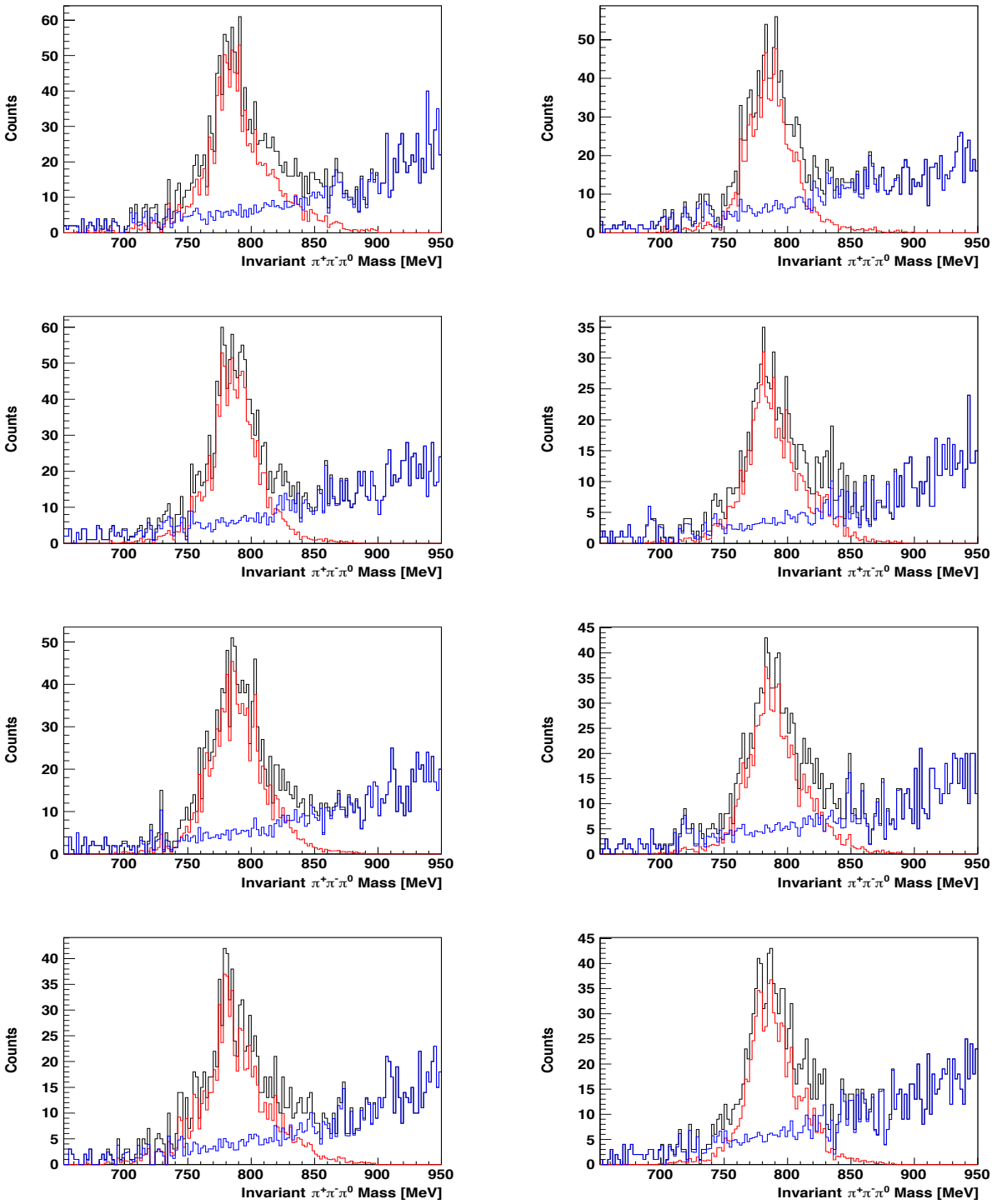


Figure 41: *Invariant $\pi^+\pi^-\pi^0$ mass distributions for $\gamma p \to p\omega$. Shown are 10-MeV-wide $W$ bins starting at $W \in [3160, 3170]$ MeV (top left), $W \in [3170, 3180]$ MeV (top right), etc.*

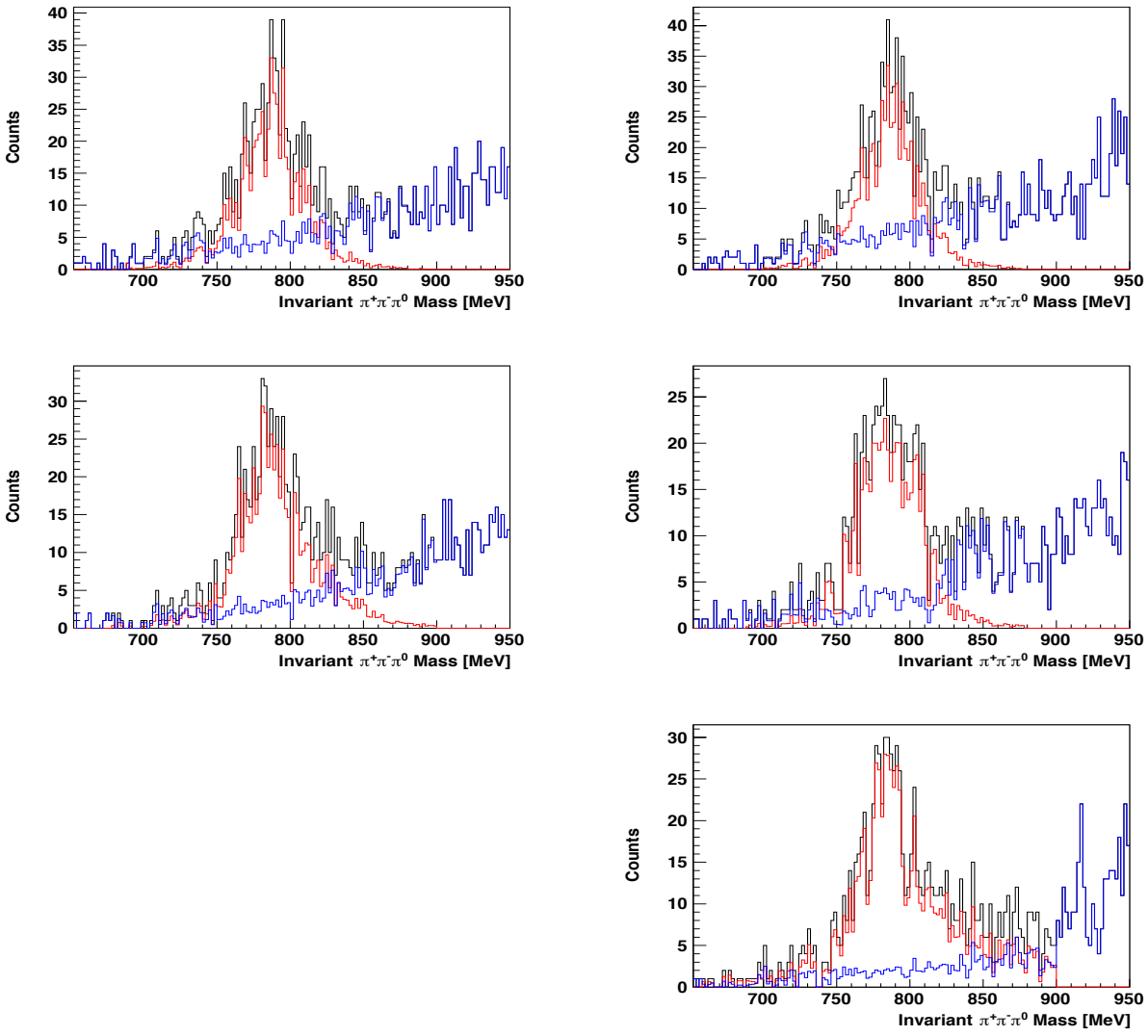


Figure 42: *Invariant $\pi^+\pi^-\pi^0$ mass distributions for $\gamma p \to p\omega$. Shown are 10-MeV-wide $W$ bins starting at $W \in [3240, 3250]$ MeV (top left), $W \in [3250, 3260]$ MeV (top right), etc.*

### 3.12.3 The Reaction $\gamma p \to p\,\eta \to p\,\pi^+\pi^-\pi^0$

The reconstruction of the $\eta$ meson is based on its $\pi^+\pi^-\pi^0$ decay mode and therefore, the invariant $\pi^+\pi^-\pi^0$ mass was used as the reference coordinate. The non-reference coordinates are the same as those used for the $\omega$ meson and are summarized in Table 12. The quantity $\lambda$ may not have a direct physical meaning in the $\eta$ decay but in defining the phase space for the nearest-neighbors search, it still serves as an independent kinematic variable.

The $\eta$ meson has a natural width of $\Gamma = 1.31 \pm 0.05$ keV [7]. For this reason, the observed width of the $\eta$ signal is dominated by the experimental resolution and the lineshape should be describable by a Gaussian. However, we noticed that a simple Gaussian could not describe very well the very low- and high-mass tails of the signal peak, which caused some enhancements in the background description. A double-Gaussian in combination with a second-order Chebychev polynomial for the background solved this issue. Table 14 summarizes the parameters of the signal and background pdfs and the constraints imposed on them.

To compare with published CLAS results [9], we have used the following binning scheme in $W$:

1. $W \in$ [1720, 2100] MeV in 10-MeV-wide $W$ bins ($E_\gamma \in$ [1707, 1881] MeV),
2. $W \in$ [2100, 2360] MeV in 20-MeV-wide $W$ bins ($E_\gamma \in$ [1881, 2499] MeV),
3. $W \in$ [2360, 3320] MeV in 40-MeV-wide $W$ bins ($E_\gamma \in$ [2499, 5405] MeV).

Figures 43 - 46 show the invariant $\pi^+\pi^-\pi^0$ mass distributions for the $W \in$ [1780, 2100] MeV range, which corresponds to about $E_\gamma \in$ [1219, 1881] MeV. The black solid line denotes the full mass distribution, the red solid is the signal, and the blue solid line represents the background distribution. Note that $E_\gamma = 1100$ MeV is at the very low end of the tagging range. For this reason, the first truly available $W$ bin would be 1750 - 1760 MeV; the statistics is low in this bin, though. Full statistics is then available in CLAS-g12 from $W = 1780$ MeV (Fig. 43, top row). The background exhibits an almost linear behavior but we chose a second-order polynomial and a slightly broader fit range of 455 - 650 MeV to avoid ambiguities between the background pdf and the second (broader) signal Gaussian. The broader fit range also required us to use 500 events (up from initially 300 events) in the search for nearest neighbors to accumulate sufficient signal statistics in the individual mass distributions. Figs. 47 - 49 show the $\pi^+\pi^-\pi^0$ distributions for the $W \in$ [2100, 3000] MeV range.

| Probability Density Function | Parameters | Initial Value | Fit Range |
|---|---|---|---|
| Gaussian I | Mean, $\mu$ | 547.86 [7] MeV | fixed |
| | Width, $\sigma$ | 5.0 MeV | 1.5 - 9.5 MeV |
| Gaussian II | Mean, $\mu$ | 548.40 MeV | 540.0 - 560.0 MeV |
| | Width, $\sigma$ | 10.0 MeV | 6.0 - 28.0 MeV |
| Chebychev | $c_0$ | 0.8 | 0.0 - 1.6 |
| | $c_1$ | 0.19 | $-0.6$ - 1.5 |

Table 14: *Parameters of the signal and background probability-density functions. A double-Gaussian was used to describe the $\eta$ signal and a second-order Chebychev polynomial was used to describe the background over the $\pi^+\pi^-\pi^0$ mass range 455-650 MeV.*

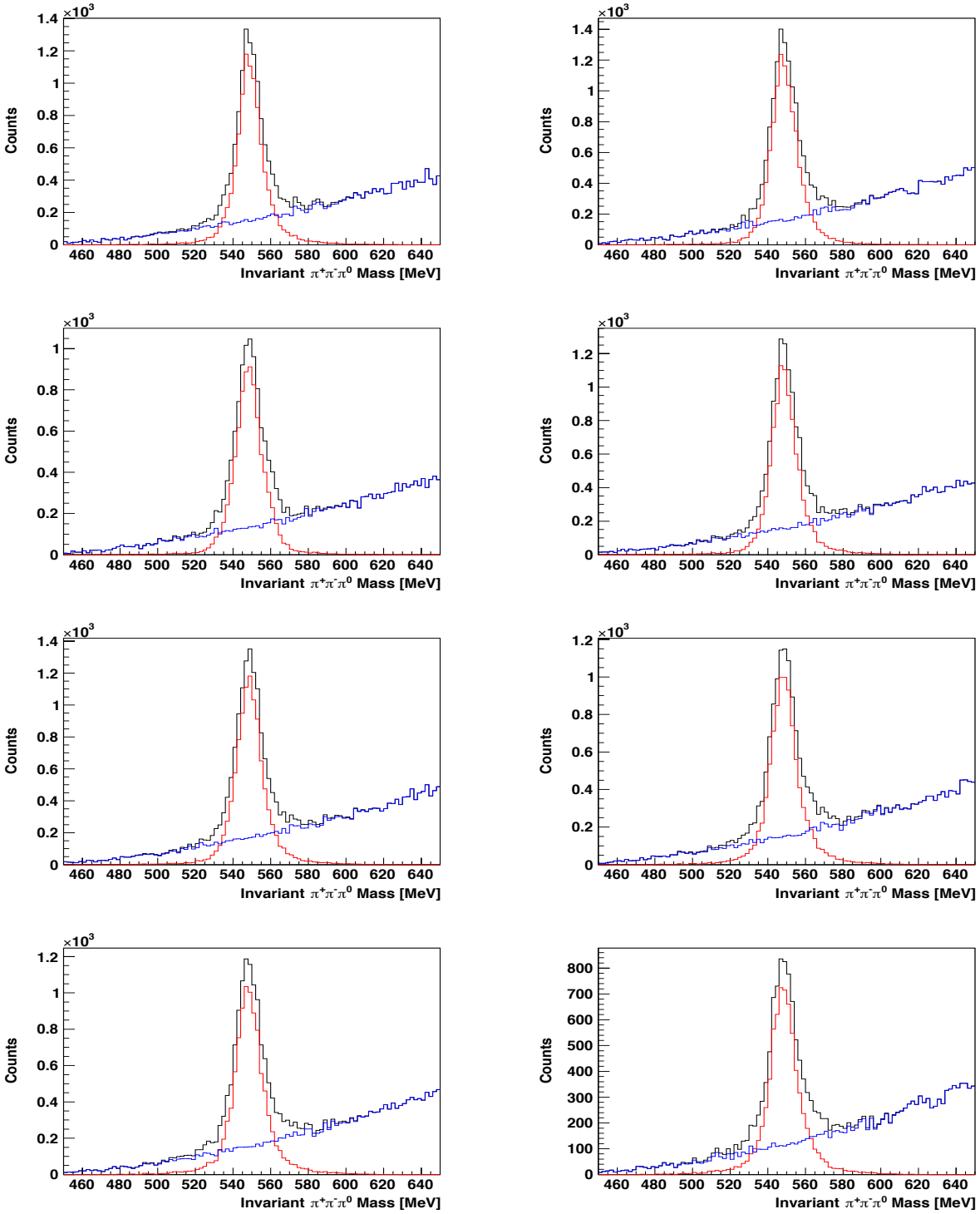


Figure 43: *Invariant $\pi^+\pi^-\pi^0$ distributions for the reaction $\gamma p \to p\eta$. Shown are 10-MeV-wide $W$ bins starting at $W \in [1780, 1790]$ MeV (top left), $W \in [1790, 1800]$ MeV (top right), etc.*

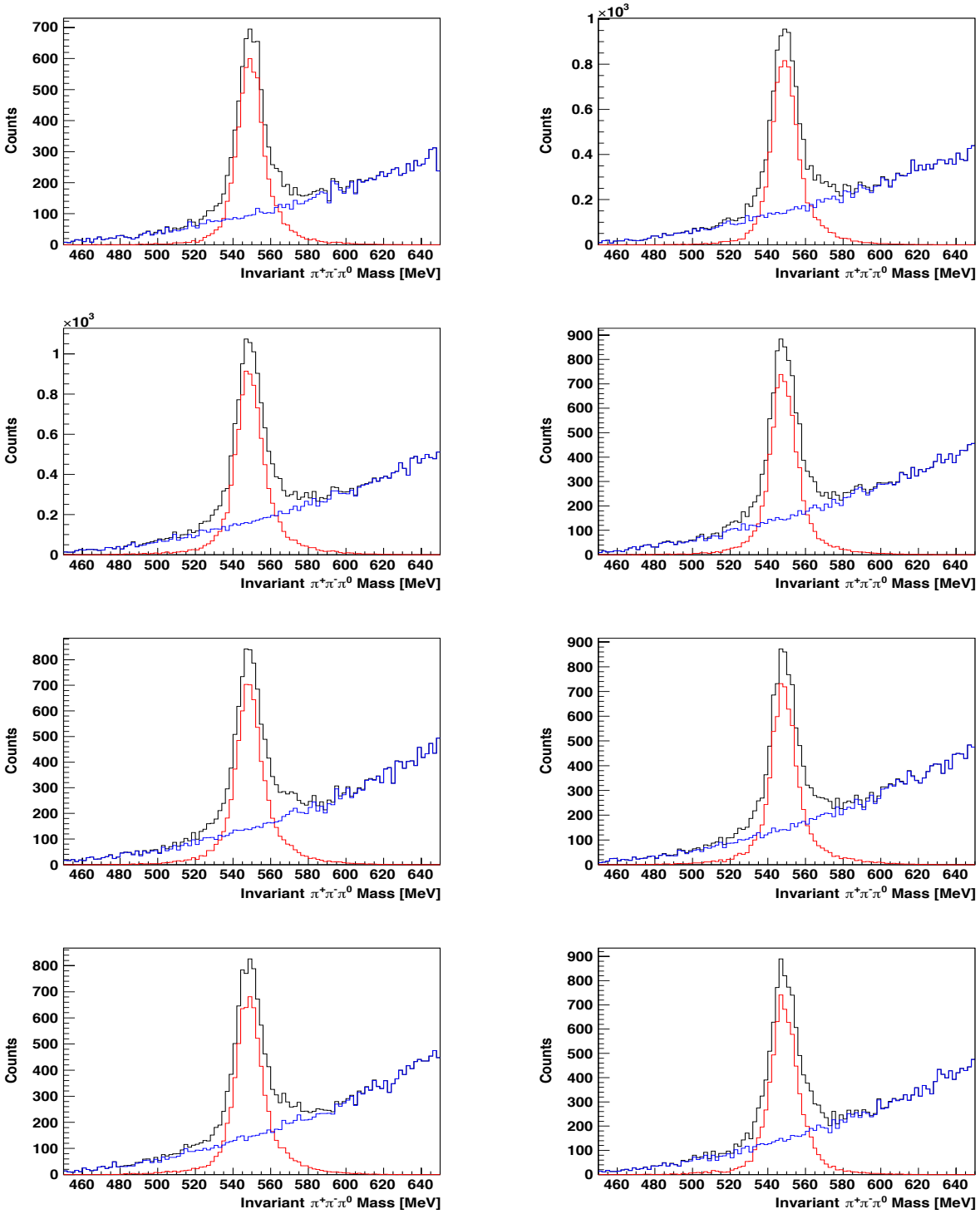


Figure 44: *Invariant $\pi^+\pi^-\pi^0$ distributions for the reaction $\gamma p \to p\eta$. Shown are 10-MeV-wide $W$ bins starting at $W \in [1860, 1870]$ MeV (top left), $W \in [1870, 1880]$ MeV (top right), etc.*

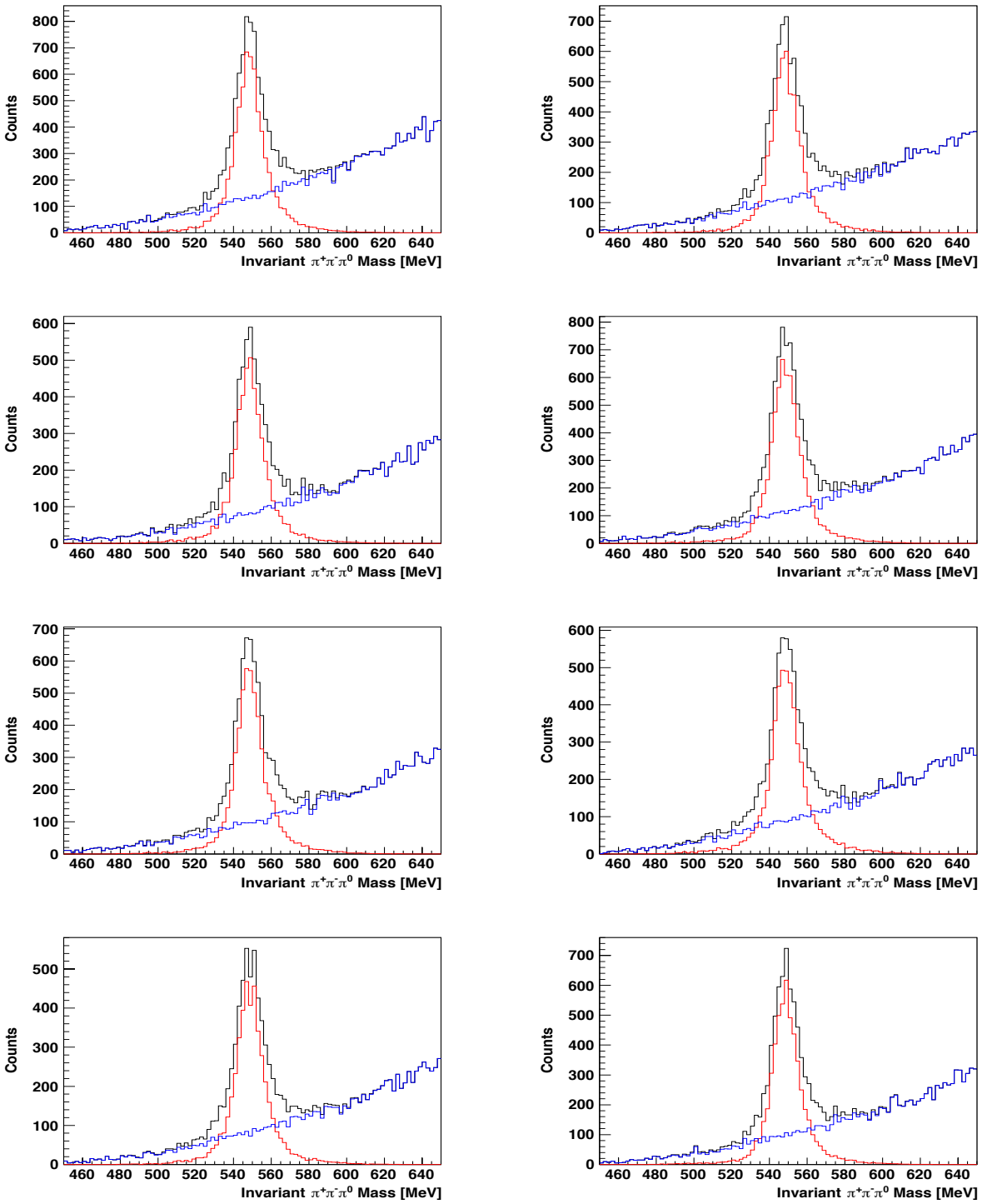


Figure 45: *Invariant $\pi^+\pi^-\pi^0$ distributions for the reaction $\gamma p \to p\eta$. Shown are 10-MeV-wide W bins starting at $W \in [1940, 1950]$ MeV (top left), $W \in [1950, 1960]$ MeV (top right), etc.*

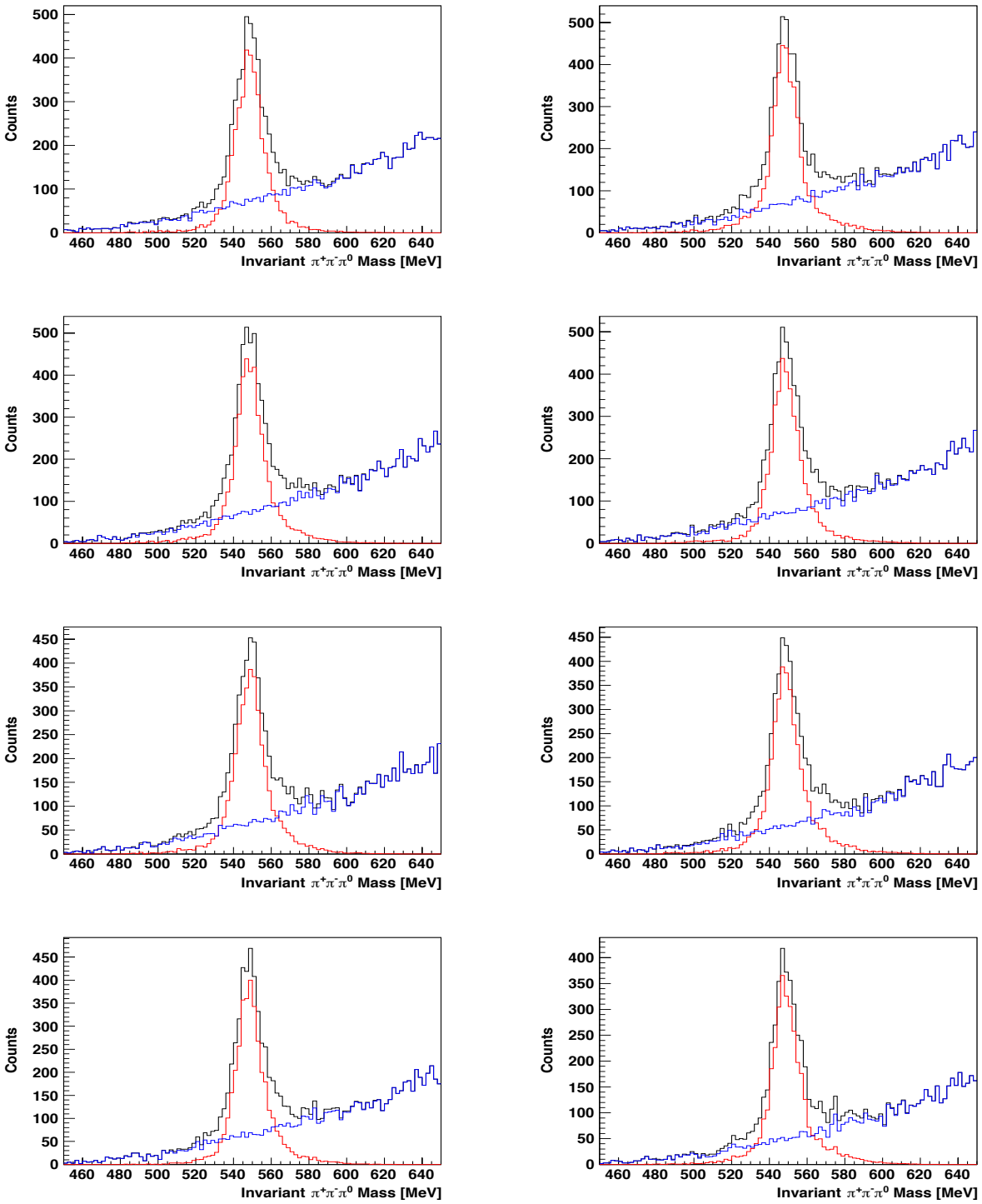


Figure 46: *Invariant $\pi^+\pi^-\pi^0$ distributions for the reaction $\gamma p \to p\eta$. Shown are 10-MeV-wide W bins starting at $W \in [2020, 2030]$ MeV (top left), $W \in [2030, 2040]$ MeV (top right), etc.*

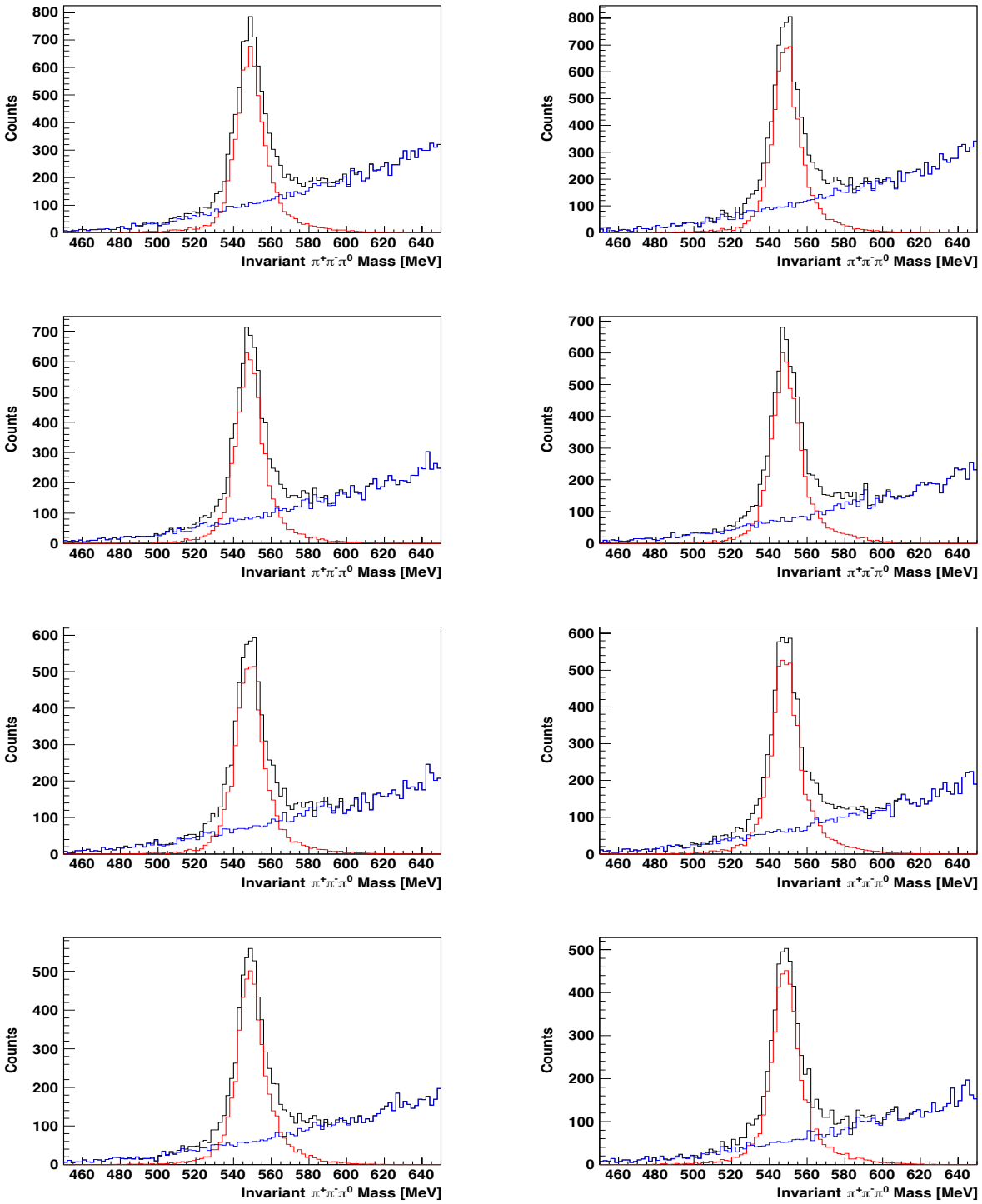


Figure 47: *Invariant $\pi^+\pi^-\pi^0$ distributions for the reaction $\gamma p \to p\eta$. Shown are 20-MeV-wide W bins starting at $W \in [2100, 2120]$ MeV (top left), $W \in [2120, 2140]$ MeV (top right), etc.*

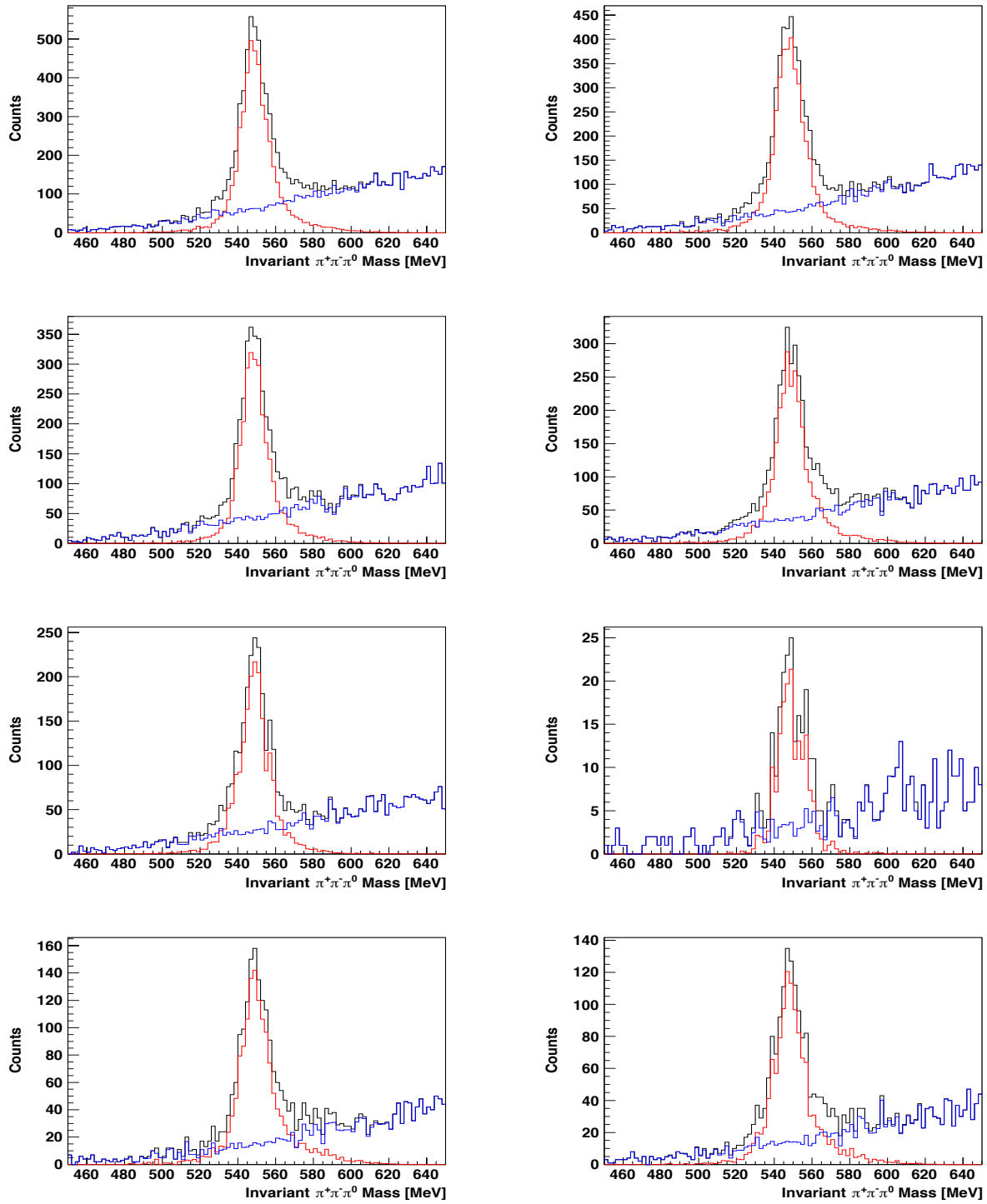


Figure 48: *Invariant $\pi^+\pi^-\pi^0$ distributions for the reaction $\gamma p \to p\eta$. Shown are 40-MeV-wide W bins starting at $W \in [2360, 2400]$ MeV (top left), $W \in [2400, 2440]$ MeV (top right), etc.*

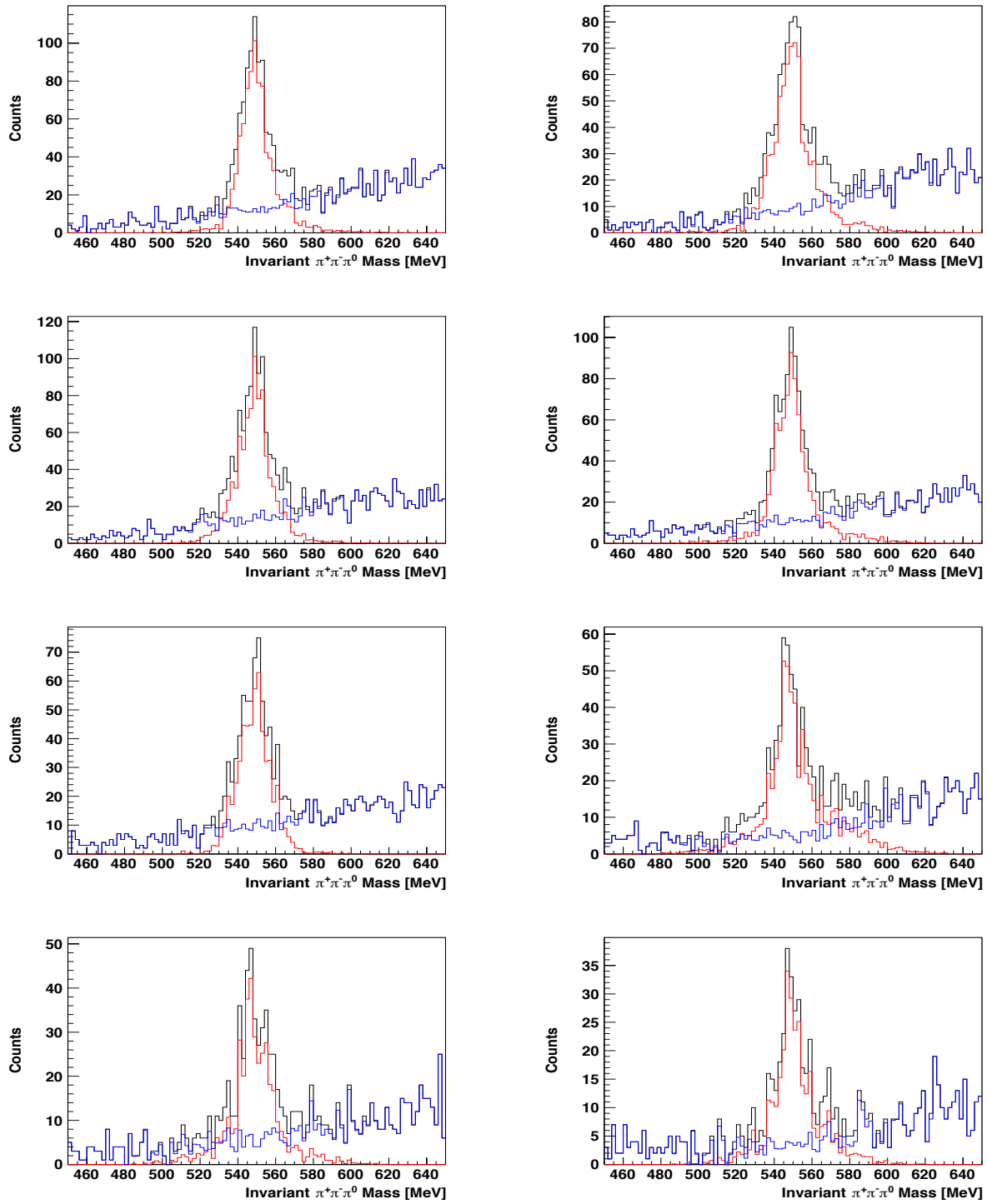


Figure 49: *Invariant $\pi^+\pi^-\pi^0$ distributions for the reaction $\gamma p \to p\eta$. Shown are 40-MeV-wide W bins starting at $W \in [2680, 2720]$ MeV (top left), $W \in [2720, 2760]$ MeV (top right), etc.*

### 3.12.4 The Reaction $\gamma p \to K^0_S \Sigma^+$

The reconstruction of the $K^0_S \Sigma^+$ final state differs from the $\omega$ and the $\eta$. While the latter two are based directly on the $\pi^+\pi^-\pi^0$ system, the strange $K_S$ is reconstructed from the $\pi^+\pi^-$ system and the remaining $\pi^0$ originates from the baryon decay. Since the $K_S \to \pi^+\pi^-$ and the $\Sigma^+ \to p\pi^0$ are highly correlated (associated strangeness production), the reference quantity can either be the invariant $\pi^+\pi^-$ mass or the invariant $p\pi^0$ mass. We determined $Q$ values independently applying both approaches, which serves as a cross check when comparing the cross sections. Table 15 shows the non-reference variables used for the background subtraction in this reaction. The quantities in parentheses are the non-reference coordinates used for the $Q$ values based on the invariant $p\pi^0$ mass.

Since the cross section for the reaction $\gamma p \to K^0 \Sigma^+$ is relatively small, the observed statistics is low and the invariant $\pi^+\pi^-$ mass is dominated by background in the mass region of the $K_S$ (see Fig. 50, top left). Therefore, we considered two mass cuts before we applied the $Q$-factor method:

1. Strangeness is conserved in electromagnetic and strong interactions. For this reason, the $K_S$ meson is produced together with a $\Sigma^+$ baryon (in our analysis). The life time of the $\Sigma^+$ ($\tau = (0.8018 \pm 0.0026) \times 10^{-10}$ s) is fairly long since it can only decay weakly. We thus applied a narrow cut of 20 MeV around the $\Sigma^+$ mass of 1189.37 MeV [7]. The effect can be seen in Figure 50 (top row). The left side shows the *raw* $\pi^+\pi^-$ distribution of all g12 $\pi^+\pi^-\pi^0$ events in Period 2 (see Table 2), whereas the right side shows the same distribution after the $\Sigma^+$ cut. The background is significantly reduced and the $K_S$ peak is clearly visible; the $K_S \Sigma^+$ statistics is only marginally affected.

2. The dominant reaction contributing to the $p\,\pi^+\pi^-\pi^0$ final state is $\omega$ production. The bottom row of Figure 50 shows the invariant $\pi^+\pi^-\pi^0$ mass vs. the corresponding $\pi^+\pi^-$ mass (left side). The vertical band for the $\omega$ is clearly visible and moreover, it exhibits a maximum intensity in the vicinity of the $K_S$ in the projection onto the $\pi^+\pi^-$ axis. Therefore, we applied a mass cut to remove contributions from $\omega$ production: $m_{\pi^+\pi^-\pi^0} < 752$ MeV and $m_{\pi^+\pi^-\pi^0} > 812$ MeV. The resulting (final) $\pi^+\pi^-$ mass distribution showing the $K_S$ peak is given on the right side. A comparison of Figure 50 (top right) and Figure 50 (bottom right) indicates that only little $K_S \Sigma^+$ statistics is lost due to the $\omega$ cut.

| $\Gamma_i$ | Non-Reference Coordinate | Maximum Range $\Delta_i$ |
|---|---|---|
| $\Gamma_0$ | incident-photon energy $E_\gamma$ | 50 MeV |
| $\Gamma_1$ & $\Gamma_2$ | $\cos\theta_{\pi^+}$ ($\cos\theta_p$) & $\phi_{\pi^+}$ ($\phi_{\pi^0}$) in the $\pi^+\pi^-$ ($p\pi^0$) rest frame | 2 & $2\pi$ |
| $\Gamma_3$ | $\cos\Theta^{K_S}_{\text{c.m.}}$ in the center-of-mass frame | 2 |
| $\Gamma_4$ | $\phi^{K_S}_{\text{lab}}$ | $2\pi$ |
| $\Gamma_5$ | $\cos$ (opening angle $\angle(p, \pi^0)$) | 2 |

Table 15: *The non-reference coordinates $\Gamma_i$ and their ranges $\Delta_i$. Note that we used 100-MeV-wide incident-photon bins for the induced polarization.*

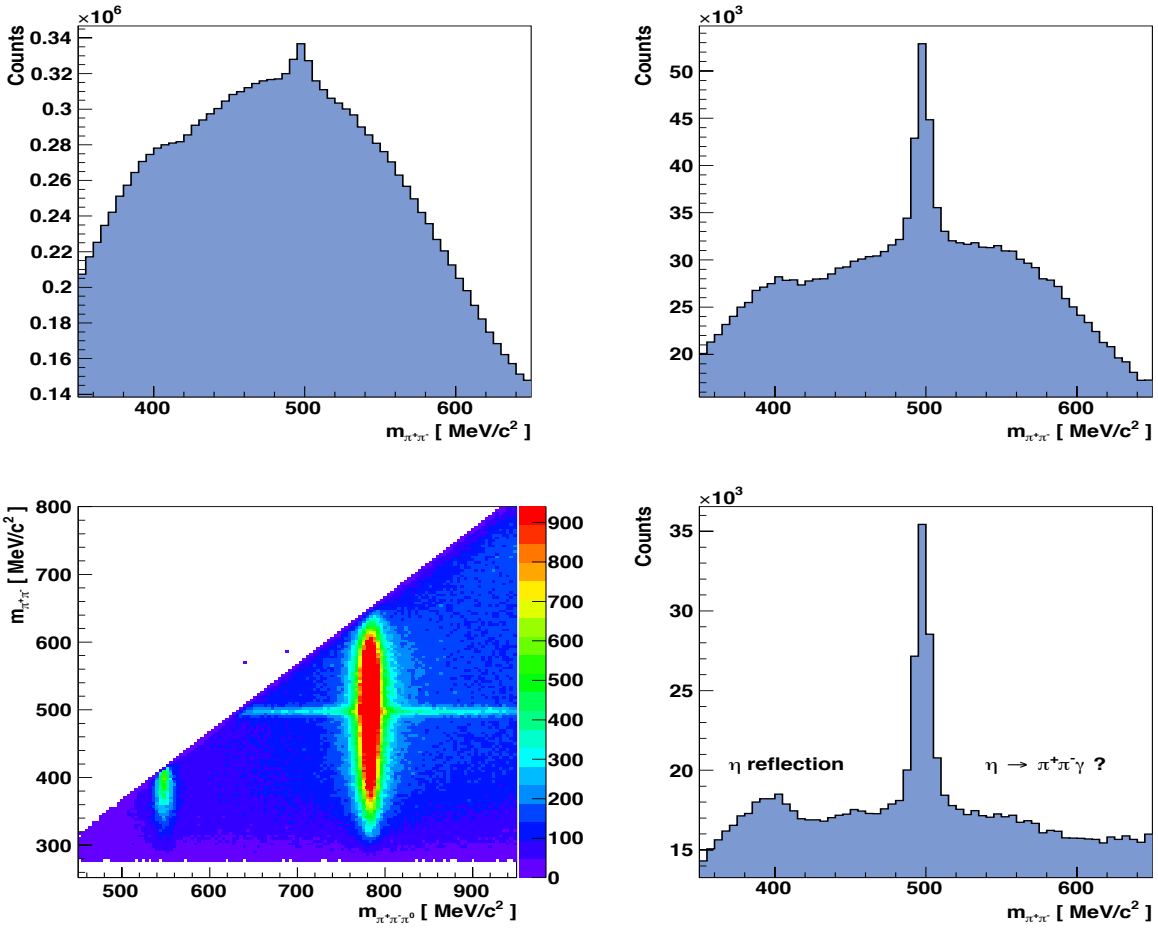


Figure 50: *Top row: Invariant $\pi^+\pi^-$ mass distribution of all g12 $\pi^+\pi^-\pi^0$ events in Period 2 (left) and the same invariant $\pi^+\pi^-$ mass distribution after the $\Sigma^+$ cut (right). Bottom row: Invariant $\pi^+\pi^-\pi^0$ mass vs. the corresponding $\pi^+\pi^-$ mass of all g12 $\pi^+\pi^-\pi^0$ events in Period 2 (left) and the same invariant $\pi^+\pi^-$ mass distribution shown in the top row after the $\omega$ and the $\Sigma^+$ cuts (right).*

The two-dimensional distribution also explains the two structures which can be observed in the projection onto the $\pi^+\pi^-$ axis (right side of Figure 50): (1) The peak around 400 MeV is the reflection of the $\eta \to \pi^+\pi^-\pi^0$ which is cut off at the phase-space boundary, and (2) the enhancement around 550 MeV is most likely based on the $\eta$ decaying into $\pi^+\pi^-\gamma$.

To subtract the background for the $K_S\,\Sigma^+$ final state, the selected g12 data were divided into 50-MeV-wide incident-photon energy bins for the cross-section measurement and 100-MeV-wide energy bins for the measurement of the induced polarization. We then chose a 1000 nearest-neighbor events for each signal candidate in the phase space spanned by the non-reference coordinates. The invariant $\pi^+\pi^-$ mass distribution of these 1000 events was fitted over the mass range 473 - 523 MeV for the $K_S$ and independently, the $p\pi^0$ distribution was fitted over the mass range 1149 - 1229 MeV

| | | Ref. Coordinate: $\pi^+\pi^-$ Mass | | Ref. Coordinate: $p\pi^0$ Mass | |
|---|---|---|---|---|---|
| | | Initial Value | Fit Range | Initial Value | Fit Range |
| Gaussian pdf | Mean, $\mu$ | 497.61 MeV [7] | fixed | 1189.37 MeV [7] | fixed |
| | Width, $\sigma$ | 4.5 MeV | 2.0 - 8.0 MeV | 4.5 MeV | 0.0 - 9.0 MeV |
| Chebychev pdf | $c_0$ | 0.1 | $-1.5$ - 1.5 | 0.1 | $-1.5$ - 1.5 |
| | $c_1$ | 0.1 | $-1.5$ - 1.5 | 0.1 | $-1.5$ - 1.5 |

Table 16: *Parameters of the signal & background probability-density functions. A Gaussian was used to describe the signal and a second-order Chebychev polynomial to describe the background.*

for the $\Sigma^+$ using the unbinned maximum-likelihood technique. Since the $K_S$ decays weakly into $\pi^+\pi^-$ with a mean life $\tau$ of about $(8.954 \pm 0.004) \times 10^{-11}$ s [7] (and has thus a narrow natural width), we chose a Gaussian function for the signal pdf and a second-order Chebychev polynomial for the background. Table 16 shows the parameters of the signal and background pdfs and the constraints imposed on them.

Figures 52 - 56 show the complete set of invariant $\pi^+\pi^-$ mass distributions (left) and the corresponding $p\pi^0$ mass distributions (right) for 100-MeV-wide incident-photon energy bins in the range $E_\gamma \in [\,1100,\, 3000\,]$ MeV (full statistics used in this analysis). Moreover, Table 17 shows the total number of events (as a sum over all $Q$ values) for all 100-MeV-wide energy bins and for two selected angle bins. Finally, Fig. 51 presents example distributions of $E_\gamma$ Bins 4 & 5 (shown in Table 17).

Note that a full set of Q values for all events is not necessarily unique. If the $Q$ values are determined for the $K_S$, then the weighted $\pi^+\pi^-$ mass distribution will show a clear separation of $K_S$ signal and background. However, the $p\pi^0$ mass distribution weighted with the same $Q$ values will still exhibit some background under the $\Sigma^+$ signal. The same is true if the $Q$ values are determined for the $\Sigma^+$, in which case some background under the $K_S$ will be observed. For a counting experiment like a cross-section measurement, either approach can be used. For an analysis however which requires the full event information, a more sophisticated method would be needed, e.g. a simultaneous fit of both mass distributions.

The measurement of the $\Sigma^+$ recoil polarization was based on the asymmetry between the proton count rate above and below the reaction plane, taken in the $\Sigma^+$ rest frame (for more details, see Section 4.4). For this reason, we used the invariant $p\pi^0$ mass as the reference coordinate in the determination of $Q$ values for both the final cross sections and the polarization observable. The (kinematic) decay information – the crucial opening angle between the proton and the $\pi^0$ – was added to the distance metric (Table 15). The $K_S$-peak-beased $Q$ values were used to cross-check our final cross-section results.

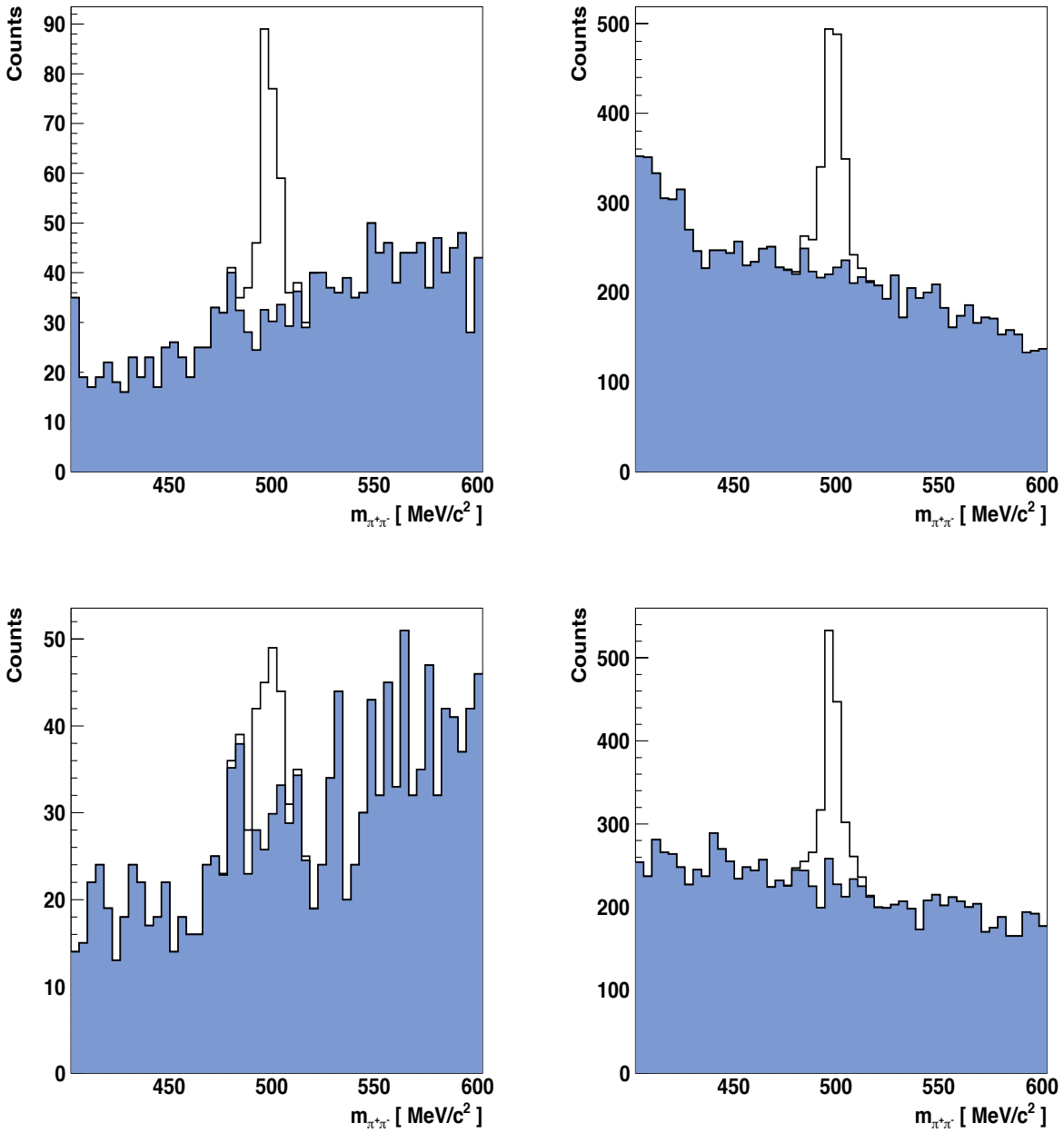


Figure 51: *Examples of $\pi^+\pi^-$ distributions for $\gamma p \to K_S \Sigma^+$. Top row: $E_\gamma \in [1400, 1500]$ MeV. Bottom row: $E_\gamma \in [1600, 1700]$ MeV. The left side is for $-0.6 < \cos\theta^{K_S}_{\text{c.m.}} < -0.4$, the right side is for $0.0 < \cos\theta^{K_S}_{\text{c.m.}} < 0.2$ (according to Table 17).*

| Energy Bin | # of Events in $E_\gamma$ Bin | $-0.6 < \cos\theta^{K_S}_{\text{c.m.}} < -0.4$ | $0.0 < \cos\theta^{K_S}_{\text{c.m.}} < 0.2$ |
|---|---|---|---|
| 0 | 45918.5 | 992.7 | 7014.6 |
| 1 | 248.0 | 17.5 | 44.1 |
| 2 | 3253.5 | 121.2 | 411.1 |
| 3 | 4024.9 | 148.0 | 559.6 |
| 4 | 5624.9 | 172.1 | 866.0 |
| 5 | 5684.8 | 75.8 | 842.9 |
| 6 | 5483.8 | 73.7 | 795.9 |
| 7 | 3989.4 | 44.0 | 630.8 |
| 8 | 3304.3 | 61.3 | 603.1 |
| 9 | 2249.3 | 34.8 | 378.8 |
| 10 | 2305.7 | 35.2 | 428.2 |
| 11 | 2078.9 | 41.8 | 354.6 |
| 12 | 2022.2 | 37.5 | 342.6 |
| 13 | 1463.9 | 32.8 | 241.0 |
| 14 | 1086.5 | 18.9 | 145.5 |
| 15 | 925.2 | 14.5 | 111.3 |
| 16 | 604.4 | 18.1 | 86.1 |
| 17 | 828.9 | 25.5 | 91.7 |
| 18 | 431.0 | 9.5 | 47.9 |
| 19 | 309.0 | 10.7 | 33.4 |

Table 17: *Total number of* $\gamma p \to K_S \Sigma^+$ *events in 100-MeV-wide energy bins (full statistics of Period 2), where Bin 0 denotes the full energy range* $1.1 < E_\gamma < 3.0$ *GeV, and Bin 1 corresponds to* $1.1 < E_\gamma < 1.2$ *GeV, etc. The statistics is also given for two randomly-chosen angle bins.*

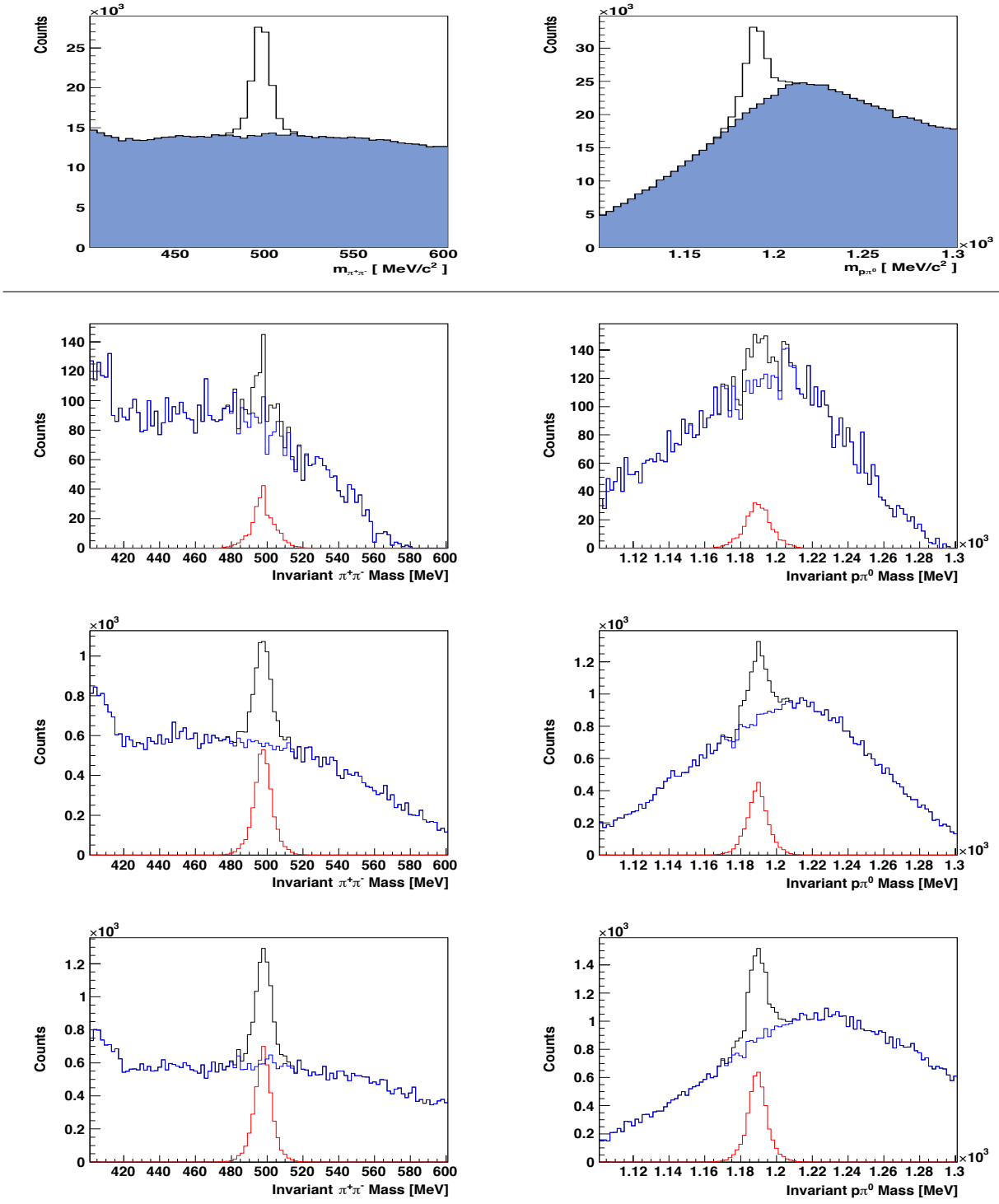


Figure 52: *Invariant $\pi^+\pi^-$ distributions (left column) and the corresponding $p\pi^0$ distributions (right column) for the reaction $\gamma p \to K_S\,\Sigma^+$. Shown are the full statistics (top row) and 100-MeV-wide energy bins starting at $E_\gamma \in [1.1, 1.2]$ GeV (second row), $E_\gamma \in [1.2, 1.3]$ GeV (third row), etc.*

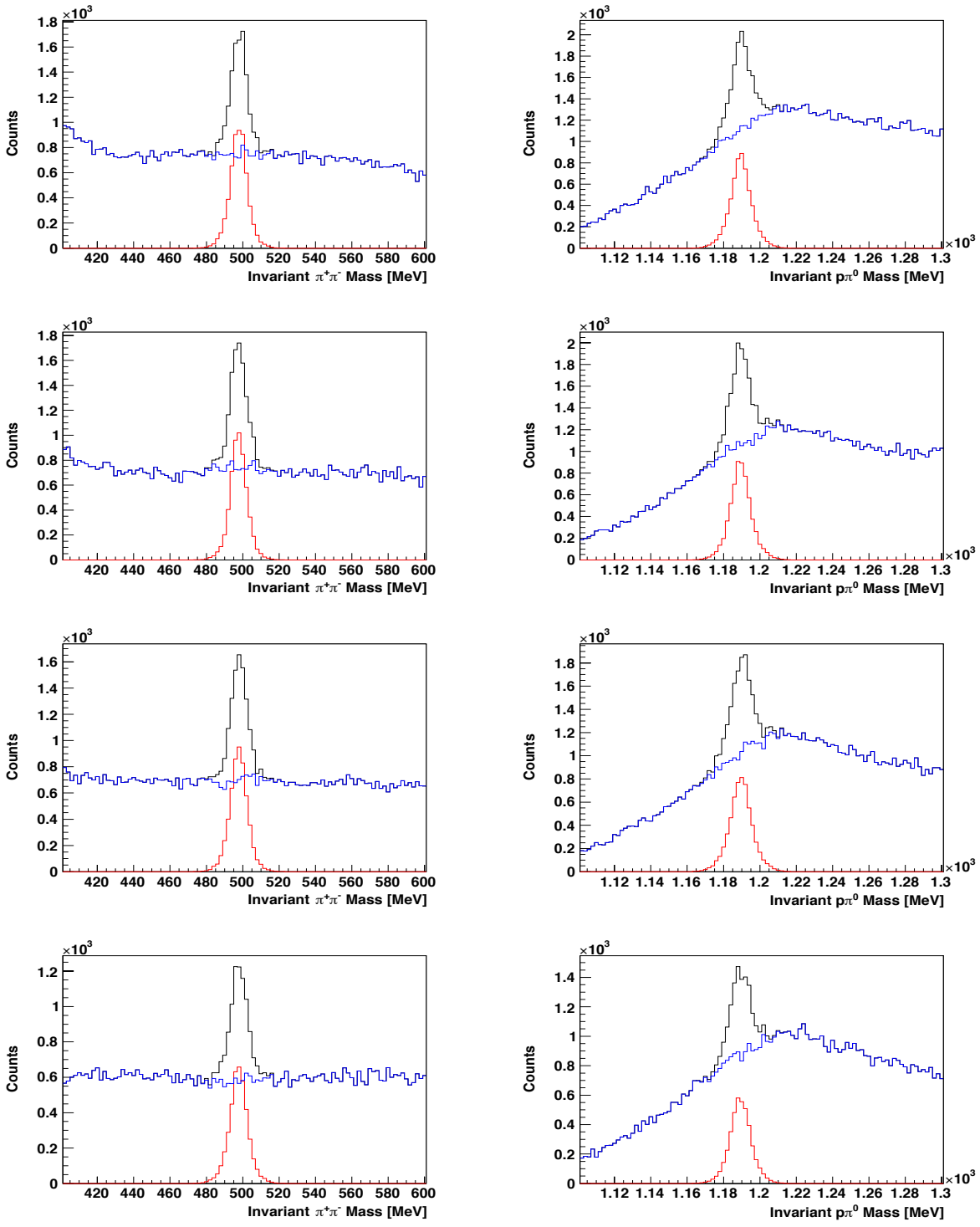


Figure 53: *Invariant $\pi^+\pi^-$ distributions (left column) and the corresponding $p\pi^0$ distributions (right column) for the reaction $\gamma p \to K_S \Sigma^+$. Shown are 100-MeV-wide energy bins starting at $E_\gamma \in [1400, 1500]$ MeV (top row), $E_\gamma \in [1500, 1600]$ MeV (second row), etc.*

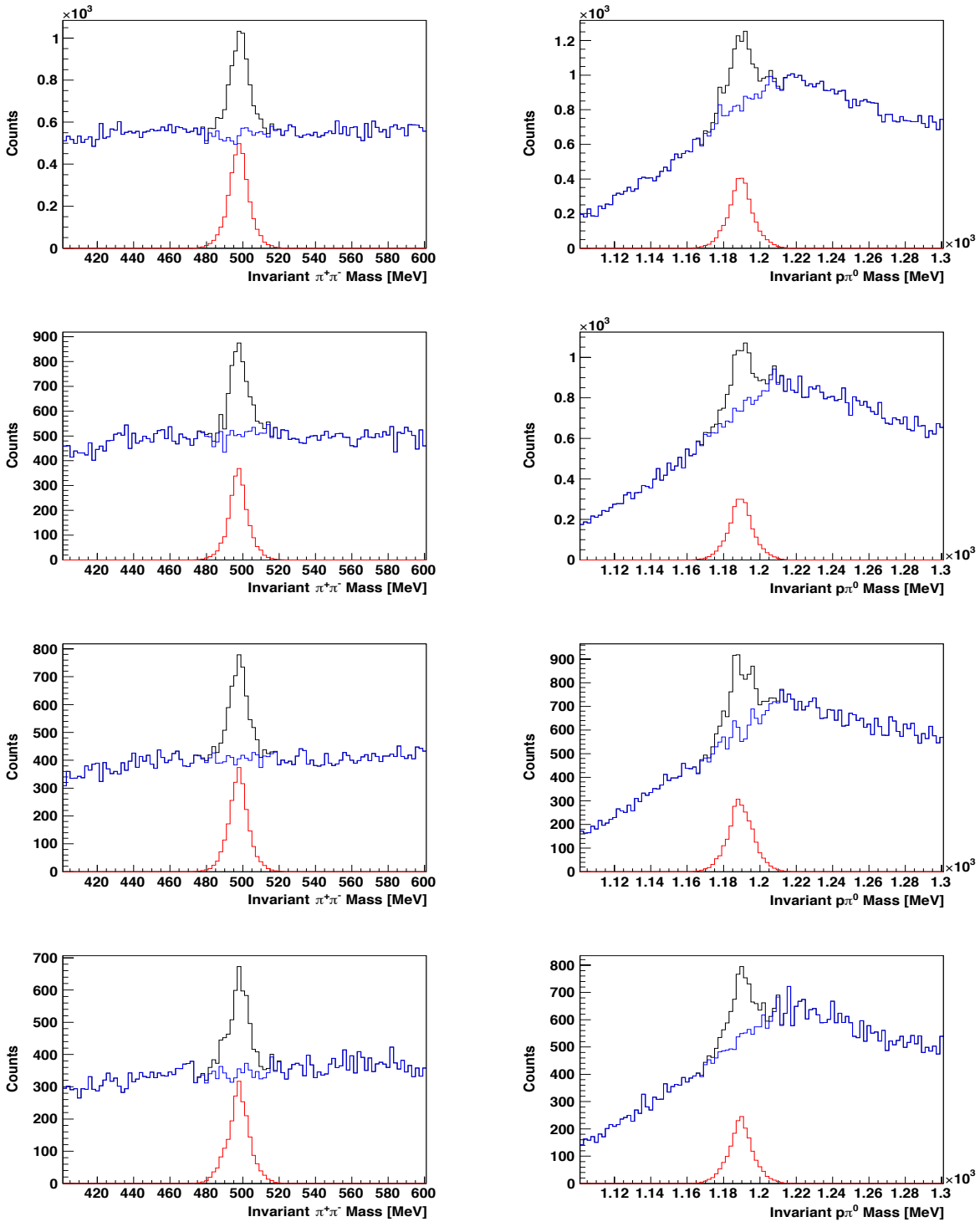


Figure 54: *Invariant $\pi^+\pi^-$ distributions (left column) and the corresponding $p\pi^0$ distributions (right column) for the reaction $\gamma p \to K_S \Sigma^+$. Shown are 100-MeV-wide energy bins starting at $E_\gamma \in [1800, 1900]$ MeV (top row), $E_\gamma \in [1900, 2000]$ MeV (second row), etc.*

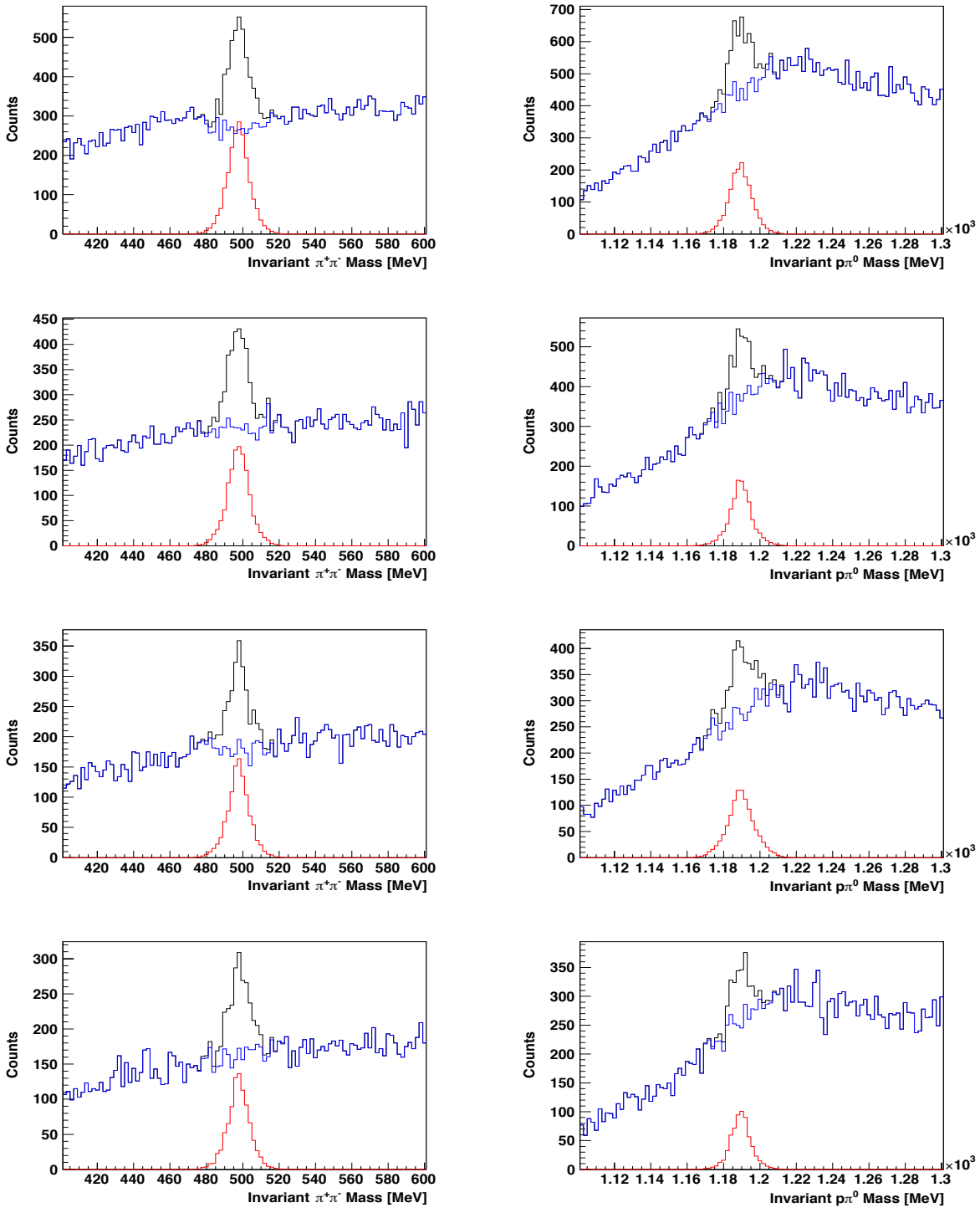


Figure 55: *Invariant $\pi^+\pi^-$ distributions (left column) and the corresponding $p\pi^0$ distributions (right column) for the reaction $\gamma p \to K_S \Sigma^+$. Shown are 100-MeV-wide energy bins starting at $E_\gamma \in [2200, 2300]$ MeV (top row), $E_\gamma \in [2300, 2400]$ MeV (second row), etc.*

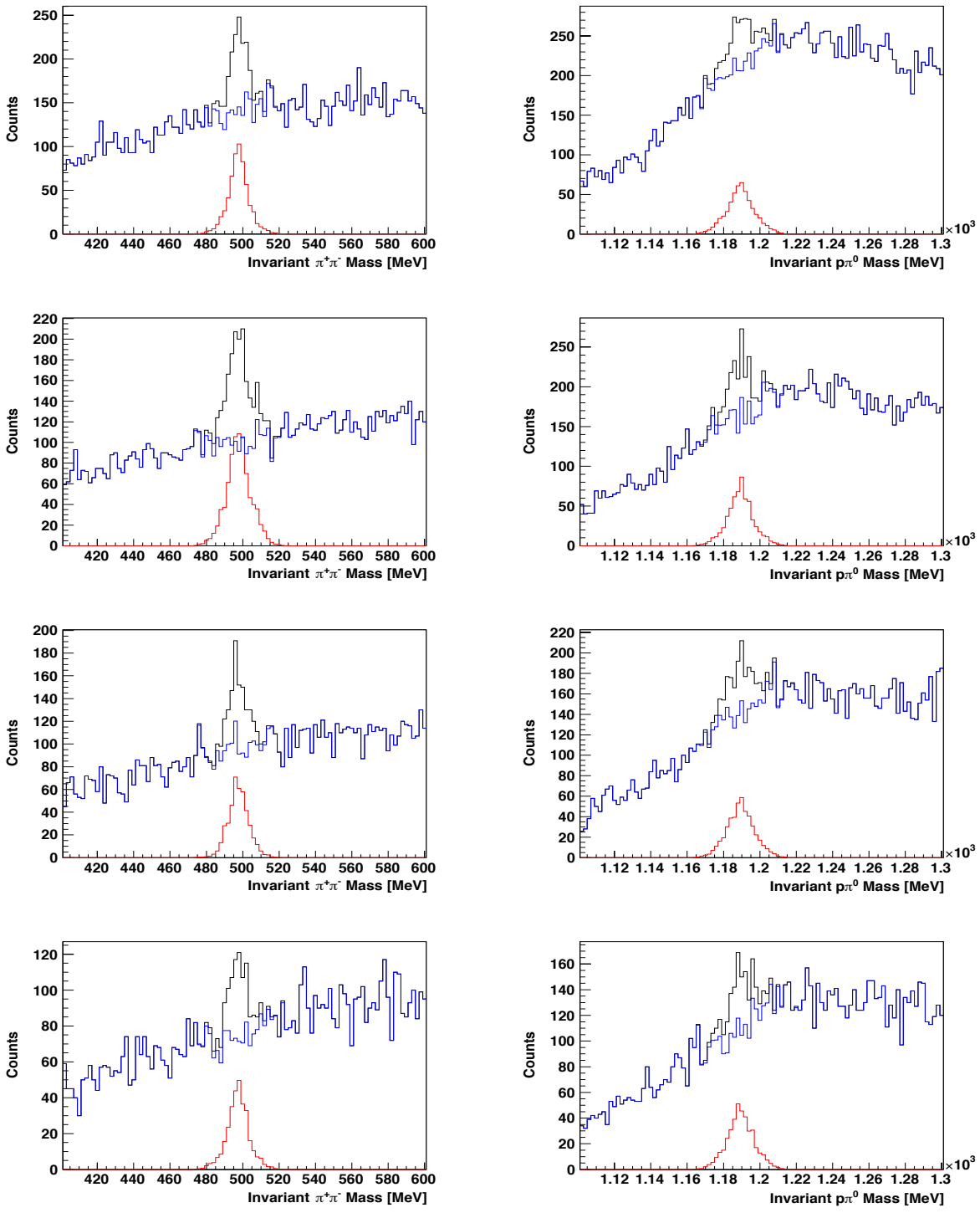


Figure 56: *Invariant $\pi^+\pi^-$ distributions (left column) and the corresponding $p\pi^0$ distributions (right column) for the reaction $\gamma p \to K_S \Sigma^+$. Shown are 100-MeV-wide energy bins starting at $E_\gamma \in [2600, 2700]$ MeV (top row), $E_\gamma \in [2700, 2800]$ MeV (second row), etc.*

### 3.12.5 The Reaction $\gamma p \to p\,\phi$

The reconstruction of the $\phi$ meson was based on the $K^+K^-$ decay mode and therefore, the invariant $K^+K^-$ mass was used as the reference coordinate.

Under construction ... Material will be added in the second round of this review.

# 4 General Physics Analysis

After all corrections and cuts were applied and signal-background separation was carried out, the extraction of cross sections (and some polarization observables) from the carefully selected events could commence. This chapter presents the methodology used in the extraction of these observables from the experimental data.

## 4.1 Kinematics and Observables

### 4.1.1 Binning and Angles in the $\gamma p \to p\omega$ Analysis

**Summary:** We have extracted differential cross sections, $\mathrm{d}\sigma/\mathrm{d}\Omega$ and $\mathrm{d}\sigma/\mathrm{d}t$, as well as spin-density matrix elements (SDMEs), for the incident-photon energy range $1.5 < E_\gamma < 5.4$ GeV or $1.92 < W < 3.3$ GeV.

The kinematics of $\omega$ photoproduction off the proton can be completely described by two kinematic variables. We chose these variables to be the incident photon energy, $E_\gamma$ (alternatively $W$), and the cosine of the polar angle of the $\omega$ meson in the center-of-mass frame, $\cos\Theta^{\omega}_{\mathrm{c.m.}}$, where the $z$-axis was defined along the incoming photon beam (see Figure 57). Alternatively, we also used the Mandelstam variable $t$ and a representation of the differential cross sections in $\mathrm{d}\sigma/\mathrm{d}t$. The data were binned in 20-MeV-wide center-of-mass energy bins for $1.92 < W < 2.12$ GeV and in 10-MeV-wide center-of-mass energy bins for $2.12 < W < 3.30$ GeV. Note that CLAS had poor acceptance for three-track events in the very forward and backward directions in the center-of-mass frame.

### 4.1.2 Binning and Angles in the $\gamma p \to p\eta$ Analysis

**Summary:** We have extracted the differential cross sections, $\mathrm{d}\sigma/\mathrm{d}\Omega$ and $\mathrm{d}\sigma/\mathrm{d}t$, for the incident-photon energy range $1.1 < E_\gamma < 5.4$ GeV.

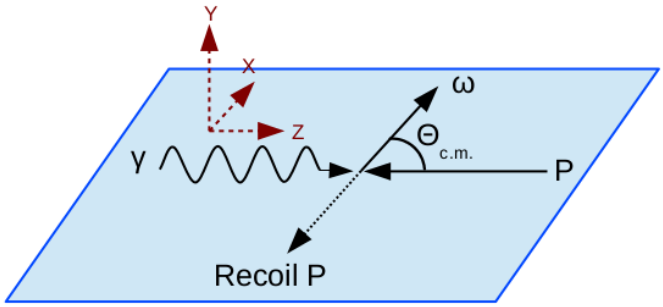


Figure 57: *A diagram describing the kinematics of the reaction $\gamma p \to p\omega$. The blue plane represents the center-of-mass production plane composed of the initial photon and the recoiling proton. The angle $\Theta_{c.m.}$ denotes the angle between the initial proton and the $\omega$ meson in the center-of-mass system. The $z$-axis is chosen to be along the direction of the incoming photon beam. The $y$-axis is defined as $\hat{y} = \frac{\hat{p}_{rec}\times\hat{z}}{|\hat{p}_{rec}\times\hat{z}|}$, where $\hat{p}_{rec}$ is a unit vector along the momentum of the recoil proton. The $x$-axis then lies in the production plane.*

The description of the reaction kinematics in $\gamma p \to p\,\eta$ and the kinematic variables used in this analysis were identical to those for the reaction $\gamma p \to p\,\omega$. In Figure 57, the $\omega$ can simply be replaced with the $\eta$. Both mesons were reconstructed from the $\pi^+\pi^-\pi^0$ system. For the presentation of the differential cross sections, the available statistics allowed us to use 10-MeV-wide $W$ bins at lower energies below $E_\gamma \approx 1900$ MeV. Then we used 20-MeV-wide $W$ bins and 40-MeV-wide $W$ bins toward higher energies (see also Section 3.12.3).

### 4.1.3 Binning and Angles in the $\gamma p \to K^0\,\Sigma^+$ Analysis

**Summary:** We have extracted the differential cross sections $\mathrm{d}\sigma/\mathrm{d}\Omega$ for the incident-photon energy range $1.15 < E_\gamma < 3.0$ GeV and the induced polarization, $P$, of the $\Sigma^+$ hyperon.

The $K^0\,\Sigma^+$ final state is a two-body final state consisting of a meson (M) and a baryon (B), very similar to the previous two reactions (M = $\omega$ or $\eta$; B = $p$). For this reason, the kinematics is again represented by the diagram in Figure 57 when the recoil $p$ is replaced with the $\Sigma^+$ and the $\omega$ is replaced with the $K^0$. For the cross sections, we have used 50-MeV-wide $E_\gamma$ bins in the incident-photon energy and 0.1-wide angle bins in $\cos\Theta^{K_S}_{\mathrm{c.m.}}$.

#### Polarization Observables

The angular distribution of the decay nucleon is given by [20, 21]:

$$W\left(\Theta_N\right) \;=\; \frac{1}{2}\left(1 \;+\; \alpha\, P \cos\left(\Theta_N\right)\right), \tag{18}$$

where the parameter $P$ denotes the hyperon polarization and $\Theta_N$ is the decay angle of the nucleon measured with respect to the normal of the production plane of $K^0_S$ and $\Sigma^+$ in the $\Sigma^+$ rest frame. For the recoil polarization, we have used 100-MeV-wide $E_\gamma$ bins in the incident-photon energy and 0.1-wide angle bins in $\cos\Theta_{\mathrm{c.m.}}$ of the $K_S$.

### 4.1.4 Binning and Angles in the $\gamma p \to p\,\phi$ Analysis

**Summary:** We have extracted the differential cross sections, $\mathrm{d}\sigma/\mathrm{d}\Omega$ and $\mathrm{d}\sigma/\mathrm{d}t$, for the incident-photon energy range $1.1 < E_\gamma <$ X.X GeV.

The description of the reaction kinematics in $\gamma p \to p\,\phi$ and the kinematic variables used in this analysis were identical to those for the reaction $\gamma p \to p\,\omega$. In Figure 57, the $\omega$ can simply be replaced with the $\phi$. However, the $\phi$ meson was reconstructed from the $K^+K^-$ system. For the presentation of the differential cross sections, the available statistics allowed us to use XX-MeV-wide $W$ bins.

### 4.1.5 Binning and Angles in the $\gamma p \to p\,\pi^+\pi^-$ Analysis

**Summary:** We have extracted the beam-helicity asymmetry, $\mathbf{I}^{\odot}$.

The kinematics of $\gamma p \to p\,\pi^+\pi^-$ required a selection of five independent kinematic variables. For this analysis, $\cos\Theta^{p}_{\text{c.m.}}$, a mass ($m_{p\pi^+}$, $m_{p\pi^-}$, or $m_{\pi^+\pi^-}$), the center-of-mass energy, $W$, as well as $\theta_{\pi^+}$ and $\phi_{\pi^+}$ were chosen. The latter two angles denote the polar and azimuthal angles of the $\pi^+$ in the rest frame of the $\pi^+\pi^-$ system. A diagram showing the kinematics of the reaction can be seen in Figure 58. The blue plane represents the center-of-mass production plane composed of the initial photon and the recoil proton, whereas the red plane represents the decay plane formed by two of the final-state particles.

The angle $\phi^*$ shown in Figure 58 is a kinematic variable unique to a final state containing two pseudoscalar mesons. It describes the orientation of the decay plane with respect to the production plane. It was also given by the azimuthal angle of one of the particles from the chosen pair in this pair's rest frame. In our analysis, we chose the $\pi^+$ meson (the corresponding azimuthal angle will be denoted by $\phi_{\pi^+}$ instead of $\phi^*$). The angle $\phi_{\pi^+}$ was calculated via two boosts. The first being a boost along the beam axis into the overall center-of-mass frame. The second boost occured along the axis antiparallel to the recoiling proton and resulted in the two-$\pi$ rest frame, wherein the two final-state pions departed back-to-back. Mathematically, $\phi_{\pi^+}$ was uniquely determined by the following expression:

$$\cos\phi_{\pi^+} \;=\; \frac{(\vec{p}\times\vec{a})\;\cdot\;(\vec{b}_2\times\vec{b}_1)}{|\vec{p}\times\vec{a}|\;|\vec{b}_2\times\vec{b}_1|}\,, \tag{19}$$

where $\vec{p}$, $\vec{a}$, $\vec{b}_1$, and $\vec{b}_2$ were the initial-state proton, the recoil proton, the $\pi^+$ and $\pi^-$, respectively.

The CLAS-g12 data were initially binned for the experimental analysis in two of the five independent kinematic variables [6]. These binning variables were the center-of-mass energy, $W$, and the azimuthal angle, $\phi_{\pi^+}$. The choice of $\phi_{\pi^+}$ was important since the behavior of the polarization observables with respect to this variable has been predicted as either *even* or *odd* [22] and thus, served as a good check for our results. To compare the beam-helicity asymmetry, $\mathbf{I}^{\odot}$, with the results from the CLAS-g1c analysis [16], the center-of-mass energy, $W$, was divided into 50-MeV wide bins. This resulted in a total of 16 bins in the center-of-mass energy, covering a $W$ range from 1.75 to 2.55 GeV. For the azimuthal angle, $\phi_{\pi^+}$, 20 bins were used, covering a range from $0 \le \phi_{\pi^+} \le 2\pi$. This represented an improvement over the previous CLAS analysis which used only 11 bins in the same angular range. Thus, we were able to show structures in the observable more clearly. This binning choice resulted in a total of 320 bin combinations per final-state topology.

#### Polarization Observables in $\gamma\,p \to p\,\pi^+\pi^-$

For $\gamma p \to p\,\pi\pi$, without measuring the polarization of the recoiling nucleon, the general cross section, $\sigma$, is given by [22]:

$$\begin{aligned}\sigma \;=\; \sigma_0\,\{\,(\,1 \;+\; \vec{\Lambda}_i\cdot\vec{\mathbf{P}}\,)\\ &+\;\delta_{\odot}\,(\mathbf{I}^{\odot} \;+\; \vec{\Lambda}_i\cdot\vec{\mathbf{P}}^{\,\odot}\,)\\ &+\;\delta_l\,[\,\sin 2\beta\,(\,\mathbf{I}^{\mathbf{s}} \;+\; \vec{\Lambda}_i\cdot\vec{\mathbf{P}}^{\,\mathbf{s}}\,) \;+\; \cos 2\beta\,(\,\mathbf{I}^{\mathbf{c}} \;+\; \vec{\Lambda}_i\cdot\vec{\mathbf{P}}^{\,\mathbf{c}}\,)\,]\,\}\,,\end{aligned} \tag{20}$$

[6] It is important to note that the binning scheme presented here was chosen only for our experimental analysis and the presentation of the data. A different scheme or even combinations of different kinematic variables will likely be used for the interpretation of the data in a partial wave analysis.

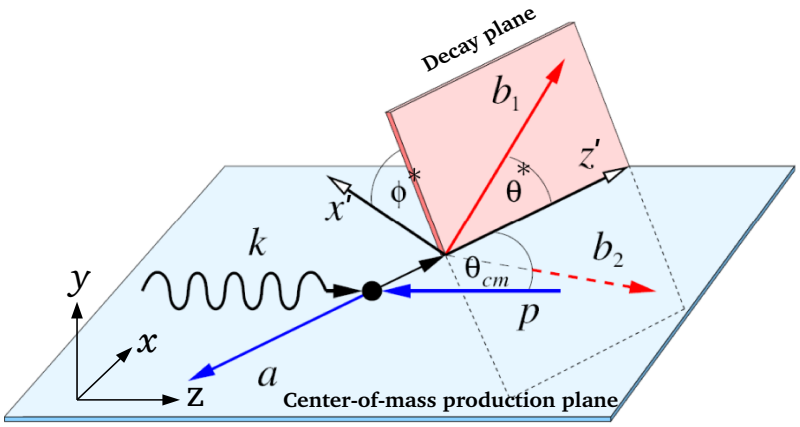


Figure 58: *A diagram describing the kinematics of the reaction* $\gamma p \to p\pi^+\pi^-$. *The blue plane represents the center-of-mass production plane composed of the initial photon and one of the final-state particles, whereas the red plane represents the decay plane formed by the other two final-state particles.* $a$, $b_1$, *and* $b_2$ *denote the three particles of the final state. The* $z$*-axis is chosen along the direction of the incoming photon beam. The* $y$*-axis is defined as* $\hat{y} = \frac{\hat{p}_{rec} \times \hat{z}}{|\hat{p}_{rec} \times \hat{z}|}$, *where* $\hat{p}_{rec}$ *is a unit vector along the momentum of one of the final-state particles. If the chosen particle is represented by particle* $a$, *then the* $y$*-axis will point in the direction as shown in the figure. Moreover,* $k$ *is the momentum of the initial photon and the particle* $p$ *denotes the target proton. If we assume that particle* $a$ *is the recoiling proton, then* $b_1$ *and* $b_2$ *will be the two pions,* $\pi^+$ *and* $\pi^-$. *The angle* $\Theta_{c.m.}$ *denotes the angle between the initial proton and the particle* $a$ *in the center-of-mass system. Finally,* $\phi^*$ *and* $\theta^*$ *denote the azimuthal and polar angles of the particle* $b_1$ *in the rest frame of* $b_1$ *and* $b_2$. *In our analysis, we chose* $\pi^+$ *as* $b_1$. *Hence, we will use the notations* $\phi_{\pi^+}$ *(*$\theta_{\pi^+}$*) instead of* $\phi^*$ *(*$\theta^*$*) in our results.*

where $\sigma_0$ is the unpolarized cross section. $\vec{\Lambda}_i$ denotes the polarization of the initial nucleon and $\delta_\odot$ is the degree of circular polarization of the incident-photon beam, while $\delta_l$ is the degree of linear polarization. The angle $\beta$ denotes the angle of inclination between the linearly-polarized photon beam relative to the $x$-axis in the center-of-mass production plane. It is defined as positive if the $x$-axis is rotated counter-clockwise from the beam polarization.

Equation 20 contains 15 polarization observables. The beam asymmetries, $\mathbf{I^\odot}$, $\mathbf{I^s}$, and $\mathbf{I^c}$ are observables which arise from beam polarization. The observables $\vec{\mathbf{P}}$ (with components $\mathbf{P_x}$, $\mathbf{P_y}$, $\mathbf{P_z}$) describe the target asymmetries which arise if only the target nucleon is polarized, and $\vec{\mathbf{P}}^\odot$ as well as $\vec{\mathbf{P}}^{s,c}$ represent the double-polarization observables.

The reaction rate for $\gamma p \to p\pi\pi$, in the case of a circularly-polarized beam incident on an unpolarized target (CLAS-g12 data), reduces to:

$$\sigma = \sigma_0 \{ 1 + \delta_\odot \mathbf{I}^\odot \}, \tag{21}$$

where $\delta_\odot$ is again the degree of circular polarization of the incident-photon beam.

## 4.2 Extraction of Cross Sections

The differential cross sections for all reactions were determined according to

$$\frac{\mathrm{d}\sigma}{\mathrm{d}\Omega} = \frac{N_{\mathrm{reaction}}}{A_{\mathrm{reaction}}} \frac{1}{N_\gamma \, \rho_{\mathrm{target}}} \frac{1}{\Delta\Omega} \frac{1}{BR}, \tag{22}$$

where

$\rho_{\mathrm{target}}$ : target area density
$N_{\mathrm{reaction}}$ : number of reconstructed data events in an ($E_\gamma$, $\cos\theta_{\mathrm{c.m.}}$) or ($W$, $\cos\theta_{\mathrm{c.m.}}$) bin
$N_\gamma$ : number of photons in an $E_\gamma$ bin (photon flux)
$A_{\mathrm{reaction}}$ : acceptance in an ($E_\gamma$, $\cos\theta_{\mathrm{c.m.}}$) or ($W$, $\cos\theta_{\mathrm{c.m.}}$) bin
$\Delta\Omega$ : solid-angle interval $\Delta\Omega = 2\pi\,\Delta\cos(\theta_{\mathrm{c.m.}})$
BR : decay branching fraction.

### Target Cross Sectional Area

The target area density, i.e. the number of atoms in the target material per cross-sectional area (orthogonal to the photon beam), is given by

$$\rho_{\mathrm{target}} = 2\,\frac{\rho(\mathrm{H_2})\,N_A\,L}{M_{\mathrm{mol}}\,(\mathrm{H_2})}, \tag{23}$$

where $\rho(\mathrm{H_2}) = 0.0711 \pm 1.75 \cdot 10^{-5}$ g/cm$^3$ [3] is the density and $M_{\mathrm{mol}} = 2.01588$ g/mol the molar mass of liquid $\mathrm{H_2}$. $N_A = 6.022 \cdot 10^{23}$ mol$^{-1}$ is the Avogadro number and $L = 40.0$ cm the length of the target cell. The factor of two accounts for the molecular composition of hydrogen ($\mathrm{H_2}$).
We have used a value of $\rho_{\mathrm{target}} = 16.992 \cdot 10^{-7}\mu\mathrm{b}^{-1}$ for all cross sections.

### Solid-Angle Interval

An object's solid angle in steradians is equal to the area of the segment of a unit sphere, centered at the angle's vertex, that the object covers. A solid angle in steradians equals the area of a segment of a unit sphere in the same way a planar angle in radians equals the length of an arc of a unit circle. The solid angle of a sphere measured from any point in its interior is $4\pi$ sr. In spherical coordinates:

$$\Omega = \iint_S \sin\theta\,\mathrm{d}\theta\,\mathrm{d}\phi = 2 \cdot 2\pi = 4\pi, \tag{24}$$

where $2\pi$ originates from integrating over $\mathrm{d}\phi$ and the factor of 2 from integrating over $\sin\theta\,\mathrm{d}\theta$. Since the differential cross sections are integrated over $\phi_{\mathrm{lab}}$ but are binned in $\cos\theta_{\mathrm{c.m.}}$, we used $\Delta\Omega = 2\pi\,\Delta\cos(\theta_{\mathrm{c.m.}})$ in Equation 22 and $\Delta\cos(\theta_{\mathrm{c.m.}}) = 2$ / (# of angle bins):

- $\Delta\Omega = 2\pi \cdot 2\,/\,20 = 0.6283$ (for $\eta$, $\omega$, and $K^0\,\Sigma^+$ production).
- $\Delta\Omega = 2\pi \cdot 2\,/\,20 = 0.6283$ (for $\phi$ production).

**Branching Fractions**

We have used the following values [7]:

$$p\,\omega : \text{Fraction } \Gamma_i\,/\,\Gamma = (89.2 \pm 0.7)\,\%\ (\omega \rightarrow \pi^+\pi^-\pi^0), \text{ i.e. } BR = 0.892.$$

$$p\,\eta : \text{Fraction } \Gamma_i\,/\,\Gamma = (22.92 \pm 0.28)\,\%\ (\eta \rightarrow \pi^+\pi^-\pi^0), \text{ i.e. } BR = 0.2292.$$

$$p\,\phi : \text{Fraction } \Gamma_i\,/\,\Gamma = (48.9 \pm 0.5)\,\%\ (\phi \rightarrow K^+K^-), \text{ i.e. } BR = 0.489.$$

$$K^0\,\Sigma^+ : \text{Fraction } \Gamma_i\,/\,\Gamma = (69.20 \pm 0.05)\,\%\ (K_S \rightarrow \pi^+\pi^-) \text{ as well as}$$
$$\Gamma_i\,/\,\Gamma = (51.57 \pm 0.30)\,\%\ (\Sigma^+ \rightarrow p\,\pi^0), \text{ i.e. } BR = 0.5 \cdot 0.5157 \cdot 0.6920 = 0.1784.$$

The factor of 0.5 for $K^0\,\Sigma^+$ accounts for the mixture of $K^0$ being 50 % $K_S$ and 50 % $K_L$.

**Photon Flux**

For the absolute normalization, we have used the standard CLAS GFLUX package which was originally developed by James Ball and Eugene Pasyuk [23]. A detailed description on how to use GFLUX for the CLAS-g12 experiment can be found in Ref. [3]. Table 18 gives the actual numbers we have used for all four cross sections: $\gamma p \rightarrow p\,\omega$, $\gamma p \rightarrow p\,\eta$, $\gamma p \rightarrow p\,\phi$, $\gamma p \rightarrow K_S\,\Sigma^+$.

**Absolute Normalziation: NGRF Correction**

CEBAF delivers electrons in bunches separated by 2 ns. Increasing the current in the accelerator increases the number of electrons in each bunch. Most of the g12 data were recorded at high curents of 60 - 65 nA, which corresponded to a photon flux of about $5 \times 10^8\,\gamma$ per second. The high current of the g12 experiment led to some ambiguity in selecting the correct photon for some events. About 14.26 % of all events had more than one incident photon that passed the *coincidence-time* cut or $|\Delta\,t_{\,\mathrm{TGPB}}| < 1$ ns (Section 3.3.1).

In the determination of the cross sections, we had to correct for the 14.26 % of all events which had more than one photon candidate within the allowed coincidence-time window. Since the Monte Carlo did not simulate the incident photons and the corresponding timing, we corrected the photon flux by 85.74 % or simply multiplied the signal yield by $1\,/\,0.8574 = 1.166$.

## 4.3 Extraction of Spin-Density Matrix Elements

The decay distribution of the $\omega$ meson yields information about its polarization. This polarization information can also be used to gain insight into the nature of the production amplitudes. The description of the angular distribution of the decay-plane normal relative to the production rest frame is often referred to as Schilling equation [24]. Since the $\omega$ is a spin-1 particle, its polarization information contained in the spin-density matrix has nine complex elements. For an unpolarized photon beam however, parity, hermiticity and normalization reduce the number of independent elements to four real quantities, three of which are measurable. These are typically chosen to be $\rho^0_{00}$, $\rho^0_{1-1}$ and $\mathrm{Re}(\rho^0_{10})$.

| $E_\gamma$ [GeV] | Photon Flux | $E_\gamma$ [GeV] | Photon Flux | $E_\gamma$ [GeV] | Photon Flux |
|---|---|---|---|---|---|
| | | 2.50 - 2.55 | 302735185984.0 | 4.00 - 4.05 | 140606283698.0 |
| | | 2.55 - 2.60 | 259964248500.0 | 4.05 - 4.10 | 149223684420.0 |
| 1.10 - 1.15 | 4337260656.3 | 2.60 - 2.65 | 254886921499.0 | 4.10 - 4.15 | 140423638221.0 |
| 1.15 - 1.20 | 337833236168.0 | 2.65 - 2.70 | 259744931434.0 | 4.15 - 4.20 | 167418318127.0 |
| 1.20 - 1.25 | 574495330532.0 | 2.70 - 2.75 | 224963728409.0 | 4.20 - 4.25 | 152175155236.0 |
| 1.25 - 1.30 | 496274905472.0 | 2.75 - 2.80 | 203753682420.0 | 4.25 - 4.30 | 160068141472.0 |
| 1.30 - 1.35 | 485238697908.0 | 2.80 - 2.85 | 242060106771.0 | 4.30 - 4.35 | 128465044374.0 |
| 1.35 - 1.40 | 349080941294.0 | 2.85 - 2.90 | 238390370808.0 | 4.35 - 4.40 | 90453090800.2 |
| 1.40 - 1.45 | 508526554976.0 | 2.90 - 2.95 | 231067058790.0 | 4.40 - 4.45 | 64699027048.5 |
| 1.45 - 1.50 | 497502848514.0 | 2.95 - 3.00 | 201595160599.0 | 4.45 - 4.50 | 158368725065.0 |
| 1.50 - 1.55 | 460473338930.0 | 3.00 - 3.05 | 233214036559.0 | 4.50 - 4.55 | 158892370026.0 |
| 1.55 - 1.60 | 399150479194.0 | 3.05 - 3.10 | 184728636406.0 | 4.55 - 4.60 | 136955763789.0 |
| 1.60 - 1.65 | 446872653860.0 | 3.10 - 3.15 | 213765127885.0 | 4.60 - 4.65 | 137198213594.0 |
| 1.65 - 1.70 | 395792605738.0 | 3.15 - 3.20 | 164173778322.0 | 4.65 - 4.70 | 139594283568.0 |
| 1.70 - 1.75 | 415054272952.0 | 3.20 - 3.25 | 199344803385.0 | 4.70 - 4.75 | 142168709686.0 |
| 1.75 - 1.80 | 408411797706.0 | 3.25 - 3.30 | 207673397085.0 | 4.75 - 4.80 | 102093637851.0 |
| 1.80 - 1.85 | 397650894046.0 | 3.30 - 3.35 | 178704643413.0 | 4.80 - 4.85 | 123160541637.0 |
| 1.85 - 1.90 | 345708998882.0 | 3.35 - 3.40 | 196705358312.0 | 4.85 - 4.90 | 147419199730.0 |
| 1.90 - 1.95 | 365121651368.0 | 3.40 - 3.45 | 191004264574.0 | 4.90 - 4.95 | 155283230557.0 |
| 1.95 - 2.00 | 304992117538.0 | 3.45 - 3.50 | 179980234595.0 | 4.95 - 5.00 | 120930458861.0 |
| 2.00 - 2.05 | 336131767024.0 | 3.50 - 3.55 | 77594303520.0 | 5.00 - 5.05 | 116822823306.0 |
| 2.05 - 2.10 | 347415226190.0 | 3.55 - 3.60 | 284139117094.0 | 5.05 - 5.10 | 150662097632.0 |
| 2.10 - 2.15 | 291012042438.0 | 3.60 - 3.65 | 186509696181.0 | 5.10 - 5.15 | 139170116274.0 |
| 2.15 - 2.20 | 329423974509.0 | 3.65 - 3.70 | 155345103910.0 | 5.15 - 5.20 | 129656508095.0 |
| 2.20 - 2.25 | 349551671915.0 | 3.70 - 3.75 | 159517908396.0 | 5.20 - 5.25 | 137811011294.0 |
| 2.25 - 2.30 | 260462654486.0 | 3.75 - 3.80 | 160555585107.0 | 5.25 - 5.30 | 116376757558.0 |
| 2.30 - 2.35 | 306607804116.0 | 3.80 - 3.85 | 170460273002.0 | 5.30 - 5.35 | 135718523976.0 |
| 2.35 - 2.40 | 289476321935.0 | 3.85 - 3.90 | 162365775438.0 | 5.35 - 5.40 | 125968316090.0 |
| 2.40 - 2.45 | 256426694871.0 | 3.90 - 3.95 | 164569658388.0 | 5.40 - 5.45 | 134541705938.0 |
| 2.45 - 2.50 | 241361136501.0 | 3.95 - 4.00 | 173623146606.0 | 5.40 - 5.45 | 134541705938.0 |
| | | | | 5.45 - 5.50 | |

Table 18: Total g12 photon flux for 50-MeV-wide incident photon-energy bins used in our analyses for the run range 56521 - 56646 (Period 2).

The Schilling equation for the normalized angular distribution in vector-meson photoproduction using an unpolarized beam and an unpolarized target is given by:

$$\begin{aligned}\frac{dN}{d\cos\theta\, d\phi} &= W(\theta,\,\phi) \\ &= \frac{3}{4\pi}\left(\frac{1}{2}\big(1-\rho^0_{00}\big)+\frac{1}{2}\big(3\rho^0_{00}-1\big)\cos^2\theta-\rho^0_{1-1}\sin^2\theta\,\cos 2\phi-\sqrt{2}\,Re(\rho^0_{10})\sin 2\theta\cos\,\phi\right),\end{aligned} \tag{25}$$

where the $(\theta,\phi)$ distribution is defined in the *Adair* frame. If the four-momentum of the incident photon and $\omega$ meson in the overall center-of-mass frame are denoted by $k$ and $q$, respectively, the coordinate system in the Adair frame is defined as:

$$\hat{z} = \hat{k} \qquad \hat{y} = \frac{\vec{k}\times\vec{q}}{|\vec{k}\times\vec{q}|} \qquad \hat{x} = \hat{y}\times\hat{z}. \tag{26}$$

The decay angles are defined as:

$$\cos\theta = \hat{\pi}\cdot\hat{z} \tag{27}$$

$$\cos\phi = \frac{\hat{y}\cdot(\hat{z}\times\hat{\pi})}{|\hat{z}\times\hat{\pi}|} \qquad \sin\phi = -\frac{\hat{x}\cdot(\hat{z}\times\hat{\pi})}{|\hat{z}\times\hat{\pi}|}\,, \tag{28}$$

where $\hat{\pi}$ is equal to the normal to the decay plane in the $\omega$ rest frame.

The set of Spin-Density Matrix Elements (SDMEs) for each $(\cos\theta^{\omega}_{\text{c.m.}}, \sqrt{s})$ bin can be extracted using the event-based Extended Maximum Likelihood Method (EMLM). We begin by defining the likelihood function as:

$$\mathcal{L} = \left(\frac{\bar{n}^n}{n!}e^{-\bar{n}}\right)\prod_i^n \mathcal{P}(\vec{x}, X_i)\,, \tag{29}$$

where the term in parentheses is the Poisson probability of obtaining $n$ events with the expected value $\bar{n}$. $\mathcal{P}(\vec{x}, X_i)$ is the probability density function of event $i$ with parameter set $\vec{x}$ and kinematic factors $X_i$.

The goal is to find the set of parameters $\vec{x} = \{\rho^0_{00},\, \rho^0_{1-1},\, Re(\rho^0_{10})\}$ that maximizes $\mathcal{L}$. The likelihood function in the form of Eqn. 29, when iterated over a large number of events, grows quickly to very large values. Since the natural logarithm is a monotonously-increasing function, it is computationally easier to work with $-\ln\mathcal{L}$ instead of $\mathcal{L}$. Thus, minimizing $-\ln\mathcal{L}$ is equivalent to maximizing $\mathcal{L}$. From Eqn. 29, we can write the *log likelihood* as:

$$-\ln\mathcal{L} = -n\ln\bar{n} + \ln n! + \bar{n} - \sum_i^n \ln\mathcal{P}(\vec{x},\, X_i)\,. \tag{30}$$

The probability density for each event is proportional to the production cross section $\sigma_{\gamma p\to p\omega}(X_i)$, the decay amplitude $A_{\omega\to\pi^+\pi^-\pi^0}(X_i)$, the normalized angular distribution $W(\vec{x},\, X_i)$, and the detector acceptance $\eta(X_i)$. Therefore, we can write the probability density as:

$$\mathcal{P}(\vec{x}, X_i) = \frac{\sigma_{\gamma p\to p\omega}(X_i)\, A_{\omega\to\pi^+\pi^-\pi^0}(X_i)\, W(\vec{x},\, X_i)\,\eta(X_i)}{\int \sigma_{\gamma p\to p\omega}(X_i)\, A_{\omega\to\pi^+\pi^-\pi^0}(X_i)\, W(\vec{x},\, X_i)\,\eta(X_i)\, d\Phi}\,. \tag{31}$$

The goal is to measure the set of $\vec{x} = \{\rho^0_{00},\, \rho^0_{1-1},\, Re\rho^0_{10}\}$ for each $(\cos^{\omega}_{\rm c.m.},\, \sqrt{s})$ bin. Since the production cross section, $\sigma_{\gamma p \to p\,\omega}\,(\cos^{\omega}_{c.m}, \sqrt{s})$, is just a number, it can be dropped from the probablity density function:

$$\mathcal{P}(\vec{x}, X_i) \;=\; \frac{A_{\omega \to \pi^+\pi^-\pi^0}\,(X_i)\, W(\vec{x},\, X_i)\, \eta(X_i)}{\int A_{\omega \to \pi^+\pi^-\pi^0}\,(X_i)\, W(\vec{x},\, X_i)\, \eta(X_i)\, d\Phi}\;. \tag{32}$$

The cross section for $\omega$ photoproduction is defined as:

$$\sigma_{\gamma p \to p\,\omega} \;=\; \frac{N}{\mathcal{F}\,\rho_{\rm target}\, l_{\rm target}\, N_A \,/\, A_{\rm target}}\,, \tag{33}$$

where $N$ is the number of scattering events, $\mathcal{F}$ is the photon flux, $\rho_{\rm target}$, $l_{\rm target}$, $A_{\rm target}$ are the density, length, and atomic weight of the target, respectively; $N_A$ is Avogadro's number. Therefore, the expected number of data events $\bar{n}$ is:

$$\bar{n} \;=\; \frac{\mathcal{F}\,\rho_{\rm target}\, l_{\rm target}\, N_A}{A_{\rm target}}\, \sigma_{\gamma p \to p\,\omega} \int A_{\omega \to \pi^+\pi^-\pi^0}\,(X_i)\, W(\vec{x},\, X_i)\, \eta(X_i)\, d\Phi\,. \tag{34}$$

The log likelihood function now takes the form:

$$-\ln \mathcal{L} \;=\; T_F\, \sigma_{\gamma p \to p\,\omega} \int A_{\omega \to \pi^+\pi^-\pi^0}\,(X_i)\, W(\vec{x},\, X_i)\, \eta(X_i)\, d\Phi \;-\; \sum_i^n \ln W(\vec{x},\, X_i) \;+\; F(X_i) \;+\; C\,, \tag{35}$$

where

$$T_F \;=\; \frac{\mathcal{F}\,\rho_{\rm target}\, l_{\rm target}\, N_A}{A_{\rm target}}\,, \tag{36}$$

$C$ is a constant and $F(X_i)$ is a function that depends only on the kinematics. We can drop $C$ and $F(X_i)$ from the Eqn. 35 since they do not depend on the parameters $\vec{x}$. The integration is done numerically using the *Monte Carlo* technique.

For this technique, $N_{\rm raw}$ events are randomly generated according to $\gamma p \to p\,\omega$, with $\omega \to \pi^+\pi^-\pi^0$ phase space. The integral can then be approximated by:

$$\int A_{\omega \to \pi^+\pi^-\pi^0}\,(X_i)\, W(\vec{x},\, X_i)\, \eta(X_i)\, d\Phi \;\approx\; \frac{\int d\Phi}{N_{\rm raw}} \sum_i^{N_{\rm raw}} A_{\omega \to \pi^+\pi^-\pi^0}\,(X_i)\, W(\vec{x},\, X_i)\, \eta(X_i)\,. \tag{37}$$

To obtain the values for $\eta(X_i)$, each event is run through a GEANT-based detector simulation package, discussed in detail in Section 3.7. This procedure simulates the acceptance of the CLAS detector by rejecting those events that do not survive the data analysis. Thus, for each event, the acceptance is $\eta(X_i) = 0$ or 1. We denote the number of accepted Monte Carlo events by $N_{\rm acc}$. We can then rewrite the integral approximation as:

$$\int A_{\omega \to \pi^+\pi^-\pi^0}\,(X_i)\, W(\vec{x},\, X_i)\, \eta(X_i)\, d\Phi \;\approx\; \frac{\int d\Phi}{N_{\rm raw}} \sum_i^{N_{\rm acc}} A_{\omega \to \pi^+\pi^-\pi^0}\,(X_i)\, W(\vec{x},\, X_i)\,. \tag{38}$$

The decay amplitude $A_{\omega \to \pi^+\pi^-\pi^0}$ is proportional to the pion's momentum in the $\omega$ rest frame [19] and proportional to the $\lambda$ quantity that we defined in Section 3.12.2:

$$A_{\omega \to \pi^+\pi^-\pi^0} \;\propto\; \lambda \;=\; \frac{|\vec{p}_{\pi^+} \,\times\, \vec{p}_{\pi^-}\,|^2}{T^2 \left(\frac{T^2}{108} \;+\; \frac{mT}{9} \;+\; \frac{m^2}{3}\right)}\;, \tag{39}$$

where $T$ is the sum of the $\pi^{\pm,0}$ and $m$ is the $\pi^{\pm}$ mass.The value of $\lambda$ varies between 0 and 1. Thus, the phase-space integral on the right side of Eqn. 38 is:

$$\int d\Phi \;=\; \int d\Omega\, d\lambda \;=\; 4\pi\,. \tag{40}$$

Finally, the log-likelihood function takes on the form:

$$-\ln\mathcal{L} \;=\; T_F\,\sigma_{\gamma p\to p\,\omega}\,\frac{4\pi}{N_{\rm raw}}\,\sum_i^{N_{\rm acc}}\lambda_i\,W(\vec{x},\,X_i) \;-\; \sum_i^{n}\ln W(\vec{x},\,X_i)\,. \tag{41}$$

After obtaining the $Q$ value for each event, which provides the probability that the event is a $p\,\omega$ event, this $Q$ value can be used to weight the event's contribution to the log likelihood:

$$-\ln\mathcal{L} \;=\; T_F\,\sigma_{\gamma p\to p\,\omega}\,\frac{4\pi}{N_{\rm raw}}\,\sum_i^{N_{\rm acc}}\lambda_i\,W(\vec{x},\,X_i) \;-\; \sum_i^{n}Q_i\,\ln W(\vec{x},\,X_i)\,, \tag{42}$$

where $Q_i$ is the $Q$ value for event $i$. The CERNLIB package MINUIT was used to minimize $-\ln\mathcal{L}$. The minimization algorithm that we used is called MIGRAD.

### 4.4 Extraction of the Hyperon Polarization in $\gamma p \to K^0\,\Sigma^+$

The $\Sigma^+$ is produced via the electromagnetic (or strong) interaction but decays to a proton and a $\pi^0$ via the weak interaction. Since the weak decay violates parity, the polarization of the $\Sigma^+$ can be extracted from the angular distribution of one of the decay products in the $\Sigma^+$ rest frame. This observable is called recoil (or induced) polarization and is named $P$ (Eqn. 18).

The kinematic situation is shown schematically in Fig. 59. The incident photon and the recoiling $K^0$ define the reaction plane. The angular distribution of the proton in the $\Sigma^+$ rest frame is then described by (see Eqn. 18):

$$W(\theta_p) \;=\; \frac{1}{2}\,(1 \;+\; \alpha P\,\cos\,(\theta_p))\,,$$

where $\theta_p$ is the angle between the proton momentum vector in the $\Sigma^+$ rest frame and the normal of the reaction plane. The parameter $\alpha$ is the degree of parity mixing and for $\Sigma^+ \to p\pi^0$, has a value of $\alpha \;=\; -0.98 \pm 0.016$ [7].

To determine the polarization observable, we integrate over all the events above the reaction plane (up) as well as below the reaction plane (down). The $P$ observable can then be expressed as:

$$P \;=\; \frac{2}{\alpha}\,\frac{\sigma_{\rm up} \;-\; \sigma_{\rm down}}{\sigma_{\rm up} \;+\; \sigma_{\rm down}}\;. \tag{43}$$

Since the whole detector is $\phi$ symmetric, acceptance effects in the enumerator and the denominator cancel out. Therefore, we can also express the polarization observable $P$ simply in terms of count rates:

$$P \;=\; \frac{2}{\alpha}\,\frac{N_{\rm up} \;-\; N_{\rm down}}{N_{\rm up} \;+\; N_{\rm down}}\;, \tag{44}$$

where $N_{\rm up}$ and $N_{\rm down}$ are the number of events with the proton in the direction above and below the reaction plane, respectively.

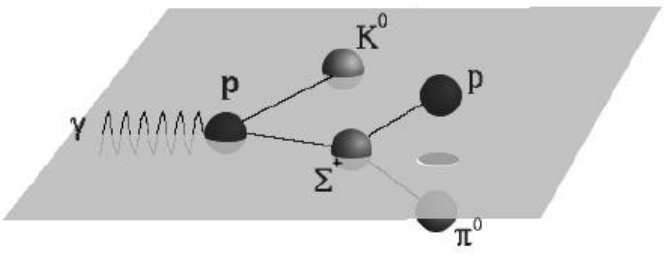


Figure 59: *The recoil polarization of the $\Sigma^+$ shown schematically. The plane indicates the reaction plane defined by the incoming $\gamma$ and the outgoing $\Sigma^+$ in the center-of-mass frame.*

## 4.5 Extraction of the Beam-Helicity Asymmetry in $\gamma p \to p\,\pi^+\pi^-$

### Data with an Azimuthal Symmetry in the Lab Frame

Data with an unpolarized- or a circularly-polarized beam in combination with an unpolarized- or a longitudinally-polarized target are isotropic in the lab azimuthal angle since the polarization(s) lie along the $z$-axis in the lab frame. Hence, the angular distribution in the lab frame of any final-state particle will be flat after an acceptance correction. In such cases, the asymmetry – in any kinematic bin – between the number of events with orthogonal polarization orientations is just a number (instead of a function of the lab azimuthal angle). The polarization observables are then easily extracted from these measured asymmetries.

In the case of the beam-helicity asymmetry, $\mathbf{I}^{\odot}$, the data consist of two subsets based on opposite beam helicities, $\rightarrow$ and $\leftarrow$, where $\rightarrow$ ($\leftarrow$) denotes that the helicity is parallel (antiparallel) to the beam axis. Since the beam helicity flips at a large rate, the flux, $\Phi$, and the acceptance, $\epsilon$, are the same for both subsets. For the same reason, the degree of beam polarization for the two helicity states can be considered the same and is denoted by $\delta_{\odot}$. Then, in any kinematic bin, the number of $\rightarrow$ events and $\leftarrow$ events can be related to $\mathbf{I}^{\odot}$ using Equation 21. The numbers $N_{\rightarrow}$ and $N_{\leftarrow}$ are given by:

$$\begin{aligned} N_{\rightarrow} &= F\,C\,\epsilon\,\sigma_0\,(\,1\,+\,\delta_{\odot}\,\mathrm{I}^{\odot}\,)\,, \\ N_{\leftarrow} &= F\,C\,\epsilon\,\sigma_0\,(\,1\,-\,\delta_{\odot}\,\mathrm{I}^{\odot}\,)\,, \end{aligned} \tag{45}$$

where $\delta_{\odot}$ denotes the degree of circular-beam polarization. The asymmetry, $A$, between the two numbers in a kinematic bin is given by:

$$A \,=\, \frac{N_{\rightarrow}\,-\,N_{\leftarrow}}{N_{\rightarrow}\,+\,N_{\leftarrow}} \,=\, \delta_{\odot}\,\mathrm{I}^{\odot}\,. \tag{46}$$

Hence, the beam-helicity observable can be extracted from the asymmetry:

$$\mathrm{I}^{\odot} \,=\, \frac{A}{\delta_{\odot}}\,. \tag{47}$$

If each event is assigned a weight, $w_i$ (a $Q$ value, for instance), then the effective number of signal events for the two beam-helicity states will be given by:

$$N'_{\rightarrow} = \sum_{i=1}^{N^{\rightarrow}} w_i \,, \qquad N'_{\leftarrow} = \sum_{i=1}^{N^{\leftarrow}} w_i \,. \tag{48}$$

The asymmetry is then formed from these effective counts:

$$A = \frac{N'_{\rightarrow} - N'_{\leftarrow}}{N'_{\rightarrow} + N'_{\leftarrow}} \,, \tag{49}$$

and $\mathbf{I}^{\odot}$ is obtained using Equation 47.

### 4.6 Dalitz-Plot Analysis of $\omega \rightarrow \pi^+\pi^-\pi^0$

# 5 Systematic Uncertainties

## 5.1 Contribution from the $Q$-Factor Method

Assigning a $Q$ value to a particular event required to fit the mass distribution of the event and its neighbors using the likelihood technique. The covariance matrix, $C_\eta$, for the set of fit parameters, $\vec{\eta}$, could be used to determine the uncertainty of the $Q$ value for the given event:

$$\sigma_Q^2 = \sum_{i,j} \frac{\partial Q}{\partial \eta_i} \left(C_\eta^{-1}\right) \frac{\partial Q}{\partial \eta_j} \ . \tag{50}$$

The $Q$ factor method led to some correlations among events and their nearest neighbors because events could serve as neighbors for many *seed* events. The systematic "correlation" uncertainty of the $\omega$ yield due to this method in a particular kinematic bin was then given by:

$$\sigma_\omega^2 = \sum_{i,j} \sigma_Q^i \, \rho_{ij} \, \sigma_Q^j \, , \tag{51}$$

where the sum $i$, $j$ was taken over the events in the bin, $\sigma_Q^i$ and $\sigma_Q^j$ were the fit uncertainties for events $i$ and $j$, and $\rho_{ij}$ was the correlation factor between events $i$ and $j$. The correlation factor simply represented the fraction of shared nearest-neighbor events.

If we assumed 100 % correlation between events in a kinematic bin, then the uncertainty of the $\omega$ yield could be written as:

$$\sigma_\omega^2 = \Big( \sum_i^N \sigma_Q^i \Big)^2 . \tag{52}$$

This assumption could significantly overestimate the uncertainty. In this analysis, we did not use the assumption of 100 %-correlated events but properly determined the uncertainties according to Eqn. 51. The uncertainty contribution from the $Q$-factor method could then be added to the statistical uncertainty to obtain the total "statistics-based" uncertainty:

$$\sigma^2 = \sigma_\omega^2 + \sigma_{\text{statistical}}^2 \, . \tag{53}$$

We also implemented this procedure for all other channels.

### 5.1.1 Propagation of the Uncertainty from the $Q$-Factor Method

Consider a *simple* counting experiment, for example the determination of the induced polarization in the decay of the $\Sigma^+$ hyperon (Eqn. 44):

$$P = \frac{2}{\alpha} \frac{N_{\text{up}} - N_{\text{down}}}{N_{\text{up}} + N_{\text{down}}} = \frac{2\,A}{\alpha} \ ,$$

where $N_{\text{up}}$ and $N_{\text{down}}$ were the total number of events with the proton in the direction above and below the reaction plane, respectively. The uncertainty in the $Q$ value of each event only affected the counts, and not the parameter $\alpha$. Equation 51 showed that the uncertainty of the count in a particular bin due to the $Q$-factor method was:

$$\sigma_N^2 = \sum_{i,j} \sigma_Q^i \, \rho_{ij} \, \sigma_Q^j \, ,$$

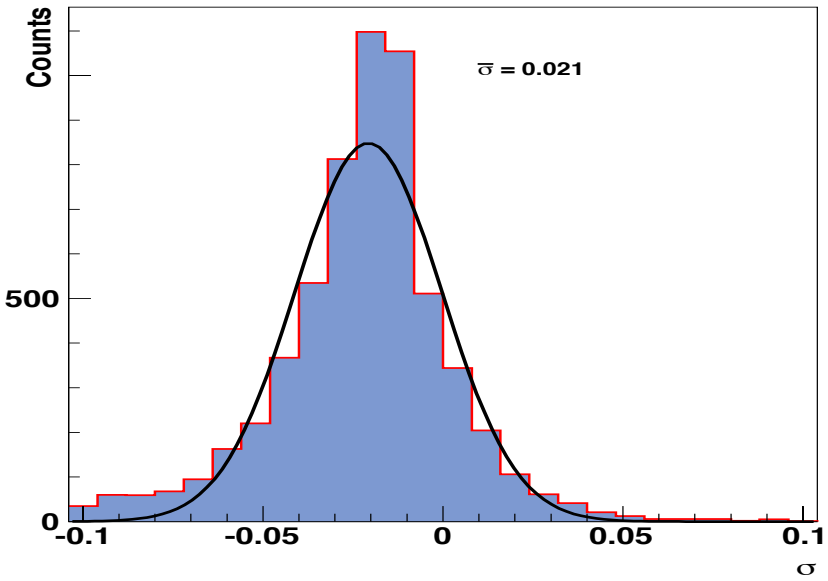


Figure 60: *The distribution of contributions to the total systematic uncertainty from the CL cut, integrated over all energy and angle bin.*

where $\sigma_Q^i$ is the fit uncertainty in the $Q$ value of the $i^{\text{th}}$ event, $N$ is the total number of events and $\rho_{ij}$ is the correlation between the $i^{\text{th}}$ and the $j^{\text{th}}$ event (which is equal to the fraction of the number of common nearest neighbors. Depending on the available statistics in an analysis, it is often more convenient to assume that all events are 100 % correlated and to overestimate the uncertainties than to calculate the actual correlations, $\rho_{ij}$. This can be very time consuming and computationally demanding. In our g12 analysis, we chose to find the actual correlations because we found that $\sigma_N$ was significantly over (under)estimated when 100 % (0 %) correlation between events was assumed.

From standard error propagation, and writing $P$ as a function of the counts, $P = f(N_{\text{up}}, N_{\text{down}})$:

$$\begin{aligned} \sigma_P &= \sqrt{\left(\frac{\partial f}{\partial N_{\text{up}}}\right)^2 \sigma_{N_{\text{up}}}^2 + \left(\frac{\partial f}{\partial N_{\text{down}}}\right)^2 \sigma_{N_{\text{down}}}^2} \\ &= \frac{4}{\alpha\,(N_{\text{up}} + N_{\text{down}})^2} \sqrt{N_{\text{down}}^2\,\sigma_{N_{\text{up}}}^2 + N_{\text{up}}^2\,\sigma_{N_{\text{down}}}^2} \quad . \end{aligned} \tag{54}$$

If $\sigma_{N_{\text{up}}} = \sigma_{N_{\text{down}}} = \sigma_N$, the above equation simplified to:

$$\sigma_P = \frac{4\,\sigma_N}{\alpha\,(N_{\text{up}} + N_{\text{down}})} \sqrt{\frac{N_{\text{up}}^2 + N_{\text{down}}^2}{(N_{\text{down}} + N_{\text{up}})^2}} \quad . \tag{55}$$

Therefore, $\sigma_{N_{\text{up}}}$ and $\sigma_{N_{\text{down}}}$ could be found by using Eqn. 51, and substituting them into Eqn. 54 then yielded $\sigma_P$. Similarly, one could follow the method outlined above to analytically find the contribution of the $Q$-factor method to the total systematic uncertainty in any other observable associated with a simple counting experiment (cross section measurements, for instance).

### 5.2 Contribution from the Confidence-Level Cut

Another source of the total systematic uncertainty that we considered was the confidence-level (CL) cut. The procedure to determine the uncertainty of this cut was to re-calculate the cross sections based on various CL-cut values. We have studied various CL cuts from 0.1 % to 5 %.

Denoting the originally-measured value of the differential cross section for a kinematic bin $A_0$, and the newly-measured value based on the new CL cut $A_n$, then the absolute uncertainty will be:

$$\sigma_{\mathrm{CL}} = \frac{|A_n - A_o|}{A_o}. \tag{56}$$

The corresponding distribution of Eqn. 56 for all energy and angle bins is shown in Fig. 60. We fitted this distribution with a Gaussian and used the width, $\bar{\sigma} = 2.1\,\%$, as the contribution to the systematic uncertainty from the CL cut.

### 5.3 Further Contributions from the g12 Systematics

The general study of the g12 systematics has been discussed in the g12 analysis note [3] and is summarized in Table 19 below.

| Source | % Uncertainty |
|---|---|
| Sector by Sector | 5.9 |
| Flux | 1.7 |
| Per-Track Inefficiency | 3.0 |
| Beam Polarization | 3.3 |
| Target | 0.5 |
| $z$-vertex | 0.4 |
| Fiducial Selection | ~2.4 |
| Normalization Uncertainty | 1.8 |

Table 19: Summary of contributions to the total systematic uncertainty [3].

As an example, the sector-by-sector normalization was derived using the acceptance-corrected yields for different sectors as shown in Figure 61. The uncertainty was calculated using the deviation of the yield in each sector from the average acceptance-corrected yield of all six sectors.

### 5.4 Contribution from the Beam Polarization

The beam-helicity asymmetry (in a simple counting experiment) is inversely proportional to the average degree of the beam polarization. This relation has been shown for the observable $\mathbf{I}^{\odot}$ in the $\gamma p \to p\,\pi^+\pi^-$ reaction (see Eqn. 47) and, in a similar way, for the hyperon recoil-polarization $P$ in the reaction $\gamma p \to K_S\,\Sigma^+$ (see Eqn. 44), where the asymmtry is inversely proportional to the parameter $\alpha$. Hence, from error propagation, it is clear that any uncertainty in the determination of the average beam polarization led to the same percentage uncertainty in the polarization observable.

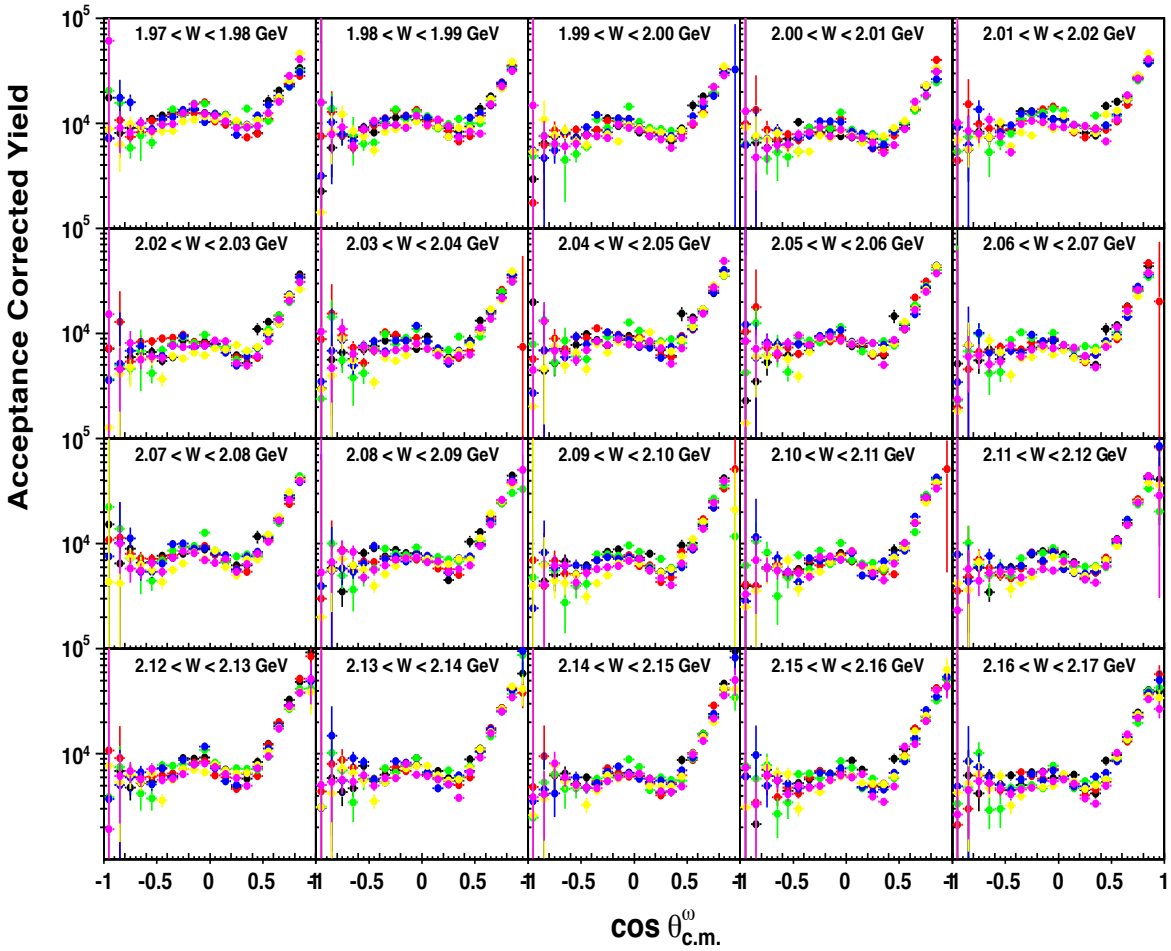


Figure 61: *The acceptance-corrected $\omega$ yields for different sectors. The six different colors represent the six different CLAS sectors.*

## 5.5 Contribution from the Beam-Charge Asymmetry

Section 3.11.3 discussed the beam-charge asymmetry in detail. Since these contributions were very small, effects on the observables were considered negligible.

## 5.6 Contribution from the Accidental Photons

In Section 3.3.1, we discussed how initial photons were selected. Even after following the full selection procedure, some accidental photons remained. The fraction could be estimated from a comparison in the yields between the central peak with the neighboring beam buckets in the coincidence-time distribution. For example, the fraction was at most 2.5 % in g12 (see Figure 62). These accidentals led to a small overestimation in the photon flux by the same factor in all data sets. Therefore, in counting experiments, the accidentals did not affect the polarization observables since the factor canceled out in the asymmetry.

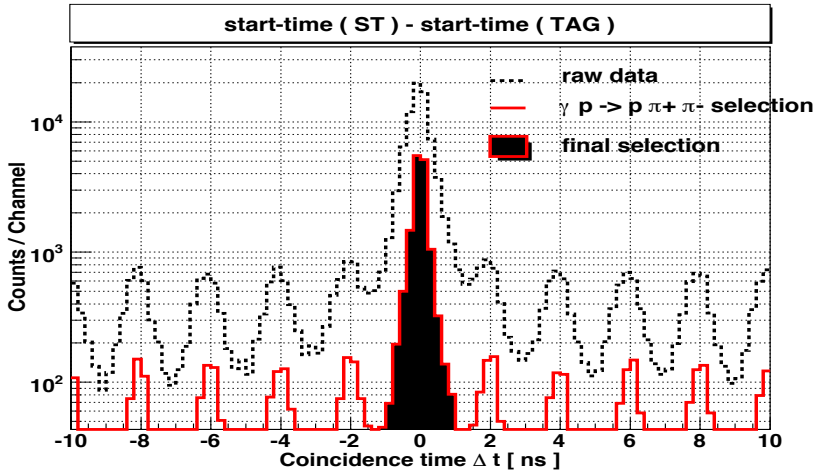


Figure 62: *Coincidence-time distributions of tagged photons for the raw data (dotted histogram) and after applying all $\gamma p \to p\,\pi^+\pi^-$ selection cuts (solid histogram). Events of the center bins filled in black indicate the candidates of the final selection. The fraction of remaining accidental photons in the central bucket was at most* 2.5 %.

## 5.7 Systematic Uncertainties in the Determination of SDMEs

If we Taylor-expand $-\ln\mathcal{L}(\alpha)$ around $\alpha = \alpha^*$ where $\alpha^*$ is the correct parameter that minimizes $-\ln\mathcal{L}$:

$$-\ln\mathcal{L}(\alpha) \;=\; -\ln\mathcal{L}(\alpha^*) \;-\; (\alpha \;-\; \alpha^*)^2 \;\frac{1}{2}\,\frac{\mathrm{d}^2\ln\mathcal{L}}{\mathrm{d}\alpha^2}\bigg|_{\alpha\,=\,\alpha^*}\,, \tag{57}$$

then we can write $-\ln\mathcal{L}$ as:

$$-\ln\mathcal{L}(\alpha) \;=\; C\,e^{\frac{(\alpha\,-\,\alpha^*)^2}{2\sigma^2}}\,, \tag{58}$$

where $C$ is a constant and $\sigma^2 = \left(\frac{d^2\ln\mathcal{L}}{d\alpha^2}\Big|_{\alpha=\alpha^*}\right)^{-1}$.

Therefore, $-\ln\mathcal{L}$ shows a Gaussian distribution with $\sigma$ as the statistical uncertainty that is returned by MINUIT. However, we then multiply $\ln\mathcal{L}$ by a factor of two so that it takes the approximate form of a $\chi$-square distribution and the interpretation of the deviation is similar to the interpretation of the sum of squares in least-square regression. Therefore, the final function that needs to be minimized is $-2\ln\mathcal{L}$ which gives us:

$$\sigma^2 \;=\; \frac{1}{2}\left(\frac{d^2\ln\mathcal{L}}{d\alpha^2}\bigg|_{\alpha\,=\,\alpha^*}\right)^{-1} \tag{59}$$

as the statistical uncertainty.

We considered the propagated $Q$-value uncertainties as the systematic uncertainties for the SDMEs. The procedure was based on the variation of the $Q$ value according to:

$$Q \;-\; \sigma_Q \;<\; Q \;<\; Q \;+\; \sigma_Q\,,$$

where $\sigma_Q$ was the uncertainty of $Q$.

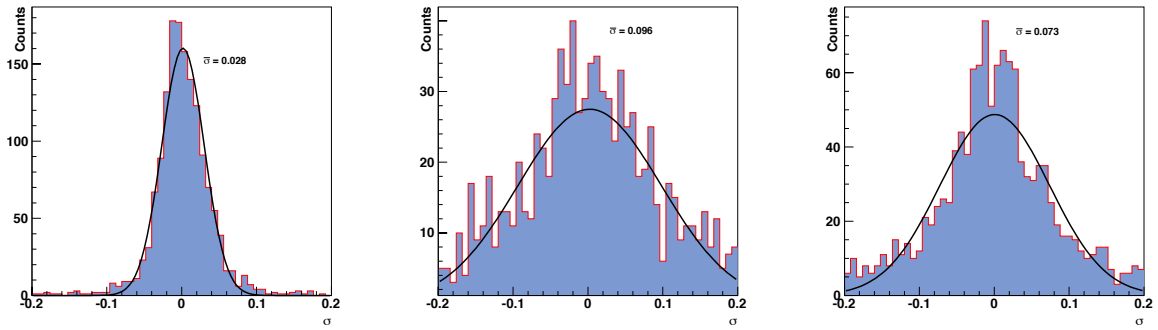


Figure 63: *Distributions of the systematic uncertainties for the spin-density matrix elements* $\rho^0_{00}$ *(top left),* $\rho^0_{1-1}$ *(top right), and* $Re\rho^0_{10}$ *(bottom row), integrated over all energies and angles.*

If we denote the originally-measured value of the SDME by $A_o$ and the newly-determined value (based on the new $Q$) as $A_n$, then the uncertainty was calculated as

$$\sigma_\rho = \frac{|A_n - A_o|}{A_o}. \tag{60}$$

The SDMEs' uncertainty distributions – integrated over all energies and angles – are shown in Figure 63. We considered $\bar{\sigma} = 2.1\,\%$, $9.6\,\%$ and $7.3\,\%$ the values of the systematic uncertainties for the elements $\rho^0_{00}$, $\rho^0_{1-1}$ and $\mathrm{Re}(\rho^0_{10})$, respectively.

## 5.8 Total Systematic Uncertainty

The error bars shown in all preliminary results include the $Q$-factor uncertainties that have been combined with the statistical uncertainties in quadrature. The total systematic uncertainty for each observable is listed in Table 20. The uncertainties stem from the relevant sources that have been described in previous sections and als include some channel-specific uncertainties, i.e. branching fractions of the decay mode.

| Source | $\gamma p \to p\,\omega$ | $\gamma p \to p\,\eta$ | $\gamma p \to p\,\phi$ | $\gamma p \to K^0\,\Sigma^+$ | $P_{\Sigma^+}$ |
|---|---|---|---|---|---|
| Sector by Sector | 5.9 % | 5.9 % | 5.9 % | 5.9 % | 5.9 % |
| Flux | 1.7 % | 1.7 % | 1.7 % | 1.7 % | 1.7 % |
| Target | 0.5 % | 0.5 % | 0.5 % | 0.5 % | 0.5 % |
| z-vertex | 0.4 % | 0.4 % | 0.4 % | 0.4 % | 0.4 % |
| Fiducial Selection | 2.4 % | 2.4 % | 2.4 % | 2.4 % | 2.4 % |
| Normalization | 1.8 % | 1.8 % | 1.8 % | 1.8 % | 1.8 % |
| Branching Fraction | 0.7 % | 0.28 % | | 0.05 % and 0.3 % | - |
| Parity Mixing, $\alpha$ | - | - | - | - | 0.02 % |

Table 20: *Total systematic uncertainty for each observable.*

# 6 Final Results

## 6.1 Results for the $\gamma p \to p\,\omega$ Reaction

The following section presents and discusses our final results in $\omega$ photoproduction. We compare with previous CLAS results whenever these are available.

### 6.1.1 Differential Cross Sections in $\gamma p \to p\,\omega$

Figures 66-71 show the differential cross sections for the reaction $\gamma p \to p\,\omega$, covering the center-of-mass energy range $1.92 < W < 3.30$ GeV. The CLAS-g12 results are shown in black. Also shown in the figures (if available) are the previous results from the CLAS-g11a experiment (red points) [8]. The uncertainties for both data sets (CLAS g11a and g12) include the $Q$-factor uncertainties and the statistical uncertainties added in quadrature. We simply followed the example of g11a to properly compare our results. Figure 65 shows the energy dependence of the cross sections for the same energy range: g12 (red points) and g11a (blue points).

The following results (Figs. 66-71) are presented in 20-MeV-wide center-of-mass energy bins for $1.92 < W < 2.12$ GeV and in 10-MeV-wide center-of-mass energy bins for $2.12 < W < 3.30$ GeV, which yields a total of 118 energy bins. Please note that some g12 bins are missing due to some tagger inefficiencies: (1) $2.73 < W < 2.75$ GeV and (2) $2.55 < W < 2.61$ GeV. The reason for the larger binning at lower energies is that most of the systematic discrepancies between CLAS-g12 and CLAS-g11a seemed to emerge at lower energies, $W < 2.3$ GeV. While the angular shapes were observed to be in reasonable agreement, the g12 cross section appeared to be fluctuating around the g11a cross section for both the $\eta$ and the $\omega$ cross sections in the same $W$ bins. Therefore, we concluded that the problem was related to some fluctuations in the photon flux. Note that the g12 experiment was running at a CEBAF energy of 5.715 GeV resulting in about $E_\gamma = 1200$ MeV or $W = 1770$ MeV as the lowest available tagged photon energy.

We concluded that some of the discrepancies between CLAS-g11a and g12 are related to the g12 resolution at the very low end of the tagging range. The element in the covariance matrix for the g12 photon measurement is:

$$\sigma^2 = \frac{(0.001 \times 5715\ \text{MeV})^2}{3} = 10.89\ \text{MeV}^2\,.$$

Close to the $\omega$ threshold of 1109.1 MeV, a 10-MeV-wide $W$ bin corresponds to a fairly big 18 MeV-wide $E_\gamma$ bin; the measurement uncertainty is thus about $\sigma/18 \approx 18\,\%$. Following the example of the published CLAS-g11a results, we initially used the following $W$ binning scheme for the $\eta$ and $\omega$ reactions:

| | $< 2.1$ GeV | 2.10 - 2.36 GeV | $> 2.36$ GeV |
|---|---|---|---|
| $\gamma p \to p\,\eta$ | 10 MeV | 20 MeV | 40 MeV |

| | 1.92 - 2.92 GeV |
|---|---|
| $\gamma p \to p\,\omega$ | 10 MeV |

However, since the CLAS-g12 experiment does not provide the resolution to use 10-MeV-wide $W$ bins below $W \approx 2.3$ GeV, we decided to use broader, 20-MeV-wide $W$ bins at these energies. Note that this resolution effect does not affect the $K^0\,\Sigma^+$ channel since we use broader energy bins.

The agreement with the previous CLAS-g11a measurements is very good, the agreement of the angular distributions is excellent (Fig. 65). Some discrepancies are still observed but toward higher energies, the agreement becomes significantly better. As a matter of fact, the agreement can be considered excellent at center-of-mass energies above 2.18 GeV (with the exception of some bins above $W \approx 2.77$ GeV). The g12/g11a ratio distribution is shown in Fig. 64 (left). Note that this distribution is not necessarily expected to be Gaussian (for mathematical reasons) but we used a Gaussian fit to determine a mean value. Our g12 results still appear systematically lower than the g11a data but it is worth noting here that a live-time correction was applied in the g11a analysis that is still somewhat mysterious. Quote from the g11a analysis note [10]: *Of course, the question still remains as to why this correction works. Unfortunately, the answer will probably never be known. The piece of hardware reponsible for this measurement was replaced after the g11a run period. This discrepancy between the Faraday cup and clock live times appears to only exist in the runs taken in 2004. Both earlier and later runs show no signs of any live time discrepancies.* At the time, the g11a run group had noticed a current-dependent normalization issue and observed an almost linear current dependence between the *busy-gated* clock live time and the Faraday cup live time. They assumed that the Faraday cup live time was the accurate one and therefore, they applied a correction to their normalized yields by replacing the clock live time by its square. The efficiency of this correction is shown in Fig. 64 (right). We do not doubt that such a correction was needed and also do not question that the squared live time was used. However, we noticed that no systematic uncertainty was assigned to this correction. The overall g11a normalization uncertainty was given as 1.8 % [10].

The data at $E_\gamma > 4.0$ GeV are first-time measurements with unprecendented statistical quality and will bridge the gap between these lower-energy CLAS data and data from the 12-GeV era.

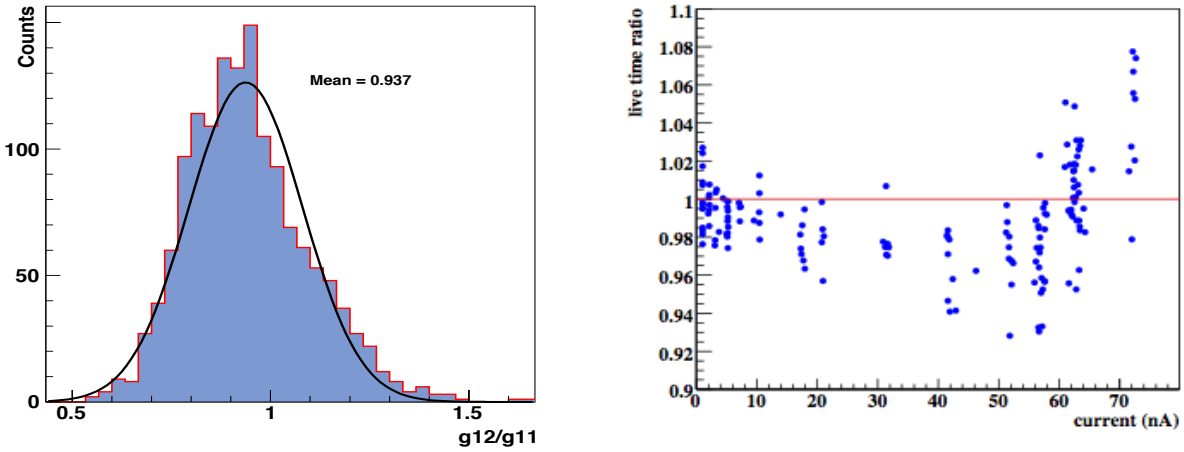


Figure 64: *Left: The g12/g11a ratio distribution of the $\gamma p \to p\omega$ cross sections results. Right: The g11a Faraday cup live time divided by the square of the clock live time ($LT_{FCUP}/LT^2_{CLOCK}$) vs. current (nA). The g11a analysis note claims that the ratio is close to one at all currents.*

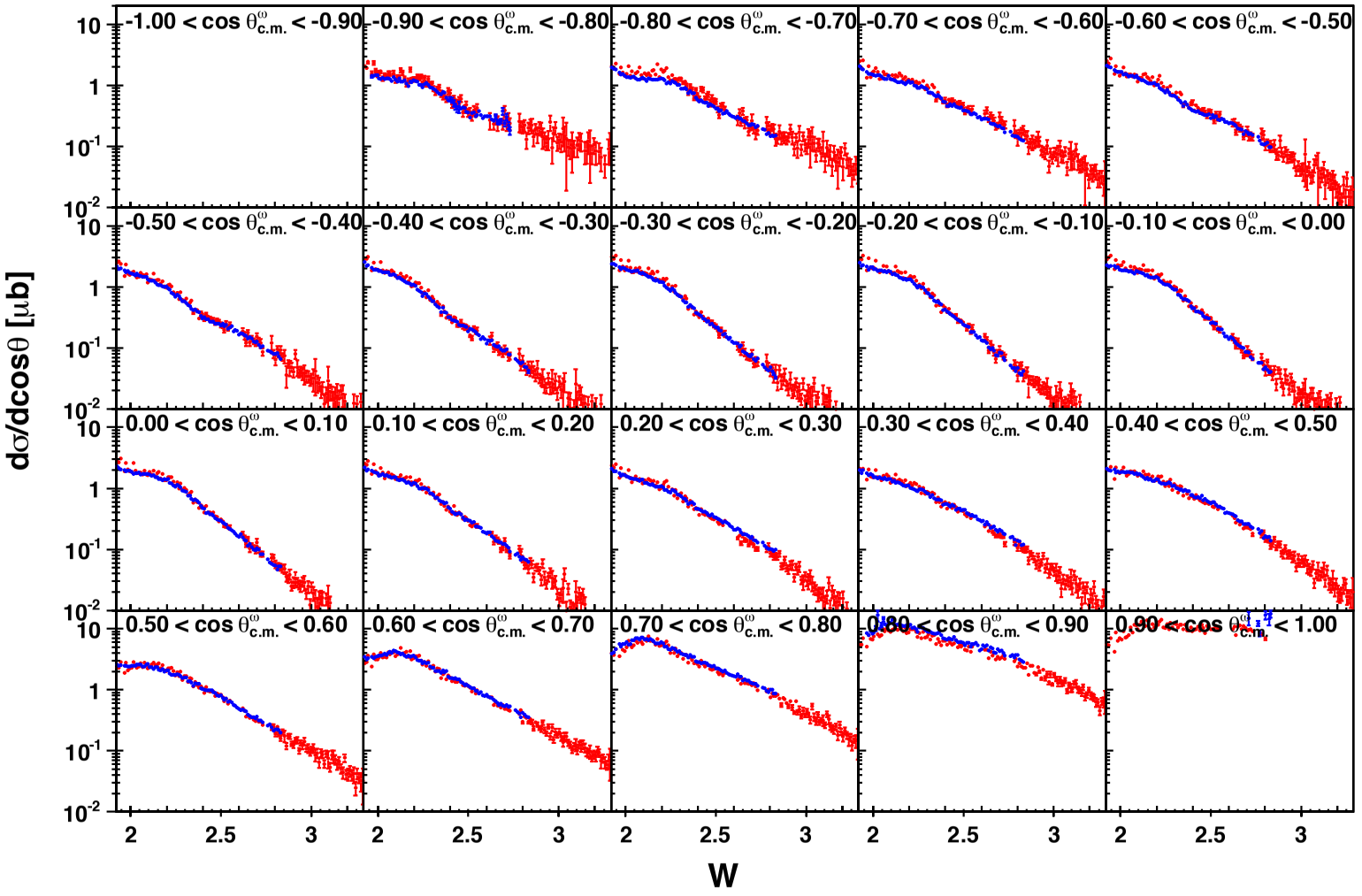


Figure 65: *The energy dependence of the differential cross sections in the reaction $\gamma p \to p\omega$ for the center-of-mass energy range $1.92 < W < 3.30$ GeV from g12 (red data points) in comparison with the previous CLAS measurements from g11a [8] (blue points).*

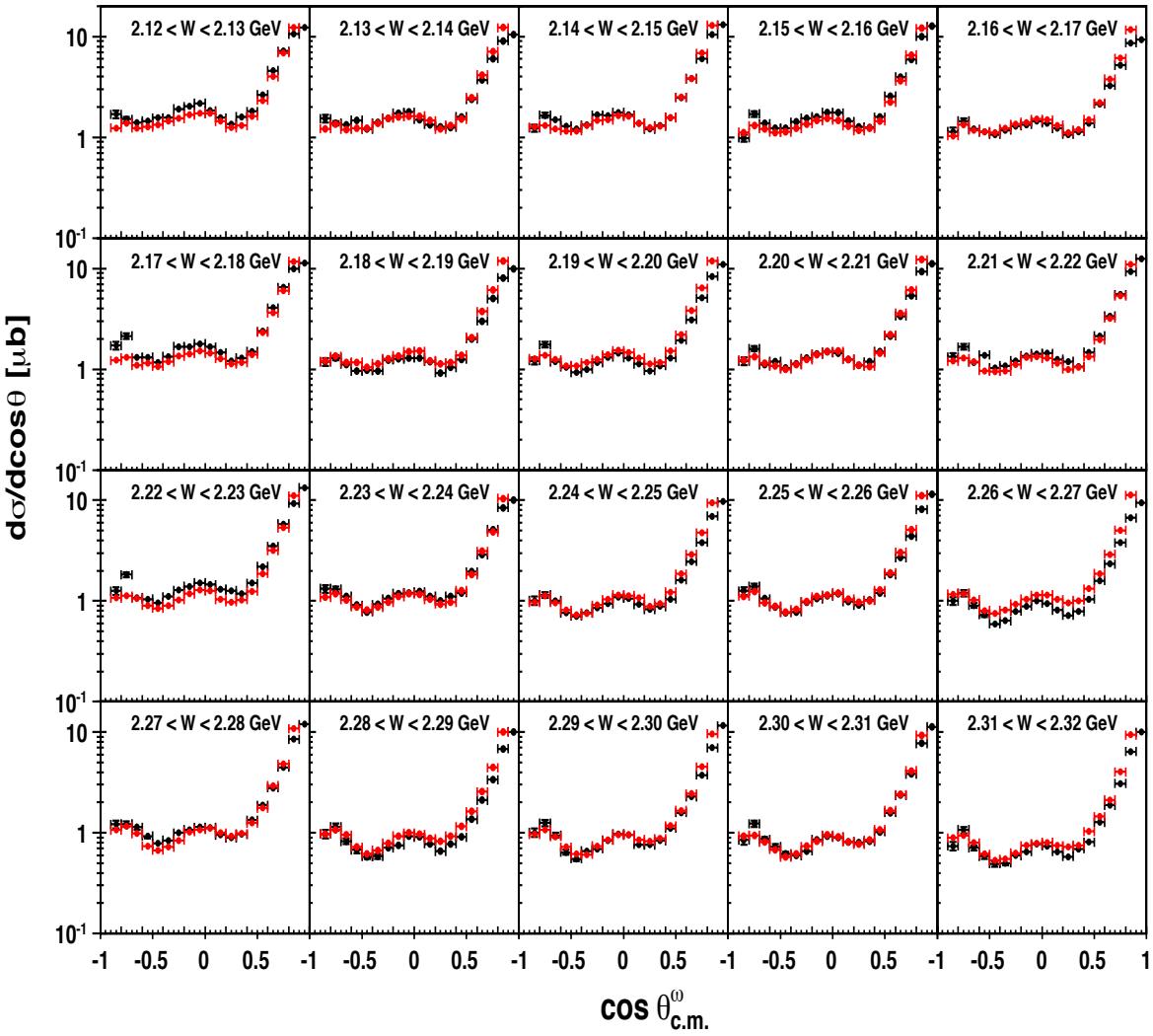


Figure 66: *The differential cross sections in the reaction $\gamma p \to p\omega$ for the center-of-mass energy range $2.12 < W < 2.32$ GeV from g12 (black data points) in comparison with the previous CLAS measurements from g11a [8] (red points). The given uncertainties for both data sets comprise the statistical uncertainties and the Q-factor uncertainties added in quadrature.*

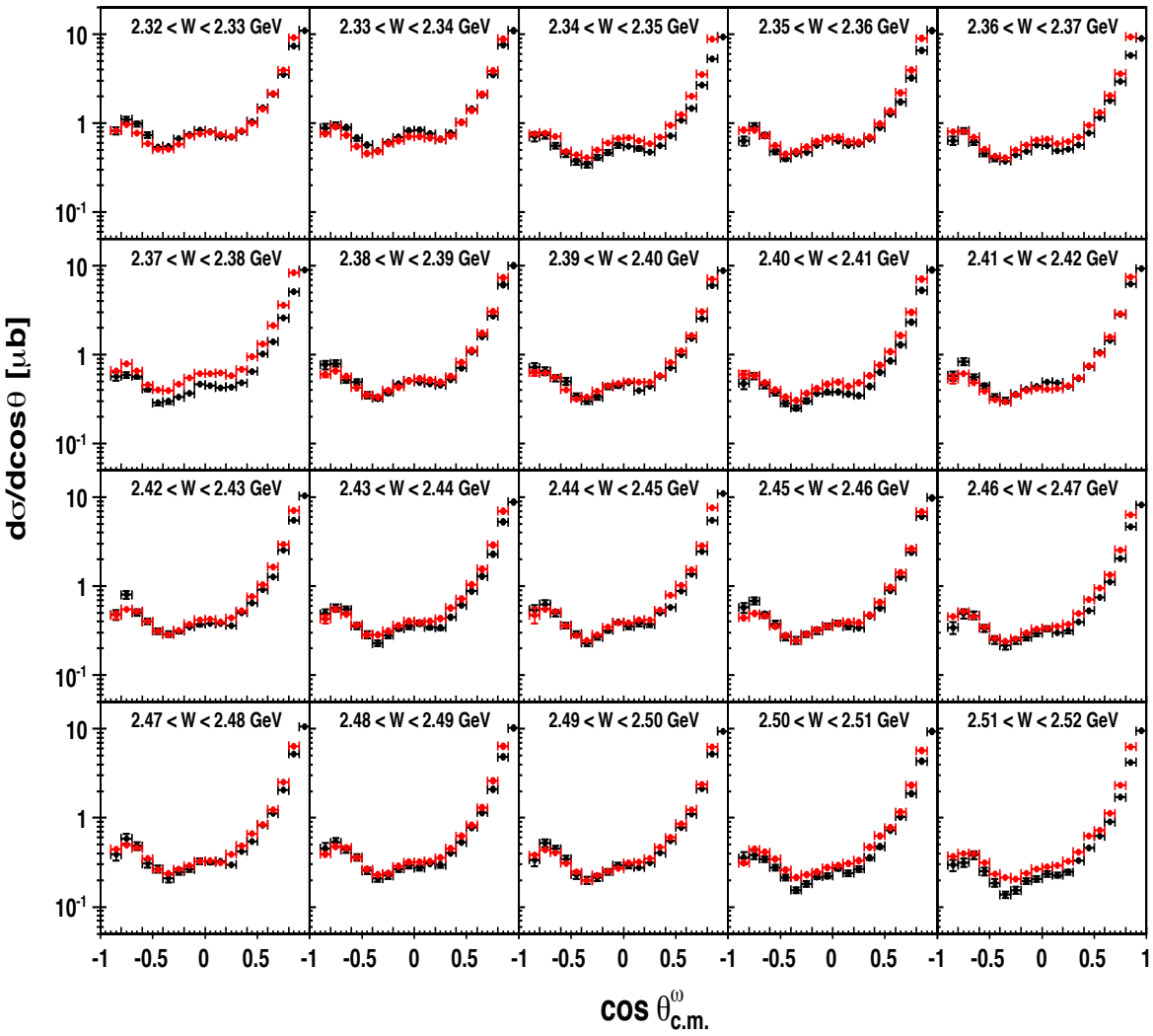


Figure 67: *The differential cross sections in the reaction $\gamma p \to p\omega$ for the center-of-mass energy range $2.32 < W < 2.52$ GeV from g12 (black data points) in comparison with the previous CLAS measurements from g11a [8] (red points). The given uncertainties for both data sets comprise the statistical uncertainties and the Q-factor uncertainties added in quadrature.*

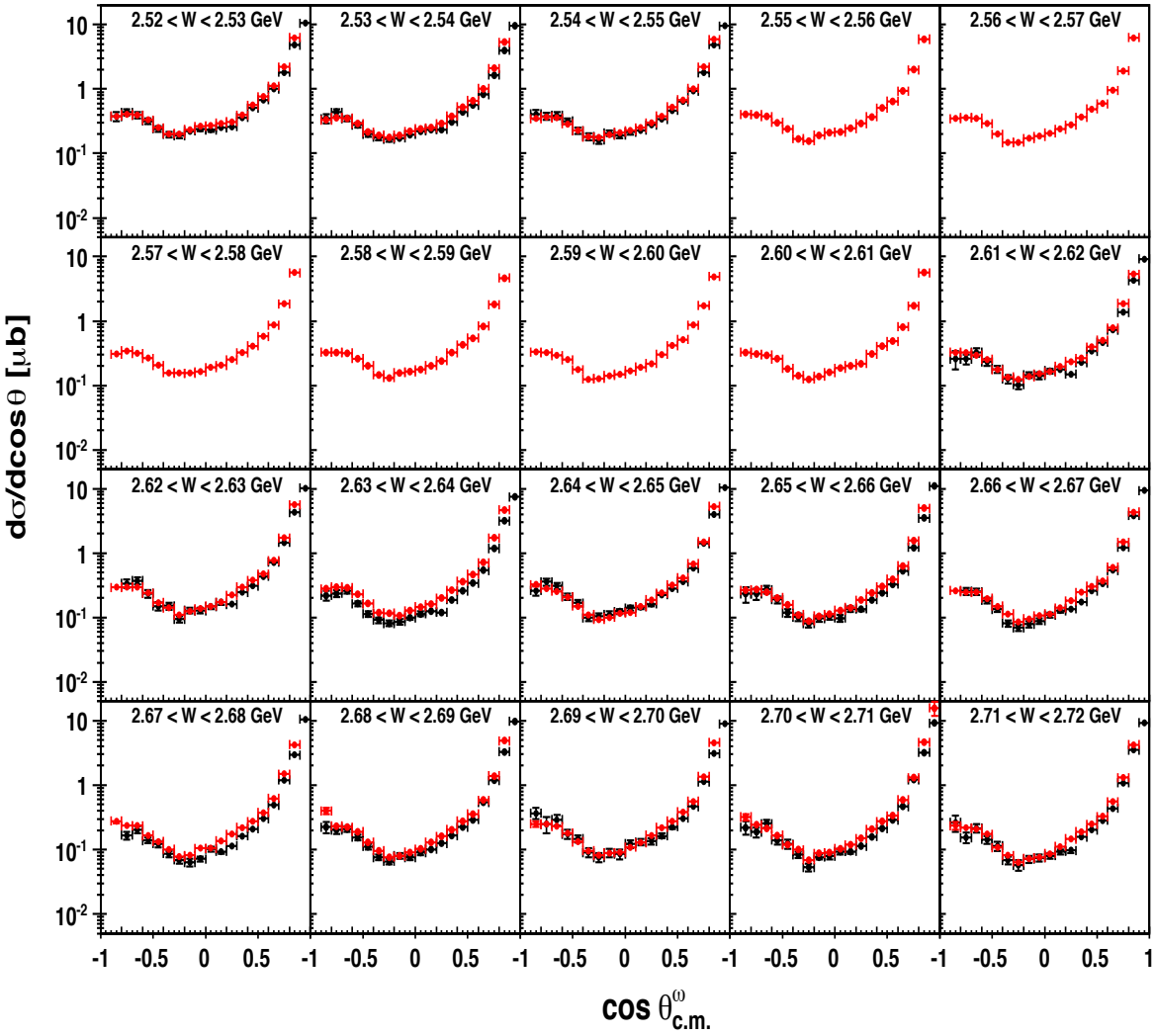


Figure 68: *The differential cross sections in the reaction $\gamma p \to p\omega$ for the center-of-mass energy range $2.52 < W < 2.72$ GeV from g12 (black data points) in comparison with the previous CLAS measurements from g11a [8] (red points). The given uncertainties for both data sets comprise the statistical uncertainties and the Q-factor uncertainties added in quadrature. Please note that the g12 data suffer from broken tagger paddles in the energy range $2.55 < W < 2.61$ GeV (around $E_\gamma \approx 3.0$ GeV).*

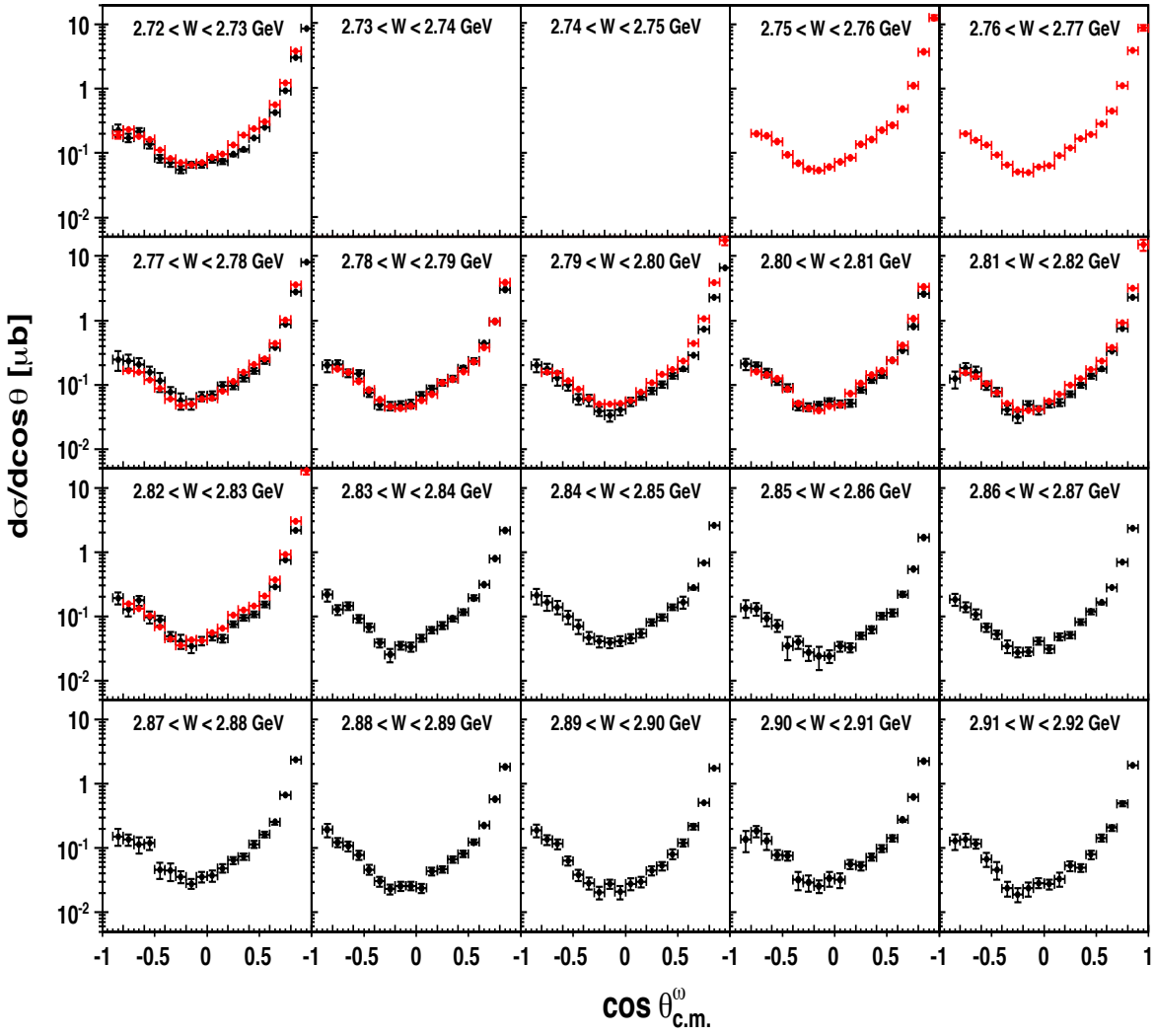


Figure 69: *The differential cross sections in the reaction $\gamma p \to p\omega$ for the center-of-mass energy range $2.72 < W < 2.92$ GeV from g12 (black data points) in comparison with the previous CLAS measurements from g11a [8] (red points). The given uncertainties for both data sets comprise the statistical uncertainties and the Q-factor uncertainties added in quadrature. Please note again that the g12 data suffer from broken tagger paddles in the energy range $2.73 < W < 2.77$ GeV (around $E_\gamma \approx 3.6$ GeV).*

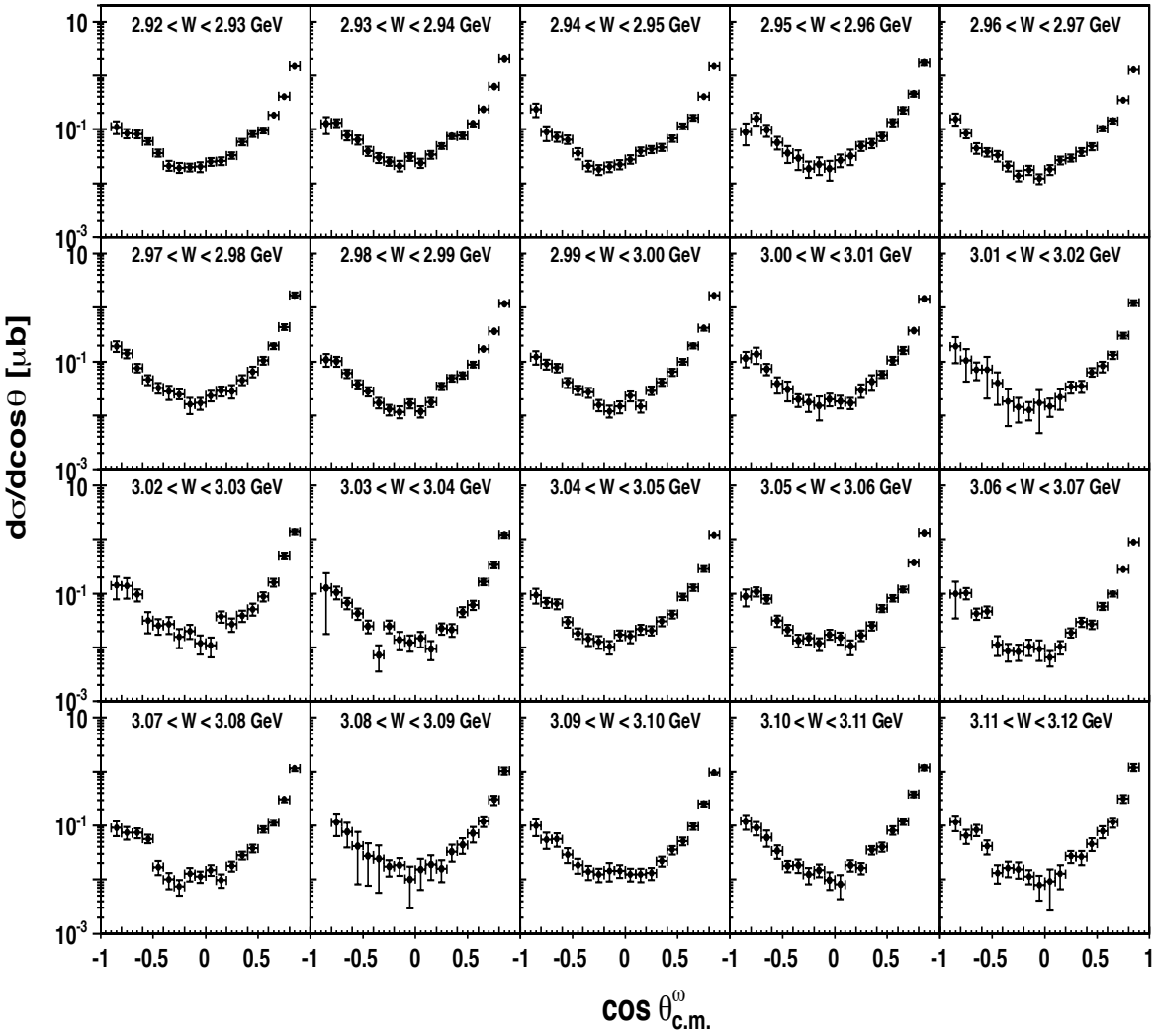


Figure 70: *The differential cross sections in the reaction $\gamma p \to p\omega$ for the center-of-mass energy range $2.92 < W < 3.12$ GeV from g12 (black data points). The given uncertainties comprise the statistical uncertainties and the Q-factor uncertainties added in quadrature. These data represent first-time measurements.*

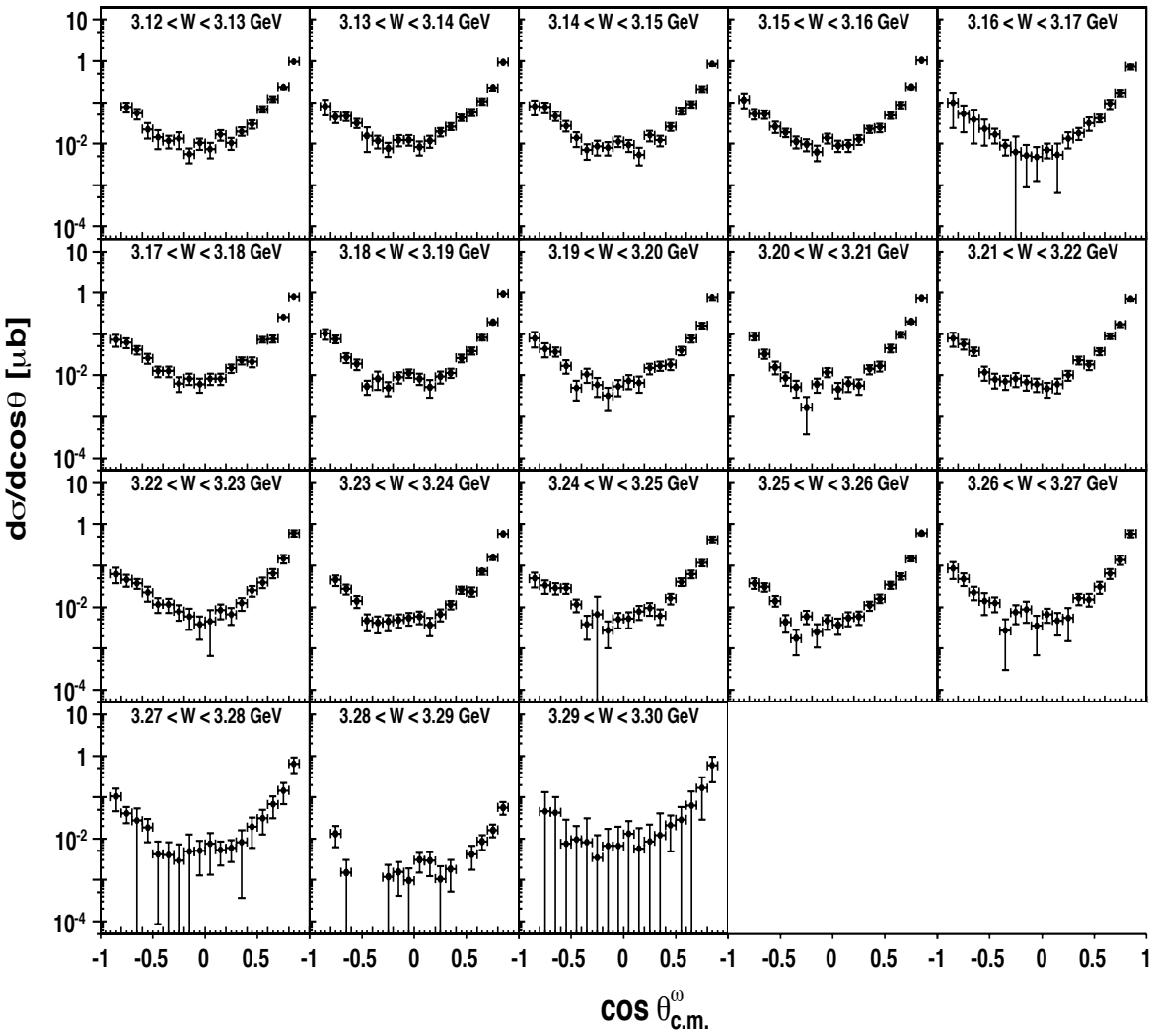


Figure 71: *The differential cross sections in the reaction $\gamma p \to p\omega$ for the center-of-mass energy range $3.12 < W < 3.30$ GeV from g12 (black data points). The given uncertainties comprise the statistical uncertainties and the Q-factor uncertainties added in quadrature. These data represent first-time measurements.*

### 6.1.2 Spin-Density Matrix Elements in $\gamma p \to p\omega$

Figure 72-86 show the spin-density matrix elements (SDMEs) – $\rho^0_{00}$, Re($\rho^0_{10}$), and $\rho^0_{1-1}$ – for the reaction $\gamma p \to p\omega$, covering the center-of-mass energy range $1.92 < W < 3.12$ GeV. The CLAS g12 results are shown as black data points. Also shown in the figure are the previous results from the CLAS-g11a experiment (red data points) [8]. The shown uncertainties for both data sets are only statistical.

The results are presented in 10-MeV-wide $W$ bins for $1.92 < W < 2.72$ GeV, and in 20-MeV-wide energy bins for $2.72 < W < 3.12$ GeV. Please note the broken tagger modules in the g12 data at $2.73 < W < 2.75$ GeV and $2.55 < W < 2.61$ GeV. Our data are in good agreement with the previous CLAS g11a results for the element $Re(\rho^0_{10})$ results, while the agreement for the elements $\rho^0_{00}$ and $\rho^0_{1-1}$ is acceptable. Some discrepancies are observed in the forward direction at low energies. The high-energy results ($E_\gamma > 4.0$) GeV are first-time measurements.

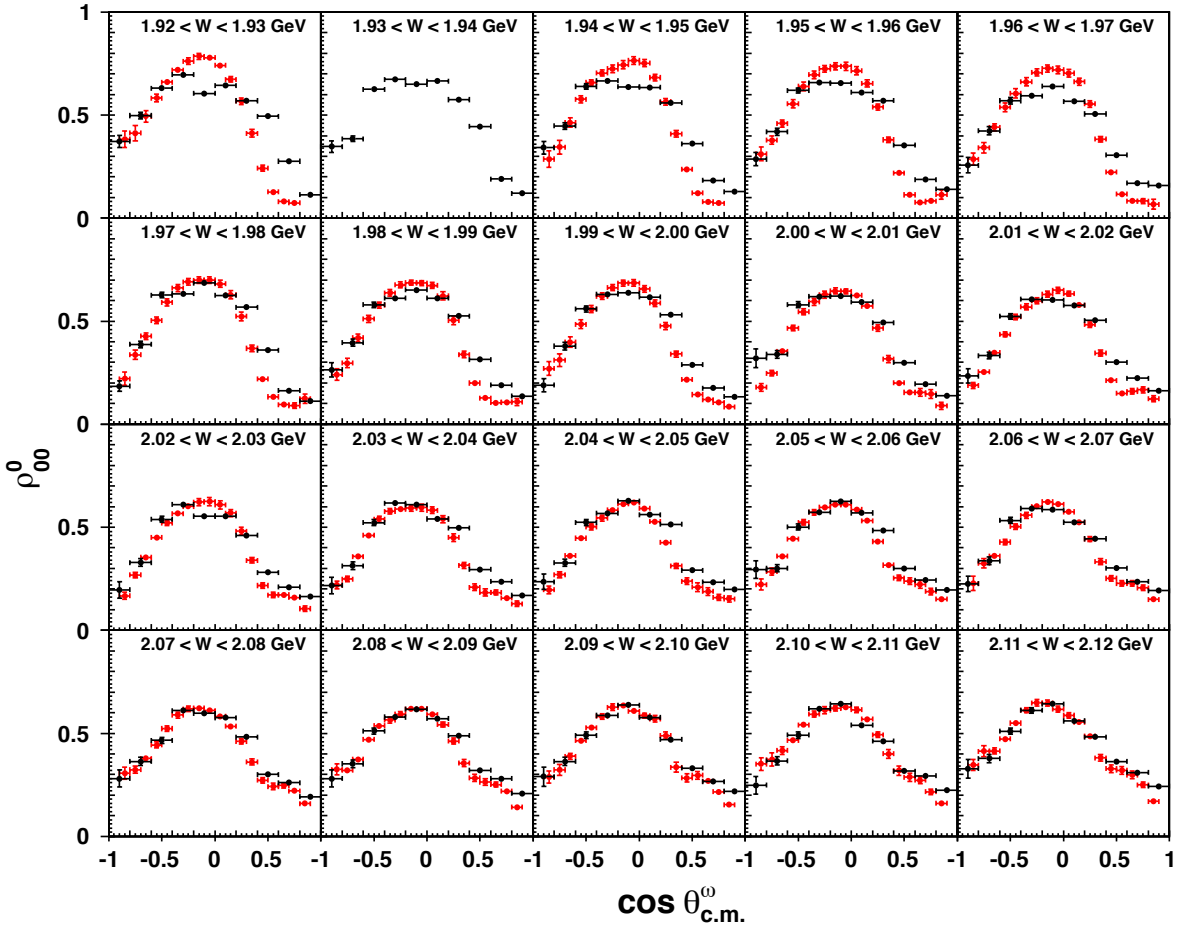


Figure 72: *The Spin-density matrix element $\rho^0_{00}$ in the reaction $\gamma p \to p\omega$ for $1.92 < W < 2.12$ GeV from g12 (black data points) in comparison with the previous CLAS measurements from g11a (red data points). The shown uncertainties for both data sets are statistical only.*

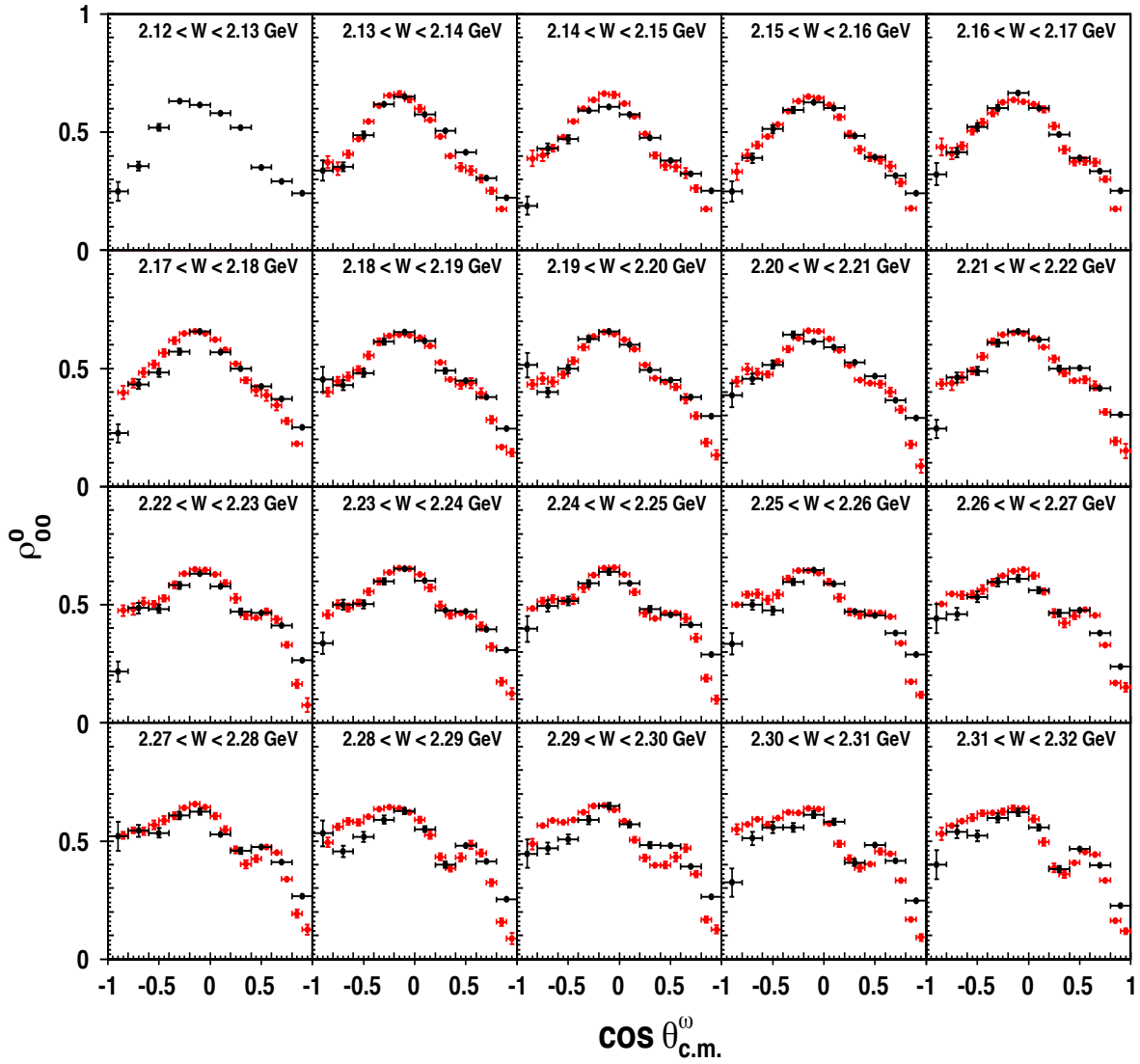


Figure 73: *The Spin-density matrix element* $\rho^0_{00}$ *in the reaction* $\gamma p \to p\,\omega$ *for* $2.12 < W < 2.32$ *GeV from g12 (black data points) in comparison with the previous CLAS measurements from g11a (red data points). The shown uncertainties for both data sets are statistical only.*

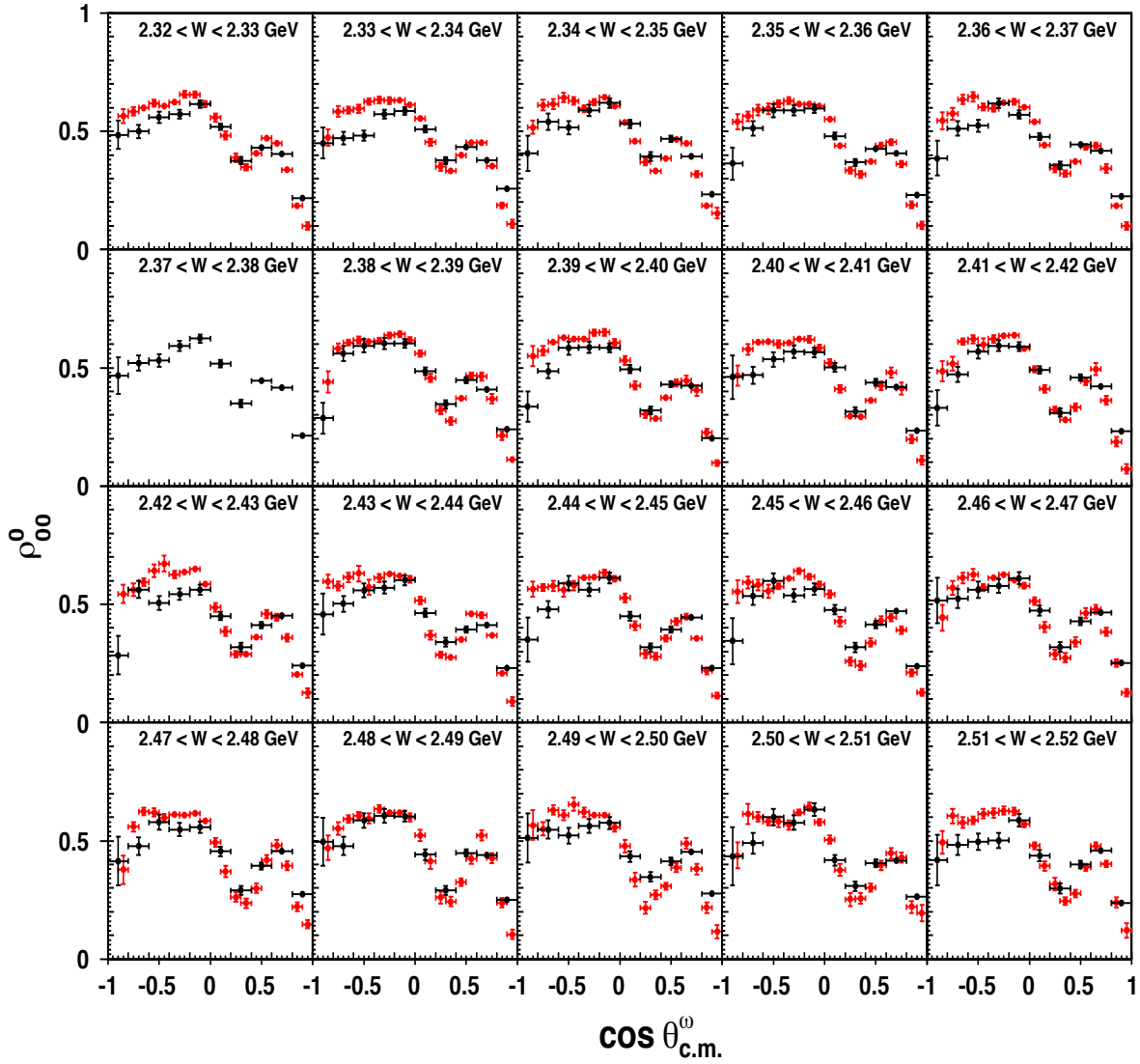


Figure 74: *The Spin-density matrix element* $\rho^0_{00}$ *in the reaction* $\gamma p \to p\,\omega$ *for* $2.32 < W < 2.52$ *GeV from g12 (black data points) in comparison with the previous CLAS measurements from g11a (red data points). The shown uncertainties for both data sets are statistical only.*

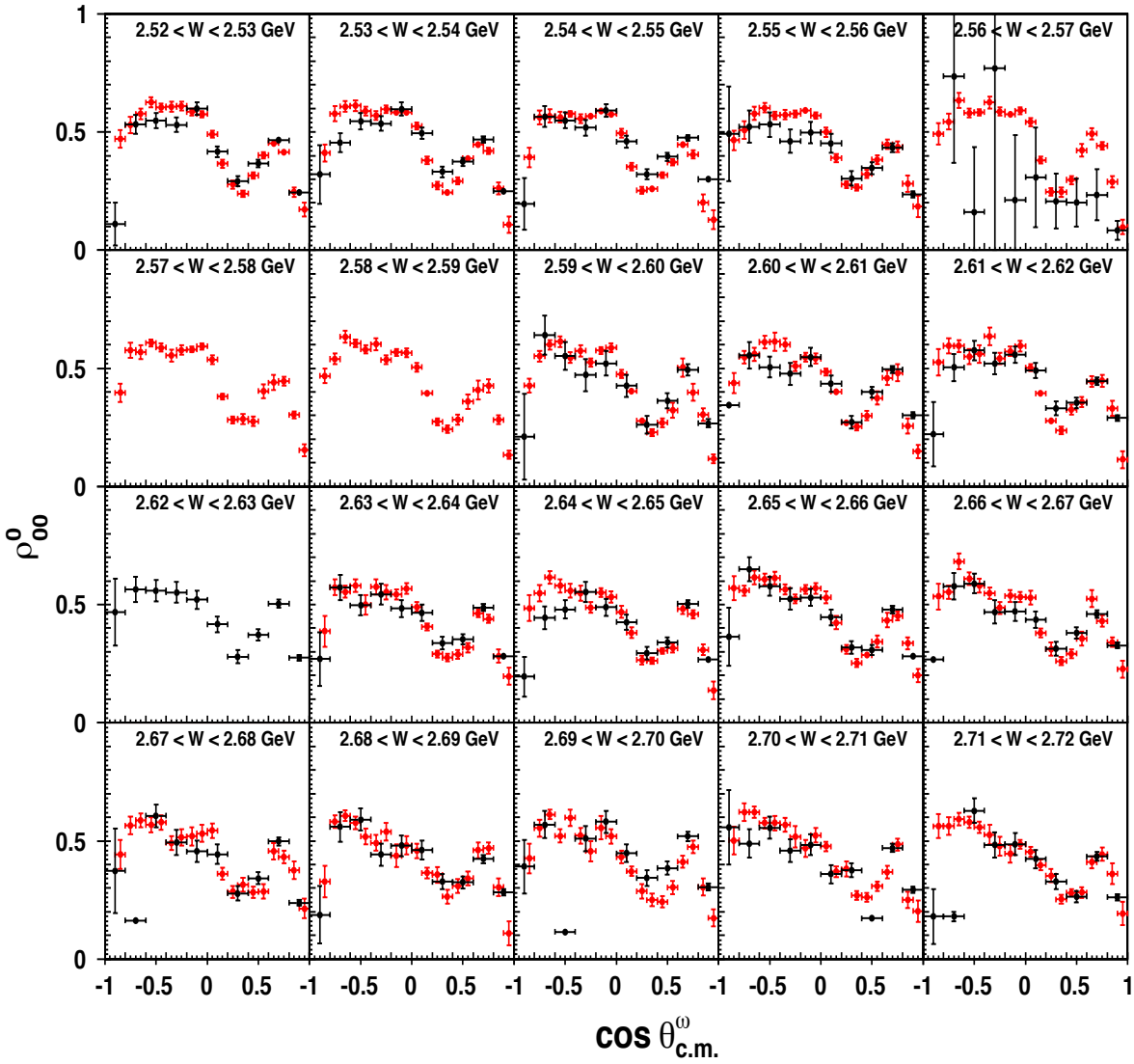


Figure 75: *The Spin-density matrix element $\rho^0_{00}$ in the reaction $\gamma p \to p\omega$ for $2.52 < W < 2.72$ GeV from g12 (black data points) in comparison with the previous CLAS measurements from g11a (red data points). Please note that the g12 data suffer from broken tagger paddles that affected the energy range $2.56 < W < 2.59$ GeV (around $E_\gamma \approx 3.0$ GeV). The shown uncertainties for both data sets are statistical only.*

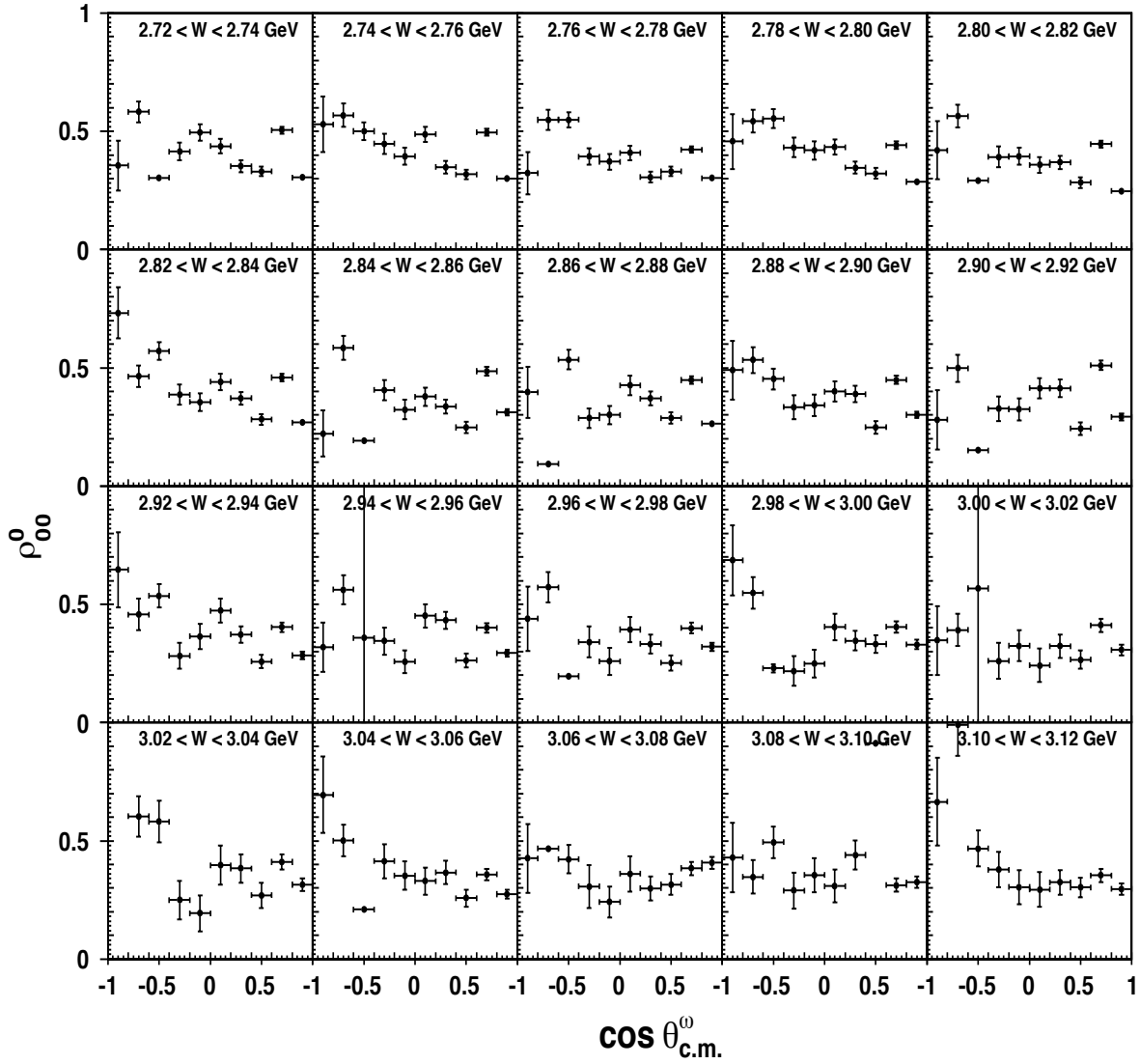


Figure 76: *The Spin-density matrix element $\rho^0_{00}$ in the reaction $\gamma p \to p\,\omega$ for $2.72 < W < 3.12$ GeV from g12 (black data points) in comparison with the previous CLAS measurements from g11a (red data points). The shown uncertainties for both data sets are statistical only.*

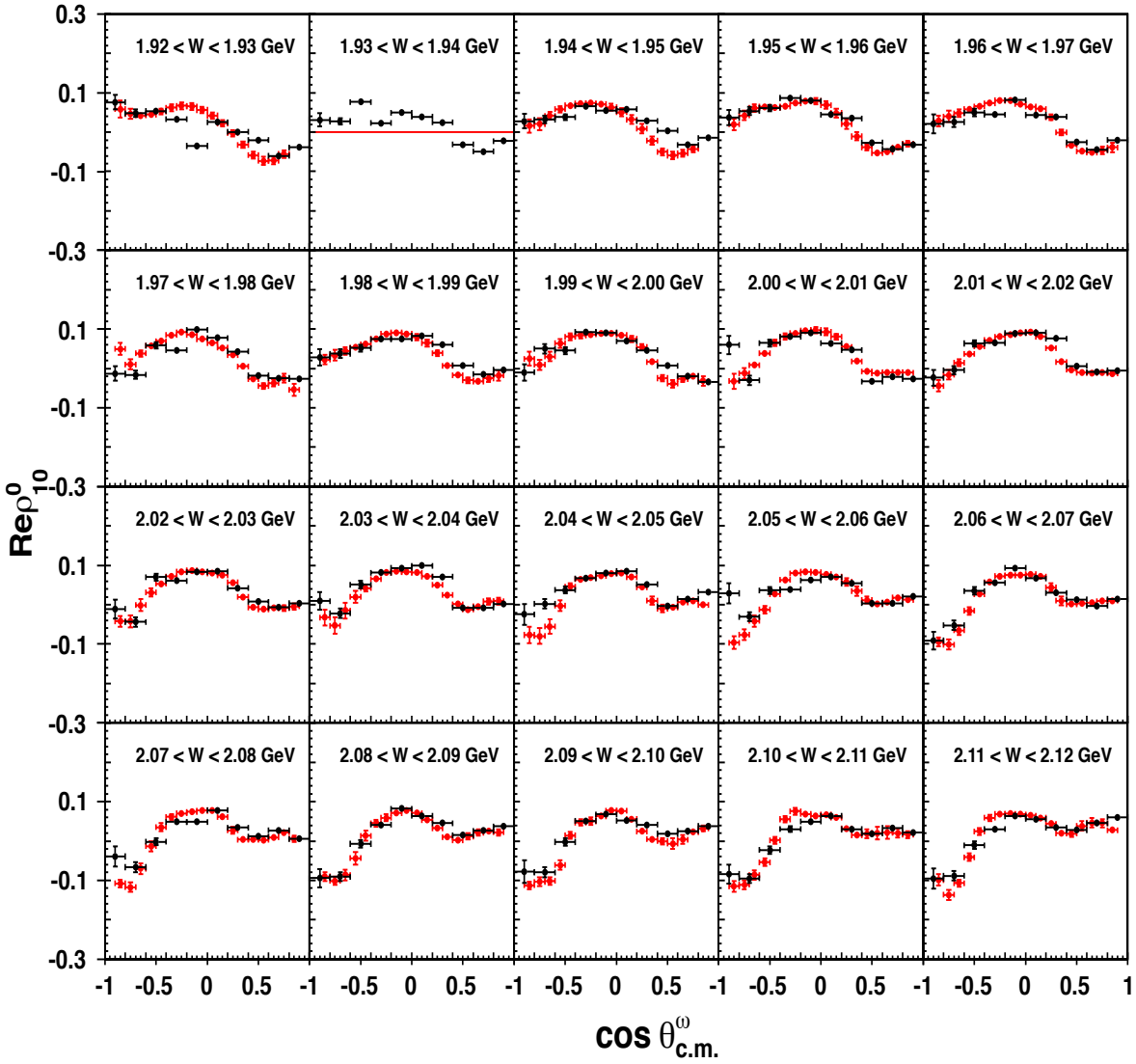


Figure 77: *The Spin-density matrix element* $Re(\rho^0_{10})$ *in* $\gamma p \to p\omega$ *for* $1.92 < W < 2.12$ *GeV from g12 (black data points) in comparison with the previous CLAS measurements from g11a (red data points). The shown uncertainties for both data sets are statistical only.*

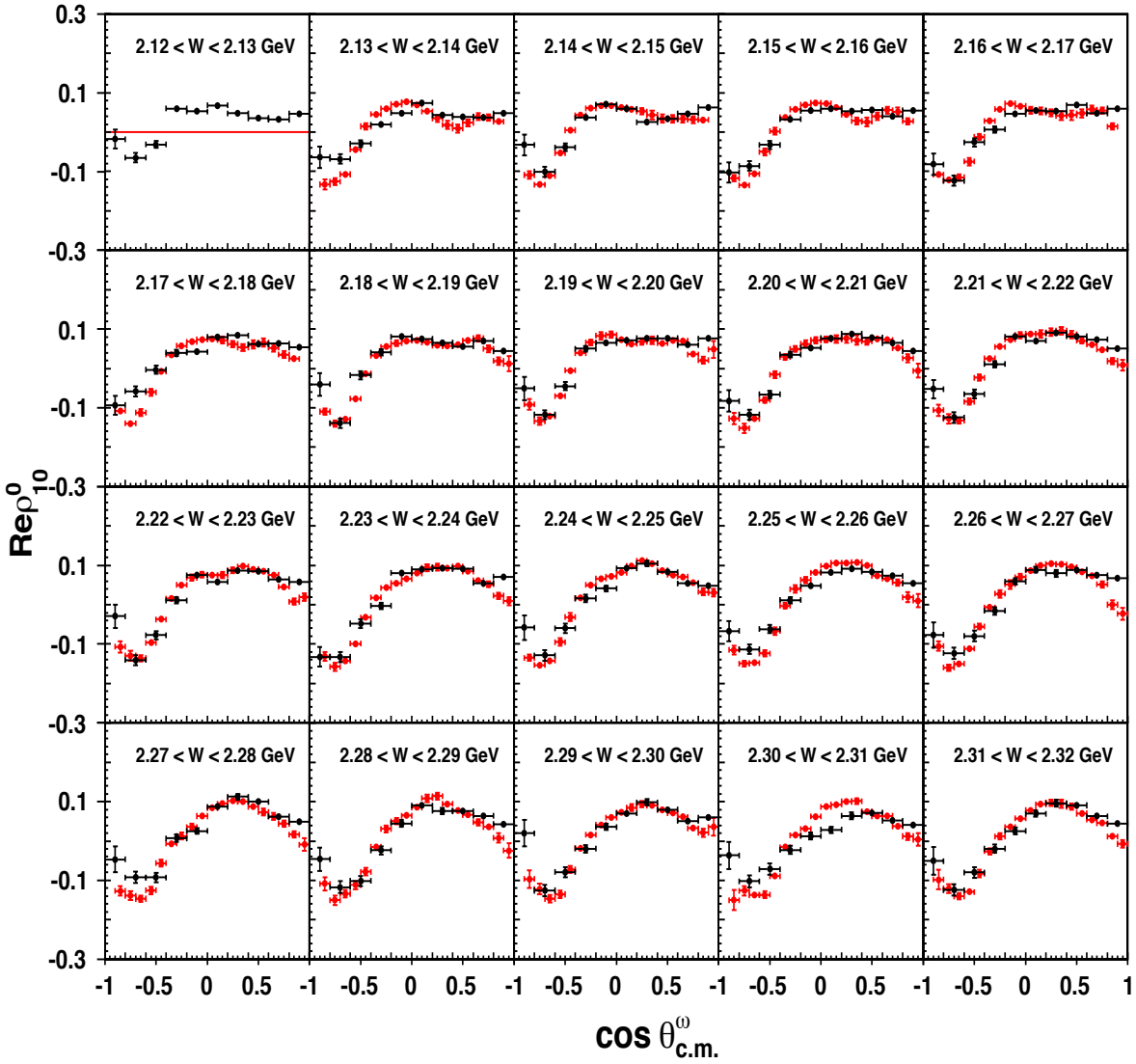


Figure 78: *The Spin-density matrix element* $Re(\rho^0_{10})$ *in* $\gamma p \to p\omega$ *for* $2.12 < W < 2.32$ *GeV from g12 (black data points) in comparison with the previous CLAS measurements from g11a (red data points). The shown uncertainties for both data sets are statistical only.*

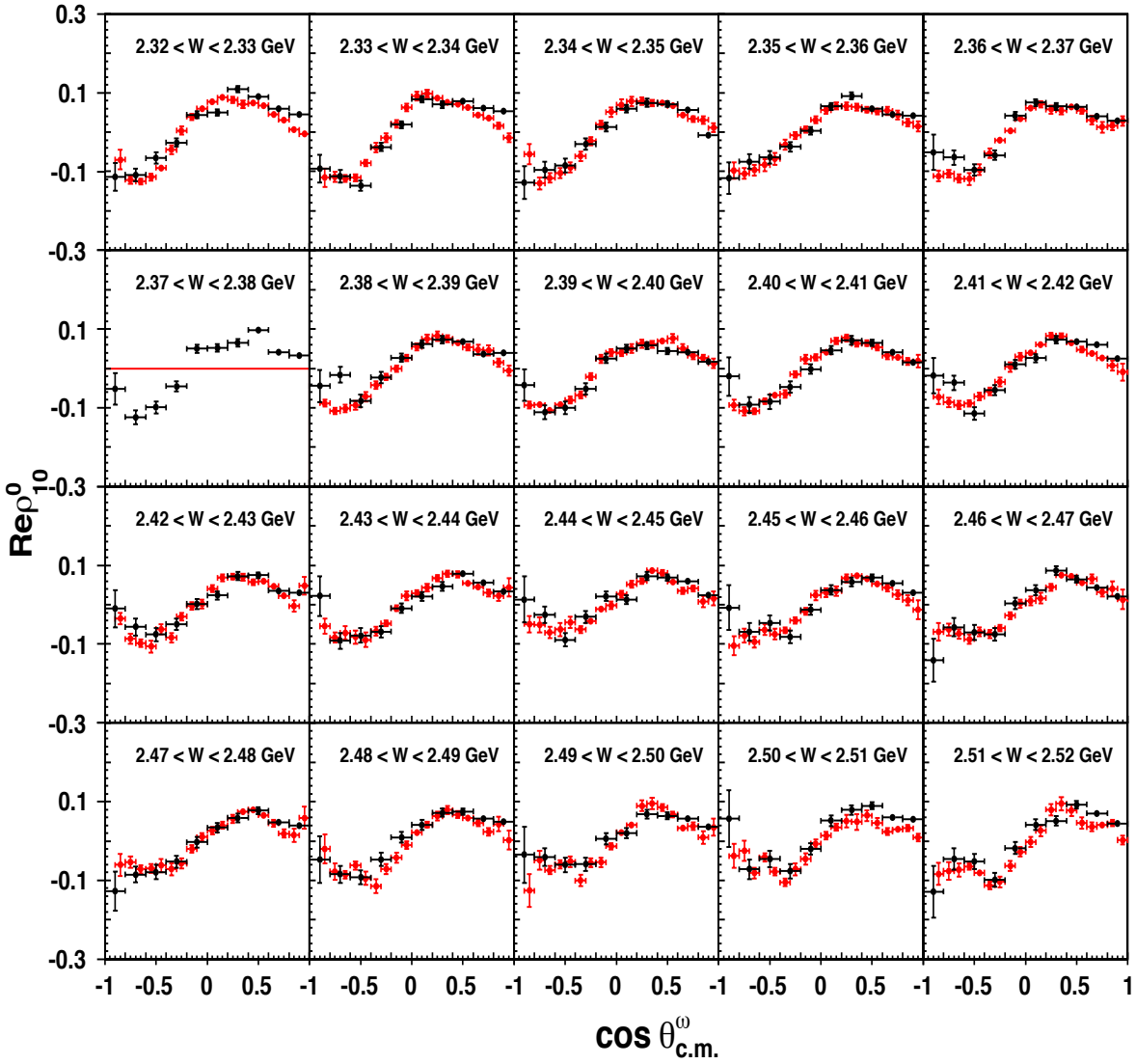


Figure 79: *The Spin-density matrix element* $Re(\rho^0_{10})$ *in* $\gamma p \to p\omega$ *for* $2.32 < W < 2.52$ *GeV from g12 (black data points) in comparison with the previous CLAS measurements from g11a (red data points). The shown uncertainties for both data sets are statistical only.*

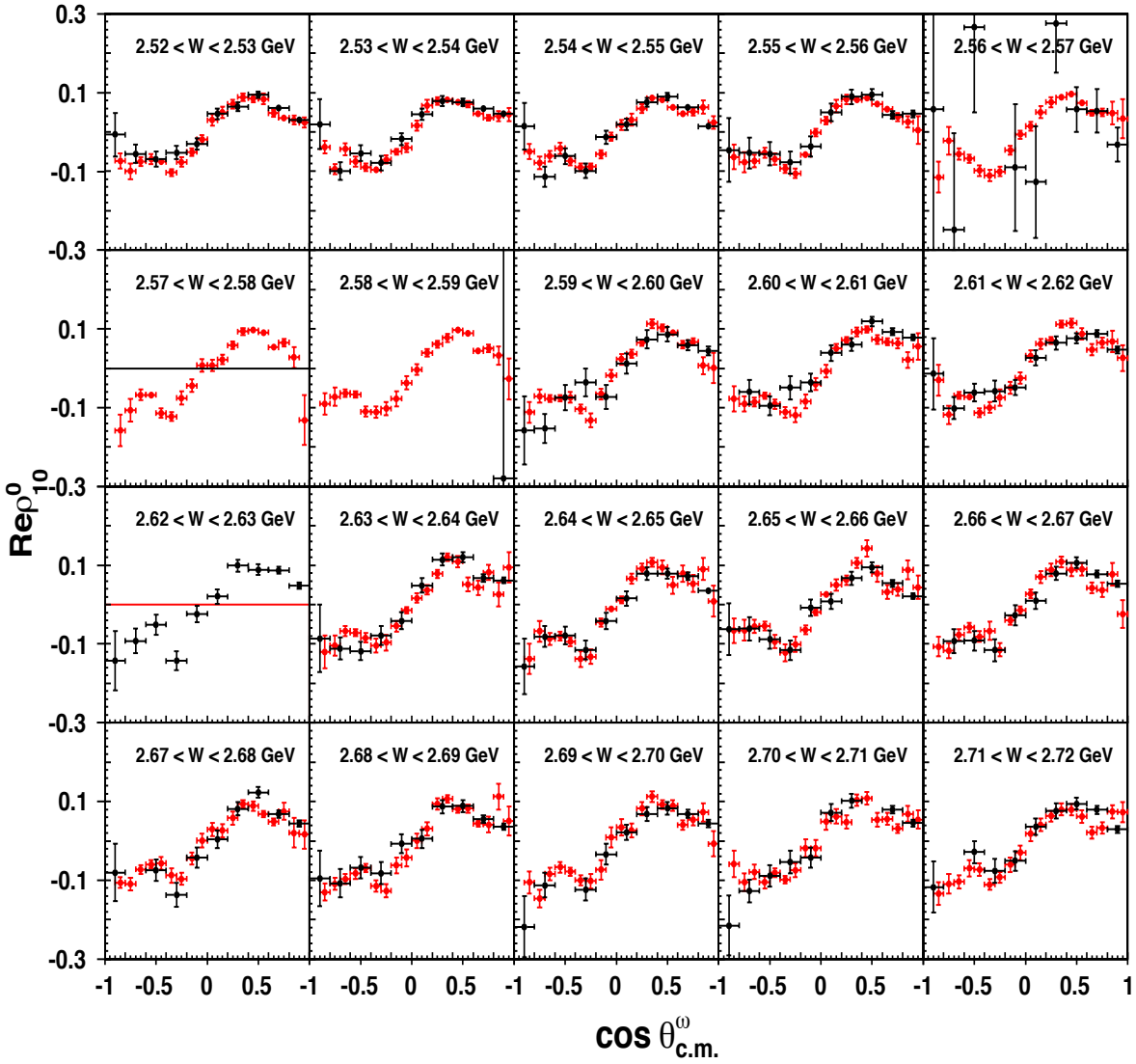


Figure 80: *The Spin-density matrix element* $Re(\rho^0_{10})$ *in* $\gamma p \to p\omega$ *for* $2.52 < W < 2.72$ *GeV from g12 (black data points) in comparison with the previous CLAS measurements from g11a (red data points). Please note that the g12 data suffer from broken tagger paddles that affected the energy range* $2.56 < W < 2.59$ *GeV (around* $E_\gamma \approx 3.0$ *GeV). The shown uncertainties for both data sets are statistical only.*

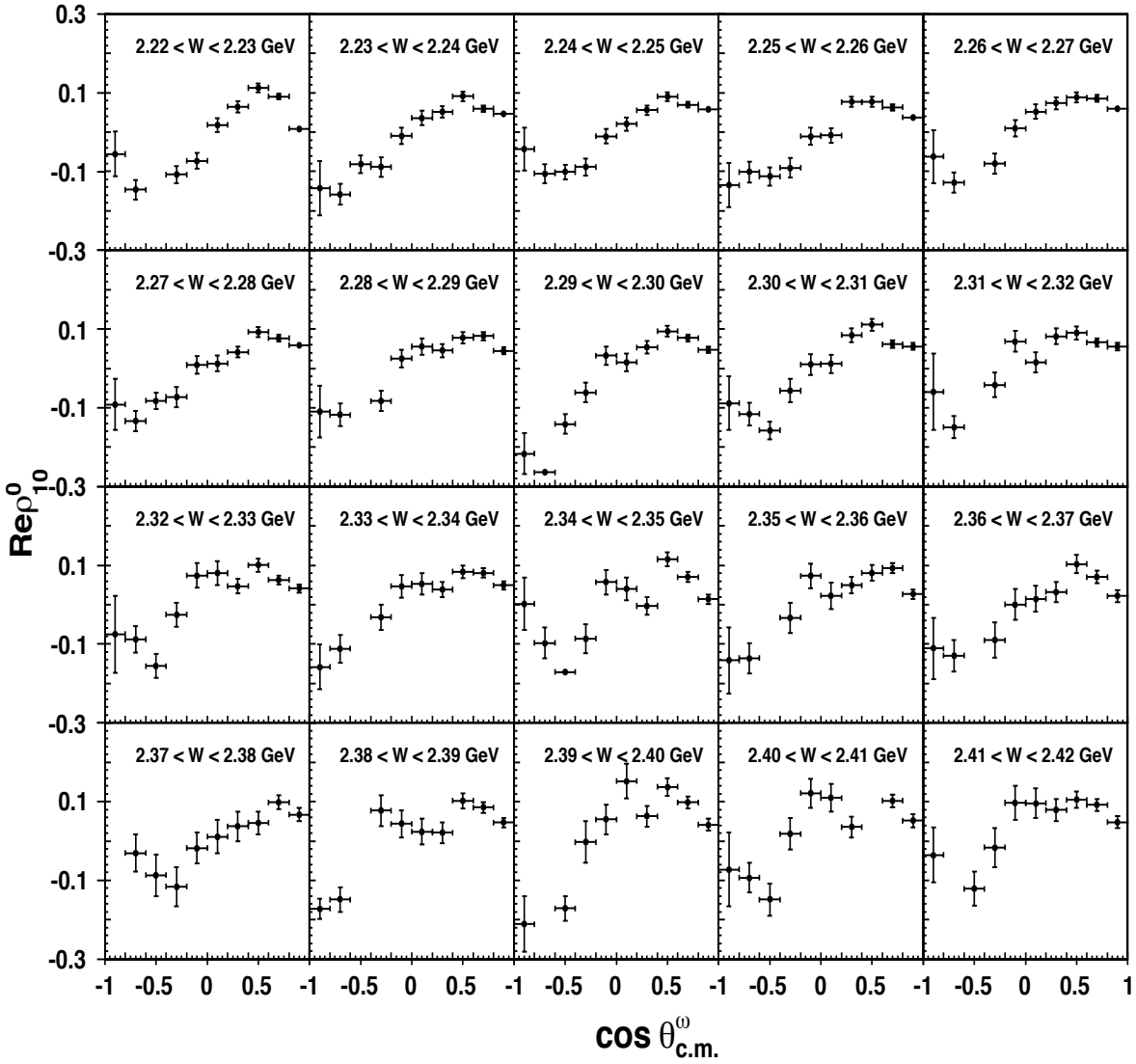


Figure 81: *The Spin-density matrix element* $Re(\rho^0_{10})$ *in* $\gamma p \to p\omega$ *for* $2.72 < W < 3.12$ *GeV from g12 (black data points) in comparison with the previous CLAS measurements from g11a (red data points). The shown uncertainties for both data sets are statistical only.*

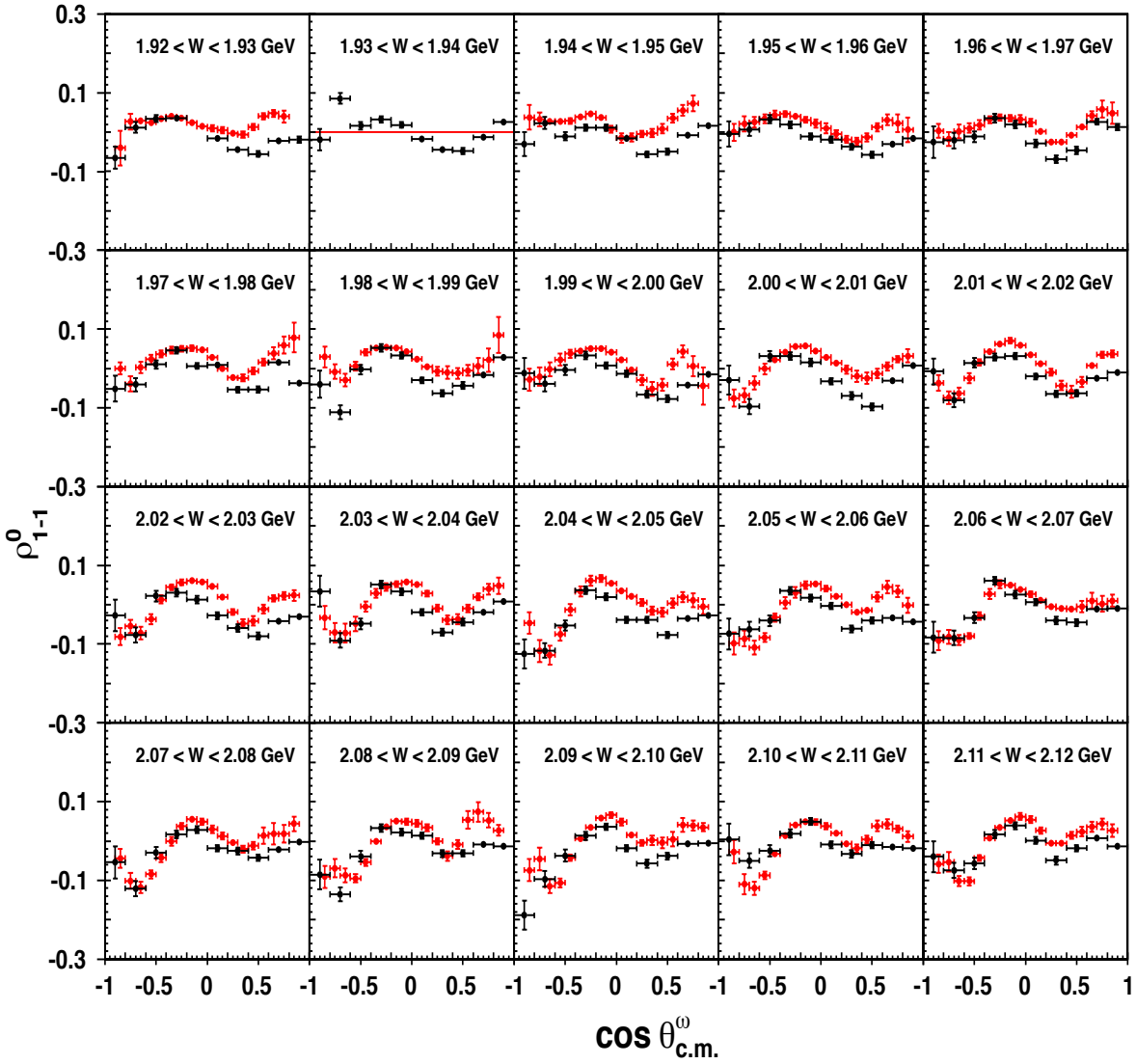


Figure 82: *The Spin-density matrix element $\rho^0_{1-1}$ in the reaction $\gamma p \to p\,\omega$ for $1.92 < W < 2.12$ GeV from g12 (black data points) in comparison with the previous CLAS measurements from g11a (red data points). The shown uncertainties for both data sets are statistical only.*

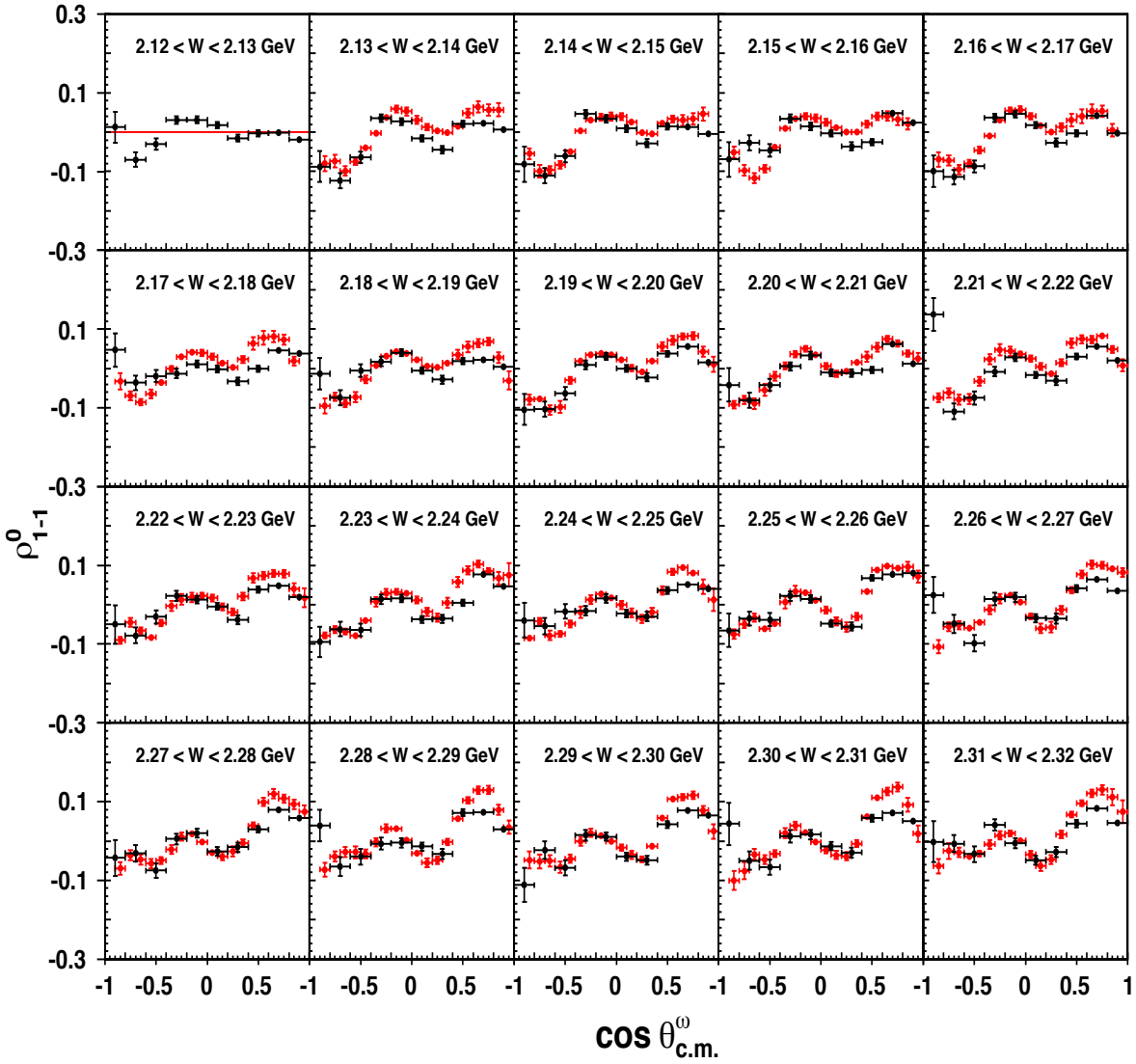


Figure 83: *The Spin-density matrix element $\rho^0_{1-1}$ in the reaction $\gamma p \to p\,\omega$ for $2.12 < W < 2.32$ GeV from g12 (black data points) in comparison with the previous CLAS measurements from g11a (red data points). The shown uncertainties for both data sets are statistical only.*

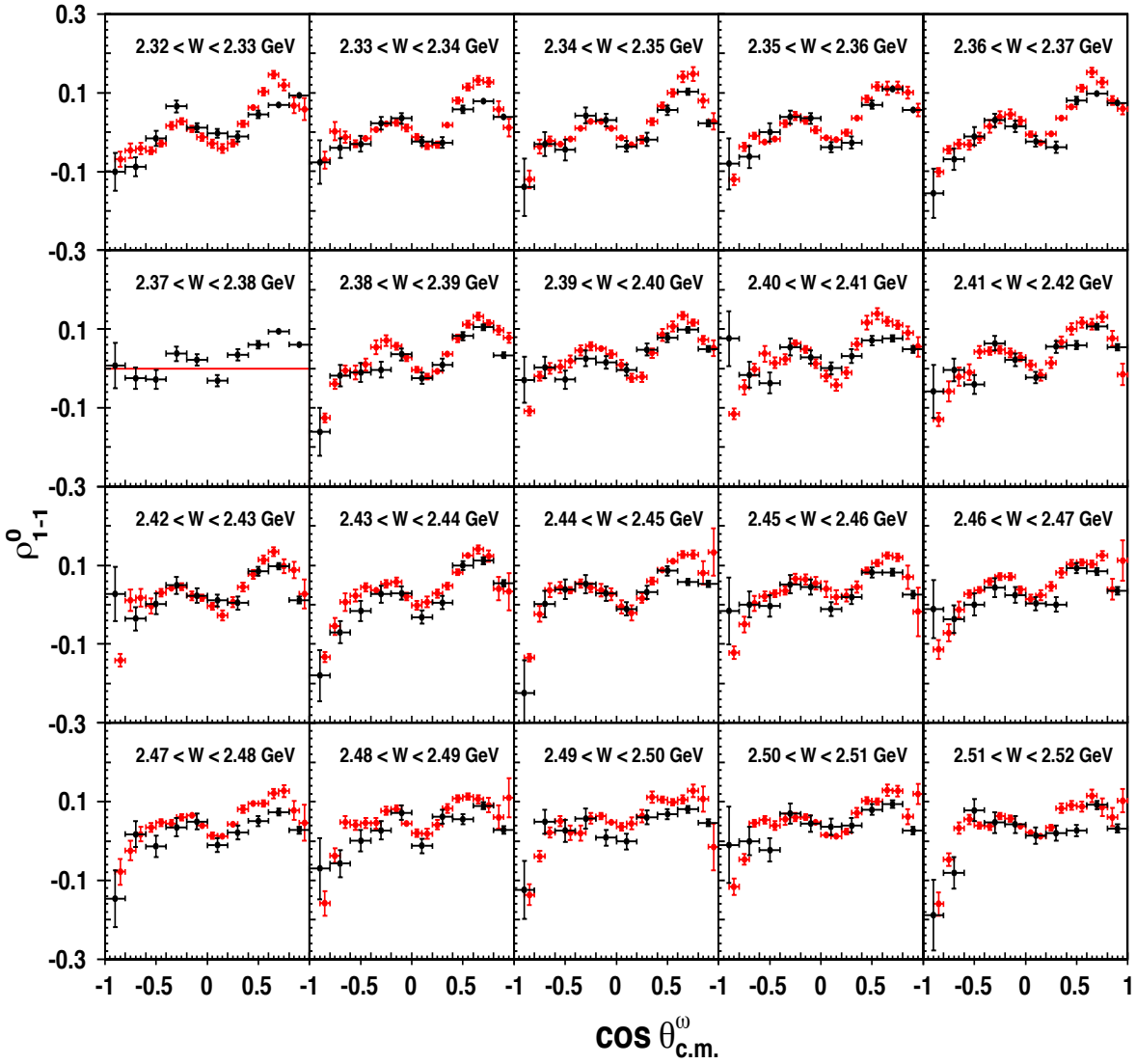


Figure 84: *The Spin-density matrix element* $\rho^0_{1-1}$ *in the reaction* $\gamma p \to p\,\omega$ *for* $2.32 < W < 2.52$ *GeV from g12 (black data points) in comparison with the previous CLAS measurements from g11a (red data points). The shown uncertainties for both data sets are statistical only.*

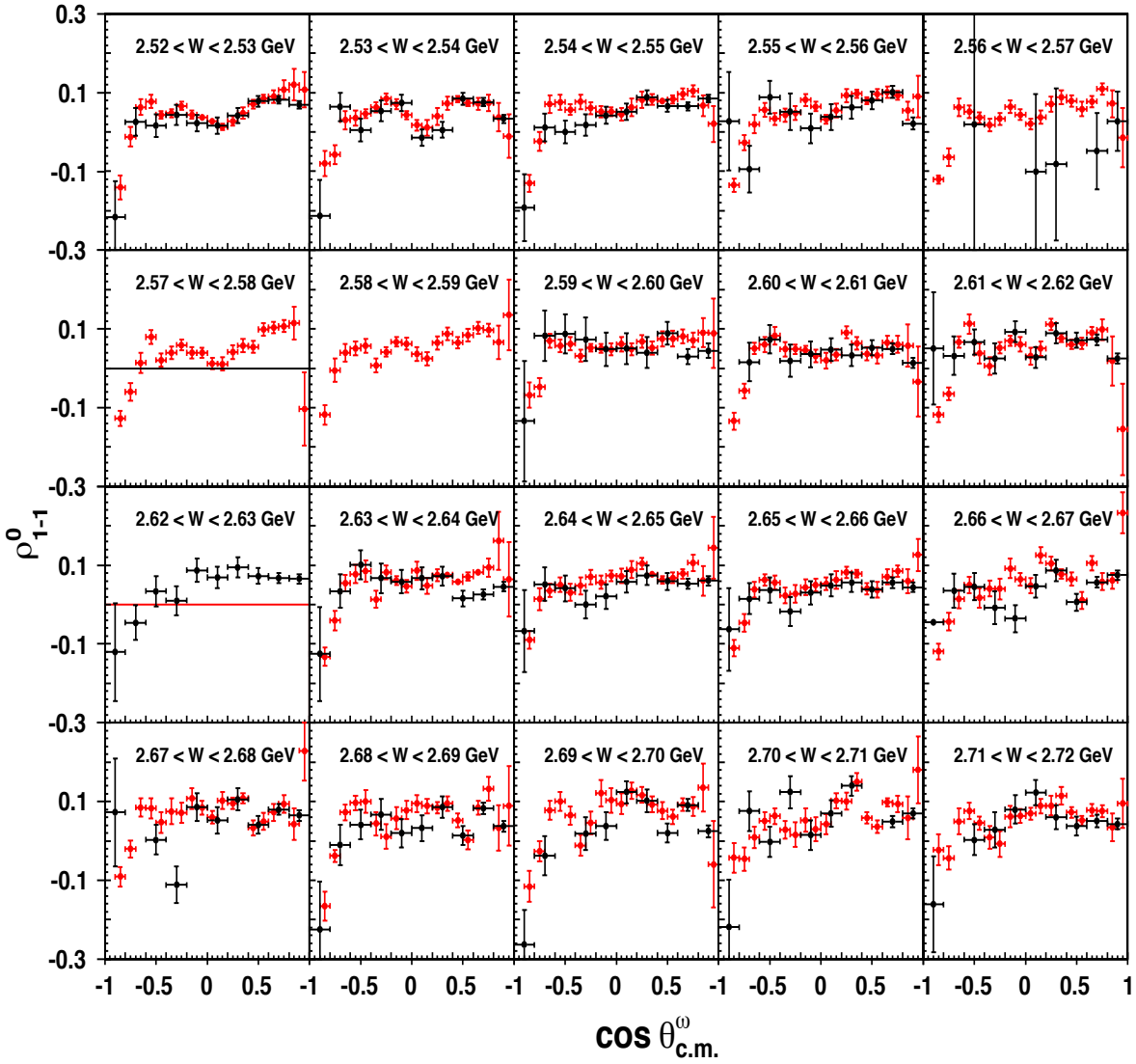


Figure 85: *The Spin-density matrix element* $\rho^0_{1-1}$ *in the reaction* $\gamma p \to p\,\omega$ *for* $2.52 < W < 2.72$ *GeV from g12 (black data points) in comparison with the previous CLAS measurements from g11a (red data points). Please note that the g12 data suffer from broken tagger paddles that affected the energy range* $2.56 < W < 2.59$ *GeV (around* $E_\gamma \approx 3.0$ *GeV). The shown uncertainties for both data sets are statistical only.*

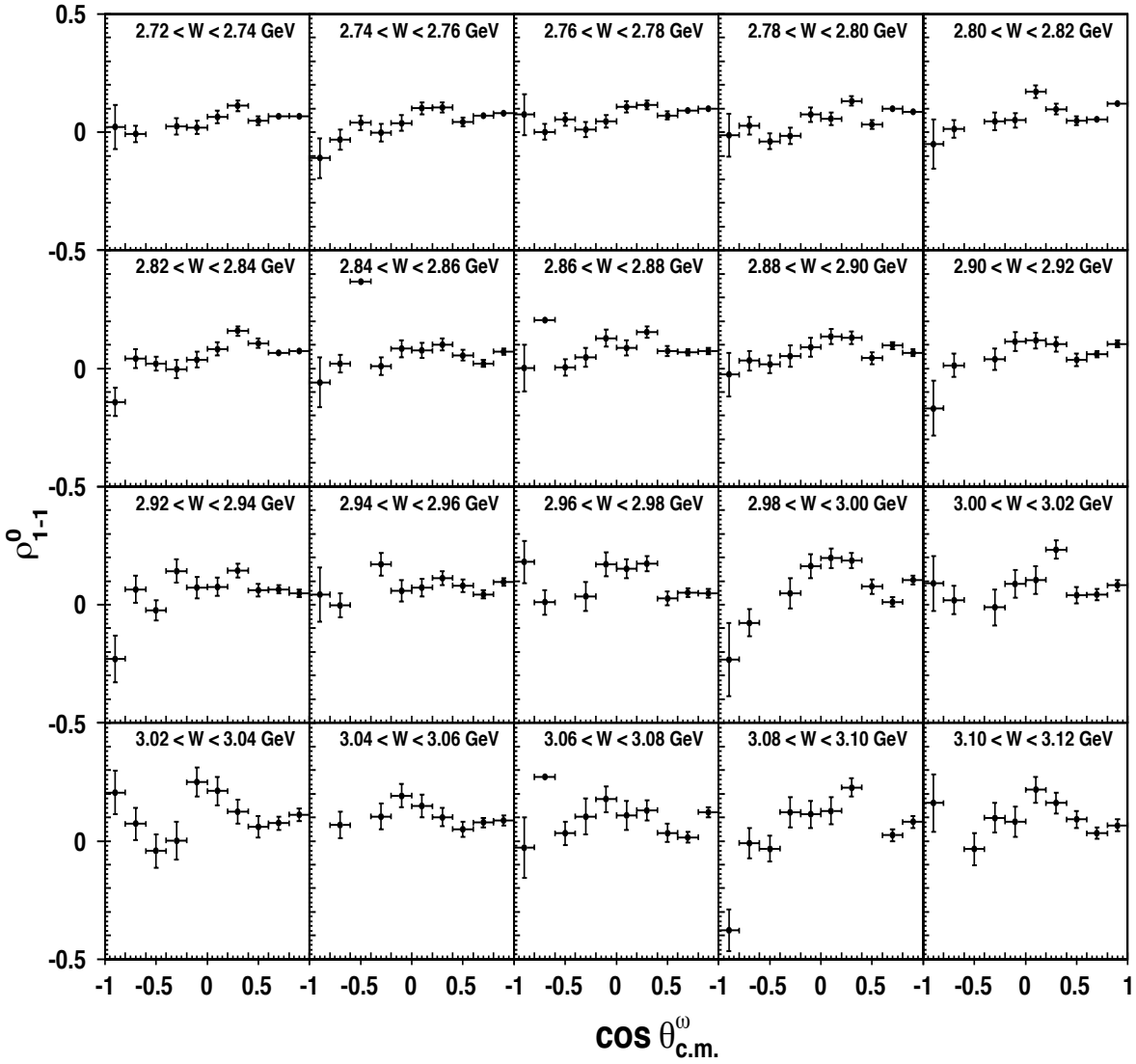


Figure 86: *The Spin-density matrix element $\rho^0_{1-1}$ in the reaction $\gamma p \to p\,\omega$ for $2.72 < W < 3.12$ GeV from g12 (black data points) in comparison with the previous CLAS measurements from g11a (red data points). The shown uncertainties for both data sets are statistical only.*

## 6.2 Results for the $\gamma p \to p\,\eta$ Reaction

The following section presents and discusses our final results in $\eta$ photoproduction. We compare with previous CLAS results whenever these are available. Similar to the $\omega$ final state, our results extend the available energy range to $W = 3.12$ GeV. The data at $E_\gamma > 4.0$ GeV are first-time measurements and will bridge the gap between these lower-energy CLAS data and data from the 12-GeV era. In addition to the efforts on extracting contributions from baryon resonances, we are working with the Joint Physics Analysis Center (JPAC) at JLab on understanding the photoproduction of $\eta$ mesons beyond the baryon resonance regime.

### 6.2.1 Differential Cross Sections in $\gamma p \to p\,\eta$

Figures 88-90 show the differential cross sections of the reaction $\gamma p \to p\,\eta$, covering the center-of-mass energy range $1.77 < W < 3.12$ GeV. The CLAS-g12 results are shown in black. Also shown in the figures (if available) are the previous resuts from CLAS-g11a experiment (red points) [9]. The uncertainties for both data sets (CLAS g11a and g12) include the $Q$-factor uncertainties and the statistical uncertainties added in quadrature. We simply followed the example of g11a to properly compare our results.

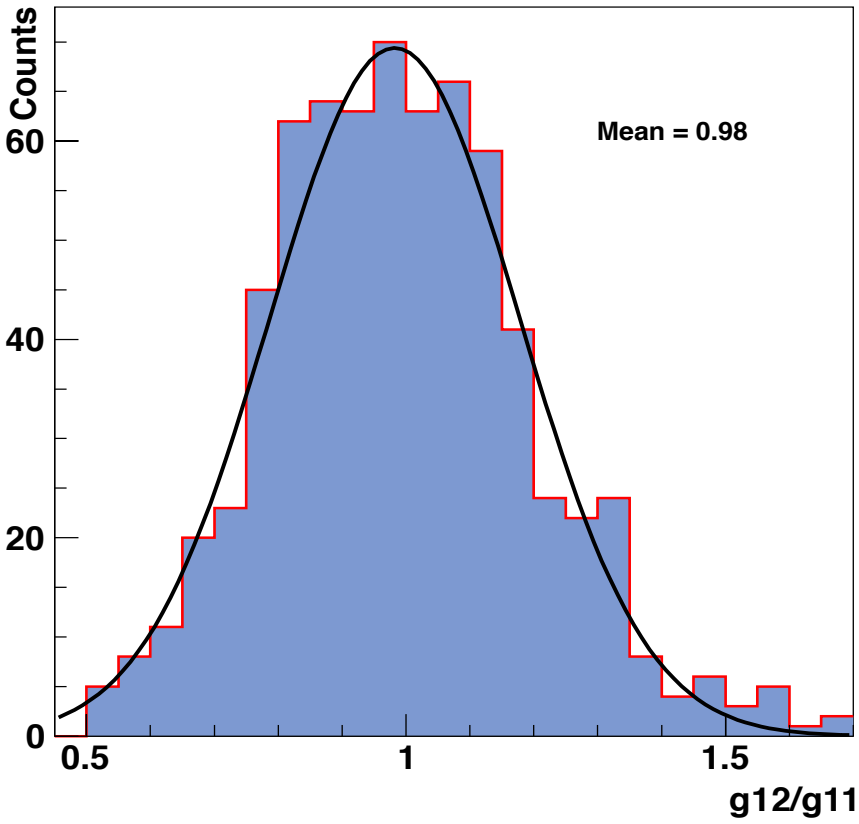


Figure 87: *The g12/g11a ratio distribution of the $\gamma p \to p\,\eta$ cross sections results.*

Our results are presented in 20-MeV-wide center-of-mass energy bins for $1.77 < W < 2.36$ GeV and in 40-MeV-wide energy bins for $2.36 < W < 3.12$ GeV. Please note that some g12 energy bins are missing due to tagger inefficiencies (broken modules), e. g. $2.56 < W < 2.60$ GeV. Similar to the discussion on the normalization issue for the $\omega$ channel in the previous section, we have to present our $\eta$ data also in 20-MeV-wide center-of-mass energy bins owing to the poor g12 tagger resolution below 2 GeV. This is somewhat disappointing since the available CLAS-g12 statistics would be sufficient for a finer binning. In the comparison, we had to combine adjacent g11a energy bins, which may lead to very small discrepancies with our data.

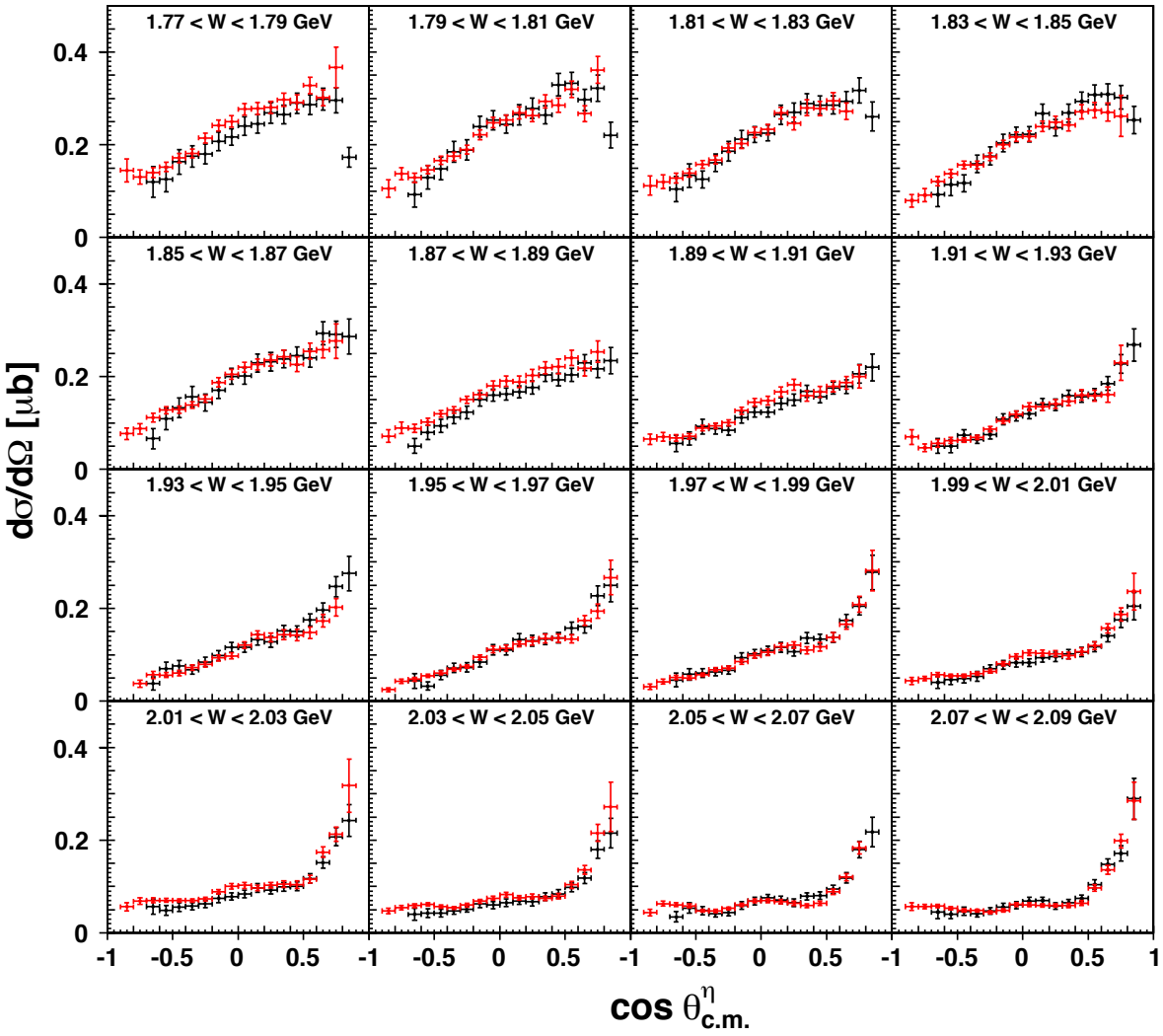


Figure 88: *The differential cross sections in the reaction $\gamma p \to p\eta$ for the center-of-mass energy range $1.77 < W < 2.09$ GeV from CLAS g12 (black data points) in comparison with the previous CLAS measurements from g11a (red point). The given uncertainties for both data sets comprise the statistical uncertainties and the Q-factor uncertainties added in quadrature.*

In general, the agreement with the previous CLAS-g11a measurements is very good. Some minor discrepancies in selected energy bins at very low energies are observed (Fig. 88), but toward higher energies, we consider the agreement very good. Note the small gap in the transition from Fig. 88 to Fig. 89, the $W$ bin $2.09 < W < 2.10$ GeV is missing. The reason is not a lack of g12 data but the comparison with g11a. The g12/g11a ratio distribution of the $\eta$ cross section results is shown in Figure 87. A Gaussian fit to this distribution yields a mean value of about 0.98, which is consistent with the value for the $\omega$ channel. The slightly below-one mean values for the two reactions are not necessarily surprising given the uncertainty on the g11a live-time correction (see also the discussion on the CLAS-g11a normalization issue in Section 6.1.1).

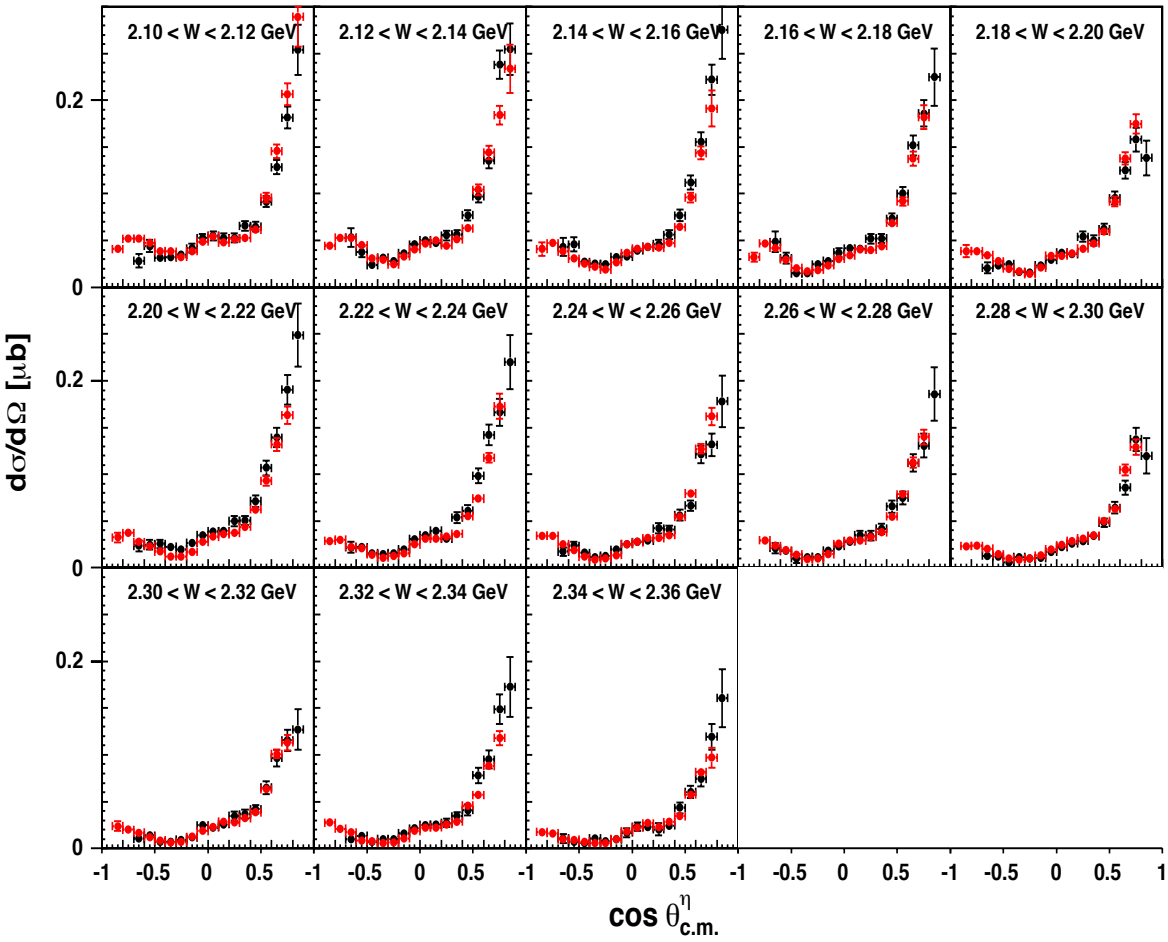


Figure 89: *The differential cross sections in the reaction $\gamma p \to p\eta$ for the center-of-mass energy range $2.10 < W < 2.36$ GeV from g12 (black data points) in comparison with the previous CLAS measurements from g11a (red point). The given uncertainties for both data sets comprise the statistical uncertainties and the Q-factor uncertainties added in quadrature.*

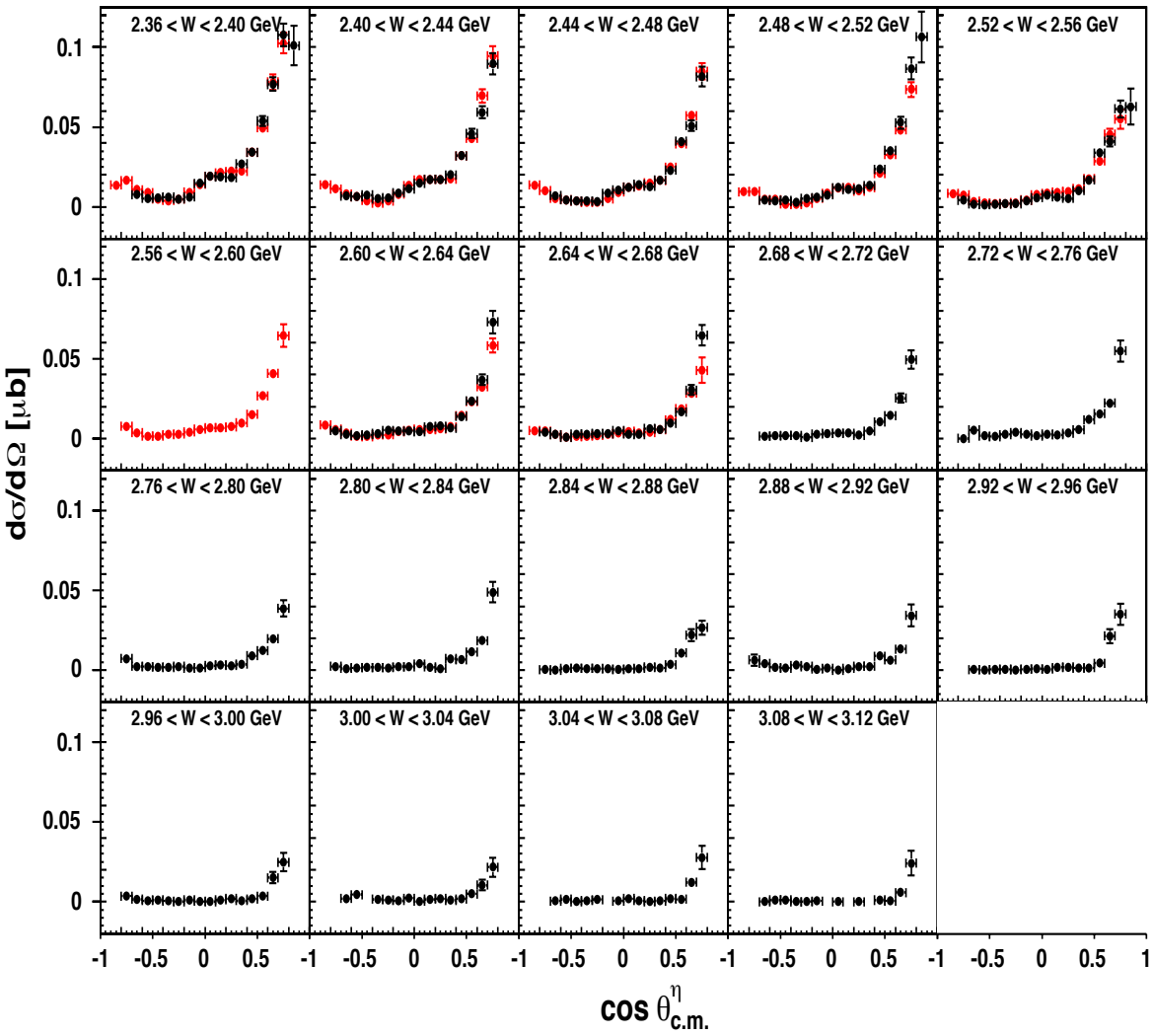


Figure 90: *The differential cross sections in the reaction $\gamma p \to p\eta$ for the center-of-mass energy range $2.36 < W < 3.12$ GeV from g12 (black data points) in comparison with the previous CLAS measurements from g11a (red point). The given uncertainties for both data sets comprise the statistical uncertainties and the Q-factor uncertainties added in quadrature.*

## 6.3 Results for the $\gamma p \to K^0\,\Sigma^+$ Reaction

Charged $K$ photoproduction, e.g. in $\gamma p \to K^+\,\Lambda$ and $\gamma p \to K^+\Sigma^0$, has been extensively studied in recent years at CLAS and elsewhere. However, the $K^0$ channel has tended to be sidelined. This appears entirely unjustified, though. To study $s$-channel resonance excitations, the photoproduction of neutral kaons offers some distinctive advantages over charged ones, because the photons cannot directly couple to the (vanishing) charge of the meson. Data on the isospin-related $K^0\,\Sigma^+$ and $K^+\,\Sigma^0$ channels are also important to disentangle contributions from $N^*$ and $\Delta^*$ resonances.

At CLAS, the differential cross sections for the reaction $\gamma p \to K^0\,\Sigma^+$ have been studied using g1c data [25] and g11a data [26, 27] but results have never been published. The additional extraction of the $\Sigma^+$ hyperon transverse polarization was also part of the research of Ref. [27] and was published as a standalone analysis in Physical Review C [31].

### 6.3.1 Differential Cross Sections in $\gamma p \to K^0\,\Sigma^+$

Figure 91 and 92 show the g12 differential cross sections of the reaction $\gamma p \to K^0\,\Sigma^+$ in 50-MeV-wide incident-photon energy bins, covering the energy range $1.15 < E_\gamma < 2.90$ GeV. The uncertainties include the $Q$-factor uncertainties and the statistical uncertainties added in quadrature.

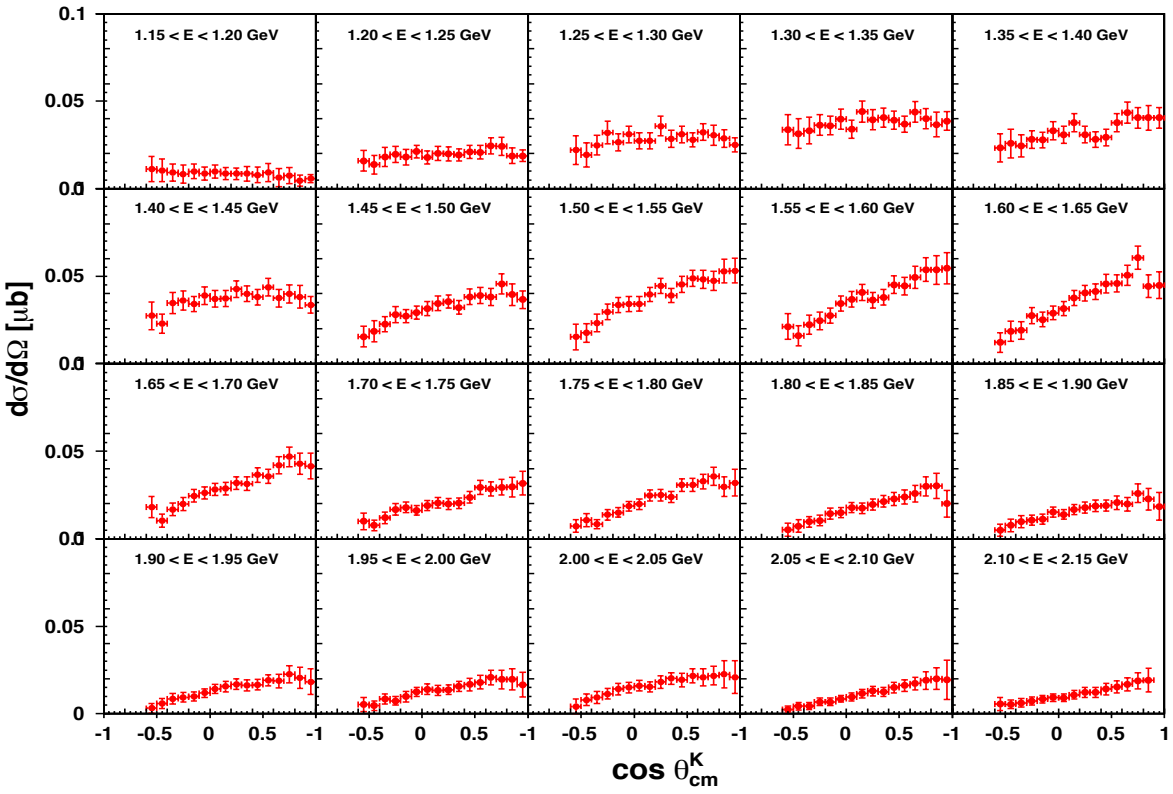


Figure 91: *The differential cross sections in the reaction $\gamma p \to K^0\,\Sigma^+$ for the incident-photon energy range $1.15 < E_\gamma < 2.15$ GeV from CLAS g12. The given uncertainties comprise the statistical uncertainties and the Q-factor uncertainties added in quadrature.*

Figure 93 shows again our CLAS-g12 differential cross sections for the reaction $\gamma p \to K^0 \Sigma^+$ (black data points), now presented in 100-MeV-wide incident-photon energy bins and covering the energy range $1.15 < E_\gamma < 2.25$ GeV. Also shown in the figure are the previous results from the CB-ELSA Collaboration (red data points) [28] and from the CBELSA/TAPS Collaboration (blue data points) [29]. We have adjusted our energy binning to these published results to facilitate the comparison. The shown uncertainties are statistical only for all data points. We consider the agreement among the data sets reasonably good.

In general, all data sets show a similar trend. The cross sections exhibit a flat distribution close to the reaction threshold, which indicates baryon resonance contributions, and then develop an almost linear forward-angle peaking behavior toward higher energies. The slope of these distributions starts to decrease again above $E_\gamma \approx 1.7$ GeV. Figure 94 shows the energy dependence of all cross section results (CLAS g12, CB-ELSA, CBELSA/TAPS) in 0.1-wide $\cos\theta_{\rm c.m.}$ bins for the $K^0$.

The CBELSA/TAPS Collaboration previously reported on an anomaly [29] which was considered visible in the CBELSA/TAPS data as a sudden drop of the cross section at forward angles around $E_\gamma \approx 1.7$ GeV. Taken directly from Ref. [29], the authors claim that *the differential cross*

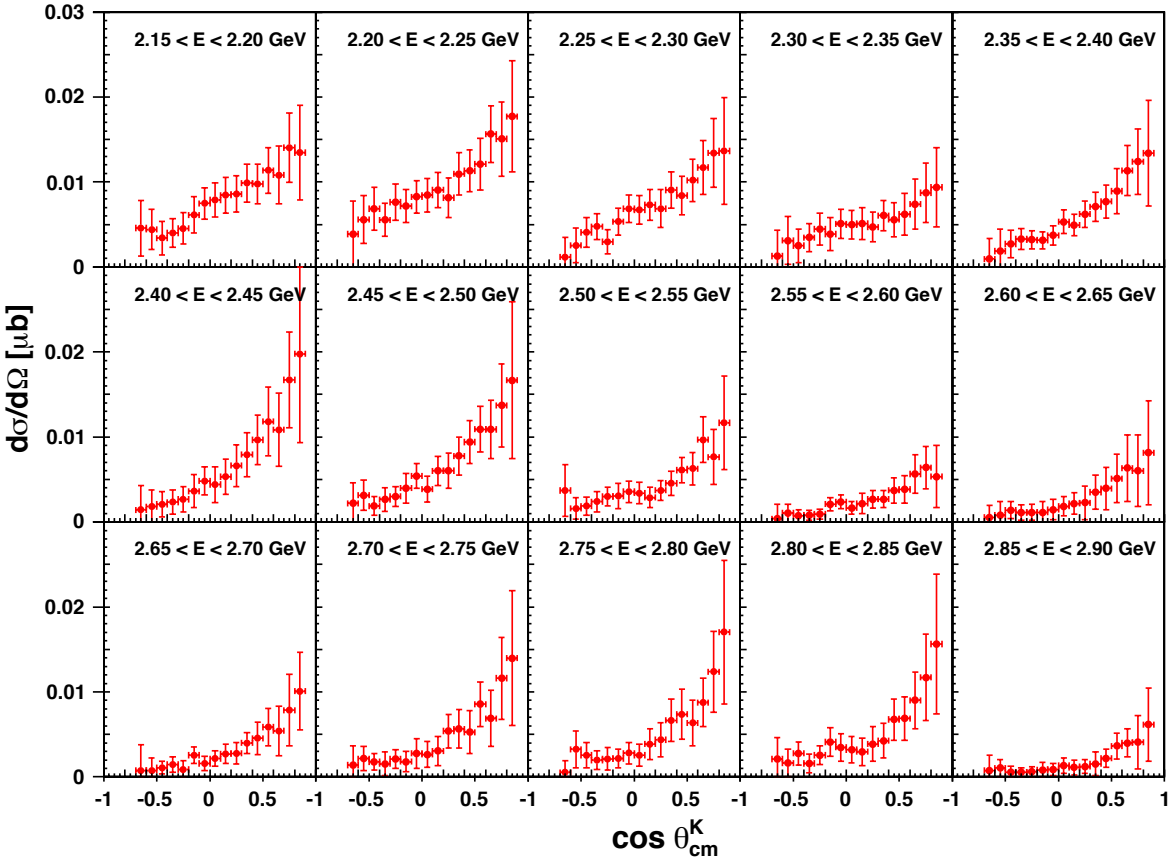


Figure 92: *The differential cross sections in the reaction $\gamma p \to K^0 \Sigma^+$ for the incident-photon energy range $2.15 < E_\gamma < 2.90$ GeV from CLAS g12. The given uncertainties comprise the statistical uncertainties and the Q-factor uncertainties added in quadrature.*

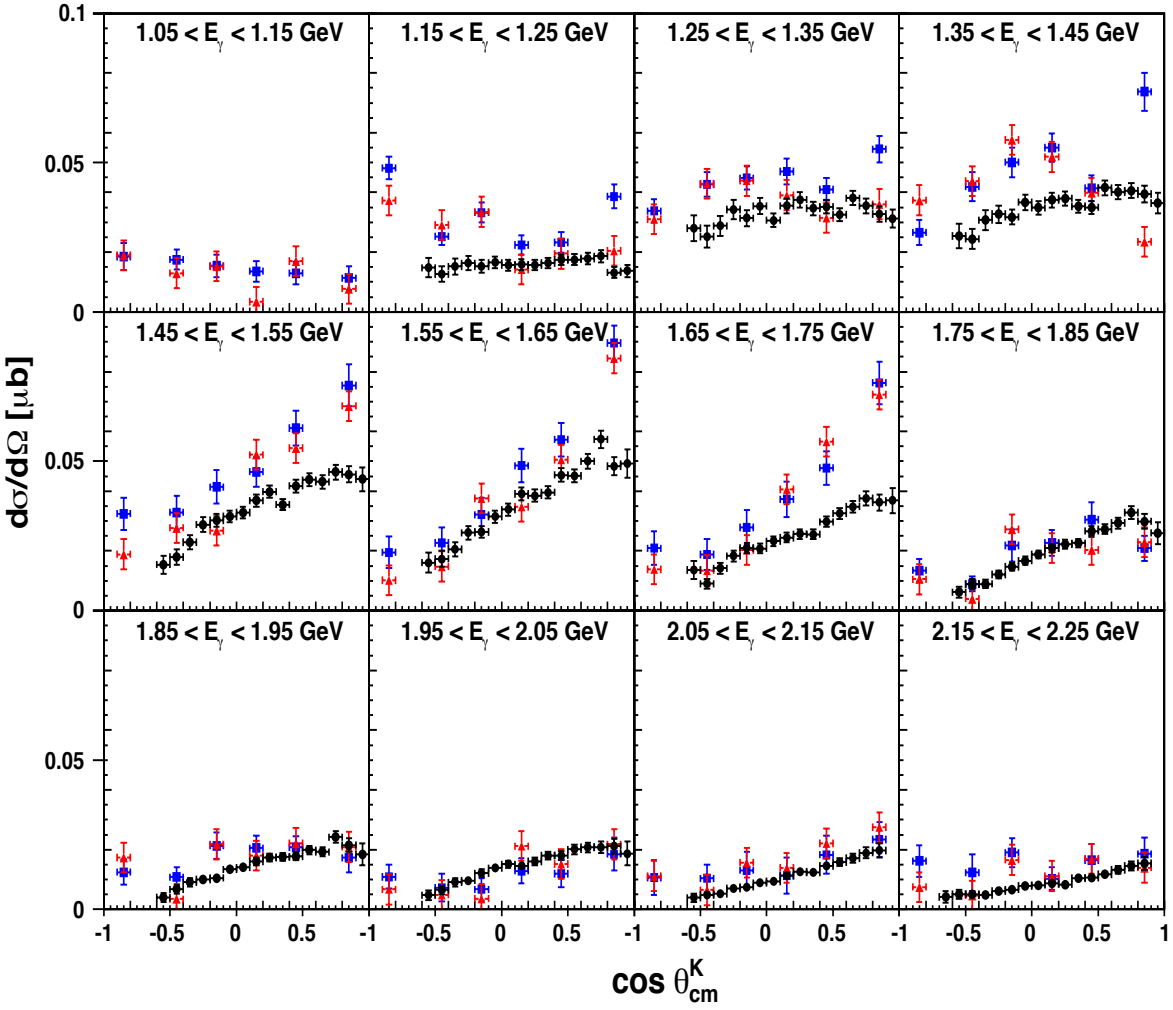


Figure 93: *The differential cross sections in the reaction $\gamma p \to K^0\,\Sigma^+$ for the incident-photon energy range $1.15 < E_\gamma < 2.25$ GeV in 100-MeV-wide energy bins from g12 (black data points) in comparison with the previous measurements from CBELSA/TAPS [29] (blue data points) and CB-ELSA [28] (red data points). The given uncertainties for the g12 data are statistical only to facilitate the comparison.*

*section exhibits increasing forward-peaking with energy, but only up to the $K^*$ threshold. Beyond, it suddenly returns to a flat distribution with the forward cross section dropping by a factor of four. In the total cross section, a pronounced structure is observed between the $K^*\,\Lambda$ and $K^*\,\Sigma$ thresholds.* In fact, the incident-photon energy bin $1.65 < E_\gamma < 1.75$ GeV (see Fig. 93) shows a fairly large discrepancy between our results and the CBELSA/TAPS results and the sudden intensity drop of the CBELSA/TAPS data is clearly seen. However, Fig. 93 also shows that our data do not exhibit this anomaly. On the contrary, the g12 cross sections show a smooth transition across all energy bins. We believe that an instrumental effect in the CBELSA/TAPS data (e.g. affecting the photon flux determination) is likely the origin for the observed sudden drop.

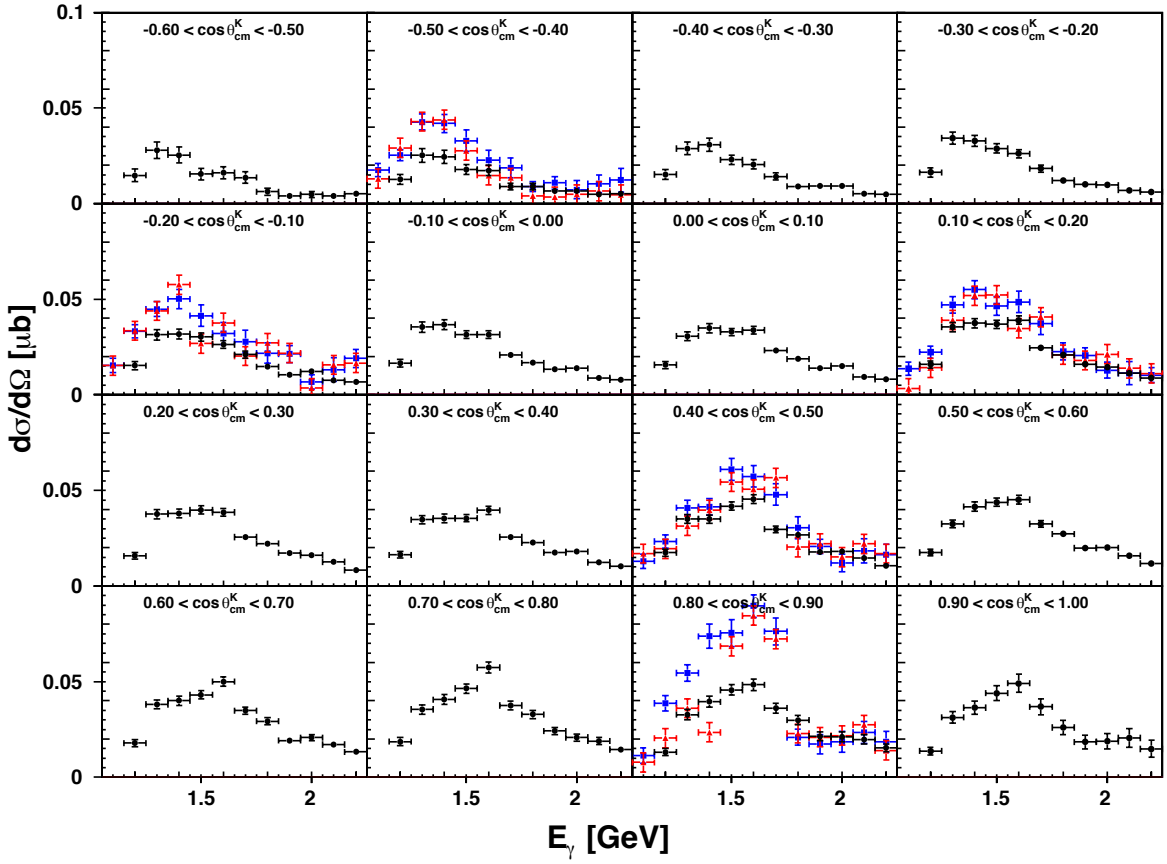


Figure 94: *The differential cross sections in the reaction* $\gamma p \to K^0\,\Sigma^+$ *for the incident-photon energy range* $1.15 < E_\gamma < 2.25$ *GeV in 0.1-wide* $\cos\theta_{\rm c.m.}$ *bins from g12 (black data points) in comparison with the previous measurements from CBELSA/TAPS [29] (blue data points) and Crystal Barrel [28] (red data points). The given uncertainties for the g12 data are statistical only to facilitate the comparison.*

### 6.3.2 Induced Hyperon Polarization in $\gamma p \to K^0\,\Sigma^+$

Figure 95, 96, and 97 show the hyperon polarization in the reaction $\gamma p \to K^0\,\Sigma^+$ from CLAS g12 in comparison with the results from three previous measurements.

(1) Figure 95 shows the hyperon polarization from CLAS g12 (red points), presented in 100-MeV-wide energy bins and covering the energy range $1.15 < E_\gamma < 3.05$ GeV. Also shown in the figure are the previous results from CBELSA/TAPS (blue points) [30]. The given uncertainties for the g12 data are the statistical uncertainties and the $Q$-factor uncertainties added in quadrature. The agreement is good within the statistical uncertainties.

(2) Figure 96 shows the hyperon polarization from CLAS g12 (red points), presented in 300-MeV-wide energy bins and covering the energy range $1.15 < E_\gamma < 2.25$ GeV. Also shown in the figure are the previous results from CB-ELSA (blue points) [28]. The given uncertainties for the g12 data are statistical only. The agreement is again good within the statistical uncertainties.

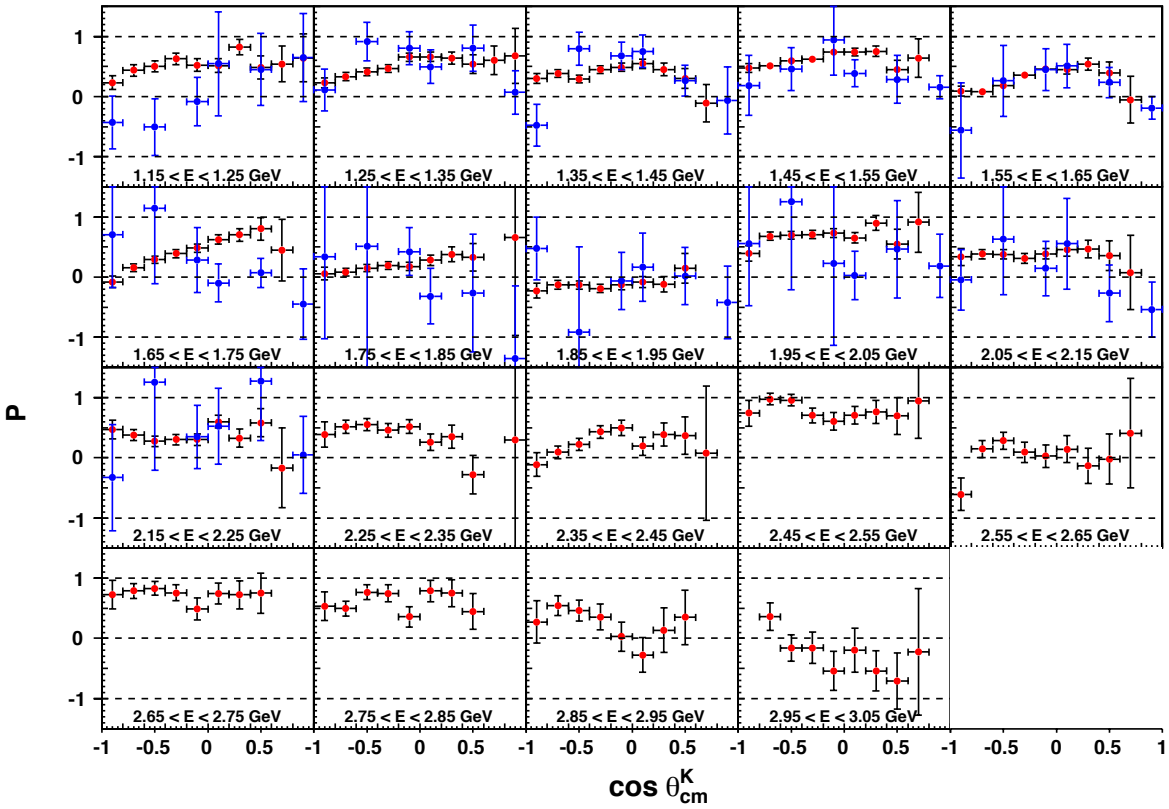


Figure 95: *The hyperon polarization in the reaction* $\gamma p \to K^0 \Sigma^+$ *for the incident-photon energy range* $1.15 < E_\gamma < 3.05$ *GeV from CLAS g12 (red points) in comparison with the previous measurements from CBELSA/TAPS [30] (blue points). The given uncertainties for the g12 data are the statistical uncertainties and the Q-factor uncertainties added in quadrature.*

(3) Figure 97 shows the hyperon transverse polarization from CLAS g12 (red points), presented in 170-MeV-wide energy bins and covering the energy range $1.16 < E_\gamma < 3.03$ GeV. Also shown in the figure are the previous results from CLAS-g11a (blue points) [31]. Please note that in this comparison, we used the incident photon and the recoiling $\Sigma^+$ to define the reaction plane, which resulted in a sign flip. The given uncertainties for the g12 data are statistical only. Major discrepancies are clearly observed, in particular at lower energies.

We have compared the unpublished cross section results of Ref. [27], which were based on the same data used for the polarization observable of Ref. [31], with our cross section results (not shown here) and also found major discrepancies. However, our angular distributions are in reasonable agreement with the unpublished cross section results of Ref. [26] (also not shown here). We do not believe that the blue data points are correct in Fig. 97, particularly for the two energy bins $1.50 < E_\gamma < 1.67$ and $1.67 < E_\gamma < 1.84$.

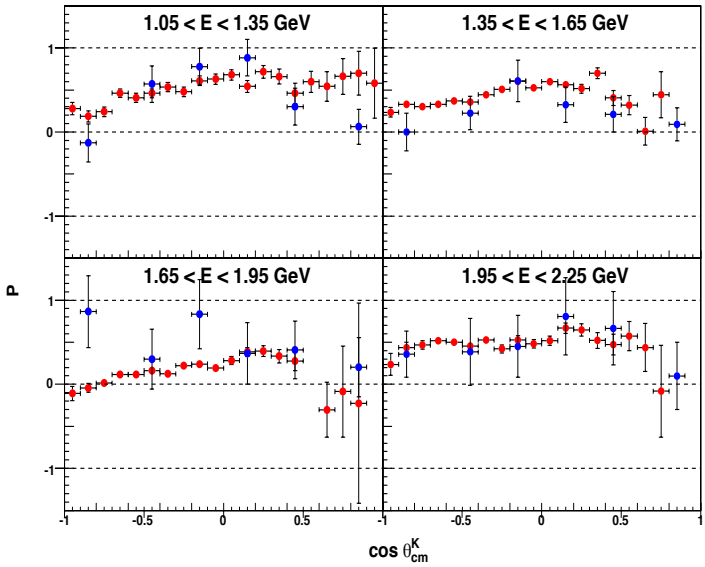


Figure 96: *The hyperon polarization for* $\gamma p \to K^0\,\Sigma^+$ *in the energy range* $1.15 < E_\gamma < 2.25$ *GeV from CLAS g12 (red points) in comparison with previous measurements from CB-ELSA [28] (blue points). The given uncertainties for the g12 data are statistical only.*

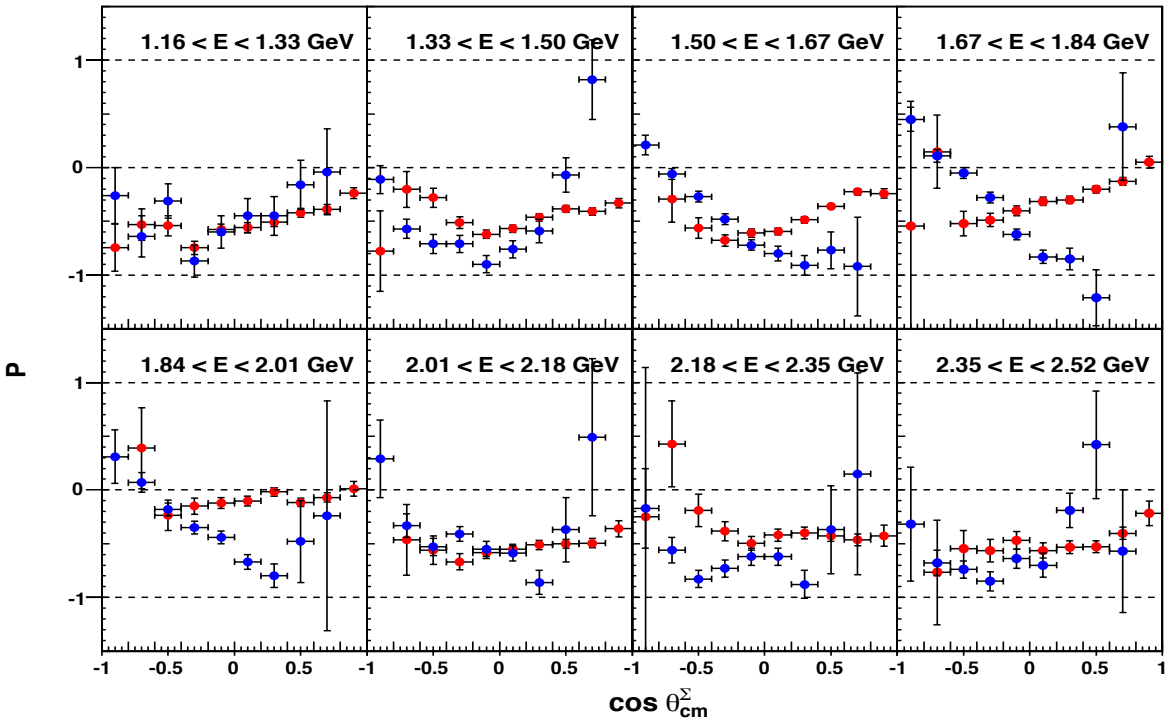


Figure 97: *The hyperon polarization for* $\gamma p \to K^0\,\Sigma^+$ *in the energy range* $1.16 < E_\gamma < 2.52$ *GeV from CLAS g12 (red points) in comparison with the previous measurements from CLAS g11a (blue points). The given uncertainties for the g12 data are statistical only.*

## 6.4 Results for the $\gamma p \to p\,\phi$ Reaction

Under construction ... Results will be added in the second iteration of this review. We apologize for the inconvenience but we would very much like the $\phi$ cross section to be part of this review.

## 6.5 Results for the $\gamma p \to p\,\pi^+\pi^-$ Reaction

The goal of our $\gamma p \to p\,\pi^+\pi^-$ analysis is to perform an event-based partial wave analysis in collaboration with the Bonn-Gatchina group. We initially included the measurement of the five-fold differential cross sections in our analysis but results are not yet available. As part of this review, we present our final results for the beam-helicity asymmetry $\mathbf{I}^{\odot}$ (see Eqn. 20).

### 6.5.1 The Beam-Helicity Asymmetry in $\gamma p \to p\,\pi^+\pi^-$

Figure 98 shows the beam-helicity asymmetry in the double-pion reaction $\gamma p \to p\,\pi^+\pi^-$, presented in 50-MeV-wide center-of-mass energy bins, covering the $W$ range $1.75 < W < 2.55$ GeV. The expected odd symmetry is clearly observed. Our results from CLAS g12 are given as blue data points; also shown in the figure are the previous results from CLAS g1c [16] (red data points). The agreement ranges from very good to excellent. The new g12 data extend the g1c energy range and provide a finer angular resolution.

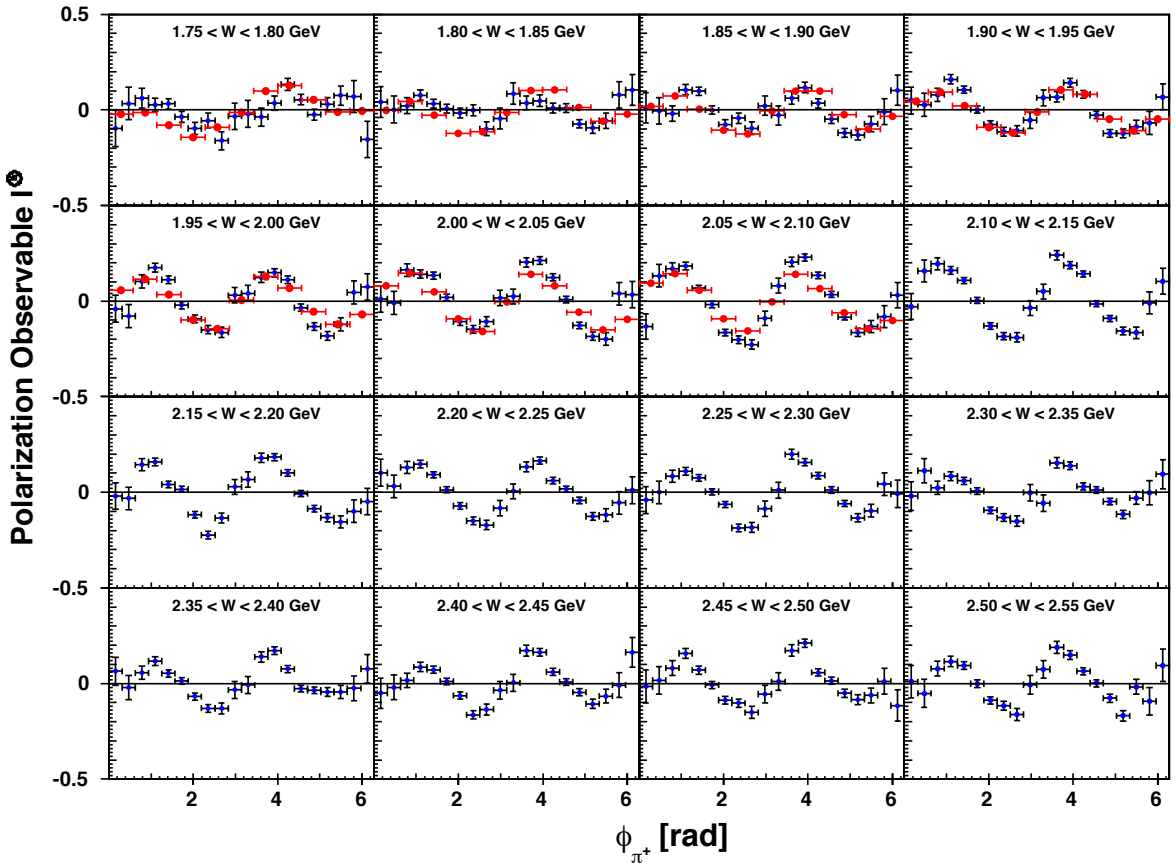


Figure 98: *The beam-helicity asymmetry in the reaction $\gamma p \to p\,\pi^+\pi^-$ for the center-of-mass energy range $1.75 < W < 2.55$ GeV from CLAS g12 (blue points) in comparison with the previous measurements from CLAS-g1c (red point). The given uncertainties in this figure for the g12 data are statistical only.*

## References


[1] B. A. Mecking *et al.*, "The CEBAF Large Acceptance Spectrometer (CLAS)," Nucl. Instrum. Meth. A **503**, 513 (2003).

[2] D. I. Sober *et al.*, "The bremsstrahlung tagged photon beam in Hall B at JLab," Nucl. Instrum. Meth. A **440**, 263 (2000).

[3] Z. Akbar *et al.*, "g12 Analysis Procedures, Statistics and Systematics," CLAS Note 2017-002 (2017).

[4] M. D. Mestayer *et al.*, "The CLAS drift chamber system," Nucl. Instrum. Meth. A **449**, 81 (2000).

[5] E. S. Smith *et al.*, "The Time-of-Flight System for CLAS," Nucl. Instrum. Meth. A **432**, 265 (1999).

[6] E. Pasyuk, "Energy-loss corrections for charged particles in CLAS," CLAS Note 2007-016 (2007).

[7] C. Patrignani *et al.* [Particle Data Group], "Review of Particle Physics," Chin. Phys. C **40**, no. 10, 100001 (2016).

[8] M. Williams *et al.* [CLAS Collaboration], "Differential cross sections and spin density matrix elements for the reaction $\gamma p \to p\omega$," Phys. Rev. C **80**, 065208 (2009).

[9] M. Williams *et al.* [CLAS Collaboration], "Differential cross sections for the reactions $\gamma p \to p\eta$ and $\gamma p \to p\eta'$," Phys. Rev. C **80**, 045213 (2009).

[10] M. Williams, "Measurement of Differential Cross Sections and Spin Density Matrix Elements along with a Partial Wave Analysis for $\gamma p \to p\omega$ using CLAS at Jefferson Lab," PhD thesis, Carnegie Mellon University (2007).

[11] M. Williams, C. A. Meyer, "Kinematic Fitting in CLAS," CLAS Note 2003-017 (2003).

[12] S. Stepanyan *et al.*, "Energy Calibration of the JLab Bremsstrahlung Tagging System," Nucl. Instrum. Meth. A **572**, 654 (2007)

[13] M. Dugger, C. Hanretty, "Correction to the incident-photon energy for g8b data," CLAS Note 2009-030 (2009).

[14] D. Applegate *et al.*, "A Detailed Study of The Sources of Systematic Errors in the CLAS g11 Data," CLAS Note 2006-017 (2006).

[15] H. Olsen and L. C. Maximon, "Photon and Electron Polarization in High-Energy Bremsstrahlung and Pair Production with Screening," Phys. Rev. **114**, 887 (1959).

[16] S. Strauch *et al.* [CLAS Collaboration], "Beam-helicity asymmetries in double-charged-pion photoproduction on the proton," Phys. Rev. Lett. **95**, 162003 (2005).

[17] Polarization of circularly polarized photon beam in g9b, `https://clasweb.jlab.org/rungroups/g9/wiki/index.php/Circular_Beam_Polarization`.

[18] W. Verkerke, D. Kirkby, "RooFit Users Manual v2.91," Document version 2.91-33, October 14th (2008).

[19] P. Weidenauer *et al.* [ASTERIX Collaboration], Z. Phys. C **59**, 387 (1993).

[20] T. D. Lee *et al.*, "Possible Detection of Parity Nonconservation in Hyperon Decay," Phys. Rev. **106**, 1367 (1957).

[21] R. Gatto, "Relations between the Hyperon Polarizations in Associated Production," Phys. Rev. **109**, no. 2, 610 (1958).

[22] W. Roberts and T. Oed, "Polarization observables for two-pion production off the nucleon," Phys. Rev. C **71**, 055201 (2005).

[23] J. Ball, E. Pasyuk, "Photon Flux Determination Through Sampling of "out-of-time" Hits with the Hall B Photon Tagger," CLAS Note 2005-002 (2005).

[24] K. Schilling, P. Seyboth and G. E. Wolf, Nucl. Phys. B **15**, 397 (1970) Erratum: [Nucl. Phys. B **18**, 332 (1970)].

[25] B. Carnahan, "Strangeness Photoproduction in the $\gamma p \to K^{)}\Sigma^{+}$ Reaction," Doctoral Dissertation (2003), The Catholic University of America.

[26] W. Tang, "Photoproduction of $K^{*+}\Lambda/\Sigma^{0}$ and $K^{0}\Sigma^{+}$ from proton using CLAS at Jefferson Lab," Doctoral Dissertation (2012), Ohio University.

[27] C. S. Nepali, Old Dominion University.

[28] R. Castelijns *et al.* [CBELSA/TAPS Collaboration], "Nucleon resonance decay by the $K^{0}\Sigma^{+}$ channel," Eur. Phys. J. A **35**, 39 (2008).

[29] R. Ewald *et al.* [CBELSA/TAPS Collaboration], "Anomaly in the $K^{0}_{S}\Sigma^{+}$ photoproduction cross section off the proton at the $K^{*}$ threshold," Phys. Lett. B **713**, 180 (2012).

[30] R. Ewald *et al.* [CBELSA/TAPS Collaboration], "Measurement of polarisation observables in $K^{0}_{s}\Sigma^{+}$ photoproduction off the proton," Phys. Lett. B **738**, 268 (2014).

[31] C. S. Nepali *et al.* [CLAS Collaboration], "Transverse polarization of $\Sigma^{+}(1189)$ in photoproduction on a hydrogen target in CLAS," Phys. Rev. C **87**, no. 4, 045206 (2013).